
ATOMIC LAYER DEPOSITION
OF PLATINUM AND GOLD

Thesis submitted for the degree of
Doctor in Sciences: Physics

MICHIEL VAN DAELE
October 2020

Promotors: Prof. Dr. ir. Jolien Dendooven
Prof. Dr. Christophe Detavernier

Members of the Jury: Prof. Dr. ir. Toon Verstraelen (UGent, chair)
Prof. Dr. ir. Roel Baets (UGent)
Prof. Dr. Seán T. Barry (Carleton)
Prof. Dr. Adrie J. M. Mackus (TU Eindhoven)
Dr. Eduardo Solano (ALBA Cells)
Prof. Dr. ir. Henk Vrielinck (UGent)

CLOSED DEFENCE 21/09/2020

PUBLIC DEFENCE 09/10/2020

This research was supported by the Research Foundation-Flanders
(FWO-Vlaanderen).

FOREWORD

In this PhD thesis a study on the atomic layer deposition of platinum and gold is presented. The research was started in September 2015 and includes results up to December 2019. Most of the research was performed within the CoCooN research group of the Department of Solid State Sciences at Ghent University.

The thesis is paper based and contains four original research articles, which are published or submitted to international journals. This work consists of an introduction chapter, to provide some context to the reader, an experimental chapter in which the working principles of the experimental techniques are briefly explained. Followed by the four research articles, which are formatted to fit this thesis and are included as stand-alone chapters. Conclusions and a perspective on possible further research are provided in the final chapter.

After more than four years of research in the fascinating field of ALD, I hope that I have managed to present my findings in a clear way for both the expert and the layman.

Michiel Van Daele
Antwerpen, October 2020

TABLE OF CONTENTS

Nederlandstalige samenvatting	ix
Summary	xv
1 INTRODUCTION	3
1.1 Atomic Layer Deposition	3
1.1.1 An example ALD process	5
1.1.2 ALD growth characteristics	6
1.2 ALD of metals	8
1.2.1 Reaction mechanisms during metal ALD	11
1.2.2 ALD of Platinum	15
1.2.3 ALD of Gold	22
1.3 Goals and outline of this thesis	25
2 EXPERIMENTAL METHODS	37
2.1 X-ray thin film characterization	37
2.1.1 X-ray reflectivity	37
2.1.2 X-ray fluorescence	38
2.1.3 X-ray photoelectron spectroscopy	41
2.2 X-ray scattering methods	43
2.2.1 X-ray diffraction	44
2.2.2 Grazing-Incidence Small-Angle X-ray scattering	45
2.3 Scanning Electron Microscopy	51
2.4 Fourier Transform Infrared spectroscopy	52
2.4.1 Molecular vibrations	52
2.4.2 FTIR setup	55
2.4.3 Raman spectroscopy	56
2.5 Gas phase analysis	58
2.6 Atomic Force Microscopy	59
3 PAPER I: SURFACE SPECIES DURING THERMAL AND PE-ALD OF PLATINUM	65
3.1 Experimental	66
3.1.1 Experimental setup	66
3.1.2 Substrates	67
3.1.3 In situ FTIR characterization	68
3.2 Results	68
3.2.1 Temperature dependence of the growth per cycle	68
3.2.2 Reference spectrum of the MeCpPtMe ₃ precursor	69
3.2.3 In situ FTIR characterization	71
3.2.4 Thermal MeCpPtMe ₃ /O ₂ process	72

3.2.5	Plasma-enhanced MeCpPtMe ₃ /O ₂ plasma process	75
3.2.6	Comparison of the thermal and plasma-enhanced processes	79
3.2.7	First exposures during thermal ALD at 100 °C . . .	81
3.3	Discussion	82
3.4	Conclusion	90
3.5	Supporting Information	92
4	PAPER II: MONITORING OF NUCLEATION AND ISLAND GROWTH MODE DURING ALD OF PLATINUM	99
4.1	Experimental Section	100
4.1.1	Transportable setup for <i>in situ</i> investigation of ALD with synchrotron radiation	100
4.1.2	Substrate preparation and ALD of Pt	101
4.1.3	GISAXS geometry	101
4.1.4	<i>In situ</i> XRF and GISAXS measurements	104
4.1.5	GISAXS data analysis	105
4.1.6	Complementary SEM and XRR measurements . . .	105
4.2	Results	106
4.2.1	<i>In situ</i> XRF: growth curve	106
4.2.2	<i>In situ</i> GISAXS: particle nucleation	106
4.2.3	<i>In situ</i> GISAXS: particle growth and coalescence . .	108
4.2.4	Strategy for analysing the GISAXS patterns	113
4.2.5	Effect of precursor dose on the Pt nucleation	121
4.3	Discussion	124
4.3.1	Particle nucleation	124
4.3.2	Particle growth and coalescence	125
4.3.3	Influence of precursor dose	126
4.4	Conclusion	127
4.5	Supporting Information	128
4.5.1	Geometrical model for fast analysis	128
5	PAPER III: PE-ALD OF GOLD	141
5.1	Experimental Section	142
5.2	Results and Discussion	145
5.2.1	ALD properties	145
5.2.2	Physical properties and film composition	151
5.2.3	Surface morphology and Raman	155
5.3	Conclusion	160
5.4	Supporting Information	162
6	PAPER IV: REACTION MECHANISM OF GOLD PE-ALD	169
6.1	Experimental Section	170
6.2	Results and Discussion	172

6.2.1	Precursor saturation and decomposition	172
6.2.2	Surface species	174
6.2.3	Reaction by-products	181
6.2.4	Reaction scheme	183
6.2.5	Nucleation on SiO ₂	187
6.2.6	Comparison of Me ₃ Au(PMe ₃)-based PE-ALD processes with different co-reactants	189
6.3	Conclusion	192
6.4	Supporting Information	194
7	SUMMARY AND FUTURE OUTLOOK	203
7.1	Investigate an ALD process, start to finish	207
7.2	Suggestions for future work	211

NEDERLANDSTALIGE SAMENVATTING - SUMMARY IN DUTCH

INLEIDING

In dit doctoraatsproefschrift worden atoomlaagdepositie (ALD) en plasma-versterkte atoomlaagdepositie (PE-ALD) processen van platina en goud onderzocht. Dit onderzochten we om beter te begrijpen hoe de reactiemechanismen tijdens de nucleatiefase en lineaire groeifase van deze processen plaatsvinden.

Atoomlaagdepositie is een variant op chemische dampdepositie (CVD), het is een dunnefilm depositietechniek die gebruik maakt van opeenvolgende chemische gas-oppervlak reacties. Bij CVD vindt continue depositie plaats omdat de gebruikte chemicaliën gelijktijdig in de reactiekamer worden binnengebracht. ALD verloopt anders, bij deze techniek is het noodzakelijk dat de chemicaliën afwisselend worden toegelaten in de reactiekamer, waardoor het gewenste materiaal op een stapsgewijze en gecontroleerde manier kan worden afgezet. Om vermenging van de chemicaliën in de reactiekamer te vermijden worden evacuatie-/spoelstappen gebruikt tussen de blootstellingen door. Als deze stappen overgeslagen worden kunnen ongecontroleerde reacties plaatsvinden tussen de chemicaliën in de gasfase en op het substraat. Een belangrijke voorwaarde voor een ALD proces is dat de oppervlakreacties, die plaats vinden tijdens elke blootstelling van het oppervlak aan de chemicaliën, zelf-limiteerd zijn. Dit betekent dat de chemische reacties tussen de gebruikte chemicaliën en het oppervlak enkel plaats kunnen vinden met bepaalde functionele groepen. Elke reactie verbruikt minstens één functionele groep, wanneer deze zijn opgebruikt wordt dit proces stopgezet en treedt er zelfsaturatie op. Dit zelf-limiterend/saturerend gedrag zorgt ervoor dat er een (sub)monolaag van materiaal wordt toegevoegd aan het oppervlak bij elke blootstelling aan de precursor. De reactanten worden daarna gebruikt om de (organische) precursor liganden van het oppervlak te verwijderen. Hierdoor kan er tijdens de volgende blootstelling opnieuw depositie plaatsvinden op het oppervlak.

ALD heeft in vergelijking met andere depositietechnieken een aantal interessante voordelen. Zo is het mogelijk om een brede waaier aan deklagen af te zetten, zoals oxides, nitrides, sulfides, fosfaten, en (edel)metalen. De zelf-limiterende/saturerende reacties en cyclische natuur van ALD zor-

gen voor een heel precieze controle over de filmdikte. De groei per cyclus van een specifiek proces is gekend en constant (in het lineair groei regime) waardoor het aantal uitgevoerde cycli de filmdikte bepaalt. De zelfsaturerende reacties zorgen voor een extreem uniforme filmdikte over een groot substraatoppervlak. Door het substraat voldoende bloot te stellen aan de precursor en de reactanten is het mogelijk een laag met een uniforme dikte op heel complexe structuren af te zetten.

Uiteraard zijn er ook nadelen verbonden aan deze depositietechniek. De groeisnelheid van ALD processen is heel laag. Dit is het gecombineerde resultaat van een lage groei per cyclus en de relatief lange duur van één cyclus. De groei per cyclus nadert voor de meeste ALD processen de atomaire lengteschaal van ~ 0.1 nm. Afhankelijk van de tijdsduur die nodig is voor evacuatie- of spoelstappen kan een enkele ALD cyclus variëren van seconden tot enkele minuten. Het is mogelijk om de cyclustijd drastisch te verkorten door gebruik te maken van "ruimtelijke" ALD, waarbij de precursor en reactanten door fysieke bufferzones van elkaar worden gescheiden. Met deze techniek is het mogelijk om groeisnelheden van ~ 1 nm/s, of omgerekend $\sim 3.6 \mu\text{m}$ per uur, te bereiken. Om dit groeitempo in perspectief te plaatsen nemen we de stelregel dat menselijk haar ongeveer 1 cm per maand in lengte groeit, of $\sim 14 \mu\text{m}$ per uur, waardoor gezegd kan worden dat ALD films trager groeien dan menselijk haar.

PLATINUM

Naast het gebruik in siervoorwerpen wordt platina ook gebruikt in technologische toepassingen. Hiervan is het gebruik van platina in de katalysatoren van wagens waarschijnlijk het meest gekende voorbeeld. Platina in de vorm van nanodeeltjes trekt veel belangstelling voor heterogene en elektrokatalyse toepassingen. De prestatie van een katalysator wordt sterk bepaald door het actieve oppervlak van de nanodeeltjes. Hierbij speelt de vorm en de grootte van de platina nanodeeltjes ook een grote rol voor de katalytische activiteit en selectiviteit. ALD is door zijn eigenschappen een aantrekkelijke depositietechniek om platina nanodeeltjes en dunnefilms af te zetten, vooral omdat het nauwgezette controle geeft over de hoeveelheid metaal dat wordt afgezet op het oppervlak en het mogelijk maakt om conformele depositie op complexe 3D substraten uit te voeren. Om ALD platinalagen te gebruiken in technologische toepassingen en de eigenschappen van deze films te bepalen is het noodzakelijk om een goed inzicht te verwerven in de nucleatie en lineaire groeifases van deze processen. Daarom gaat het eerste deel van dit werk over de lineaire groeifase van het thermische platina ALD proces (MeCpPtMe_3 - O_2 gas),

het plasma-versterkte platina ALD proces (MeCpPtMe_3 - O_2 plasma), en de nucleatiefase van het thermische platina proces.

ARTIKEL I: GROEIMECHANISME VAN PLATINUM ALD

Dit manuscript bouwt verder op de bestaande literatuur over de reactiemechanismes in het thermische platina ALD proces. Het thermische en plasma-versterkt platina ALD proces, dat gebruik maakt van MeCpPtMe_3 als precursor en O_2 gas of plasma als reactant, wordt op verschillende substraattemperaturen bestudeerd met *in situ* reflectie absorptie infrarood spectroscopie (RAIRS). De functionele groepen, die tijdens het ALD proces gevormd worden, kunnen met deze techniek geïdentificeerd worden. De oorsprong van het temperatuursafhankelijk groeitempo voor het thermische proces wordt in dit werk ook onderzocht. Bij lage substraattemperaturen ($<150^\circ\text{C}$) wordt er na blootstelling aan de precursor CH en C=C oppervlaktegroepen gedetecteerd. Deze oppervlaktegroepen zorgen voor een passivatie van het oppervlak tijdens het thermische ALD proces, waardoor er geen depositie meer kan plaatsvinden. Door O_2 plasma te gebruiken kunnen deze oppervlaktegroepen wel verwijderd worden, dit zorgt ervoor dat PE-ALD wel gebruikt kan worden bij oppervlakte temperaturen die lager zijn dan 150°C . Boven een substraattemperatuur van 150°C worden geen CH vibraties gedetecteerd en verminderen de C=C vibraties, wijzende op dehydrogenatie reacties en reorganisatie van de liganden. Bovendien onthullen de Fourier transform infrarood spectroscopie (FTIR) metingen dat na de precursor blootstelling er extra verbrandingsproducten gevormd worden tijdens het PE-ALD proces. Voor beide processen worden de oppervlaktegroepen verwijderd tijdens de blootstelling aan het reactant. Hierbij worden hydroxyl (OH) groepen gevormd op het oppervlak, dit gebeurt zowel bij hoge en lage oppervlakte temperaturen. We besluiten dat de temperatuursafhankelijke vermindering in het groeitempo voor het thermisch proces gebeurt omdat het platinaoppervlak de precursor liganden niet kan dehydrogeneren en herstructureren, waardoor het oppervlak tijdens het proces gepassiveerd wordt.

ARTIKEL II: NUCLEATIE TIJDENS PLATINUM ALD

Het begrijpen van het nucleatiegedrag van metaal ALD processen is van groot belang voor verscheidene toepassingen. Daarom wordt de nucleatiefase van het thermische platina ALD proces bestudeerd op een vlak SiO_2 substraat op 300°C door middel van *in situ* X-stralen fluorescentie (XRF) en scherpende-inval kleine-hoek X-stralen verstrooiing (GISAXS). De evolu-

tie van de belangrijkste verstrooiingspieken geeft inzicht in de groei van de platinadeeltjes, beginnend bij kleine geïsoleerde kernen tot coalescentie van de deeltjes in wormachtige structuren. Een analyse strategie wordt geïntroduceerd om snel informatie over de grootte, vorm, en spatiëring van de platinadeeltjes te verkrijgen uit de GISAXS data. De resultaten wijzen op een nucleatiefase die gevolgd wordt door een regime waarin diffusiegedreven deeltjesgroei plaatsvindt. In het tweede groeiregime neemt de gemiddelde deeltjesdichtheid af en worden lateraal uitgerokken deeltjes gevormd. De groei van de platina nanodeeltjes wordt dus niet enkel bepaald door de adsorptie van platina precursor moleculen en de daaropvolgende verbranding van de liganden, maar is voornamelijk bepaald door de dynamische uitwisseling van migrerende platina atomen en clusters op het oppervlak tussen naburige platina nanodeeltjes en diffusiegedreven deeltjescoalescentie. Daarnaast werd de invloed van de precursordosis op de nucleatie en groei van de platinadeeltjes onderzocht. Hieruit blijkt dat de nucleatiesnelheid sterk beïnvloed wordt door de precursordosis. Verasend genoeg wordt de morfologie van de platinadeeltjes bepaald door de hoeveelheid platina dat afgezet wordt op het oppervlak en heeft de gebruikte precursordosis tijdens het thermisch proces geen invloed op de morfologie. Deze resultaten tonen aan dat het gecombineerd gebruik van *in situ* GISAXS en XRF metingen een uitstekende experimentele strategie is om fundamentele inzichten te verkrijgen over de rol van de depositieparameters op de morfologie van de platinadeeltjes.

GOUD

Omdat goud quasi niet reactief is wordt het vooral gebruikt om juwelen, munten, en andere decoratieve stukken te vervaardigen. Goud in de vorm van nanodeeltjes heeft echter een aantal heel interessante optische en katalytische eigenschappen. Hierdoor is er de laatste jaren enorm veel onderzoek uitgevoerd naar het gebruik van gouden nanodeeltjes in toepassingen voor heterogene katalyse. Gouden nanodeeltjes worden vaak voor hun inherente optische eigenschappen gebruikt in suspensies, bijvoorbeeld in het vervaardigen van robijn glas. Deze optische eigenschappen zijn afkomstig van resonanties van gelokaliseerde oppervlak plasmonen die aanwezig zijn op het metaaloppervlak. Met behulp van deze plasmomen kunnen elektromagnetische hotspots gecreëerd worden tussen metalen structuren waardoor het Ramansignaal enorm versterkt kan worden. Typisch zijn hiervoor heel goed geordende nanostructuren nodig om dergelijke oppervlak-versterkte Ramanspectroscopie (SERS) substraten te maken. Door de eigenschappen van deze nanostructuren op het

SERS substraat is het zelfs mogelijk om één enkele molecule te detecteren. Om ALD goudlagen te incorporeren in praktische toepassingen is het noodzakelijk om een aantal werkende ALD processen te hebben. Verder dient men te beschikken over een uitstekend begrip van de nucleatie- en lineaire groeifase van deze processen. Daarom gaat het tweede deel van deze thesis over de ALD eigenschappen van een nieuw goud PE-ALD proces dat ontwikkeld is tijdens dit proefschrift en het lineaire groei reactiemechanisme van dit nieuwe proces.

ARTIKEL III: EEN NIEUW GOUD ALD PROCES

In dit manuscript werd een nieuw goud PE-ALD proces ontwikkeld en werden de ALD eigenschappen bepaald. Het proces maakt gebruik van $\text{Me}_3\text{Au}(\text{PMe}_3)$ als de precursor en H_2 plasma als reactant. Dit proces kan gebruikt worden op lage substraattemperaturen en heeft een breed temperatuursvenster van 50°C to 120°C . Het heeft een groeitempo van 0.030 ± 0.002 nm per cyclus op een goud zaadlaag en zowel precursor als reactant vertonen zelfsaturerend gedrag. Uiterst zuivere goud films kunnen worden afgezet met dit proces; <1 atomaire % koolstof en zuurstof, en <0.1 atomaire % fosfor als onzuiverheden, zoals bepaald met X-stralen fotonelectron spectroscopie (XPS). Op oxide oppervlakken worden er gouden nanodeeltjes afgezet. Tijdens de depositie coalesceren deze deeltjes in wormachtige nanostructuren. Omdat de goudfilm afgezet wordt in de vorm van nanodeeltjes is dit geschikt om een Ramansignaal te versterken. Hiermee is het mogelijk om een Ramansignaal te versterken dat slechts één orde lager is in grootte dan de allernieuwste SERS technieken. Dit wordt bereikt zonder de eigenschappen van de goudfilm te optimaliseren. Door de katalytische eigenschappen van gouden nanodeeltjes is het mogelijk om ALD goud te gebruiken in heterogene katalyse toepassingen.

ARTIKEL IV: GROEIMECHANISME VAN GOUD ALD

In dit manuscript worden *in situ* RAIRS en *in vacuo* XPS metingen gebruikt om te bepalen welke oppervlaktegroepen er aanwezig zijn tijdens het goud ALD proces. Hieruit blijkt dat CH_3 en PMe_3 liganden op het goudoppervlak blijven na chemisorptie van de precursor. Deze oppervlaktegroepen zorgen voor het zelfsaturerend gedrag tijdens de precursordosis. De oppervlaktegroepen worden verwijderd door het H_2 plasma en omgezet naar CH_4 en waarschijnlijk naar PH_xMe_y groepen (x,y : 0-3). Hierdoor kan tijdens de volgende precursordosis opnieuw chemisorptie van de precursor plaatsvinden. Het decompositie gedrag van de precursor op

een goudoppervlak wordt onderzocht en hieruit blijkt dat de decompositie van de precursor stijgt met de temperatuur boven een substraattemperatuur van 100 °C. Op een substraattemperatuur van 120 °C wordt de decompositiecomponent groter dan de groei per cyclus van het ALD proces, waardoor het ALD proces zich begint te gedragen zoals een CVD proces. Aangezien deze liganden verantwoordelijk zijn voor het zelflimiterend gedrag tijdens het ALD proces, kan dit decompositiegedrag verklaard worden door de stabiliteit van de precursor liganden op een goudoppervlak. De CH₃ liganden desorberen tijdens de evacuatiestap naar hoog vacuüm en dit vindt plaats op elke substraattemperatuur van het ALD temperatuursvenster. Maar dit proces verloopt sneller bij een hogere temperatuur. Bij deze hogere temperaturen worden de PMe₃ liganden minder stabiel op het goudoppervlak en dit vertaalt zich in een toename van de precursordecompositie op het goudoppervlak. Dit toont aan dat het zelfsaturerend gedrag van de precursoradsorptie bepaald wordt door de temperatuursafhankelijke stabiliteit van de precursorliganden op het goudoppervlak. Verassend genoeg vindt de precursordecompositie niet plaats op een SiO₂ oppervlak en *in situ* transmissie absorptie infrarood metingen wijzen erop dat de nucleatie op een SiO₂ oppervlak plaatsvindt op Si-OH oppervlaktegroepen. Het gebruik van andere reactanten (O₂ plasma en H₂O) werd onderzocht in een pomp-type ALD systeem en dit werd vergeleken met een goudfilm die afkomstig is van een spoel-type reactor. Door een O₂ plasma te gebruiken als reactant wordt er een amorfe goud-fosfaat film afgezet in plaats van een metallische goudfilm. Wanneer H₂O wordt vervangen door H₂ plasma als reactant is het mogelijk om metallische goud films te verkrijgen, echter dit is niet voldoende om de fosfaat onzuiverheden te verwijderen van het oppervlak.

SUMMARY

INTRODUCTION

In this thesis atomic layer deposition (ALD) and plasma-enhanced atomic layer deposition (PE-ALD) processes of platinum and gold are investigated. The aim is to obtain a better understanding of the reaction mechanisms that govern the steady growth and nucleation of these processes.

ALD is a variant of chemical vapour deposition (CVD) and can be defined as a thin-film deposition technique that is based on the sequential use of self-terminating gas-solid reactions. While for CVD the used chemicals are introduced simultaneously in the reaction chamber, allowing continuous deposition, ALD uses alternating exposures of vapour/gas phase chemicals (precursor and co-reactants) to deposit the desired material on a substrate in a step wise and controlled manner. The precursor and co-reactant exposures are separated by pump or purge steps to avoid mixing of the chemicals, which can lead to uncontrolled reactions in the gas-phase or on the substrate. An important requirement for an ALD process is that the surface reactions, occurring during every exposure, are self-terminating. This means that the used chemical is only able to react with certain sites on the substrate and during the reaction these reactive sites are consumed. Because of this self-limiting reaction behaviour, the precursor, that carries the metal atom of the desired material, usually adds a (sub)monolayer of material to the surface during every exposure step. The purpose of the co-reactants is to remove the precursor ligands from the surface and make it possible for the following precursor exposure to react with the surface, which allows the deposition process to continue.

ALD as a deposition method has some interesting properties and advantages compared to other deposition methods. It is possible to deposit a wide variety of coating materials, including oxides, nitrides, sulphides, phosphates, and (noble) metals. The combination of the self-saturating behaviour and cyclical nature gives ALD precise control over the film thickness. The growth per cycle (GPC) for a process is known and constant (in the linear growth regime) and the film thickness can be selected by adjusting the number of ALD cycles. The self-saturating behaviour also results in excellent uniformity of the film thickness over large substrates and excellent conformality on complex structures. This can be achieved by using

sufficient exposures of the used precursors and co-reactants, which given enough exposure will eventually fully coat very complex 3D substrates.

These advantages inevitably come at a cost, which is a slow deposition speed for most ALD processes, due to the combination of a low GPC and the relatively long duration of a single cycle. The GPC for most processes lies close to the atomic length scale of ~ 0.1 nm/cycle. For time separated purge steps the total time for a single ALD cycle can vary between a few seconds to several minutes, depending on the used exposure and purge times. It is possible to reduce the time for a single cycle significantly when using spatial ALD, for which the precursor and co-reactants are not separated in time but in space and growth speeds up to ~ 1 nm/s, or ~ 3.6 μm per hour can be achieved. To put this number in perspective, assuming the rule of thumb that human hair grows at roughly 1 cm per month or ~ 14 μm per hour it can be said that ALD films grow slower than human hair.

PLATINUM

Apart from the use in ornamental pieces, platinum finds its use in technological applications. Probably the most known example is the use of Pt as a catalyst in the catalytic converter of automotive vehicles. Platinum in the form of nanoparticles and nanoclusters on a support is of major interest for heterogeneous catalysis and electrocatalysis applications. For catalytic applications the particle shape and size is closely linked to their catalytic activity and selectivity, while the performance of a supported catalyst also depends on the nanoparticle coverage and active surface area. This makes ALD an attractive deposition technique to deposit platinum nanoparticles and ultrathin layers as it offers sub-monolayer control over the metal loading/layer thickness and enables conformal deposition on complex 3D substrates. In order to incorporate ALD deposited platinum in practical applications and influence the properties of the deposited films it is necessary to have a good understanding of the nucleation and steady growth behaviour of these processes. Therefore, the first part of this thesis will cover the steady growth mechanism of the thermal Pt ALD process (MeCpPtMe_3 - O_2 gas) and plasma enhanced Pt ALD process (MeCpPtMe_3 - O_2 plasma) and the nucleation behaviour of the thermal Pt ALD process.

ARTICLE I: STEADY GROWTH MECHANISM OF PLATINUM ALD

This paper builds upon the body of existing literature concerning the reaction mechanisms that are involved for the thermal platinum ALD process. The thermal ALD and PE-ALD of platinum, using MeCpPtMe_3 as precursor and O_2 gas or O_2 plasma as reactant, are studied with *in-situ* reflection absorbance infrared spectroscopy (RAIRS) at different substrate temperatures. This is done to identify the functional groups that are present during platinum ALD and investigate the origin of the temperature dependent growth rate of the thermal process. Evidence is given that CH and C=C containing species are present on the surface after precursor exposure at low substrate temperatures ($<150^\circ\text{C}$), poisoning the surface during thermal ALD. Both species are removed by O_2 plasma enabling PE-ALD below 150°C through combustion reactions. Above 150°C , no CH stretching modes were detected and the C=C vibration diminished, indicating dehydrogenation reactions and ligand restructuring. In addition, the PE-ALD Fourier transform infrared spectroscopy (FTIR) spectra revealed the presence of combustion reaction products on the surface after precursor exposure. These were removed during the reactant exposure and during this exposure the formation of surface OH groups was found for both high and low substrate temperatures. We conclude that the decrease in growth rate for the thermal process is caused by the inability of the surface to properly dehydrogenate and restructure the poisoning precursor ligands.

ARTICLE II: NUCLEATION OF PLATINUM ALD

Understanding the nucleation behaviour of metal ALD processes is of significant importance for several applications. Therefore, *in situ* investigations of thermal platinum ALD at 300°C on planar SiO_2 substrates by means of X-ray fluorescence (XRF) and grazing-incidence small-angle X-ray scattering (GISAXS) are presented. The evolution in key scattering features provides insights into the growth kinetics of platinum deposits from small nuclei to isolated islands and coalesced worm-like structures. An analysis approach is introduced and verified that it is a valid method to extract dynamic information on the average real space parameters, such as Pt cluster shape, size, and spacing. The results indicate a nucleation stage, followed by a diffusion-mediated particle growth regime which is marked by a decreasing average areal density and formation of laterally elongated Pt clusters. Growth of the Pt nanoparticles is thus not only governed by the adsorption of Pt precursor molecules from the gas-phase and subse-

quent combustion of the ligands, but is largely determined by the dynamic exchange of migrating Pt species on the surface between neighbouring Pt nanoparticles and diffusion-driven particle coalescence. Moreover, the influence of the Pt precursor dose on the particle nucleation and growth is investigated. It is found that the precursor dose has a large influence on the nucleation speed, while the evolution of particle morphology as a function of Pt coverage is in fact not influenced at all by the used precursor dose for oxygen based co-reactants. These results show that combining *in situ* GISAXS and XRF measurements provides an excellent experimental strategy to obtain new fundamental insights of the role of deposition parameters on the morphology of Pt ALD depositions.

GOLD

Gold has found widespread use in jewellery, coinage, and decorative pieces due to its unreactive nature. Moreover, gold in the form of nanoparticles has some very interesting optical and catalytic properties. The catalytic properties of nanoparticulate gold has attracted significant interest for heterogeneous catalysis. Suspended gold nanoparticles (or colloidal gold) are often used for their inherent optical properties (e.g., colloidal gold in ruby glass). The optical properties arise due to the localised surface plasmon resonances (LSPR) that develop at the metal surface. The LSPR can create electromagnetic hotspots between metallic structures and these hotspots can cause enormous enhancement of a Raman signal. In general, highly ordered nanostructures are required for solid state surface enhanced Raman spectroscopy (SERS) substrates. By tuning the properties of the nanostructures on the SERS substrate, it is possible to achieve single molecule detection. In order to incorporate ALD deposited gold layers/films in practical applications it is beneficial to have a decent selection of ALD processes and have a good understanding of their nucleation and steady growth behaviour. Therefore, second part of this thesis will report the ALD properties of a new gold PE-ALD process and investigate its steady growth reaction mechanism.

ARTICLE III: A NEW GOLD ALD PROCESS

A new PE-ALD process for gold deposition was developed and its ALD characteristics were determined. The process utilizes $\text{Me}_3\text{Au}(\text{PMe}_3)$ as the precursor and H_2 plasma as the co-reactant. The process can be employed at low substrate temperatures and over a broad temperature window: $50\text{ }^\circ\text{C}$ to $120\text{ }^\circ\text{C}$. A growth rate of 0.030 ± 0.002 nm per cycle on gold

seed layers is achieved and both precursor and co-reactant exposures exhibit saturating behaviour. The process deposits very pure gold films (<1 atomic % carbon and oxygen impurities, and <0.1 atomic % phosphorous obtained from X-ray photoelectron spectroscopy (XPS)). The process forms gold nanoparticles on oxide surfaces, which coalesce into worm-like nanostructures during deposition. The particular nanostructure of as-deposited films offers stable free-space Raman enhancement, slightly more than one order of magnitude lower than state-of-the-art solid-state substrates, but with room for further optimization. Beyond the use in surface-enhanced Raman spectroscopy (SERS), nanoparticulate gold has very interesting and useful catalytic properties, making the reported gold nanoparticle ALD process also highly relevant towards heterogeneous catalysis applications.

ARTICLE IV: STEADY GROWTH MECHANISM OF GOLD ALD

In situ RAIRS and *in vacuo* XPS measurements confirm that CH₃ and PMe₃ ligands remain on the gold surface after chemisorption of the precursor, causing self-limiting adsorption. Remaining surface groups are removed by the H₂ plasma in the form of CH₄ and likely as PH_xMe_y groups (x,y: 0-3), allowing chemisorption of new precursor molecules during the next exposure. The decomposition behaviour is investigated and it is found that above 100 °C the amount of precursor decomposition increases with substrate temperature and at 120 °C the decomposition becomes larger than the GPC of the ALD process, leading to chemical vapour deposition (CVD) growth behaviour. This decomposition behaviour is linked to the stability of the precursor ligands that govern the self-limiting growth during ALD. Desorption of the CH₃ ligands occurs at all substrate temperatures during evacuation to high vacuum, occurring faster at higher temperatures. The PMe₃ ligand is found to be less stable on a gold surface at higher substrate temperatures and is accompanied by an increase in precursor decomposition on a gold surface, indicating that the temperature dependent stability of the precursor ligands is an important factor to ensure self-limiting precursor adsorption during ALD. Remarkably, precursor decomposition does not occur on a SiO₂ surface, *in-situ* transmission absorption infrared experiments indicate that nucleation on a SiO₂ surface occurs on Si-OH groups. The use of O₂ plasma and H₂O as co-reactants in a pump-type ALD system is compared to the gold films that are obtained in a flow-type reactor. Instead of a metallic gold film, amorphous gold-containing phosphate films were obtained. Changing the H₂O

exposure to H₂ plasma leads to the formation of metallic films, although it is not sufficient to remove the phosphate impurities.

ACRONYMS

AFM	atomic force microscopy
ALD	atomic layer deposition
CVD	chemical vapour deposition
DWBA	distorted wave Born approximation
EDX	energy dispersive X-ray spectroscopy
FTIR	Fourier transform infrared spectroscopy
GISAXS	grazing-incidence small-angle X-ray scattering
GPC	growth per cycle
IMFP	inelastic mean free path
IR	infrared
LMA	local monodisperse approximation
LSPR	localised surface plasmon resonances
PE-ALD	plasma-enhanced atomic layer deposition
PVD	physical vapour deposition
QMS	quadrupole mass spectrometry
RAIRS	reflection absorbance infrared spectroscopy
RBS	Rutherford backscattering spectrometry
SDD	sample-to-detector distance
SEM	scanning electron microscopy
SERS	surface-enhanced Raman spectroscopy
TEM	transmission electron microscopy
UHV	ultra-high vacuum
XPS	X-ray photoelectron spectroscopy
XRD	X-ray diffraction
XRF	X-ray fluorescence
XRR	X-ray reflectivity

ACRONYMS AND ABBREVIATIONS OF CHEMICAL COMPOUNDS

acac	acetylacetone
Cp	cyclopentadienyl
TMA	trimethylaluminium
MeCpPtMe ₃	trimethyl(methylcyclopentadienyl)platinum(IV)
Pt(acac) ₂	platinum(II) acetylacetonate
Pt(DDAP)	dimethyl(N,N-dimethyl-3-butene-1-amine-N)platinum
PtMe ₂ -hexadiene	[(1,2,5,6-η)-1,5-hexadiene]-dimethyl-platinum(II)
Me ₃ Au(PMe ₃)	trimethylphosphinotrimethylgold(III)
Me ₂ Au(S ₂ CNEt ₂)	dimethylgold(III)-(diethylthiocarbamate)

Part I

INTRODUCTION

"I'm going on an adventure"
— J.R.R. Tolkien, *The Hobbit*

INTRODUCTION

The research topic of this thesis lies in the field of atomic layer deposition (ALD), in particular the sub-field of metal ALD. This chapter aims to familiarize the reader with this field and to provide some context to the research results that will be presented in the following chapters.

1.1 ATOMIC LAYER DEPOSITION

ALD is a variant of chemical vapour deposition (CVD) and can be defined as a film deposition technique that is based on the sequential use of self-terminating gas–solid reactions.^[1] While for CVD the used chemicals are introduced simultaneously in the reaction chamber, allowing continuous deposition, ALD uses alternating exposures of vapour/gas phase chemicals (precursor and co-reactants) to deposit the desired material on a substrate in a step wise and controlled manner. The precursor and co-reactant exposures are separated by pump or purge steps to avoid mixing of the chemicals, which can lead to uncontrolled reactions in the gas-phase or on the substrate. An important requirement for an ALD process is that the surface reactions, occurring during every exposure, are self-terminating. This means that the used chemical is only able to react with certain sites on the substrate and during the reaction these reactive sites are consumed. Self-limiting also requires that the gas-solid reactions do not create additional reactive sites and thus the amount of available reactive sites decreases with every gas-solid reaction that occurs. Because of this self-limiting reaction behaviour, the precursor, that carries the metal atom of the desired material, usually adds a (sub)monolayer of material to the surface during every exposure step. The purpose of the co-reactants is to remove the precursor ligands from the surface and make it possible for the following precursor exposure to react with the surface, which allows the deposition process to continue. Thus ALD processes are cyclical and with every cycle a fixed amount of material is deposited. Due to the self-limiting nature it is possible to deposit materials on very complex substrates.

ALD as a deposition method has some interesting properties and advantages compared to other deposition methods. It is possible to deposit a wide variety of coating materials, including oxides, nitrides, sulphides,

phosphates, and (noble) metals. The substrate temperature for most ALD processes lies below 400 °C, which makes these processes back end of line compatible and allows their use in the production of integrated circuits. For some processes it is possible to use substrate temperatures below 100 °C and even room temperature, which is ideal for applications that require temperature sensitive substrates. The combination of the self-saturating behaviour and cyclical nature gives ALD precise control over the film thickness. The growth per cycle (GPC) for a process is known and constant (in the linear growth regime) and the film thickness can be selected by adjusting the number of ALD cycles. The self-saturating behaviour also results in excellent uniformity of the film thickness over large substrates and excellent conformality on complex structures. This can be achieved by using sufficient exposures of the used precursors and co-reactants, which given enough exposure will eventually fully coat very complex 3D substrates. This is not easy to achieve for a pure line-of-sight technique such as physical vapour deposition, or for CVD for which the deposition rate depends on the flux of precursor, which tends to vary with penetration depth for high-aspect ratio structures.

These advantages inevitably come at a cost, which is a slow deposition speed for most ALD processes, due to the combination of a low GPC and the relatively long duration of a single cycle. The GPC for most processes lies close to the atomic length scale of ~ 0.1 nm/cycle. Although, depending on the ALD process the GPC may vary over one or two orders of magnitude. For time separated purge steps the total time for a single ALD cycle can vary between a few seconds to several minutes, depending on the used exposure and purge times. It is possible to reduce the time for a single cycle significantly when using spatial ALD, for which the precursor and co-reactants are not separated in time but in space. For example, in the case of the thermal Al_2O_3 ALD process growth speeds up to ~ 1 nm/s, or $\sim 3.6 \mu\text{m}$ per hour, can be achieved in spatial ALD systems.^[2] To put this number in perspective, assuming the rule of thumb that human hair grows at roughly 1 cm per month or $\sim 14 \mu\text{m}$ per hour it can be said that ALD films grow slower than human hair. Of course time is money,¹ making ALD a rather expensive technique due to these low deposition speeds and on the other hand it requires some very specific equipment and (precursor) chemicals and generally these are not cheap.

¹ With an estimated word count of 60 000 and an average reading speed of 200-250 words per minute, this manuscript consists of roughly 4-5 hours of reading fun.

1.1.1 An example ALD process

This section will explain the steps that are required to bring one ALD cycle to completion. For this purpose, the thermal aluminium oxide ALD process, using trimethylaluminium (TMA) and water (H_2O), will be explained as it is generally considered to be a standard and well understood ALD process.^[1] The sequence of steps to perform a single ALD cycle is displayed in Figure 1.1;

A) **TMA EXPOSURE** TMA vapour is brought into the ALD reaction chamber and will react with reactive sites that are present on the substrate surface, in this case hydroxyl groups (-OH) (Figure 1.1a). The methyl (CH_3) ligands of the TMA molecule react with the hydroxyl groups, forming methane (CH_4) as a by-product and creating a bond between the oxygen atom and aluminium atom as given by:



with (s) and (g) denoting surface and gas-phase species, respectively. The reaction between the TMA molecules and the surface stops when the accessible hydroxyl groups are consumed, resulting in self-limiting behaviour of the TMA exposure.

B) **PUMP/PURGE STEP** The formed CH_4 and excess TMA molecules are removed from the reaction chamber (Figure 1.1b). Depending on the type of ALD reactor this is either done by evacuating the chamber to its base pressure or purging it by using a flow of inert gas.

C) **H_2O EXPOSURE** After the TMA and reaction by-products are removed from the chamber the surface is exposed to H_2O vapour (Figure 1.1c). The water molecules will react with the surface CH_3 groups (Figure 1.1d), producing surface -OH groups and CH_4 as a by-product, given by:



D) **SECOND PUMP/PURGE STEP** The formed CH_4 groups and excess H_2O molecules are removed from the reaction chamber (Figure 1.1d). This is either done by evacuating the chamber or purging it by using a flow of inert gas. After this step, the surface has gained a (sub)monolayer of Al_2O_3 , terminated with reactive -OH groups. The surface can then be exposed to TMA molecules to continue the ALD process.

This discussion of the thermal TMA/ H_2O ALD process is an idealised and simplified version of this process, serving as an illustration of the ALD

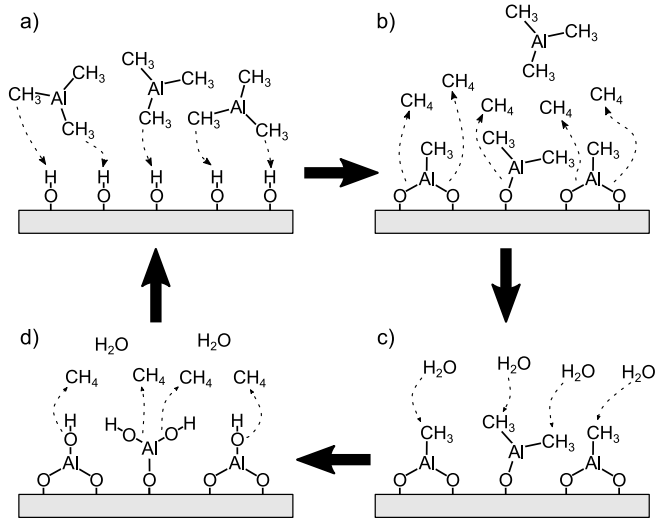


Figure 1.1: Schematic representation of an aluminium oxide ALD process, using TMA and H_2O as precursor and co-reactant, respectively. a) TMA exposure, b) purge of excess precursor and by-products, c) H_2O exposure, d) purge of excess H_2O vapour and by-products.

technique. It does not account for the inclusion of H and C impurities in the film due to incomplete reactions and steric hindrance.

1.1.2 ALD growth characteristics

SATURATION One requirement of an ALD process is that each exposure step needs to exhibit self-limiting chemical reactions. This is achieved when chemisorbing molecules reduce the total number of reactive chemical sites on the substrate. When all reactive sites have been consumed the chemisorption process stops and saturation of the surface is achieved, as shown in the saturation curves in Figure 1.2a. The shown curves rise quickly at the beginning and then flatten out once saturation is achieved. For very reactive precursors and surface groups (solid grey line) the point of saturation, marked by the grey arrow, is achieved very quickly, while for less reactive species (dashed black line) more exposure is required to reach this point, marked by the black arrow. If the molecules decompose on the surface the "apparent" GPC will increase linearly with the used exposure (indicated by the solid red line). This type of behaviour is referred to as CVD-type growth and is undesired in an ALD process as it leads to uncontrolled deposition. While an ideal ALD precursor does not exhibit

any decomposition, reality is often less ideal and some precursors will have a small decomposition fraction on the surface. This will add a slope to the flat section of the saturation curve, as shown by the dashed red line in Figure 1.2a.

TEMPERATURE DEPENDENCE Chemical reactions determine the growth mechanism of ALD and usually temperature has a large influence on the reaction rate. Because of this it can be expected that the substrate temperature is an important parameter in any ALD process. While the influence of the temperature depends on the specific process there are some typical effects the temperature has on the GPC, as depicted in Figure 1.2b.

For a low substrate temperature chemical reactions may be hindered because of a lack of thermal activation energy, leading to a decrease in the GPC. On the other hand, a low temperature may cause condensation of the precursor on the surface. This will lead to the unsaturated physisorption of precursor on the surface and an increase in the GPC.

For a high substrate temperature the thermal stability of the precursor plays a key role. Thermal decomposition of the precursor on the surface will lead to unsaturated growth behaviour as there is no limit to how much of the precursor can adsorb during each exposure. As a result, the GPC will increase due to the CVD-type growth. Another possibility is that chemically active surface groups are removed from the surface, deactivating the surface and leading to a decrease in the GPC.

Between this high and low temperature regions the ALD process exhibits a region of saturated behaviour, which is typically called the ALD temperature window. The GPC in this window does not have to be constant, as the main requirement is the saturating behaviour of the surface reactions and with varying temperature the concentration of functional groups or steric hindrance can have an influence on the obtained GPC.

LINEARITY The saturation property, that is expected for an ALD process, leads to a predictable film thickness. The GPC determines how much material is added by each cycle and the film thickness can be expressed as:

$$\text{Thickness} = \text{GPC} \times (\text{Number of cycles}) \quad (1.1)$$

This results in linear growth behaviour as is depicted in Figure 1.2c. In the ideal case there is no delay of deposition on a surface, due to nucleation (marked by the grey line). (Un)fortunately, a lot of ALD processes are not ideal and the linear growth is preceded by a nucleation region (marked by the black line). This is especially the case for the deposition of

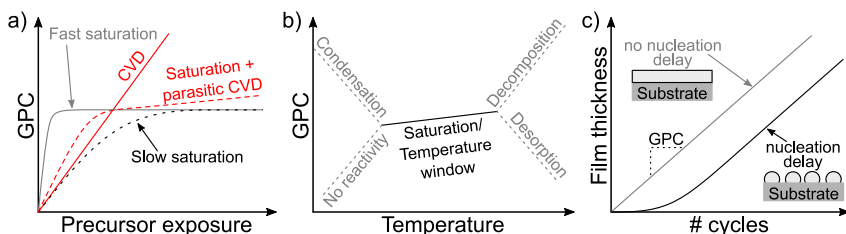


Figure 1.2: Simplified graphs depicting typical ALD growth properties. a) Saturation behaviour, b) GPC temperature dependence, c) growth behaviour. Figure adapted from [3, 4]

(noble) metals, for which discontinuous films are generally deposited on oxide surfaces, unless special pretreatments are used on the substrate to enhance the nucleation and formation of a closed film.

1.2 ALD OF METALS

Depositing elemental metallic films is rather difficult using ALD. A first reason is due to the typical precursors that are used during ALD which generally consist of a metal cation as the central atom, surrounded by ligands. To deposit oxides and nitrides ligand exchange can occur to deposit the desired material in thermal processes, during which no change in oxidation state occurs for the metal cation. While in processes that use plasma as the co-reactant the cation is often oxidised further. This is fine for depositing oxides and nitrides, however, in order to deposit metallic films it is necessary to use an additional reduction step. Another reason is that most metals are easily oxidised when they come in contact with oxygen. This means that only extremely low background concentrations of oxygen can be tolerated in the ALD chamber, or the deposited film will oxidise during deposition. In addition, the use of oxidising co-reactants needs to be avoided for elements that form strong bonds with oxygen, because it is often not straightforward to reduce the metal oxide once it is formed. An exception is the class of noble metals, which are elements that are known for their resistance to corrosion and oxidation.

Although it is difficult to deposit elemental films of transition metals this has not stopped researchers from developing ALD processes for them, see Figure 1.3 and the bottom section of Table 1.1. Surprisingly it is possible to deposit noble metals using oxidising co-reactants, due to the relative ease to reduce them to their metallic state. Since this discovery a lot of research has been performed to investigate the reaction mechanism of these

Element	First process	Publications by 2010	Publications by 2020
Al	2002[6]	2	3
Ti	2000[7]	2	4
Cr	2013[8]	0	1
Fe	2003[9]	1	2
Co	2003[9]	22	32
Ni	2000[10]	9	19
Cu	1997[11]	29	40
Mo	2011[12]	0	1
Ru	2003[13]	51	74
Rh	2005[14]	2	2
Pd	2003[15]	11	17
Ag	2007[16]	2	10
Sn	2018[17]	0	1
Ta	2000[7]	6	6
W	2000[18]	33	41
Re	2018[19]	0	1
Os	2012[20]	0	1
Ir	2004[21]	16	20
Pt	2003[5]	37	43
Au	2015[22]	0	3

Table 1.1: Reference counts are obtained from the atomic limits website.[23]

noble metal processes and the thermal platinum ALD process, introduced by Aaltonen et al. in 2003,^[5] has become a model system for noble metal ALD.

Metal films have a broad range of potential applications in the fields of microelectronics, catalysis, (surface enhanced) Raman spectroscopy... Depending on the application the deposited film needs to be a continuous layer or can be made up of individual particles, for which the particle size, shape, and inter-particle distance will be important parameters to tune the properties of the particles (catalytic, optical, ...). Most metal ALD processes tend to have a long nucleation period and particle growth mode before forming fully closed layers. The nucleation and particle growth mode behaviour can be influenced in several ways, for example by using different substrates, performing additional pre-treatment steps, or using different ALD process parameters (precursor/co-reactant exposure, substrate temperature). This gives some control over the type of film that is deposited, closed layers or composed of particles, by carefully choosing the appropriate parameters.

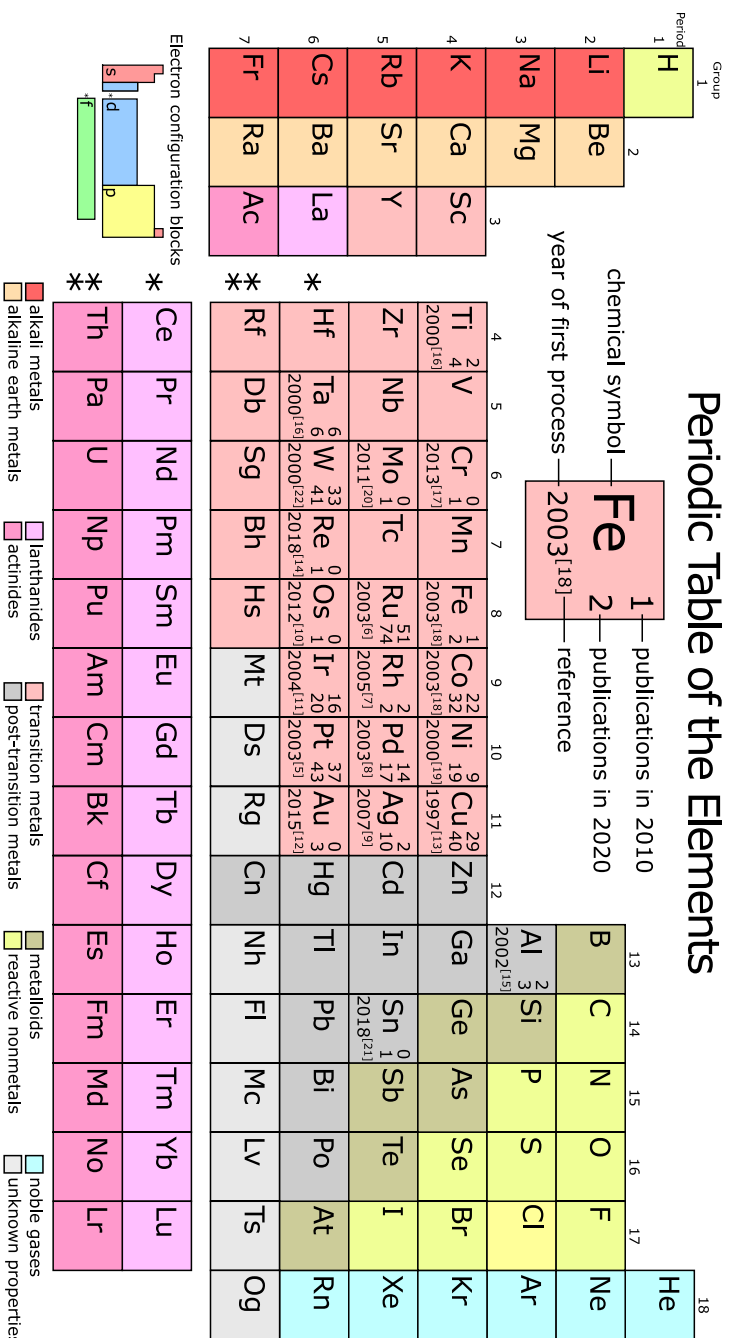


Figure 1.3: Periodic table of metal ALD processes. The reference counts are obtained from the atomic limits website.[23]

Of course in order to properly control the properties of the deposited films it is important to have a good understanding of the reaction mechanisms during the steady growth of metal-on-metal, as well as the mechanisms that control and can therefore be used to tailor the nucleation behaviour of the metal on different substrates. The following section will sketch the current understanding of the reaction mechanisms that govern metal ALD processes. A literature overview on ALD of platinum and gold is given in the last section of this chapter.

1.2.1 *Reaction mechanisms during metal ALD*

The organometallic precursors that are used for metal ALD typically consist of a cation metal center surrounded by anionic organic ligands. The metal center needs to be reduced to a neutral oxidation state in order to deposit metallic films and to avoid gas phase side-reactions this redox reaction needs to take place on the surface of the substrate. The precursor needs to chemisorb in a self-limiting manner on the substrate during steady growth conditions. The chemisorption step can be dissociative for which the precursor ligands are transferred to the surface. Under steady growth conditions, the surface will be metallic and hence have electrons in the conduction band that can be used during surface reactions. Density functional theory calculations indicate that during adsorption the electronic charge is delocalised between the surface and precursor.^[24] This means that the metallic center is partially reduced and the surface atoms are partially oxidised and the precursor ligands may be transferred to the surface atoms (dissociative chemisorption). Saturation occurs when no more precursor molecules can adsorb due to steric hindrance by the precursor ligands or because the surface is no longer metallic in nature, preventing redox reactions between the surface and additional precursor molecules.

After saturation, the surface is covered with precursor ligands and partially oxidised (see step 1b in Figure 1.4 and Figure 1.5). To continue the ALD process the surface needs to be reduced and the ligands need to be removed or replaced with other functional groups. The metal ALD processes can be divided in two main classes, depending on the source of electrons that are required for the reduction step. Both classes are used in this thesis and are discussed in the following sections.²

² The explained mechanisms are based on the paper by Elliot et al.^[24]

1.2.1.1 Reducing with the co-reactant

After saturation with the precursor the metal atoms of the surface are partially oxidised (M^{n+}) and covered with precursor ligands (X). A reducing co-reactant ($Y + e^-$) can be used as the electron source for the reduction step. There are several types of co-reactants that can be, and have been, used in ALD processes, such as: H_2 , hydrides, amines, hydrazines, organometallic compounds, and organic molecules. An electron of the co-reactant is donated to the surface atoms and the co-reactant will react with the precursor ligands and form a volatile molecule (XY) that is removed from the surface. This continues until the entire surface is reduced to its metallic state, and the precursor ligands are removed from the surface (step 2a).

The co-reactant is then able to further reduce the surface (step 2b) and is able to form surface groups on the surface. The following step is to expose the surface to the precursor ($M^{n+}X_n$ in step 1a), which will oxidise the surface to a neutral state, remove the surface groups that are formed during step 2b, and add metal atoms to the surface. It is possible that the adsorbed surface groups are not formed at all or that they are so unstable that only negligible amounts will be present during the following precursor exposure. In this case a so-called "abbreviated cycle" will take place and the addition of metal atoms will only occur in step 1b. This means that processes with an abbreviated cycle tend to have a lower GPC than processes with a complete cycle.

1.2.1.2 Reducing with the precursor-ligands

Instead of using an external electron source for reduction, it is also possible to use the metal precursor itself as the reducing agent. Because spontaneous reduction would lead to CVD reactions, the precursor needs to be metastable against intermolecular reduction, which allows for controlled saturating behaviour.^[24] The reduction step needs to be triggered by the interaction between the co-reactant and the precursor ligands. For these reactions an oxidizing co-reactant is used, such as oxygen gas, oxygen plasma, or ozone.

After the surface is exposed to and saturated by the precursor (Figure 1.5 step 1b) the surface is exposed to the oxidizing agent. The co-reactant will combust the hydrocarbon precursor ligands (C_xH_z) and create CO_2 , H_2O , and C_xH_{z+1} as the combustion by-products (step 2a). This reaction continues until the precursor ligands are removed, leaving the surface in a partially metallic (M^0) and partially oxidized state ($M^{n+}O$). This is followed by further oxidation of the metallic surface (step 2b). For

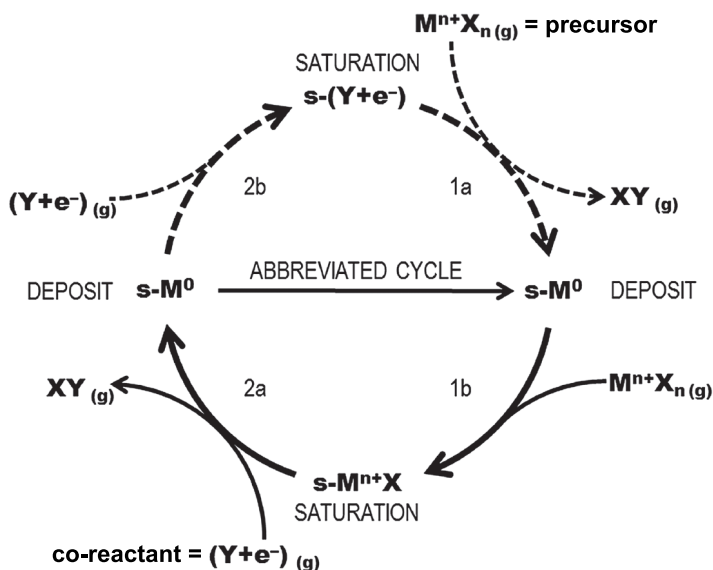


Figure 1.4: The schematic mechanistic cycle for a co-reactant as the reducing agent. MX_n is the metal precursor (pulse 1) and $(Y + e^-)$ symbolizes a reducing co-reactant (pulse 2); for example, if $Y = H^+$, then $H = (Y + e^-)$ is a hydrogen radical or half of a H_2 molecule. "s" refers to the surface and "(g)" to the gas phase. The dashed arrows indicate uncertainty in steps 2b and 1a and a cycle without these steps is termed "abbreviated". Reprinted from [24], with permission from AIP publishing.

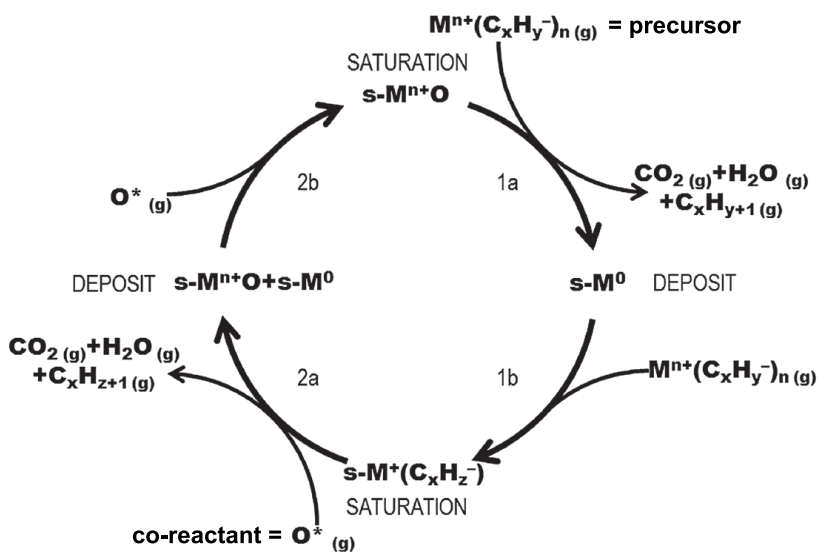


Figure 1.5: Cyclic mechanism of metal ALD when a hydrocarbon-based ligand of the metal precursor acts as a reducing agent while the co-reactant is an oxidizing agent (such as O-plasma). Reprinted from [24], with permission from AIP publishing.

metals that are resistant to oxidation, the oxide layer will remain limited to the top layer, while for easily oxidized metals it is possible that sub-surface oxide layers are formed. If a sub-surface oxide layer is formed it is difficult to completely remove the oxide from the film during the following precursor exposure. This indicates that for most metals this reaction scheme will not work and a reducing co-reactant needs to be used. After the top layer is oxidised it can be reduced during the precursor exposure (step 1a). During this step the oxygen atoms from the MO_x surface layer will combust the precursor ligands, again forming CO_2 , H_2O , and $\text{C}_x\text{H}_{2x+1}$ as the combustion by-products. Once the oxygen atoms are consumed, the surface will be metallic in nature and adsorption of additional precursor molecules can occur (step 1b).

1.2.2 ALD of Platinum

Apart from the use in ornamental pieces, platinum finds its use in technological applications. Probably the best known example is the use of Pt as a catalyst in the catalytic converter of automotive vehicles. Because of the electrical, electrochemical, and catalytic properties of platinum there is a lot of interest to use it as an electrode material for fuel cells, electrolyzers and as a catalyst in chemical production.^[25-33] Platinum in the form of nanoparticles and nanoclusters on a support is of major interest for heterogeneous catalysis and electrocatalysis applications. For example, for CO/NO_x oxidation in catalytic converters, hydrogen reforming, production of nitric acid, the oxygen reduction reaction in fuel cells, and the hydrogen evolution reaction in water electrolysis.^[34-38] For catalytic applications there are several factors that influence the behaviour and performance. For instance, the particle shape and size is closely linked to their catalytic activity and selectivity, while the performance of a supported catalyst also depends on the nanoparticle coverage and active surface area.^[39,40]

Therefore, to deposit platinum nanoparticles and ultrathin layers ALD is an attractive deposition technique as it offers sub-monolayer control over the metal loading/layer thickness and enables conformal deposition on complex 3D substrates.^[49] In order to incorporate ALD deposited platinum in a practical application it is advantageous to have a decent selection of available ALD processes and a good understanding of their nucleation and steady growth behaviour. The reported platinum ALD processes are summarized in Table 1.2 and the used precursors are shown in Figure 1.6. The most successful platinum precursor is the MeCpPtMe_3 molecule and its thermal process, at 300°C using O_2 gas as the co-reactant,

Precursor	Reactant	T_{sub} (in °C)	GPC(Å/cycle)	Author (et al.)/Year
Pt(acac) ₂	H ₂			Utriainen/2000 [10]
	O ₃	140-200	0.55-0.75	Hämäläinen/2008 [41]
MeCpPtMe ₃	O ₂	150-300	0.45	Aaltonen/2003 [5]
	O ₂ [*]	200-300	0.45	Knoops/2009 [42]
	H ₂	170		Hoover/2009 [43]
	O ₂ [*] /H ₂ [*]	21-300	0.4	Mackus/2013 [44]
	O ₃	100-300	0.45	Dendooven/2013 [45]
	N ₂ [*]	250-300	0.3	Longrie/2012 [46]
	NH ₃ [*]	250-300	0.4	Longrie/2012 [46]
Pt(DDAP)	O ₂	100-340	0.6-0.85	Lee WJ./2019 [47]
PtMe ₂ -hexadiene	O ₂	80-300	0.2-0.9	Lee J./2016 [48]

Table 1.2: Reported platinum ALD processes, with their ALD temperature window and GPC. (*) denotes the use of plasma as co-reactant.

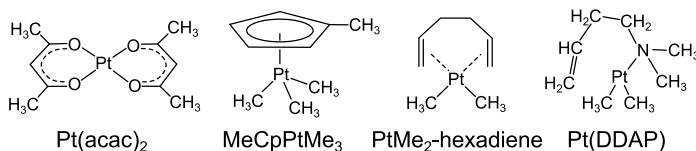


Figure 1.6: Platinum precursors that have been used for ALD.

is the most widely adopted platinum ALD process. This process was introduced in 2003 by Aaltonen et al. and was rapidly followed by a large amount of publications, that investigate the reaction mechanism of the process.^[5] The following sections will discuss the literature concerning the steady growth regime reaction mechanism and the nucleation behaviour for the standard thermal Pt process and the MeCpPtMe₃/O₂ plasma process. The steady growth mechanism of the thermal Pt ALD process (MeCpPtMe₃ - O₂ gas) and plasma enhanced Pt ALD process (MeCpPtMe₃ - O₂ plasma) are discussed in Chapter 3, and the nucleation behaviour of the thermal Pt ALD process is discussed in Chapter 4.

1.2.2.1 Steady growth regime and its reactions

Aaltonen et al. proposed a combustion reaction mechanism in which molecular O₂ is dissociated on the Pt surface, yielding atomic O that can combust the ligands of the MeCpPtMe₃ molecules. After the O₂ gas exposure, the surface is covered with a layer of adsorbed O. During the subsequent precursor exposure, the O atoms that are present on the surface can re-

act with incoming precursor molecules and partially combust the ligands, leaving reaction products on the surface, see Figure 1.7a.

The proposed combustion chemistry during both the MeCpPtMe₃ precursor exposure and the O₂ reactant exposure were corroborated by *in situ* quadrupole mass spectrometry (QMS) measurements, revealing the production of CO₂ and H₂O during both ALD half-cycles.^[13] Later, the formation of CH₄ during the precursor exposure was detected by Kessels et al. using gas phase Fourier transform infrared spectroscopy (FTIR).^[53] The formation of CH₄ was explained by hydrogenation of the methyl groups in the MeCpPtMe₃ precursor, occurring through ligand exchange between the methyl ligands and surface hydroxyl (OH) groups. The formation of CH₄ during the precursor exposure was also reported by Christensen et al. using QMS.^[51] They found that 79% of the precursor carbon is released during the O₂ exposure and the other 21% is released during the MeCpPtMe₃ exposure as CO₂ (3%) and CH₄ (18%), see Figure 1.7b. The CH₄ signal was broad compared to that of CO₂ indicating that the hydrogenation reactions are slower than the combustion of the precursor ligands with available surface oxygen.

Hydrogenation of methyl groups is possible through two reaction mechanisms. The first mechanism, which was proposed by Elliot, involves hydrogenation by transient hydroxyl groups as each combustion reaction can form one hydroxyl group.^[54] The formed hydroxyl species can recombine with other hydroxyl groups to form water or hydrogenate a methyl ligand to form methane. Mackus et al. proposed a second mechanism,^[50] where the hydrogenation of methyl groups occurs through hydrogen species that are present on the surface. These species can originate from dehydrogenation reactions of the precursor ligands. This idea is based on surface science literature that shows the dehydrogenation of cyclopentadienyl (Cp) ligands on a platinum surface at substrate temperatures above 207 °C.^[55]

The thermal ALD process is usually applied at 250-300 °C because the growth rate significantly decreases for lower temperatures and complete growth inhibition occurs below 150 °C, see Figure 1.7c.^[42,50,56] To achieve growth below 150 °C other reactants than O₂ gas can be used, for example O₂ plasma or ozone. A thermal process able to deposit metallic Pt down to a substrate temperature of 100 °C using ozone as the reactant was reported by Dendooven et al.^[45] Bosch et al. were able to grow metallic Pt at room temperature using a three step process that included O₂ plasma and H₂ plasma.^[57] The temperature dependence of the growth rate of the thermal process was investigated using a time-resolved QMS analysis of the formation of CH₄ (by hydrogenation) and CO₂ (by combustion) during both ALD half-cycles at different temperatures by Erkens et al.^[56] They

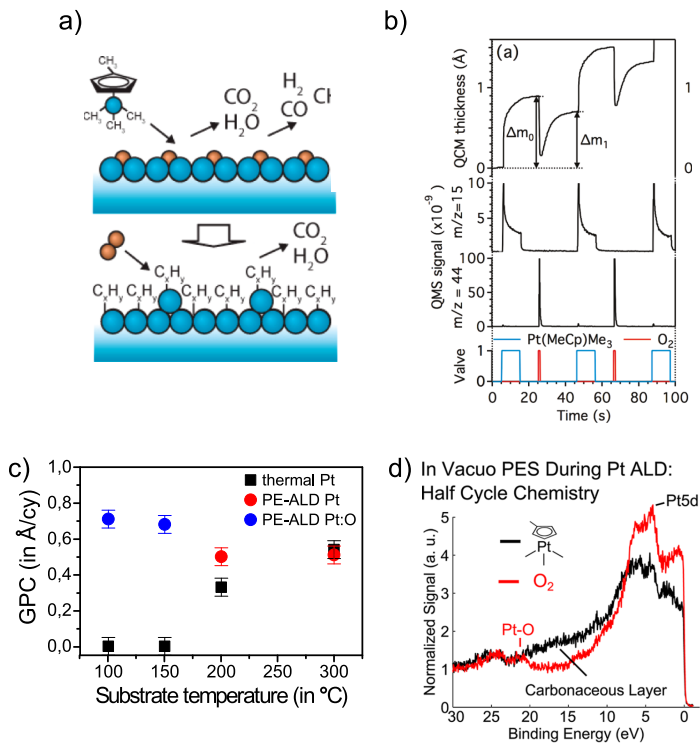


Figure 1.7: Composite figure of literature data. a) Surface groups that are present after both half-cycles for the MeCpPtMe₃ - O₂ ALD process. Reprinted with permission from [50]. Copyright 2012 American Chemical Society. b) QCM data and QMS data for CH₃⁺ and O₂⁺ reaction by-products during the MeCpPtMe₃ - O₂ ALD process. Reprinted with permission from [51] Copyright 2009 American Chemical Society. c) Growth curves of MeCpPtMe₃ - O₂ (plasma) as a function of substrate temperature. d) Photoemission data showing the presence of a carbonaceous layer after the MeCpPtMe₃ exposure in the MeCpPtMe₃ - O₂ ALD process. Reprinted with permission from [52]. Copyright 2013 American Chemical Society.

showed that there is a correlation between the temperature dependence of the combustion rate and the Pt growth rate. Below 100 °C no combustion is able to take place. Between 100 and 250 °C combustion occurs but at a slower rate when compared to the third region above 250 °C. For this third region the combustion happens almost instantaneously. The temperature dependence of the combustion rate was furthermore linked to the state of the surface following the precursor pulse based on knowledge from surface science studies. The deposition temperature is suggested to influence the nature of the carbonaceous or hydrocarbon layer on the surface which inhibits the oxidation reactions and may prevent hydrogenation reactions of methyl to methane. However, experimental evidence for the nature of the surface species during Pt ALD is still lacking.

Only a limited number of surface studies have been performed to directly identify the surface species during Pt ALD. Synchrotron radiation has been used in a vacuo photo emission study by Geyer et al., see Figure 1.7d.^[52] They found that a carbonaceous layer is formed during precursor exposure and gets removed after the reactant exposure. Recently, Vandalon et al. reported a broadband sum-frequency generation spectroscopy study of the thermal Pt ALD process at different temperatures in the range 80-300 °C. They detected CH₃ groups and C=C bonds on the surface following the Pt precursor pulse. The coverage of CH₃ groups decreased with temperature, while the C=C contribution was found to be relatively constant over the whole temperature range.^[58] Performing FTIR spectroscopy during the steady state growth regime of Pt ALD has proven challenging because free carriers in Pt absorb infrared radiation.^[59,60] This limits transmission FTIR studies to either gas phase measurements or nucleation studies.^[53,57] By using a reflection geometry for the FTIR measurements it is possible to circumvent the experimental limitation that is encountered in a transmission geometry. In this thesis *in situ* reflection absorbance infrared spectroscopy (RAIRS) experiments were used to identify the surface species that are present during the thermal and plasma-enhanced platinum ALD processes and the obtained insights will be discussed in Chapter 3.

1.2.2.2 Nucleation

Although ALD is traditionally perceived as a layer-by-layer technique, ALD processes for noble metals are often characterized by a nucleation-controlled growth on oxide surfaces. Due to a lack of sufficient chemisorption sites for the precursor and dissociation sites for the co-reactant (which aids in the removal of the precursor ligands) on the substrate, and the need for metals to form a crystal structure. After a certain incubation pe-

riod, growth is initiated in localized islands spread across the surface. This Volmer-Weber type island growth can be used advantageously for the deposition of noble metal particles, e.g. for applications in catalysis.^[61–64]

Despite numerous reports on noble metal nanoparticle deposition by ALD and tuning of the particle size by the number of ALD cycles,^[49,62,65–68] the mechanisms that govern the very initial stages of growth are still not fully understood. Surface processes such as diffusion of deposited atoms,^[49,62,69–73] adsorption of precursor ligands on the substrate,^[50,62,73–76] thermal decomposition of the metal precursor,^[73,77,78] and reactions catalyzed by the deposited nanoparticles^[62,73] are suggested to play a role. The kinetics of these processes are expected to vary with the noble metal loading and morphology and will therefore likely evolve during the ALD process.^[62] Moreover, the nucleation and island growth mechanisms and kinetics are influenced by the choice of ALD process conditions, e.g. precursor/reactant type, exposure and deposition temperature, resulting in different incubation times and nanoparticles morphologies. Although some efforts have been made,^[49,62,70,73,74,76,77,79,80] it is essential to further improve our understanding of the role of the different deposition parameters in order to enhance the control over the ALD technique for the tailored deposition of noble metal nanoparticles.

Most experimental studies concerning the nucleation of noble metal ALD are limited by the fact that they rely on the *ex situ* study of static morphologies alone, without providing detailed insights into how the structure evolves during the ALD process. The effect of a certain deposition parameter is, for example, typically studied by transmission electron microscopy (TEM) and a comparison of the nanoparticle size (distribution) is made for a specific number of ALD cycles. However, dynamic knowledge about how the nucleation and particle growth evolve during ALD for different process conditions is crucial to deepen our understanding of the underlying mechanisms and this can only be achieved by applying *in situ* probing techniques.

Grazing incidence small angle X-ray scattering (GISAXS) is a measurement technique typically performed at a synchrotron, that can yield information about the size, morphology and distribution of nanoscale objects at surfaces, which is averaged over the macroscopic surface area of the sample due to the large footprint of the beam.^[81,82] Because no special sample preparation is required, GISAXS is ideally suited for a variety of *in situ* experiments, including the characterization of deposition processes in high vacuum.^[83–87] As an illustration, the technique has been used for real-time monitoring of noble metal growth by evaporation^[88–90] and sputtering.^[91–94] In ALD-related research, *in situ* GISAXS has been

used to study the initial growth of oxides, nitrides, and metals^[49,95-100] and has been used to study the conformal coating of nanoporous thin films^[101] and layers of quantum dots.^[102] Besides monitoring the thin film growth, it is also possible to monitor the behaviour of a deposited film under several conditions, for example, sintering of Pt nanoparticles during annealing in different oxidizing atmospheres,^[103] or the formation of bimetallic nanoparticles by annealing ALD deposited layers.^[104]

A few reports presented *ex situ*^[69,76,105-107] or *in situ*^[49] GISAXS measurements during Pt ALD. In 2009, Christensen et al. investigated the morphology of Pt nanoparticles grown by 10, 20, 30 and 40 ALD cycles on SrTiO₃ surfaces.^[69] The GISAXS patterns revealed an increase in center-to-center particle distance with increasing number of ALD cycles, suggesting that surface diffusion of Pt species influences the nanoparticle formation. In 2014, Geyer et al. recorded GISAXS patterns for a series of ALD-grown Pt nanoparticles on native SiO₂ surfaces.^[106] Assuming a model in which the total island nucleation rate is kept constant, a lateral particle growth rate of 1 Å/cycle was extracted.

Earlier work in the CoCooN research group utilized *in situ* GISAXS and X-ray fluorescence (XRF) measurements during Pt ALD, revealing that the particle size and coverage can be tuned by either utilizing O₂ or N₂ plasma as the co-reactant.^[49] This work demonstrated that using O₂ gas as the co-reactant leads to an increase in mobility of Pt on the surface, translating into a decrease of Pt nanoparticle coverage on the surface with an increase in Pt loading. In contrast, using N₂ plasma as the co-reactant leads to a constant coverage of Pt nanoparticles on the surface as a function of Pt loading. These observations formed the basis for developing a method to tune the coverage and size of Pt nanoparticles on the surface. By starting with O₂ as the co-reactant it is possible to aim for a particular Pt nanoparticle coverage, and once a desired coverage is reached the O₂ gas can be swapped with N₂ plasma as the reactant and the particle size can be changed without changing the coverage.

In this thesis *in situ* GISAXS and X-ray fluorescence (XRF) experiments were performed during the thermal Pt ALD process using O₂ gas, but instead of focusing on the tuning opportunities of ALD, the focus was on the characterization of *in situ* GISAXS to study surface mobility during noble metal ALD processes. An analysis method to treat the obtained dynamic scattering data and obtained insights into the effect of the Pt precursor dose on the nucleation behaviour of the thermal platinum ALD process will be discussed in Chapter 4.

Precursor	Reactant	T_{sub}	GPC (nm/cycle)	Author (et al.)/Year
$\text{Me}_3\text{Au}(\text{PMe}_3)$	$\text{O}_2^*/\text{H}_2\text{O}$	120 °C	0.05	Griffiths/2015 [22]
$\text{Me}_2\text{Au}(\text{S}_2\text{CNET}_2)$	O_3	120-250 °C	0.09	Mäkelä/2017 [120]
$\text{Me}_3\text{Au}(\text{PMe}_3)$	H_2^*	50-120 °C	0.03	2019 [121]

Table 1.3: Existing gold ALD processes, with reported ALD temperature window and GPC. The bold entry is presented in this thesis. (*) denotes the use of plasma as co-reactant.

1.2.3 ALD of Gold

Gold has found widespread use in jewellery, coinage, and decorative pieces due to its unreactive nature. Moreover, gold in the form of nanoparticles has some very interesting optical and catalytic properties. The catalytic properties of nanoparticulate gold have attracted significant interest for heterogeneous catalysis.^[108–110] Suspended gold nanoparticles (or colloidal gold) are often used for their inherent optical properties (e.g., colloidal gold in ruby glass).^[111] The optical properties arise due to the localised surface plasmon resonances (LSPR) that develop at the metal surface. The LSPR can create electromagnetic hotspots between metallic structures and these hotspots can cause enormous enhancement of a Raman signal.^[112,113] The most used materials for surface enhanced Raman spectroscopy (SERS) are silver and gold, due to their surface plasmon properties. A drawback of using silver in SERS substrates is that it easily tarnishes, while this is not the case for gold. In general, highly ordered nanostructures are required for solid-state SERS substrates. By tuning the properties of the nanostructures on the SERS substrate, it is possible to achieve single molecule detection.

As can be seen in Table 1.1, gold is the last noble metal for which an ALD process has been developed. This indicates that gold is a challenging element to deposit by ALD. While there exist many CVD precursors to deposit gold,^[114–118] finding precursors that are suitable for ALD has proven to be quite difficult, because they need to be thermally stable, volatile, have decent surface-limited reactions, and saturation behaviour.^[119] Currently, only two gold compounds have been successfully used for ALD ($\text{Me}_3\text{Au}(\text{PMe}_3)$ and $\text{Me}_2\text{Au}(\text{S}_2\text{CNET}_2)$), resulting in three ALD processes as listed in Table 1.3.

The first gold ALD process was reported by Griffiths et al. and consists of three exposure steps.^[22] The surface is first exposed to trimethylphosphinotrimethylgold(III) ($\text{Me}_3\text{Au}(\text{PMe}_3)$), followed by an oxygen plasma exposure and finally a water vapour exposure. Deposition of metallic gold

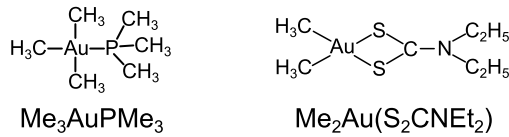


Figure 1.8: Gold precursors that have been used for ALD.

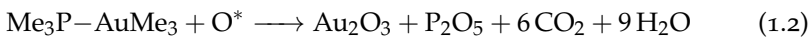
was reported at a deposition temperature of 120 °C with a growth rate of 0.05 nm per cycle. The deposited films had some impurities, 6.7 atomic % carbon and 1.8 atomic % oxygen.

The second gold ALD process was reported by Mäkelä et al.^[120] This process uses another gold precursor ($\text{Me}_2\text{Au}(\text{S}_2\text{CNEt}_2)$) and ozone as the co-reactant. Deposition between 120 °C and 180 °C was reported, with self-limiting growth at a substrate temperature of 180 °C. A relatively high growth rate of 0.09 nm per cycle was achieved. These films showed low resistivity (4.6-16 $\mu\Omega$ cm) with some impurities: 2.9 atomic % oxygen, 0.9 atomic % hydrogen, 0.2 atomic % carbon, and 0.2 atomic % nitrogen.

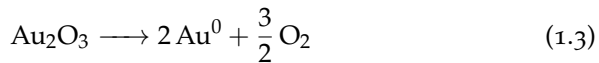
The third process utilizes the $\text{Me}_3\text{Au}(\text{PMe}_3)$ compound with H_2 plasma as the co-reactant and will be presented in Chapter 5. The reaction mechanism of this process was investigated during this thesis and will be presented in Chapter 6.

1.2.3.1 Steady growth regime and its reactions

For the $\text{Me}_3\text{Au}(\text{PMe}_3)$ - O_2 plasma - H_2O process a combustion type reaction was proposed as the reaction mechanism:



with O^* the oxygen radicals formed in the plasma. The gold oxide is then slowly reduced to metallic gold:



Without the H_2O exposure the films contained a lot of phosphorous impurities and a mixture of Au oxidation states. Adding the H_2O exposure results in the removal of the phosphorous impurities and a neutral oxidation state for the gold. It was proposed that the addition of water leads to the formation of phosphoric acid which is removed during the purge step:



The removal of the phosphate layer seems to aid the reduction of the gold oxide to metallic gold.

Experimental evidence to support the steady growth reaction mechanisms for the $\text{Me}_3\text{Au}(\text{PMe}_3)$ based processes is lacking. This is not that surprising given that these processes were only recently introduced. The existing literature (CVD, surface science, decomposition studies) concerning the use of the $\text{Me}_3\text{Au}(\text{PMe}_3)$ precursor provides a starting point to identify the reaction mechanism that occurs during the $\text{Me}_3\text{Au}(\text{PMe}_3)$ based ALD processes. Understanding possible decomposition pathways of the used precursor can provide valuable information about how the chemical reactions can occur on a substrate. The existing decomposition investigations of Au(I) and Au(III) compounds, similar to the $\text{Me}_3\text{Au}(\text{PMe}_3)$ molecule, are limited to the study of the liquid phase, which nonetheless provide important insights in the chemistry of these gold compounds. Gold compounds of the form RAuPR'_3 and $\text{R}_3\text{AuPR}'_3$ (with R = methyl, ethyl; R' = methyl, ethyl, phenyl) generally decompose into coupled R-R species, elemental gold, and the phosphine ligand.^[122-125] The decomposition pathway usually starts with the elimination of two neighbouring alkyl groups, resulting in the formation of R-R and RAuPR'_3 species. It was found that adding the phosphine ligand to the liquid results in retardation of the decomposition, indicating that for liquids the rate-limiting step in the decomposition of RAuPR'_3 molecules is the loss of the phosphine ligand. Davidson et al. reported laser induced CVD of gold tracks using MeAuPMe_3 , MeAuPEt_3 , and EtAuPEt_3 using an argon ion laser at 257 nm.^[126] The elemental composition and inclusion of precursor ligands on the surface was studied using laser ionization microprobe analysis. They observed the presence of chemisorbed PMe_3 species on the gold surface, which remained present on the surface for prolonged periods of time under high vacuum conditions. They inferred that the Au-Me surface species were less stable compared to the Au- PMe_3 surface species. In addition they found indications for the non-dissociative adsorption of MeAuPMe_3 on the gold surface. These observations are interesting for elucidating the reaction mechanism of $\text{Me}_3\text{Au}(\text{PMe}_3)$ during gold deposition. In this thesis the obtained insights concerning the reaction mechanism for the $\text{Me}_3\text{Au}(\text{PMe}_3)$ - H_2 plasma ALD process will be discussed in Chapter 6.

1.3 GOALS AND OUTLINE OF THIS THESIS

The experimental work in this thesis investigates platinum and gold ALD processes, aiming to provide a better understanding of the reaction mechanisms that occur during these ALD processes. This work has led to four original research papers that are contained in Chapters 3-6; as such, this thesis is paper based. The significance and advancements of each paper can be summarized as follows:

Paper I: "Surface species during ALD of platinum observed with *in situ* reflection IR spectroscopy"^[127]

This paper builds upon the body of existing literature concerning the reaction mechanisms that are involved for the thermal platinum ALD process ($\text{MeCpPtMe}_3 - \text{O}_2$). *In situ* (RAIRS) measurements were performed to identify the surface groups that are present during the ALD process. These groups were studied at different substrate temperatures to investigate the temperature dependent GPC of the thermal process and the role of dehydrogenation reactions. The results of the thermal platinum ALD process were systematically compared to the PE-ALD Pt process, which uses O_2 -plasma as the co-reactant instead of O_2 gas.

Paper II: "Surface mobility and impact of precursor dosing during atomic layer deposition of platinum: *in situ* monitoring of nucleation and island growth"^[128]

This paper investigates the nucleation behaviour of the thermal platinum ALD process using synchrotron based GISAXS and XRF experiments that were performed during deposition. A simple geometrical model was developed to analyse the GISAXS data and its validity was verified by performing full simulations of several 2D GISAXS patterns. The influence of high versus low precursor exposure on the nucleation and its effect on the obtained particle morphology were investigated.

Paper III: "Plasma-enhanced atomic layer deposition of nanostructured gold near room temperature"^[121]

This paper reports a PE-ALD process to deposit metallic gold, using the previously reported $\text{Me}_3\text{Au}(\text{PMe}_3)$ precursor in combination with H_2 plasma as the reactant. The typical ALD characteristics of this process are demonstrated. Compared to other existing gold ALD processes, it can be used across a broad temperature window and at low temperatures (50°C to 120°C). This is demonstrated by coating a piece of tissue paper using this process at 50°C . As for

most noble metal ALD processes, deposition on oxide surfaces leads to the formation of gold particles instead of closed layers. Because the deposition leads to closely spaced particles, the potential use of these particulate Au ALD coatings as SERS substrates was investigated.

Paper IV: "Reaction mechanism of the $\text{Me}_3\text{Au}(\text{PMe}_3) - \text{H}_2$ plasma-enhanced ALD process"^[129]

This paper continues on the work that was presented in paper III. The reaction mechanism of this new $\text{Me}_3\text{Au}(\text{PMe}_3) - \text{H}_2$ plasma process is investigated via *in situ* (RAIRS and XPS) studies. In addition, the use of the $\text{Me}_3\text{Au}(\text{PMe}_3)$ precursor in combination with O_2 plasma and $\text{H}_2\text{O}/\text{H}_2$ as the co-reactants is investigated in a pump-type ALD reactor and compared to the result that is obtained in a flow-type reactor.

A broad array of experimental characterization methods were used to obtain the research results in this thesis. Chapter 2 provides a short introduction to the theory (and the practical use) of each technique, as some of the used methods might be unfamiliar to the reader. Chapter 7 provides general conclusions that can be drawn from this work and a perspective on possible follow-up studies.

REFERENCES

- [1] Riikka L. Puurunen. "Surface chemistry of atomic layer deposition: A case study for the trimethylaluminum/water process". In: *Journal of Applied Physics* 97.12 (2005), p. 121301. DOI: 10.1063/1.1940727.
- [2] Paul Poodt, Adriaan Lankhorst, Fred Roozeboom, Karel Spee, Diederik Maas, and Ad Vermeer. "High-Speed Spatial Atomic-Layer Deposition of Aluminum Oxide Layers for Solar Cell Passivation". In: *Advanced Materials* 22.32 (2010), pp. 3564–3567. DOI: 10.1002/adma.201000766.
- [3] Thomas Dobbelaere. "Plasma-enhanced atomic layer deposition of transition metal phosphates". 2017.
- [4] Matthias M. Minjauw. "Atomic Layer Deposition of Ruthenium and Silver". 2019.
- [5] Titta Aaltonen, Mikko Ritala, Timo Sajavaara, Juhani Keinonen, and Markku Leskelä. "Atomic Layer Deposition of Platinum Thin Films". en. In: *Chemistry of Materials* 15.9 (May 2003), pp. 1924–1928. DOI: 10.1021/cm021333t.
- [6] Yong Ju Lee and Sang-Won Kang. "Atomic Layer Deposition of Aluminum Thin Films Using an Alternating Supply of Trimethylaluminum and a Hydrogen Plasma". In: *Electrochemical and Solid-State Letters* 5.10 (2002), p. C91. DOI: 10.1149/1.1503204.
- [7] S. M. Rossnagel, A. Sherman, and F. Turner. "Plasma-enhanced atomic layer deposition of Ta and Ti for interconnect diffusion barriers". In: *Journal of Vacuum Science & Technology B: Microelectronics and Nanometer Structures Processing, Measurement, and Phenomena* 18.4 (2000), pp. 2016–2020. DOI: 10.1116/1.1305809.
- [8] Lakmal C. Kalutarage, Philip D. Martin, Mary Jane Heeg, and Charles H. Winter. "Volatile and Thermally Stable Mid to Late Transition Metal Complexes Containing α -Imino Alkoxide Ligands, a New Strongly Reducing Coreagent, and Thermal Atomic Layer Deposition of Ni, Co, Fe, and Cr Metal Films". In: *Journal of the American Chemical Society* 135.34 (2013), pp. 12588–12591. DOI: 10.1021/ja407014w.
- [9] Lim Booyong S., Antti Rahtu, and Roy G. Gordon. "Atomic layer deposition of transition metals". In: *Nature Materials* 2.11 (2003), pp. 749–754. DOI: 10.1038/nmat1000.
- [10] Mikko Utriainen, Minna Kröger-Laukkanen, Leena-Sisko Johansson, and Lauri Niinistö. "Studies of metallic thin film growth in an atomic layer epitaxy reactor using M(acac)₂ (M=Ni, Cu, Pt) precursors". In: *Applied Surface Science* 157.3 (2000), pp. 151–158. DOI: 10.1016/S0169-4332(99)00562-0.
- [11] Per Mårtensson and Jan-Otto Carlsson. "Atomic Layer Epitaxy of Copper on Tantalum". In: *Chemical Vapor Deposition* 3.1 (1997), pp. 45–50. DOI: 10.1002/cvde.19970030107.
- [12] D. Seghete, G.B. Rayner, A.S. Cavanagh, V.R. Anderson, and S.M. George. "Molybdenum Atomic Layer Deposition Using MoF₆ and Si₂H₆ as the Reactants". In: *Chemistry of Materials* 23.7 (2011), pp. 1668–1678. DOI: 10.1021/cm101673u.
- [13] Titta Aaltonen, Antti Rahtu, Mikko Ritala, and Markku Leskelä. "Reaction Mechanism Studies on Atomic Layer Deposition of Ruthenium and Platinum". In: *Electrochemical and Solid-State Letters* 6.9 (2003), p. C130. DOI: 10.1149/1.1595312.
- [14] Titta Aaltonen, Mikko Ritala, and Markku Leskelä. "ALD of Rhodium Thin Films from Rh(acac)[sub 3] and Oxygen". In: *Electrochemical and Solid-State Letters* 8.8 (2005), p. C99. DOI: 10.1149/1.1940507.
- [15] J.J. Senkevich, F. Tang, D. Rogers, J.T. Drotar, C. Jezewski, W.A. Lanford, G.-C. Wang, and T.-M. Lu. "Substrate-Independent Palladium Atomic Layer Deposition". In: *Chemical Vapor Deposition* 9.5 (2003), pp. 258–264. DOI: 10.1002/cvde.200306246.

- [16] A. Niskanen, T. Hatanpää, K. Arstila, M. Leskelä, and M. Ritala. "Radical-Enhanced Atomic Layer Deposition of Silver Thin Films Using Phosphine-Adducted Silver Carboxylates". In: *Chemical Vapor Deposition* 13.8 (2007), pp. 408–413. DOI: 10.1002/cvde.200606519.
- [17] Eric C. Stevens, Moataz Bellah M. Mousa, and Gregory N. Parsons. "Thermal atomic layer deposition of Sn metal using SnCl₄ and a vapor phase silyl dihydropyrazine reducing agent". In: *Journal of Vacuum Science & Technology A* 36.6 (2018), o6A106. DOI: 10.1116/1.5055212.
- [18] J.W Klaus, S.J Ferro, and S.M George. "Atomic layer deposition of tungsten using sequential surface chemistry with a sacrificial stripping reaction". In: *Thin Solid Films* 360.1 (2000), pp. 145–153. DOI: 10.1016/S0040-6090(99)01076-7.
- [19] Jani Hämäläinen, Kenichiro Mizohata, Kristoffer Meinander, Miika Mattinen, Marko Vehkamäki, Jyrki Räisänen, Mikko Ritala, and Markku Leskelä. "Rhenium Metal and Rhenium Nitride Thin Films Grown by Atomic Layer Deposition". In: *Angewandte Chemie International Edition* 57.44 (2018), pp. 14538–14542. DOI: 10.1002/anie.201806985.
- [20] Jani Hämäläinen, Timo Sajavaara, Esa Puukilainen, Mikko Ritala, and Markku Leskelä. "Atomic Layer Deposition of Osmium". In: *Chemistry of Materials* 24.1 (2012), pp. 55–60. DOI: 10.1021/cm201795s.
- [21] Titta Aaltonen, Mikko Ritala, Väino Sammelselg, and Markku Leskelä. "Atomic Layer Deposition of Iridium Thin Films". In: *Journal of The Electrochemical Society* 151.8 (2004), G489. DOI: 10.1149/1.1761011.
- [22] Matthew B. E. Griffiths, Peter J. Pallister, David J. Mandia, and Seán T. Barry. "Atomic Layer Deposition of Gold Metal". In: *Chemistry of Materials* 28.1 (2016), pp. 44–46. DOI: 10.1021/acs.chemmater.5b04562.
- [23] Plasma & Materials Processing group at Eindhoven University of Technology. *Atomic Limits: ALD database*. URL: <https://www.atomiclimits.com/alddbatabase>. (accessed: 21/02/2020).
- [24] S. D. Elliott, G. Dey, and Y. Maimaiti. "Classification of processes for the atomic layer deposition of metals based on mechanistic information from density functional theory calculations". In: *The Journal of Chemical Physics* 146.5 (2017), p. 052822. DOI: 10.1063/1.4975085.
- [25] Yu-Hung Lin, Yang-Chih Hsueh, Po-Sheng Lee, Chih-Chieh Wang, Jyh Ming Wu, Tsong-Pyng Perng, and Han C. Shih. "Fabrication of tin dioxide nanowires with ultrahigh gas sensitivity by atomic layer deposition of platinum". en. In: *Journal of Materials Chemistry* 21.28 (2011), p. 10552. DOI: 10.1039/c1jm10785b.
- [26] A. J. M. Mackus, J. J. L. Mulders, M. C. M. van de Sanden, and W. M. M. Kessels. "Local deposition of high-purity Pt nanostructures by combining electron beam induced deposition and atomic layer deposition". en. In: *Journal of Applied Physics* 107.11 (June 2010), p. 116102. DOI: 10.1063/1.3431351.
- [27] James A. Enterkin, Worajit Setthapun, Jeffrey W. Elam, Steven T. Christensen, Federico A. Rabuffetti, Laurence D. Marks, Peter C. Stair, Kenneth R. Poeppelmeier, and Christopher L. Marshall. "Propane Oxidation over Pt/SrTiO₃ Nanocuboids". en. In: *ACS Catalysis* 1.6 (June 2011), pp. 629–635. DOI: 10.1021/cs200092c.
- [28] Chueh Liu, Chih-Chieh Wang, Chi-Chung Kei, Yang-Chih Hsueh, and Tsong-Pyng Perng. "Atomic Layer Deposition of Platinum Nanoparticles on Carbon Nanotubes for Application in Proton-Exchange Membrane Fuel Cells". In: *Small* 5.13 (2009), pp. 1535–1538. DOI: 10.1002/sml.200900278.

- [29] Steven Novak, Bongmook Lee, Xiangyu Yang, and Veena Misra. "Platinum Nanoparticles Grown by Atomic Layer Deposition for Charge Storage Memory Applications". en. In: *Journal of The Electrochemical Society* 157.6 (2010), H589. doi: 10.1149/1.3365031.
- [30] Anca Faur Ghenciu. "Review of fuel processing catalysts for hydrogen production in PEM fuel cell systems". In: *Current Opinion in Solid State and Materials Science* 6.5 (2002), pp. 389–399. doi: 10.1016/S1359-0286(02)00108-0.
- [31] Hans-Ulrich Blaser, Hans-Peter Jalett, Manfred Müller, and Martin Studer. "Enantioselective hydrogenation of α -ketoesters using cinchona modified platinum catalysts and related systems: A review". In: *Catalysis Today* 37.4 (1997). Heterogenous Catalysis in Organic Reactions, pp. 441–463. doi: 10.1016/S0920-5861(97)00026-6.
- [32] R. Burch, J.P. Breen, and F.C. Meunier. "A review of the selective reduction of NO_x with hydrocarbons under lean-burn conditions with non-zeolitic oxide and platinum group metal catalysts". In: *Applied Catalysis B: Environmental* 39.4 (2002), pp. 283–303. doi: 10.1016/S0926-3373(02)00118-2.
- [33] Shengsheng Zhang, Xiao-Zi Yuan, Jason Ng Cheng Hin, Haijiang Wang, K. Andreas Friedrich, and Mathias Schulze. "A review of platinum-based catalyst layer degradation in proton exchange membrane fuel cells". In: *Journal of Power Sources* 194.2 (2009), pp. 588–600. doi: 10.1016/j.jpowsour.2009.06.073.
- [34] Divesh Bhatia, Robert W. McCabe, Michael P. Harold, and Vemuri Balakotiah. "Experimental and kinetic study of NO oxidation on model Pt catalysts". In: *Journal of Catalysis* 266.1 (2009), pp. 106–119. doi: 10.1016/j.jcat.2009.05.020.
- [35] Aicheng Chen and Peter Holt-Hindle. "Platinum-based nanostructured materials: synthesis, properties, and applications". In: *Chemical reviews* 110.6 (2010), pp. 3767–3804. doi: 10.1021/cr9003902.
- [36] Kuo Liu, Ai Qin Wang, and Tao Zhang. "Recent advances in preferential oxidation of CO reaction over platinum group metal catalysts". In: *ACS catalysis* 2.6 (2012), pp. 1165–1178. doi: 10.1021/cs200418w.
- [37] Neil P Dasgupta, Chong Liu, Sean Andrews, Fritz B Prinz, and Peidong Yang. "Atomic layer deposition of platinum catalysts on nanowire surfaces for photoelectrochemical water reduction". In: *Journal of the American Chemical Society* 135.35 (2013), pp. 12932–12935. doi: 10.1021/ja405680p.
- [38] Niancai Cheng, Samantha Stambula, Da Wang, Mohammad Norouzi Banis, Jian Liu, Adam Riese, Biwei Xiao, Ruying Li, Tsun-Kong Sham, Li-Min Liu, et al. "Platinum single-atom and cluster catalysis of the hydrogen evolution reaction". In: *Nature communications* 7.1 (2016), pp. 1–9. doi: 10.1038/ncomms13638.
- [39] Markus Nesselberger, Melanie Roefzaad, R Fayçal Hamou, P Ulrich Biedermann, Florian F Schweinberger, Sebastian Kunz, Katrin Schloegl, Gustav KH Wiberg, Sean Ashton, Ueli Heiz, et al. "The effect of particle proximity on the oxygen reduction rate of size-selected platinum clusters". In: *Nature materials* 12.10 (2013), pp. 919–924. doi: 10.1038/nmat3712.
- [40] Hemma Mistry, Farzad Behafarid, Rulle Reske, Ana Sofia Varela, Peter Strasser, and Beatriz Roldan Cuenya. "Tuning catalytic selectivity at the mesoscale via interparticle interactions". In: *Acs catalysis* 6.2 (2016), pp. 1075–1080. doi: 10.1021/acscatal.5b02202.
- [41] Jani Hämäläinen, Frans Munnik, Mikko Ritala, and Markku Leskelä. "Atomic Layer Deposition of Platinum Oxide and Metallic Platinum Thin Films from Pt(acac)₂ and Ozone". In: *Chemistry of Materials* 20.21 (2008), pp. 6840–6846. doi: 10.1021/cm801187t.

- [42] H. C. M. Knoops, A. J. M. Mackus, M. E. Donders, M. C. M. van de Sanden, P. H. L. Notten, and W. M. M. Kessels. "Remote Plasma ALD of Platinum and Platinum Oxide Films". In: *Electrochemical and Solid-State Letters* 12.7 (2009), G34. DOI: 10.1149/1.3125876.
- [43] Robert R. Hoover and Yuriy V. Tolmachev. "Electrochemical Properties of Pt Coatings on Ni Prepared by Atomic Layer Deposition". In: *Journal of The Electrochemical Society* 156.1 (2009), A37. DOI: 10.1149/1.3002372.
- [44] Adriaan J. M. Mackus, Diana Garcia-Alonso, Harm C. M. Knoops, Ageeth A. Bol, and Wilhelmus M. M. Kessels. "Room-Temperature Atomic Layer Deposition of Platinum". In: *Chemistry of Materials* 25.9 (2013), pp. 1769–1774. DOI: 10.1021/cm400274n.
- [45] Jolien Dendooven, Ranjith K. Ramachandran, Kilian Devloo-Casier, Geert Rampelberg, Matthias Filez, Hilde Poelman, Guy B. Marin, Emiliano Fonda, and Christophe Detavernier. "Low-Temperature Atomic Layer Deposition of Platinum Using (Methylcyclopentadienyl)trimethylplatinum and Ozone". In: *The Journal of Physical Chemistry C* 117.40 (2013), pp. 20557–20561. DOI: 10.1021/jp403455a.
- [46] D. Longrie, K. Devloo-Casier, D. Deduytsche, S. Van den Berghe, K. Driesen, and C. Detavernier. "Plasma-Enhanced ALD of Platinum with O₂, N₂ and NH₃ Plasmas". In: *ECS Journal of Solid State Science and Technology* 1.6 (2012), Q123–Q129. DOI: 10.1149/1.009206jss.
- [47] Woo-Jae Lee, Zhixin Wan, Chang-Min Kim, Il-Kwon Oh, Ryosuke Harada, Kazuharu Suzuki, Eun-Ae Choi, and Se-Hun Kwon. "Atomic Layer Deposition of Pt Thin Films Using Dimethyl (N,N-Dimethyl-3-Butene-1-Amine-N) Platinum and O₂ Reactant". In: *Chemistry of Materials* 31.14 (2019), pp. 5056–5064. DOI: 10.1021/acs.chemmater.9b00675.
- [48] Jaehong Lee et al. "Highly conductive and flexible fiber for textile electronics obtained by extremely low-temperature atomic layer deposition of Pt". In: *NPG Asia Materials* 8 (2016). DOI: 10.1038/am.2016.182.
- [49] Jolien Dendooven et al. "Independent tuning of size and coverage of supported Pt nanoparticles using atomic layer deposition". In: *Nature Communications* 8.1 (2017), p. 1074. DOI: 10.1038/s41467-017-01140-z.
- [50] Adriaan J. M. Mackus, Noémi Leick, Layton Baker, and Wilhelmus M. M. Kessels. "Catalytic Combustion and Dehydrogenation Reactions during Atomic Layer Deposition of Platinum". en. In: *Chemistry of Materials* 24.10 (May 2012), pp. 1752–1761. DOI: 10.1021/cm203812v.
- [51] Steven T. Christensen and Jeffrey W. Elam. "Atomic Layer Deposition of Ir–Pt Alloy Films". In: *Chemistry of Materials* 22.8 (2010), pp. 2517–2525. DOI: 10.1021/cm9031978.
- [52] Scott M. Geyer, Rungthiwa Methaapanon, Bonggeun Shong, Piero A. Pianetta, and Stacey F. Bent. "In Vacuo Photoemission Studies of Platinum Atomic Layer Deposition Using Synchrotron Radiation". en. In: *The Journal of Physical Chemistry Letters* 4.1 (Jan. 2013), pp. 176–179. DOI: 10.1021/jz301475z.
- [53] W. M. M. Kessels, H. C. M. Knoops, S. A. F. Dielissen, A. J. M. Mackus, and M. C. M. van de Sanden. "Surface reactions during atomic layer deposition of Pt derived from gas phase infrared spectroscopy". en. In: *Applied Physics Letters* 95.1 (July 2009), p. 013114. DOI: 10.1063/1.3176946.
- [54] Simon D. Elliott. "Mechanism, Products, and Growth Rate of Atomic Layer Deposition of Noble Metals". en. In: *Langmuir* 26.12 (June 2010), pp. 9179–9182. DOI: 10.1021/la101207y.

- [55] Neu R. Avery. "Bonding and reactivity of cyclopentene on Pt(111)". In: *Surface Science* 146.2 (1984), pp. 363–381. DOI: 10.1016/0039-6028(84)90437-0.
- [56] I. J. M. Erkens, A. J. M. Mackus, H. C. M. Knoops, P. Smits, T. H. M. van de Ven, F. Roozeboom, and W. M. M. Kessels. "Mass Spectrometry Study of the Temperature Dependence of Pt Film Growth by Atomic Layer Deposition". en. In: *ECS Journal of Solid State Science and Technology* 1.6 (Sept. 2012), P255–P262. DOI: 10.1149/2.006206jss.
- [57] Roger H. E. C. Bosch, Frank L. Bloksma, Jochem M. M. Huijs, Marcel A. Verheijen, and Wilhelmus M. M. Kessels. "Surface Infrared Spectroscopy during Low Temperature Growth of Supported Pt Nanoparticles by Atomic Layer Deposition". en. In: *The Journal of Physical Chemistry C* 120.1 (Jan. 2016), pp. 750–755. DOI: 10.1021/acs.jpcc.5b10839.
- [58] Vincent Vandalon, Adrie Mackus, and W. M.M Kessels. In: *Presented at the AVS Topical Conference on ALD* (Denver, United States of America, July 16-18, 2017), Surface Chemistry during Atomic Layer Deposition of Pt Studied with Vibrational Sum-frequency Generation.
- [59] J. H. Weaver. "Optical properties of Rh, Pd, Ir, and Pt". In: *Phys. Rev. B* 11 (4 Feb. 1975), pp. 1416–1425. DOI: 10.1103/PhysRevB.11.1416.
- [60] W. S. Choi, S. S. A. Seo, K. W. Kim, T. W. Noh, M. Y. Kim, and S. Shin. "Dielectric constants of Ir, Ru, Pt, and IrO₂: Contributions from bound charges". In: *Phys. Rev. B* 74 (20 Nov. 2006), p. 205117. DOI: 10.1103/PhysRevB.74.205117.
- [61] Brandon J. O'Neill, David H. K. Jackson, Jechan Lee, Christian Canlas, Peter C. Stair, Christopher L. Marshall, Jeffrey W. Elam, Thomas F. Kuech, James A. Dumesic, and George W. Huber. "Catalyst Design with Atomic Layer Deposition". In: *ACS Catalysis* 5:3 (2015), pp. 1804–1825. DOI: 10.1021/cs501862h.
- [62] Adriaan J M Mackus, Matthieu J Weber, Nick F W Thissen, Diana Garcia-Alonso, René H J Vervuurt, Simone Assali, Ageeth A Bol, Marcel A Verheijen, and Wilhelmus M M Kessels. "Atomic layer deposition of Pd and Pt nanoparticles for catalysis: on the mechanisms of nanoparticle formation". In: *Nanotechnology* 27:3 (Dec. 2015), p. 034001. DOI: 10.1088/0957-4484/27/3/034001.
- [63] Junling Lu, Jeffrey W. Elam, and Peter C Stair. "Atomic layer deposition—Sequential self-limiting surface reactions for advanced catalyst "bottom-up" synthesis". In: *Surface Science Reports* 71.2 (2016), pp. 410–472. DOI: 10.1016/j.surfrep.2016.03.003.
- [64] Ranjith K. Ramachandran, Christophe Detavernier, and Jolien Dendooven. "Atomic Layer Deposition for Catalysis". In: *Nanotechnology in Catalysis*. John Wiley & Sons, Ltd, 2017. Chap. 14, pp. 335–358. ISBN: 9783527699827. DOI: 10.1002/9783527699827.ch14.
- [65] Han-Bo-Ram Lee, Marja N. Mullings, Xirong Jiang, Bruce M. Clemens, and Stacey F. Bent. "Nucleation-Controlled Growth of Nanoparticles by Atomic Layer Deposition". In: *Chemistry of Materials* 24.21 (2012), pp. 4051–4059. DOI: 10.1021/cm3014978.
- [66] Junling Lu, Jeffrey W. Elam, and Peter C. Stair. "Synthesis and Stabilization of Supported Metal Catalysts by Atomic Layer Deposition". In: *Accounts of Chemical Research* 46.8 (2013), pp. 1806–1815. DOI: 10.1021/ar300229c.
- [67] Yu Lei et al. "Synthesis of Porous Carbon Supported Palladium Nanoparticle Catalysts by Atomic Layer Deposition: Application for Rechargeable Lithium–O₂ Battery". In: *Nano Letters* 13.9 (2013), pp. 4182–4189. DOI: 10.1021/nl401833p.

- [68] Matthias Filez, Hilde Poelman, Ranjith K. Ramachandran, Jolien Dendooven, Kilian Devloo-Casier, Emiliano Fonda, Christophe Detavernier, and Guy B. Marin. "In situ XAS and XRF study of nanoparticle nucleation during O₃-based Pt deposition". en. In: *Catalysis Today* 229 (June 2014), pp. 2–13. DOI: 10.1016/j.cat.tod.2014.01.011.
- [69] Steven T. Christensen, Jeffrey W. Elam, Byeongdu Lee, Zhenxing Feng, Michael J. Bedzyk, and Mark C. Hersam. "Nanoscale Structure and Morphology of Atomic Layer Deposition Platinum on SrTiO₃ (001)". In: *Chemistry of Materials* 21.3 (2009), pp. 516–521. DOI: 10.1021/cm8026863.
- [70] Adriaan J. M. Mackus, Marcel A. Verheijen, Noémi Leick, Ageeth A. Bol, and Wilhelmus M. M. Kessels. "Influence of Oxygen Exposure on the Nucleation of Platinum Atomic Layer Deposition: Consequences for Film Growth, Nanopatterning, and Nanoparticle Synthesis". In: *Chemistry of Materials* 25.9 (2013), pp. 1905–1911. DOI: 10.1021/cm400562u.
- [71] Fabio Grillo, Hao Van Bui, Jacob A. Moulijn, Michiel T. Kreutzer, and J. Ruud van Ommen. "Understanding and Controlling the Aggregative Growth of Platinum Nano particles in Atomic Layer Deposition: An Avenue to Size Selection". In: *The Journal of Physical Chemistry Letters* 8.5 (2017), pp. 975–983. DOI: 10.1021/acs.jpcclett.6b02978.
- [72] Fabio Grillo, Jacob A. Moulijn, Michiel T. Kreutzer, and J. Ruud van Ommen. "Nano particle sintering in atomic layer deposition of supported catalysts: Kinetic modeling of the size distribution". In: *Catalysis Today* 316 (2018), pp. 51–61. DOI: 10.1016/j.cattod.2018.02.020.
- [73] Nathaniel E. Richey, Camila de Paula, and Stacey F. Bent. "Understanding chemical and physical mechanisms in atomic layer deposition". In: *The Journal of Chemical Physics* 152.4 (2020), p. 040902. DOI: 10.1063/1.5133390.
- [74] D. N. Goldstein and S. M. George. "Enhancing the nucleation of palladium atomic layer deposition on Al₂O₃ using trimethylaluminum to prevent surface poisoning by reaction products". In: *Applied Physics Letters* 95.14 (2009), p. 143106. DOI: 10.1063/1.3238558.
- [75] D.N. Goldstein and S.M. George. "Surface poisoning in the nucleation and growth of palladium atomic layer deposition with Pd(hfac)₂ and formalin". In: *Thin Solid Films* 519.16 (2011), pp. 5339–5347. DOI: 10.1016/j.tsf.2011.02.037.
- [76] Camila de Paula, Nathaniel E. Richey, Li Zeng, and Stacey F. Bent. "Mechanistic Study of Nucleation Enhancement in Atomic Layer Deposition by Pretreatment with Small Organometallic Molecules". In: *Chemistry of Materials* 32.1 (2020), pp. 315–325. DOI: 10.1021/acs.chemmater.9b03826.
- [77] Worajit Setthapun et al. "Genesis and Evolution of Surface Species during Pt Atomic Layer Deposition on Oxide Supports Characterized by in Situ XAFS Analysis and Water-Gas Shift Reaction". In: *The Journal of Physical Chemistry C* 114.21 (2010), 9758–9771. DOI: 10.1021/jp911178m.
- [78] Xinhua Liang, Yun Zhou, Jianhua Li, and Alan W. Weimer. "Reaction mechanism studies for platinum nanoparticle growth by atomic layer deposition". In: *Journal of Nanoparticle Research* 13 (2011), pp. 3781–3788. DOI: 10.1007/s11051-011-0299-x.
- [79] Troy D. Gould, Alia M. Lubers, April R. Corpuz, Alan W. Weimer, John L. Falconer, and J. Will Medlin. "Controlling Nanoscale Properties of Supported Platinum Catalysts through Atomic Layer Deposition". In: *ACS Catalysis* 5.2 (2015), pp. 1344–1352. DOI: 10.1021/cs501265b.

- [80] Chuandao Wang, Linhua Hu, Yuyuan Lin, Kenneth Poeppelmeier, Peter Stair, and Laurence Marks. "Controllable ALD synthesis of platinum nanoparticles by tuning different synthesis parameters". In: *Journal of Physics D: Applied Physics* 50.41 (Sept. 2017), p. 415301. DOI: 10.1088/1361-6463/aa8709.
- [81] G. Renaud, R. Lazzari, and F. Leroy. "Probing surface and interface morphology with Grazing Incidence Small Angle X-Ray Scattering". In: *Surface Science Reports* 64.8 (2009), pp. 255–380. DOI: 10.1016/j.surfrep.2009.07.002.
- [82] D. Babonneau, S. Camelio, E. Vandenhecke, S. Rousselet, M. Garel, F. Pailloux, and P. Boesecke. "Quantitative analysis of nanoripple and nanoparticle patterns by grazing incidence small-angle x-ray scattering 3D mapping". In: *Phys. Rev. B* 85 (June 2012), p. 235415. DOI: 10.1103/PhysRevB.85.235415.
- [83] Joanne R. Levine, J.B. Cohen, and Y.W. Chung. "Thin film island growth kinetics: a grazing incidence small angle X-ray scattering study of gold on glass". In: *Surface Science* 248.1 (1991), pp. 215–224. DOI: 10.1016/0039-6028(91)90075-4.
- [84] Gilles Renaud et al. "Real-Time Monitoring of Growing Nanoparticles". In: *Science* 300.5624 (2003), pp. 1416–1419. DOI: 10.1126/science.1082146.
- [85] Myung Hwa Kim et al. "Growth of Metal Oxide Nanowires from Supercooled Liquid Nanodroplets". In: *Nano Letters* 9.12 (2009), pp. 4138–4146. DOI: 10.1021/nl902357q.
- [86] Leyla Çolakerol Arslan, Christopher Sanborn, Eitan Anzenberg, and Karl F. Ludwig. "Evidence for Family-Meakin Dynamical Scaling in Island Growth and Coalescence during Vapor Phase Deposition". In: *Phys. Rev. Lett.* 109 (10 Sept. 2012), p. 106102. DOI: 10.1103/PhysRevLett.109.106102.
- [87] Alexander Demasi, Meliha G. Rainville, and Karl F. Ludwig. "Real-time x-ray studies of indium island growth kinetics". In: *Journal of Vacuum Science & Technology A* 33.2 (2015), p. 021406. DOI: 10.1116/1.4905498.
- [88] Rémi Lazzari, Frédéric Leroy, and Gilles Renaud. "Grazing-incidence small-angle x-ray scattering from dense packing of islands on surfaces: Development of distorted wave Born approximation and correlation between particle sizes and spacing". In: *Phys. Rev. B* 76 (12 Sept. 2007), p. 125411. DOI: 10.1103/PhysRevB.76.125411.
- [89] J. Olander, R. Lazzari, J. Jupille, B. Mangili, J. Goniakowski, and G. Renaud. "Size- and temperature-dependent epitaxy for a strong film-substrate mismatch: The case of Pt/MgO (001)". In: *Phys. Rev. B* 76 (7 Aug. 2007), p. 075409. DOI: 10.1103/PhysRevB.76.075409.
- [90] R. Lazzari, G. Renaud, C. Revenant, J. Jupille, and Y. Borensztein. "Adhesion of growing nanoparticles at a glance: Surface differential reflectivity spectroscopy and grazing incidence small angle x-ray scattering". In: *Phys. Rev. B* 79 (12 Mar. 2009), p. 125428. DOI: 10.1103/PhysRevB.79.125428.
- [91] Gunar Kaune, Matthias A. Ruderer, Ezzeldin Metwalli, Weinan Wang, Sebastien Couet, Kai Schlage, Ralf Röhlberger, Stephan V. Roth, and Peter Müller-Buschbaum. "In Situ GISAXS Study of Gold Film Growth on Conducting Polymer Films". In: *ACS Applied Materials & Interfaces* 1.2 (2009), pp. 353–360. DOI: 10.1021/am800072f.
- [92] Matthias Schwartzkopf et al. "From Atoms to Layers: in situ Gold Cluster Growth Kinetics during Sputter Deposition". In: *Nanoscale* 5 (11 2013), pp. 5053–5062. DOI: 10.1039/C3NR34216F.

- [93] G. Santoro, S. Yu, M. Schwartzkopf, P. Zhang, Sarathlal Koyiloth Vayalil, J. F. H. Risch, M. A. Rübhausen, M. Hernández, C. Domingo, and S. V. Roth. "Silver Substrates for Surface Enhanced Raman Scattering: Correlation between Nanostructure and Raman Scattering Enhancement". In: *Applied Physics Letters* 104.24 (2014), p. 243107. DOI: 10.1063/1.4884423.
- [94] Shun Yu et al. "Following the Island Growth in Real Time: Ag Nanocluster Layer on Alq₃ Thin Film". In: *The Journal of Physical Chemistry C* 119.8 (2015), pp. 4406–4413. DOI: 10.1021/jp512675w.
- [95] K. Devloo-Casier, J. Dendooven, K. F. Ludwig, G. Lekens, J. D'Haen, and C. Detavernier. "In situ synchrotron based x-ray fluorescence and scattering measurements during atomic layer deposition: Initial growth of HfO₂ on Si and Ge substrates". In: *Applied Physics Letters* 98.23 (2011), p. 231905. DOI: 10.1063/1.3598433.
- [96] Virginia R. Anderson et al. "Plasma-assisted atomic layer epitaxial growth of aluminum nitride studied with real time grazing angle small angle x-ray scattering". In: *Journal of Vacuum Science & Technology A* 35.3 (2017), p. 031508. DOI: 10.1116/1.4979007.
- [97] Neeraj Nepal, Virginia R. Anderson, Scooter D. Johnson, Brian P. Downey, David J. Meyer, Alexander DeMasi, Zachary R. Robinson, Karl F. Ludwig, and Charles R. Eddy. "Real-time growth study of plasma assisted atomic layer epitaxy of InN films by synchrotron x-ray methods". In: *Journal of Vacuum Science & Technology A* 35.3 (2017), p. 031504. DOI: 10.1116/1.4978026.
- [98] Jeffrey M. Woodward et al. "Influence of temperature on atomic layer epitaxial growth of indium nitride assessed with in situ grazing incidence small-angle x-ray scattering". In: *Journal of Vacuum Science & Technology A* 37.3 (2019), p. 030901. DOI: 10.1116/1.5081919.
- [99] Neeraj Nepal, Virginia R. Anderson, Scooter D. Johnson, Brian P. Downey, David J. Meyer, Zachary R. Robinson, Jeffrey M. Woodward, Karl F. Ludwig, and Charles R. Eddy. "Understanding the effect of nitrogen plasma exposure on plasma assisted atomic layer epitaxy of InN monitored by real time grazing incidence small angle x-ray scattering". In: *Journal of Vacuum Science & Technology A* 37.2 (2019), p. 020910. DOI: 10.1116/1.5063340.
- [100] Jolien Dendooven, Eduardo Solano, Matthias M. Minjauw, Kevin Van de Kerckhove, Alessandro Coati, Emiliano Fonda, Giuseppe Portale, Yves Garreau, and Christophe Detavernier. "Mobile setup for synchrotron based in situ characterization during thermal and plasma-enhanced atomic layer deposition". In: *Review of Scientific Instruments* 87.11 (2016), p. 113905. DOI: 10.1063/1.4967711.
- [101] Jolien Dendooven, Kilian Devloo-Casier, Matthias Ide, Kathryn Grandfield, Mert Kurttepe, Karl F. Ludwig, Sara Bals, Pascal Van Der Voort, and Christophe Detavernier. "Atomic layer deposition-based tuning of the pore size in mesoporous thin films studied by in situ grazing incidence small angle X-ray scattering". In: *Nanoscale* 6 (24 2014), pp. 14991–14998. DOI: 10.1039/C4NR05049E.
- [102] Kilian Devloo-Casier, Pieter Geiregat, Karl F. Ludwig, Koen van Stiphout, André Vantomme, Zeger Hens, Christophe Detavernier, and Jolien Dendooven. "A Case Study of ALD Encapsulation of Quantum Dots: Embedding Supported CdSe/CdS/ZnS Quantum Dots in a ZnO Matrix". In: *The Journal of Physical Chemistry C* 120.32 (2016), pp. 18039–18045. DOI: 10.1021/acs.jpcc.6b04398.

- [103] Eduardo Solano, Jolien Dendooven, Ranjith K. Ramachandran, Kevin Van de Kerckhove, Thomas Dobbelaere, Daniel Hermida-Merino, and Christophe Detavernier. "Key role of surface oxidation and reduction processes in the coarsening of Pt nanoparticles". In: *Nanoscale* 9 (35 2017), pp. 13159–13170. DOI: 10.1039/C7NR04278G.
- [104] Ranjith K. Ramachandran et al. "Atomic Layer Deposition Route To Tailor Nanoalloys of Noble and Non-noble Metals". In: *ACS Nano* 10.9 (2016), pp. 8770–8777. DOI: 10.1021/acsnano.6b04464.
- [105] Kilian Devloo-Casier, Karl F. Ludwig, Christophe Detavernier, and Jolien Dendooven. "In situ synchrotron based x-ray techniques as monitoring tools for atomic layer deposition". In: *Journal of Vacuum Science & Technology A* 32.1 (2014), p. 010801. DOI: 10.1116/1.4851716.
- [106] Scott M. Geyer, Rungthiwa Methaapanon, Richard Johnson, Sean Brennan, Mike F. Toney, Bruce Clemens, and Stacey Bent. "Structural evolution of platinum thin films grown by atomic layer deposition". In: *Journal of Applied Physics* 116.6 (2014), p. 064905. DOI: 10.1063/1.4892104.
- [107] Ranjith K. Ramachandran et al. "Chemical and Structural Configuration of Pt-Doped Metal Oxide Thin Films Prepared by Atomic Layer Deposition". In: *Chemistry of Materials* 31.23 (2019), pp. 9673–9683. DOI: 10.1021/acs.chemmater.9b03066.
- [108] M.C. Daniel and D. Astruc. "Gold Nanoparticles: Assembly, Supramolecular Chemistry, Quantum-Size-Related Properties, and Applications toward Biology, Catalysis, and Nanotechnology". In: *Chemical Reviews* 104.1 (2004), pp. 293–346. DOI: 10.1021/cr030698+.
- [109] A. Stephen K. Hashmi and Graham J. Hutchings. "Gold Catalysis". In: *Angewandte Chemie International Edition* 45.47 (2006), pp. 7896–7936. DOI: 10.1002/anie.200602454.
- [110] Yan Zhang, Xinjiang Cui, Feng Shi, and Youquan Deng. "Nano-Gold Catalysis in Fine Chemical Synthesis". In: *Chemical Reviews* 112.4 (2012), pp. 2467–2505. DOI: 10.1021/cr200260m.
- [111] Ian Freestone, Nigel Meeks, Margaret Sax, and Catherine Higgitt. "The Lycurgus Cup - A Roman Nanotechnology". In: *Gold Bulletin* 40.4 (Dec. 2007), pp. 270–277. DOI: 10.1007/BF03215599.
- [112] Katherine A. Willets and Richard P. Van Duyne. "Localized Surface Plasmon Resonance Spectroscopy and Sensing". In: *Annual Review of Physical Chemistry* 58.1 (2007), pp. 267–297. DOI: 10.1146/annurev.physchem.58.032806.104607.
- [113] Kathryn M. Mayer and Jason H. Hafner. "Localized Surface Plasmon Resonance Sensors". In: *Chemical Reviews* 111.6 (2011), pp. 3828–3857. DOI: 10.1021/cr100313v.
- [114] Mark J. Hampden-Smith and Toivo T. Kodas. "Chemical Vapor Deposition of Metals: Part 1. An Overview of CVD Processes". In: *Chemical Vapor Deposition* 1.1 (1995), pp. 8–23. DOI: 10.1002/cvde.19950010103.
- [115] A.A. Bessonov, N.B. Morozova, N.V. Gelfond, P.P. Semyannikov, S.V. Trubin, Yu.V. Shevtsov, Yu.V. Shubin, and I.K. Igumenov. "Dimethylgold(III) carboxylates as new precursors for gold CVD". In: *Surface and Coatings Technology* 201.22 (2007), pp. 9099–9103. DOI: 10.1016/j.surfcoat.2007.04.030.
- [116] J. Messelhäuser, E. B. Flint, and H. Suhr. "Direct Writing of Gold Lines by Laser-Induced Chemical Vapor Deposition". In: *Applied Physics A* 55.2 (Aug. 1992), pp. 196–202. DOI: 10.1007/BF00334223.
- [117] Thomas H. Baum and Carol R. Jones. "Laser Chemical Vapor Deposition of Gold". In: *Applied Physics Letters* 47.5 (1985), pp. 538–540. DOI: 10.1063/1.96119.

- [118] Mark M. Banaszak Holl, Paul F. Seidler, Steven P. Kowalczyk, and F. Read McFeely. "Surface reactivity of alkylgold(I) complexes: substrate-selective chemical vapor deposition of gold from $\text{RAuP}(\text{CH}_3)_3$ ($\text{R} = \text{CH}_2\text{CH}_3, \text{CH}_3$) at remarkably low temperatures". In: *Inorganic Chemistry* 33.3 (1994), pp. 510–517. DOI: 10.1021/ic00081a019.
- [119] Maarit Mäkelä, Timo Hatanpää, Mikko Ritala, Markku Leskelä, Kenichiro Mizohata, Kristoffer Meinander, and Jyrki Räisänen. "Potential Gold(I) Precursors Evaluated for Atomic Layer Deposition". In: *Journal of Vacuum Science & Technology A* 35.1 (2017), 01B112. DOI: 10.1116/1.4968193.
- [120] Maarit Mäkelä, Timo Hatanpää, Kenichiro Mizohata, Jyrki Räisänen, Mikko Ritala, and Markku Leskelä. "Thermal Atomic Layer Deposition of Continuous and Highly Conducting Gold Thin Films". In: *Chemistry of Materials* 29.14 (2017), pp. 6130–6136. DOI: 10.1021/acs.chemmater.7b02167.
- [121] Michiel Van Daele et al. "Plasma-Enhanced Atomic Layer Deposition of Nanostructured Gold Near Room Temperature". In: *ACS Applied Materials & Interfaces* 11.40 (2019), pp. 37229–37238. DOI: 10.1021/acsami.9b10848.
- [122] G. E. Coates and C. Parkin. "Tertiary phosphine complexes of trimethylgold: infrared spectra of complexes of gold and some other metals". In: *J. Chem. Soc.* (o 1963), pp. 421–429. DOI: 10.1039/JR9630000421.
- [123] A. Tamaki and J.K. Kochi. "Formation and decomposition of alkyl-gold(I) complexes". In: *Journal of Organometallic Chemistry* 61 (1973), pp. 441–450. DOI: 10.1016/S0022-328X(00)86574-2.
- [124] Sanshiro Komiya, Thomas A. Albright, Roald Hoffmann, and Jay K. Kochi. "Reductive elimination and isomerization of organogold complexes. Theoretical studies of trialkylgold species as reactive intermediates". In: *Journal of the American Chemical Society* 98.23 (1976), pp. 7255–7265. DOI: 10.1021/ja00439a024.
- [125] S. Komiya and J. K. Kochi. "Electrophilic cleavage of organogold complexes with acids. The mechanism of the reductive elimination of dialkyl(aniono)gold(III) species". In: *Journal of the American Chemical Society* 98.24 (1976), pp. 7599–7607. DOI: 10.1021/ja00440a025.
- [126] Jack L. Davidson, Phillip John, Peter G. Roberts, Michael G. Jubber, and John I. B. Wilson. "Laser Photochemical Deposition of Gold from Trialkylphosphine Alkyl-gold(I) Complexes". In: *Chemistry of Materials* 6.10 (1994), pp. 1712–1718. DOI: 10.1021/cm00046a025.
- [127] Michiel Van Daele, Christophe Detavernier, and Jolien Dendooven. "Surface species during ALD of platinum observed with *in situ* reflection IR spectroscopy". In: *Phys. Chem. Chem. Phys.* 20 (39 2018), pp. 25343–25356. DOI: 10.1039/C8CP03585G.
- [128] Jolien Dendooven et al. "Surface mobility and impact of precursor dosing during atomic layer deposition of platinum: *in situ* monitoring of nucleation and island growth". In: *submitted to Nanoscale* ().
- [129] M. Van Daele, M. Griffiths, M. Minjauw, S. Barry, C. Detavernier, and J. Dendooven. "Reaction mechanism of the $\text{Me}_3\text{AuPMe}_3 - \text{H}_2$ plasma-enhanced ALD process". In: *Phys. Chem. Chem. Phys.* (2020). DOI: 10.1039/C9CP06855D.

EXPERIMENTAL METHODS

The use of a range of characterization techniques is required by the very nature of experimental research. This chapter will briefly explain the working principles behind the characterization techniques that were used for the research reported in this thesis.

2.1 X-RAY THIN FILM CHARACTERIZATION

2.1.1 *X-ray reflectivity*

X-ray reflectivity (XRR) is a surface sensitive technique that can be used to determine the layer thickness, density, and interface roughness of a thin film or a stack of thin films. Typically, a thickness between 1-100 nm can be measured with this method. The technique is based on the specular reflection of grazing-incidence X-rays.

An XRR setup consists of a monochromatic X-ray source and a detector, placed on opposite sides of the sample at a grazing angle θ (Figure 2.1a). A measurement is performed by scanning over a small θ range (usually 0-3°) and recording the intensity of the reflected X-ray beam as a function of the incident angle. Total external reflection will occur for angles below the critical angle θ_c of the measured material, as the refractive index of materials is slightly lower than 1 for X-rays. The refractive index can be expressed as $n = 1 - \delta + i\beta$, with δ ($\sim 10^{-5}$) and β , respectively, describing the dispersion and absorption of the X-rays in the material. For incident angles above the critical angle, a portion of the X-rays is reflected while the remaining fraction can penetrate the layer and reflect on the underlying interface, causing interference between X-rays that are reflected from different interfaces. For a single thin layer the intensity pattern will show periodic oscillations as a function of the observed reflection angle, known as Kiessig fringes. The spacing between the fringes $\Delta\theta$ is directly determined by the layer thickness d and is given by

$$\Delta\theta \approx \frac{\lambda}{2d} \quad (2.1)$$

with λ the wavelength of the X-rays. The fringes will be spaced closer together when the layer thickness increases. Not only the thickness has a

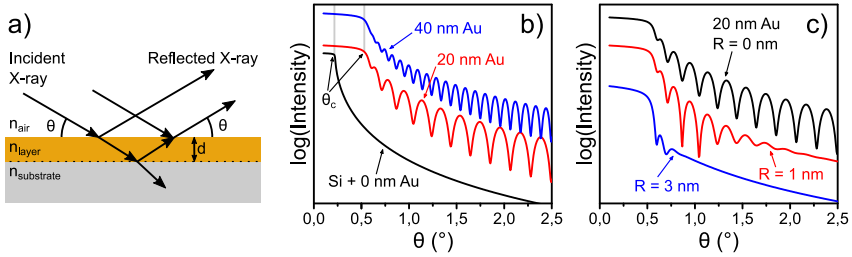


Figure 2.1: Principle of XRR. a) X-ray beam reflection from a single layer substrate. b) Simulated XRR patterns showing the effect of the layer thickness on the pattern. c) Simulated XRR patterns showing the effect of surface roughness on the Kiessig fringes. The curves were given an offset for clarity.

large influence on the pattern but also the roughness of the surface and interfaces will play a key role. Increasing the roughness will result in a faster decay of the signal and reduced fringe amplitudes at higher θ angles. Figure 2.1(b, c) shows simulated XRR patterns which demonstrate the effect of film thickness (b) and surface roughness (c) on the interference pattern. The interested reader can find more information regarding the theory and practical aspects of XRR in Daillant's excellent book.^[1]

2.1.2 X-ray fluorescence

X-ray fluorescence (XRF) relies on the excitation of a material by high-energy (monochromatic) X-rays and the detection of characteristic (or fluorescent) X-rays, which are emitted by the material. When an atom absorbs an X-ray, it can eject an (secondary) electron from a core shell, leaving behind a hole in that shell (Figure 2.2). As a result, the atom will be in an excited state and try to go back to the lower energy state by filling the hole with an electron from a higher shell. When the electron "falls" from the higher energy state to the lower energy state it can emit a photon. The energy of the emitted photon is equal to the energy difference between the electron states. The emitted X-rays are characteristic to the specific element, because the energy levels of the shells are determined by the atom, and as such, each atom will produce a fluorescence fingerprint that can be used to determine which elements are present in a given sample.

The X-ray signal is strongly attenuated by air, and of course also by the studied material. This poses a problem for the use of XRF as a replacement for XRR to perform thickness measurements. Luckily, for suf-

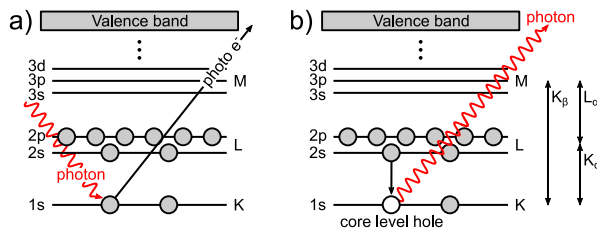


Figure 2.2: Basic working principle of XRF. a) Excitation of a core electron in the atom by a high energy photon. The excited electron receives enough energy to be ejected, leaving a hole in the core level. b) An electron from a higher energy level fills the core level hole. The energy difference is emitted as a fluorescent photon.

ficiently thin films the XRF signal scales linearly (in first approximation) with the amount of material that is present on the surface. For a 100 nm Au or Pt layer a beam of its characteristic L_{α} X-rays will have a loss in intensity of roughly 2.4% or 2.8%.¹ A 100 nm is thicker than any layer that was studied during this thesis. This means that XRF can be used for quantitative thickness measurements of a film. However, detecting light elements with XRF in atmosphere is rather difficult as their fluorescent X-rays are low in energy and will be heavily absorbed. In addition, for low Z-elements the Auger yield tends to be much larger than the fluorescence yield. This means that it is difficult to detect impurities in the films grown with atomic layer deposition (ALD), originating from the precursor ligands and the used co-reactants, which are typically constituted by light elements (e.g. C, N, O, P). These impurities are usually only present in the films in small concentrations, making it even more difficult to detect them. One way to address this issue is to perform XRF in a He atmosphere. However, this does not remove absorption from the Be windows on the detector. Another option is to perform everything in vacuum, without Be windows. This means that regular lab-based XRF is not very well suited to perform accurate compositional studies when light elements are involved.

2.1.2.1 Determine the film thickness

Most of the films prepared during the work of this thesis were very rough and as a result, XRR was not the best technique to determine the film thickness on those samples. Instead, XRF was used as an alternative, as

¹ Losses calculated with the Lambert-Beer law and mass extinction coefficients obtained from the NIST database[2]

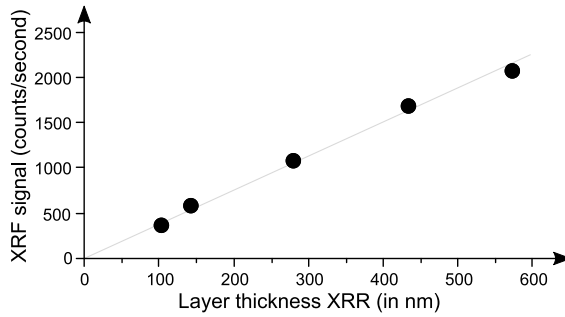


Figure 2.3: The integrated Au $L\alpha$ (9.713 keV) XRF signal of sputtered Au films on silicon (with native oxide) as a function of the Au layer thickness. The layer thickness was determined by XRR measurements.

its signal is proportional to the amount of material that is present on the surface.

The XRF signal needs to be calibrated as a function of the film thickness and of course it needs to be verified that the XRF signal does scale linearly with film thickness. Both can be verified by measuring a sequence of samples with varying film thicknesses. Figure 2.3 shows the integrated XRF intensity for the Au $L\alpha$ line (9.713 keV) as a function of Au film thickness. The films were deposited using physical vapour deposition and their thickness was determined by XRR measurements. A linear relation exists between the XRF signal intensity and the Au film thickness. In addition, it is possible to determine the expected XRF counts for a film that is 'x' nm thick. While this shows that a calibration is possible, it does not account for variations in the X-ray intensity for the X-ray source. This means that if there is any variation in the source brightness over time then our calibration will no longer be valid. To solve this issue it is useful to measure a reference sample, with a Au layer of known thickness, right before or after measuring an ALD sample for which the film thickness needs to be determined. Due to the linear relation between XRF intensity and film thickness (see Figure 2.3), the unknown film thickness of the ALD sample can then be determined using the following relation:

$$T_{sample} = T_{reference} \frac{XRF_{sample}}{XRF_{reference}} \quad (2.2)$$

with T_{sample} and $T_{reference}$ the layer thickness of the ALD sample and reference sample respectively, and XRF_{sample} , $XRF_{reference}$ the integrated XRF signal for a certain emission line of the ALD sample and reference sample.

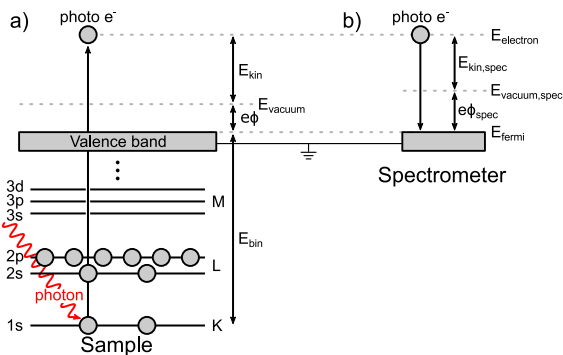


Figure 2.4: Basic working principle of XPS, depicting the energy levels of the generated and detected photoelectrons originating from a metallic sample. a) Excitation and emission of a core electron in the sample atom by a high energy photon. b) The emitted photoelectron is filtered in the electron analyser, based on its kinetic energy, and is then detected by the spectrometer. Figure adapted from [3]

As such, XRF can be used to measure the amount of material that is present/deposited on a substrate. As mentioned before, XRF performed in atmosphere is not well suited to determine the presence of light elements and therefore it is difficult to determine elemental compositions of samples containing most precursor ligands. Because of this a different technique is typically used in the CoCooN laboratory to perform compositional analysis, namely X-ray photoelectron spectroscopy.

2.1.3 X-ray photoelectron spectroscopy

X-ray photoelectron spectroscopy (XPS) is a surface sensitive technique that can provide information about elemental composition and binding energy in the top 5-10 nm of a sample.

The technique uses a monochromatic X-ray source to excite the material (typically $Al K_{\alpha}$, $E_{\gamma}=1468.7\text{eV}$). When an atom absorbs an X-ray a core electron can be ejected through a process called photo-ionization (Figure 2.4a). Before the electron can be detected it needs to overcome the workfunction of the material and leave the sample. The electrons that are emitted from the sample are then filtered in the electron energy analyzer, based on their kinetic energy E_{kin} . The electrons that pass through the analyser can be detected by the spectrometer and their binding energy E_{bin} can be calculated as:

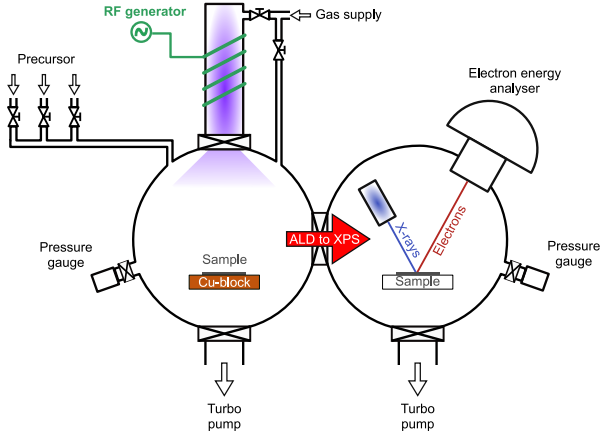


Figure 2.5: Schematic depiction of the *in-vacuo* ALD-XPS setup. On the left side the ALD reactor is depicted and on the right side the XPS chamber, the vacuum feed through allows the transfer of samples from the ALD reactor to the XPS chamber to occur without breaking vacuum. Figure made by Sofie Vandenbroucke.

$$E_{bin} = E_{\gamma} - E_{kin,spec} - e\phi_{spec} \quad (2.3)$$

with $E_{kin,spec}$ the measured kinetic energy of the electron in the spectrometer and ϕ_{spec} the spectrometer work function (a calibration constant).

Each element has characteristic binding energies, which means that XPS can be used to identify elements in a sample. Quantitative information about the composition is given by counting the number of detected electrons for each binding energy. The binding energy is slightly influenced by how the element is chemically bonded in the material, because of this XPS yields information about the chemical environment of each element.

Because electrons are strongly absorbed in atmosphere XPS measurements are typically performed in ultra-high vacuum (UHV) to prevent the absorption of electrons that are emitted from the sample. The information depth of XPS is limited by the inelastic mean free path (IMFP) of the electrons in the sample, which is the distance over which an electron travels on average through a solid before losing kinetic energy. For a kinetic energy equal to the X-ray energy (1486.7 eV), this IMFP is roughly 2.1 nm.² This limits the escape depth to a maximum of 10 nm, although

² Calculated using equation 5 in [4] to calculate the IMFP in elements

this is material dependent. As an electron loses kinetic energy it will no longer represent its original binding energy, as given in Eq. 2.3, and such an electron will contribute to the background signal in the spectrum.

Generally, XPS measurements are used *ex situ* to determine the composition of the film. However, the transfer through air results in contamination of the surface and unwanted side reactions with air, which means that information about surface species gets lost during transfer. The CoCooN research group has a dedicated *in-vacuo* ALD-XPS setup (Figure 2.5). Which allows for fast transfer (<60 s) of a sample from the ALD chamber to the XPS analyzing chamber without exposing the sample to atmosphere. This makes it possible to answer some fundamental questions about the surface reactions that occur during metal ALD growth (e.g. oxidation state, the role of surface species, incorporation of impurities, poisoning of reactive surface sites). The interested reader can find more information regarding the theory and practical aspects of XPS in Hofmann’s excellent book.^[5]

2.2 X-RAY SCATTERING METHODS

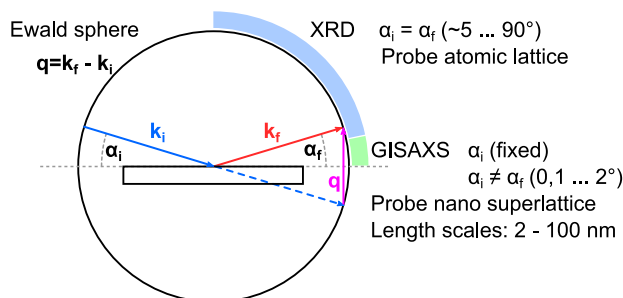


Figure 2.6: X-ray scattering, scattering angles for XRD and GISAXS.

X-ray scattering techniques detect the intensity of scattered X-rays, after they are able to interact with a sample, as a function of the incident and exit angles. The most common method in this class is X-ray diffraction (XRD), which yields information about the crystalline nature of the sample. XRD was used during this thesis to study the crystallinity of ALD grown Au and Pt films. As depicted in Figure 2.6, the incidence and exit angles (α_i and α_f , respectively) are varied over a large range during a scan and length scales of the atomic lattice are probed. For small angles the probed length scale increases and provides information about the superlattice, typically length scales up to 100 nm can be investigated. For specular

scattering, these low angles result in XRR measurements (see section 2.1.1), extending this to the detection of off-specular scattering leads to a more advanced X-ray scattering method called grazing-incidence small-angle X-ray scattering (GISAXS). Generally, this method uses a fixed incidence angle and measures the scattered intensity as a function of the exit angle, over a small 2D section. The working principle behind XRD and GISAXS will be discussed in the following sections.

2.2.1 X-ray diffraction

In XRD the periodic structure of a material is studied, i.e. it reveals how the atoms that make up the material are ordered. Highly ordered materials are called crystalline and poorly ordered materials are called amorphous or "glassy". XRD can be used to measure unknown crystalline structures of materials and construct a model for their crystal structure, or in reverse perform phase identification of a material by comparing the measured diffraction patterns to known crystal patterns.

Electromagnetic waves propagating through a material can undergo elastic scattering when they interact with the electrons in the material (Thomson scattering). The electron density in an amorphous material will have no inherent periodic structure and this will mainly cause destructive interference of the scattered waves, resulting in no measurable diffraction peaks. In crystalline materials, the atoms are arranged in a periodic structure and as a consequence so is the electron density. For these materials it is possible that constructive interference of the scattered waves occurs for certain conditions of the incoming and diffracted waves, leading to measurable diffraction peaks.

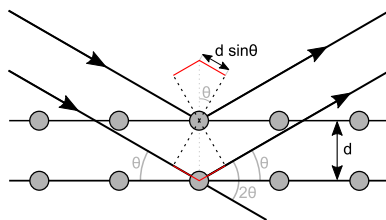


Figure 2.7: XRD and Bragg's law.

An intuitive way to understand XRD is to approach it as the reflection of X-rays on crystal planes in the material. Figure 2.7 describes the reflections on the crystal planes. For constructive interference to occur the difference

in pathlength between the X-rays (marked by the red lines) needs to be a multiple of the wavelength. This leads to Bragg's law (a special case of Laue diffraction):

$$2d \sin(\theta) = n\lambda \quad (2.4)$$

with θ the incident angle with respect to the crystal plane, d the distance between the crystal planes, and λ the wavelength of the incident X-rays. Bragg's law states that each crystal plane diffracts X-rays in a mirror-like fashion. However, this only occurs for a specific angle θ which is related to the interplanar distance d . Simultaneously scanning over θ and 2θ makes it possible to identify the reflections for planes parallel to the sample surface. Each crystal has a diffraction fingerprint, allowing the identification of the crystal phases that are present in the sample.

2.2.2 Grazing-Incidence Small-Angle X-ray scattering

GISAXS is a special case of X-ray scattering, for which all considered angles are small, typically less than 5° . Because the reciprocal space is being probed with GISAXS, the small scattering angles correlate to information about the long range order on the sample. Depending on the used energy of the photons and the sample-to-detector distance (SDD) the probed length scales can be changed, for example at BM26 of the ESRF synchrotron facility it is possible to reach length scales up to 400 nm or more. On these length scales the X-rays are not scattered by the periodic electron density of the atomic lattice, instead scattering is caused by variations of the electronic density of the studied material and the surrounding matrix on the nanometer scale. This means that the scattered signal will heavily depend on the topography and morphology of the probed sample, causing off-specular scattering. Figure 2.8 displays the involved angles of the GISAXS geometry and the resulting 2D GISAXS pattern that is caused by scattered X-rays from a particle layer on a sample. It also shows the incident (α_i) and exit angles (α_f and θ_f) of the X-rays. The scattering intensity is detected on a 2D detector, the (x,y,z) coordinates of its pixels are converted to reciprocal space coordinates, i.e. q -space, according to the following formulas:

$$q_x = k_0[\cos(2\theta_f)\cos(\alpha_f) - \cos(\alpha_i)] \approx 0 \quad (2.5)$$

$$q_y = k_0[\sin(2\theta_f)\cos(\alpha_f)] \quad (2.6)$$

$$q_z = k_0[\sin(\alpha_f) + \sin(\alpha_i)] \quad (2.7)$$

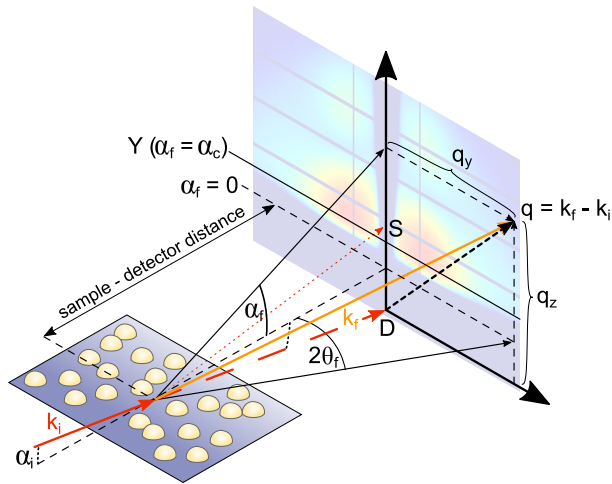


Figure 2.8: GISAXS geometry showing the incident and exit angles and the scattering pattern obtained from a layer of particles on a substrate.

The considered angles for GISAXS are small, which allows the cosine and sine functions to be expanded in a Taylor/Maclaurin series and for very small angles the second and higher order terms can be neglected. For the q_x contribution both terms cancel out, as $\cos(x) \approx 1$, and the q_x contribution is negligible, which means that the q_y component is a good and acceptable approximation for the q_{xy} component. Synchrotron radiation is typically used to perform GISAXS experiments, because a synchrotron provides several conditions that are difficult to achieve simultaneously in a lab environment. For example:

HIGH BRILLIANCE to investigate very low amounts of materials and to investigate dynamic processes. The studied layers can have a thickness of a monolayer with very low signal intensities, which requires high brilliance to obtain a good signal on a manageable time scale (order of minutes).

HIGH COLLIMATION to provide low beam divergence over large distances, as changing the sample-to-detector distance (SDD) determines the angular resolution and correspondingly the q -space and feature size that can be investigated. The SDD typically lies between 1-4 meter for most GISAXS setups, although setups with SDD of more than 10 meter exist to investigate feature sizes larger than a micron.

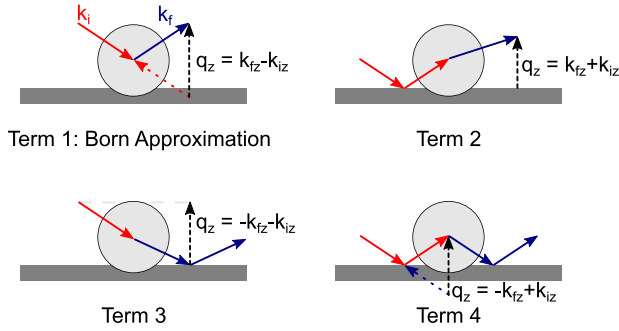


Figure 2.9: Scattering contributions for the DWBA. Term 1 is the scattering contribution for the Born approximation, the other terms are the additional terms that include reflections on the surface.

TUNABLE ENERGY to combine GISAXS with XRF measurements and to modify the observable q-space.

The measured scattering intensity, $I(\mathbf{q})$, is divided into two components and can be described as

$$I(\mathbf{q}) = |F(\mathbf{q})|^2 S(\mathbf{q}) \quad (2.8)$$

with \mathbf{q} the momentum transfer (a vector in reciprocal space), the form factor of the particle (F), and the interference function (S). The information of a particle's shape and size is described by the form factor. For an isolated particle it is the Fourier transform of the particle shape function, resulting in the simple Born approximation.^[6,7] When the particle is located on a surface additional reflection and refraction effects need to be included, leading to the distorted wave Born approximation (DWBA) (see Figure 2.9).^[8,9] The scattering contributions of every individual particle will interfere with each other. How these contributions interfere depends on the particle distribution on the sample. The particle distribution is described by the interference function, which is the Fourier transform of the particle correlation function.

After a GISAXS pattern is recorded it is possible to extract information about the particles from the scattering features. Some basic properties can be determined such as the average particle height, radius, center-to-center distance, and the average electron density on the surface. To verify that the obtained values from such a "simple" analysis of the scattering patterns reflect reality it is often necessary to use simulations of the GISAXS data and to compare this analysis of the reciprocal data with data obtained

from real space imaging techniques, such as scanning electron microscopy. Although real space microscopy is difficult to implement in a way to obtain real time *in situ* information (scanning electron microscopy will be discussed in the next section). While a whole sequence of samples can be made and the final result can analysed with *ex situ* real space imaging techniques, this is very cumbersome and time consuming to perform. Therefore, using simulations to reproduce the obtained scattering patterns is practically the only way to obtain information about the particles during their deposition. In this thesis, the simulation software IsGISAXS was used to simulate scattering patterns.^[10] Obviously, the real particle distribution is not known beforehand and some assumptions need to be made to provide a starting point for the simulations. Upon this starting point additional details can be included and simulated. However, including more and more detail will lead to more investment into simulations for diminishing returns and an increasing correlation between the growing number of fitting parameters, which means that a trade off needs to be made between the complexity of the used models and the time that can be invested in every simulation.

As the use of simulations for GISAXS is quite important, the rest of this section will describe a case for platinum particles on a silicon substrate to give the reader a better understanding on how the form factor and the structure factor affect the scattering pattern. A layer of platinum spheres on a silicon substrate was simulated with the IsGISAXS software. The obtained form factors, interference functions, and 2D GISAXS images are displayed in Figure 2.10. Figure 2.10(I) shows the square modulus of the form factor $|F(\mathbf{q})|^2$ for a particle radius of 1, 2, and 3 nm. The first row shows the 1D form factor along the q_y direction and the second row shows the 2D form factor for a Pt particle on a Si surface. It can be seen that increasing the particle radius results in a shift of the secondary minima and maxima towards lower q values, bringing additional lobes of the form factor into the measured region. The 2D form factor is not isotropic, which is unexpected as the particle shape is isotropic. The reason is that the particle is located on a surface and additional reflection and refraction effects need to be included to properly describe the scattering behaviour, which causes interference effects along q_z . For large exit angles these additional effects contribute very little to the overall scattering signal. However, signal enhancement occurs for exit angles close to the critical angle of the sample, producing a bright band of scattered intensity at the critical angle. This band is often called the Yoneda (or Vineyard) peak, marked by Y in Figure 2.10(I).

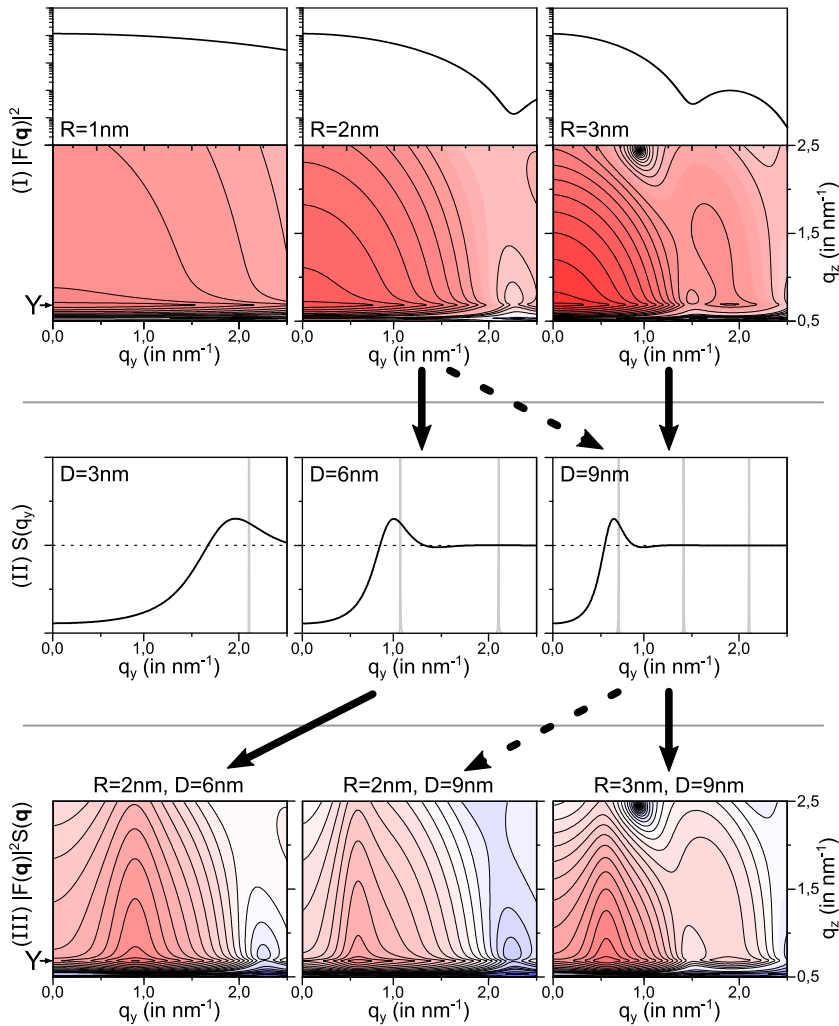


Figure 2.10: GISAXS simulations of platinum spheres on a silicon surface, performed with the IsGISAXS software. (I) The square modulus of the form factors $|F(q_y)|^2$ for Pt spheres with radius R : 1 nm, 2 nm, and 3 nm. The top panels show the 1D cut taken at q_z position Y and the bottom panel shows the 2D form factor. (II) Interference function for a one dimensional paracrystal with interparticle distance $D = 3, 6,$ and 9 nm and a disorder ratio (w/D) of $0,3$ for the black lines and no disorder ($w/D=0$) for the grey lines. (III) Simulated 2D GISAXS patterns. The q_z position for which a maximum in scattering intensity is observed, called the Yoneda peak, is marked by Y in (I, and III).

A one-dimensional paracrystal was used as the particle distribution, which is a regular lattice with loss of long range order. The interference function for an interparticle distance of 3, 6, and 9 nm is displayed in Figure 2.10(II). For every particle distance two functions are plotted, the grey lines are obtained for a perfectly ordered crystal with no disorder $w=0$ nm and for the black lines a disordered paracrystal was used ($w/D = 0,3$) this induces a loss of order for particles that are located further away from the origin. For a perfectly periodic structure ($w=0$ nm) the peaks of the interference function are sharp, while inducing disorder results in broadening of the peaks in the interference function and with sufficient disorder the secondary peaks are smoothed out completely. It can be seen that larger interparticle distances result in smaller q -values for the first peak. Which is to be expected as q -values are inversely related to real space values via the approximation $q = 2\pi/d$, meaning that small q -values correspond to large real space distances and vice versa. The first peak in the interference function has a large impact on the obtained 2D GISAXS pattern, and the mean interparticle distance can be extracted from the position of the main scattering peak in the GISAXS pattern.

The GISAXS pattern is obtained by multiplying the form factor with the interference function, see Figure 2.10(III) where the simulated 2D scattering patterns are shown. It can be seen that the interference function has a large influence on the overall scattering pattern and that the form factor results in a modulation of the peaks that are present in the interference function. The form factor usually induces a shift of the main scattering peak to lower q_y values.

These simulations show the GISAXS patterns that originate from a layer of particles without size distribution. In reality the particles will have a size distribution and potentially have multiple particle shapes, which are a priori not known. This increases the complexity of the model and several assumptions need to be made to reduce the complexity of the model to something that can actually be used to simulate the experimental patterns and iterate over the input parameters. An approximation that is often employed is the use of the local monodisperse approximation (LMA) formalism, which is commonly used for polydispersed systems. The LMA approximation assumes that over a coherent X-ray domain all particles are, approximately, of the same size-shape. The total scattering intensity can be thought of as being built up from a collection of monodisperse subsystems, each weighted by the probability that this size-shape is present on the surface. The interested reader can find more information regarding the theory and practical aspects of GISAXS in Daillant's excellent book^[1] and the review paper by Renaud et al.^[9]

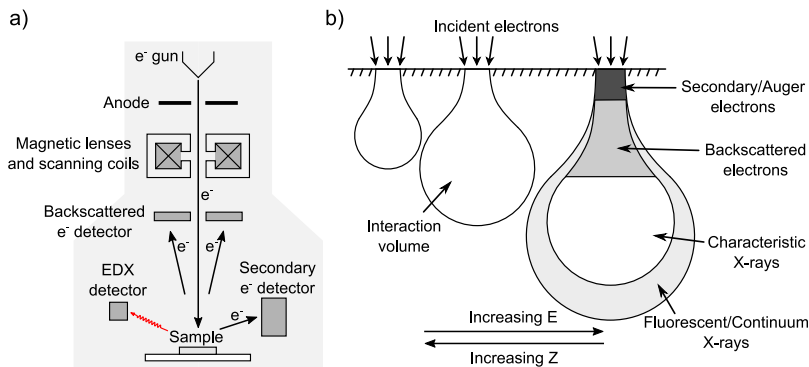


Figure 2.11: Schematic drawing of scanning electron microscopy. a) a simplified diagram of an SEM instrument and b) the interaction of the incident electron beam with a sample (E is the energy of incident electrons, Z is the atomic number of the sample atoms). Figure adapted from [11]

2.3 SCANNING ELECTRON MICROSCOPY

Real-space morphological information and a resolution at the nanoscale can be obtained in scanning electron microscopy (SEM). An SEM instrument typically consists of an electron column, sample stage, several detectors and operates under vacuum. A simplified drawing of the instrument is displayed in Figure 2.11a.

The electron column consists of several parts that are operating together to create a focused electron beam. At the top of the column a cathode filament emits electrons, which are then accelerated towards the anode by applying a voltage difference (typically several kV) between cathode and anode. The accelerated electrons are focused to a small spot (~ 1 nm diameter) on the sample by one or more magnetic lenses. The electron beam is deflected by scanning coils or deflector plates before leaving the electron column. The beam is scanned across a rectangular area of the sample by adjusting the deflection in the xy -plane.

Secondary electrons are created when a loosely bound electron is ejected from a specimen atom due to an inelastic collision with a primary electron from the incident beam. These secondary electrons have a short mean free path ~ 1 nm due to their low kinetic energy (~ 1 eV).^[4] As a consequence, the secondary electrons have an escape depth of only a few nanometers, resulting in high resolution topographic information of the sample with a large depth of view. The secondary electrons are attracted by a positively charged grid and further accelerated towards a scintillator-

photomultiplier system for detection, usually an Everhart-Thornley detector.

Elastic collisions of a primary electron with a specimen atom can result in backwards scattering of the electron. They have large kinetic energies (up to the beam energy) and due to the increased path length can originate from a much larger volume than the secondary electrons, resulting in a worse resolution than secondary electrons. However, backscattered electrons can be used to detect areas with different chemical compositions as the efficiency of backscattering increases with atomic number resulting in a brighter image.

Often energy dispersive X-ray spectroscopy (EDX) is implemented on SEM instruments. When a secondary electron is created from a core electron the hole in the electron shell can be filled by a higher energetic electron. This event causes the emission of a characteristic X-ray (similar mechanism as XRF), which can be used to identify the elements that are present in the sample. A large benefit of EDX compared to XRF is that X-ray generation and detection occurs in vacuum, which allows the detection of light elements. Composition maps of the sample can be made with a lateral resolution of a few microns (due to the size of the interaction volume). The interested reader can find more information regarding the theory and practical aspects of SEM in the excellent book by Reimer.^[12]

2.4 FOURIER TRANSFORM INFRARED SPECTROSCOPY

Infrared spectroscopy is an analytical technique that studies the characteristic rotational and vibrational energies of molecules. Probing a sample with infrared light results in transitions between vibrational and rotational energy states, leading to absorption of the incident light. The loss in intensity as a function of photon energy (or wavelength) contains "fingerprints" of the chemical functional groups that are present in the sample and by using a correlation table it is possible to quickly identify the general functional groups that are present in the sample. The energy required to excite most molecular vibrations lies in the mid-infrared region, spanning the wavelength region of 2.5 - 25 μm , or equivalent in wavenumbers ($\nu = 1/\lambda$) corresponding to the range of 4000 - 400 cm^{-1} .

2.4.1 *Molecular vibrations*

The atoms in every molecule are in motion relative to each other, leading to molecular vibrations. In a first approximation, it is possible to treat these vibrations as classical springs (simple harmonic oscillators). Based

on Hooke's law and Newton's second law of motion the following expression for the vibration frequency (ν) can be derived:

$$\nu = \frac{1}{2\pi} \sqrt{\frac{k}{\mu}} = \frac{1}{2\pi} \sqrt{\frac{k(m_1 + m_2)}{m_1 m_2}} \quad (2.9)$$

with k the force constant of the molecular bond and μ the reduced mass of the atoms on both sides of the bond. While for a classical spring every energy state is allowed, this is not the case for molecular vibrations and instead discrete energy states exist which are separated by a fixed energy difference (in the harmonic approximation), depicted in Figure 2.12a. These energy states are given by the following equation:

$$E_n = h(n + \frac{1}{2})\nu = h(n + \frac{1}{2}) \frac{1}{2\pi} \sqrt{\frac{k}{\mu}} \quad (2.10)$$

with h being Planck's constant and n the energy level, starting from the ground state (E_0).

A photon with the correct energy ($E_\gamma = h\nu$) can be absorbed by the molecule and cause a transition from one vibrational state to another. There are two transitions possible in a harmonic oscillator, the fundamental and hot-band transitions. The fundamental transition, from the ground level to the first excited state ($E_0 \rightarrow E_1$), is the main vibration mode that is observed in an infrared spectrum. This results in an absorption

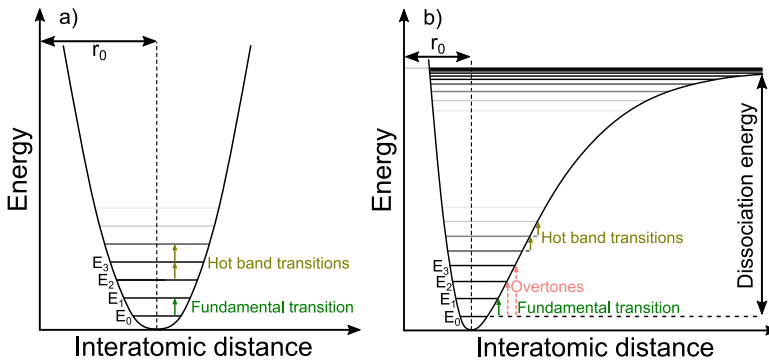


Figure 2.12: Energy levels for a harmonic and anharmonic oscillation, depending on the initial and final energy state the transitions can be fundamental, overtones, or hot bands. a) Harmonic vibrations, with equally spaced energy levels. b) Anharmonic vibrations, for which the energy difference decreases for the higher levels.

of the infrared spectrum at the frequency (ν) that corresponds to the energy difference between both levels. It is possible that transitions between neighbouring energy states above the ground state occur ($E_{n+1} \rightarrow E_{n+2}$), giving rise to the hot band transitions. The intensity of these transitions is usually low as it is unlikely for energy levels above the ground state to be heavily populated. Because of selection rules overtones are not allowed for harmonic oscillators, which are transitions between the ground state and the second, third,... state.

In reality, molecular vibrations are anharmonic in nature, which has two effects. The first is that the energy levels are no longer equally spaced, but the energy difference between consecutive energy levels decreases (Figure 2.12b). This means that the hot bands will have less energy than the fundamental transition. The second effect is that overtones are allowed for anharmonic oscillators and the first overtone ($E_0 \rightarrow E_2$) has a frequency that is slightly less than twice that of the fundamental transition.

2.4.1.1 Dipole moment

There is an additional requirement for a vibration mode to be infrared (IR) active, which is that when a photon is absorbed the transition needs to be accompanied by a change in the dipole moment of the molecule. The intensity of an IR absorption peak is related to the number of oscillators that can be excited in the material, but also related to how large the change in dipole moment is. A larger change in dipole moment usually results in a stronger absorption of IR light.

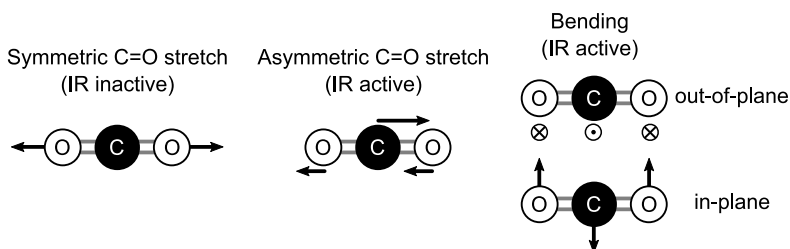


Figure 2.13: Vibrational modes of CO_2 . The symmetric C=O stretching mode is IR inactive, as it has not changing dipole moment. While the asymmetric stretching and two bending modes have a changing dipole moment and are IR active.

This means that vibrations that have no changing dipole moment will not be visible in infrared spectroscopy while the modes with a changing dipole moment can be detected in a sample. As an example the vibra-

tions of a linear CO_2 molecule are displayed in Figure 2.13. Being a linear molecule with three atoms, it has four vibration modes ($3N - 5$, $N =$ number of atoms): symmetric C=O stretch, asymmetric C=O stretch, and two bending modes along two different axes. Of these four modes, the symmetric C=O stretch does not have a change in the dipole moment during its vibration and is, therefore, IR inactive. While the other three vibrations result in a change in dipole moment and are therefore able to absorb IR radiation with the correct wavelength.

2.4.1.2 Using isotopes

Changing an atom with one of its isotopes can have a large effect on the absorption frequency of its molecular vibrations. While isotopes of an atom have no influence on its chemical properties, it does change the mass of the atom and this influences the vibration frequencies of the molecules (Eq. 2.9). The use of different isotopes can help with identifying the presence of the functional group, as the peaks that are caused by the altered functional group will appear at different positions. A nice example of such a shift in vibration frequency is the use of deuterium (D) instead of hydrogen (H) for a hydroxyl (OH) group as changing the H atom by its first isotope D doubles the mass of this atom. The reduced masses of an OH and OD group are $\mu_{\text{OH}} = (16 * 1)/(16 + 1) \simeq 0.94$ and $\mu_{\text{OD}} = (16 * 2)/(16 + 2) \simeq 1.78$, respectively. This means that the vibration frequency of the O-H stretching mode is shifted to a lower vibration frequency by a factor of $\sqrt{\mu_{\text{OD}}/\mu_{\text{OH}}} \simeq 1.376$ when the hydrogen atom is swapped with a deuterium atom, which is also observed experimentally.^[13]

2.4.2 FTIR setup

Matter is able to interact with infrared light, which results in an absorption fingerprint for each functional group. In infrared absorption spectroscopy a sample is exposed to an infrared beam and absorption by the sample can be measured as a function of the wavelength or frequency. In traditional infrared spectroscopy each wavelength is measured separately, usually by rotating a prism or a diffraction grating. A major downside is that this leads to very long measurement times for a single infrared spectrum across the wavelength region of interest.

An alternative method is Fourier transform infrared spectroscopy (FTIR), which uses an interferometer to encode the incident IR signal and then detect it after it interacts with the sample (Figure 2.14). The interferometer consists of a beam splitter that reflects half of the beam and allows the

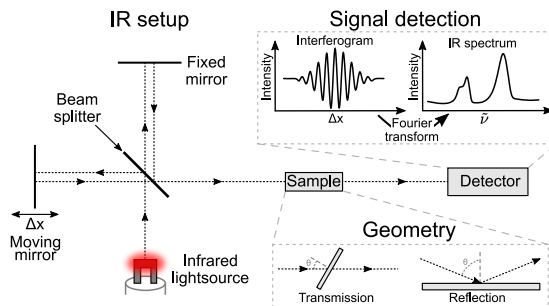


Figure 2.14: Schematic depiction of the FTIR technique, showing the IR beam paths inside the interferometer, the possible sample geometry, the interferogram, and the resulting spectrum. Figure adapted from [11]

other half to pass through. Both beams are reflected back to the beam splitter and interfere before leaving the interferometer section. By moving one of the mirrors back and forth over a small distance (Δx) a difference in pathlength is induced between both arms, resulting in constructive and destructive interference of the IR light. An interferogram is obtained when the signal intensity is measured as a function of Δx . Performing a Fourier transform on the interferogram yields the IR spectrum. By comparing this spectrum to a reference it is possible to discern IR absorption by the sample.

The IR light can either pass through the sample (transmission geometry) or be reflected from it (reflection geometry). For a transmission geometry the sample needs to be transparent for IR light, which is the case for Si substrates. A downside becomes apparent when IR opaque layers need to be studied, for example metals. These films will heavily absorb IR light, limiting the study of these films to the nucleation stage. This issue can be avoided when a reflection geometry is used, where the infrared beam is reflected from the top side of the sample. It might be necessary to use an additional reflecting layer on the sample, to avoid interference effects between the front and backside of the sample. Regardless of the used geometry it is possible to study the surface species during an ALD process. The interested reader can find more information regarding the theory and practical aspects of infrared spectroscopy in Tasumi's excellent book.^[14]

2.4.3 Raman spectroscopy

Raman spectroscopy (named after C. V. Raman) is a spectroscopic technique that can be used to determine the vibrational modes of molecules.

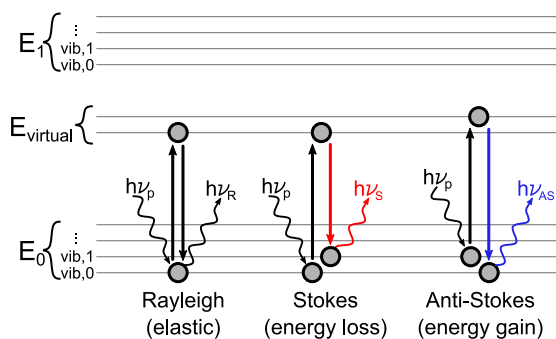


Figure 2.15: Energy diagram showing elastic (Rayleigh) and inelastic (Raman) scattering of a pump photon ($h\nu_p$). The molecule is excited to a virtual state (E_{vir}) and relaxes to a vibrational level in the electronic ground state of the molecule.

This method relies on the inelastic scattering of incident photons, known as Raman scattering. Typically, a laser beam is used to excite the molecule to a virtual energy state instead of a real vibrational state (Figure 5.9). The molecule relaxes from this virtual energy state to a real vibrational state of the electronic ground state. During relaxation photons are emitted, their energy depending on the vibrational energy levels of the molecule. The probability for a transition to a virtual state to occur is very low, making the signal generated from Raman scattering very weak. While weak signals are generated by Raman scattering it provides important complementary information to IR spectroscopy on the vibrational modes of molecules. In IR spectroscopy a change in dipole moment is required for a vibrational mode to be IR active, which is not the case for a Raman mode. Instead a Raman active mode needs to have a change in polarizability. The result of this is that a strong IR mode is typically a weak Raman scatterer and *vice versa*. While Raman scattering is a very weak effect, it is possible to increase the signal strength when molecules are adsorbed and measured on rough metal surfaces or on nanostructures that exhibit plasmonic effects. This is called surface-enhanced Raman spectroscopy (SERS) and an increase of the signal strength up to 10-11 orders of magnitude can be achieved, which allows the detection of single molecules. The interested reader can find more information regarding Raman spectroscopy in Long's excellent book^[15] and concerning the topic of SERS in the excellent book by Le Ru and Etchegoin.^[16]

2.5 GAS PHASE ANALYSIS

Separation and detection of gas phase molecules based on their mass can be done using quadrupole mass spectrometry (QMS). The incoming molecules are ionized, then they are filtered based on their mass-to-charge (m/q) ratio, and finally detected. These three steps are schematically depicted in Figure 2.16.

The ionization element consists of a heated filament that will thermionically emit electrons. They are then accelerated over a potential difference. The incoming molecules collide with the electrons, invoking ionization and producing a molecular ion M^+ . In many cases further fragmentation of the molecule occurs due to secondary reactions. After ionization, the molecular ions need to be filtered according to their mass-to-charge ratio (m/q). In a QMS the filtering occurs with a quadrupole mass filter, consisting of four conductive rods arranged as shown in the middle of Figure 2.16. Opposing rods are connected and a potential difference is applied between both pairs. Because of the arrangement an electric quadrupole moment can be generated. The mass-to-charge ratios are filtered by applying a radio frequency component to the potential difference between the rods. This allows ions with a certain m/q value to pass while the others form unstable trajectories and do not pass through the filter. The m/q value that is allowed to pass can be selected by tuning the applied voltages and/or frequency. Finally, the filtered ions collide with a metal cup, generating a small current in the cup proportional to the collection rate of the ions. The interested reader can find more information regarding the theory and practical aspects of QMS in Dawson's excellent book.^[17]

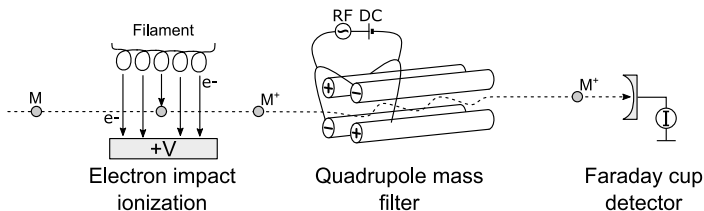


Figure 2.16: Schematic drawing of a quadrupole mass spectrometer (Hiden HPR-30). The dotted line shows the path of molecules as they are first ionized, filtered, and finally detected.

2.6 ATOMIC FORCE MICROSCOPY

Atomic force microscopy (AFM) is a type of scanning probe microscopy that is used to determine the topography of a surface on the nanoscale and is able to achieve height resolution on the level of an Å. An AFM device scans the surface with a sharp tip, mounted on a cantilever, in the xy direction and monitors the deflection of the cantilever in the z direction to obtain topographic information of the sample's surface. Due to contact forces between the tip and the surface the cantilever deflects according to Hooke's law. Usually, the deflection is measured by reflecting a laser beam off the back of the cantilever and measure the laser beam by a position-sensitive detector, which consists of a pair of closely spaced photodetectors. The AFM can be operated in contact, tapping, or non-contact mode. Tapping mode is the most frequently used measurement mode on most AFM devices. The interested reader can find more information regarding the theory and practical aspects of AFM in Voigtländer's excellent book.^[18]

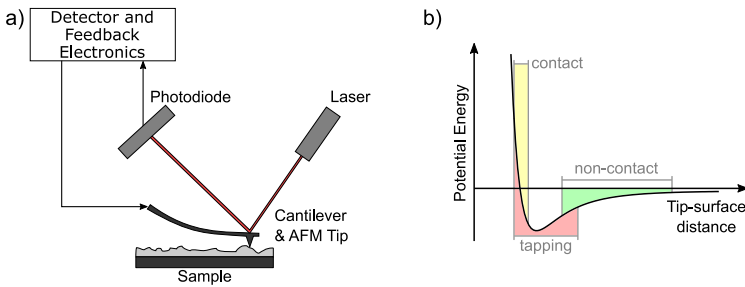


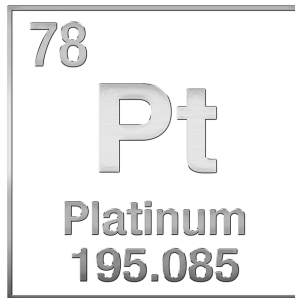
Figure 2.17: a) Schematic drawing of an atomic force microscope using beam deflection detection (image adapted from [19]) b) Lennard-Jones potential depicting the attraction and repulsion between the AFM tip and the sample surface.

REFERENCES

- [1] Jean Daillant and Alain Gibaud. *X-ray and Neutron Reflectivity: Principles and Applications*. 1st ed. Lecture Notes in Physics. Springer, 2009. ISBN: 0940-7677.
- [2] NIST. *X-Ray Mass Attenuation Coefficients*. URL: physics.nist.gov/PhysRefData/XrayMassCoef/tab3.html. (accessed: 10/01/2020).
- [3] Matthias M. Minjauw. "Atomic Layer Depositon of Ruthenium and Silver". 2019.
- [4] M. P. Seah and W. A. Dench. "Quantitative electron spectroscopy of surfaces: A standard data base for electron inelastic mean free paths in solids". In: *Surface and Interface Analysis* 1.1 (1979), pp. 2–11. DOI: 10.1002/sia.740010103.
- [5] Siegfried Hofmann. *Auger- and X-ray Photoelectron Spectroscopy in Materials Science: A User-Oriented Guide*. 1st ed. Springer Series in Surface Sciences. Springer, 2013. ISBN: 0931-5195.
- [6] Lewis Katz. "X-ray diffraction in crystals, imperfect crystals, and amorphous bodies (Guinier, A.)" In: *Journal of Chemical Education* 41.5 (1964), p. 292. DOI: 10.1021/ed041p292.2.
- [7] Bertram Eugene Warren. *X-ray Diffraction*. Courier Corporation, 1990.
- [8] George H. Vineyard. "Grazing-incidence diffraction and the distorted-wave approximation for the study of surfaces". In: *Phys. Rev. B* 26 (8 Oct. 1982), pp. 4146–4159. DOI: 10.1103/PhysRevB.26.4146.
- [9] G. Renaud, R. Lazzari, and F. Leroy. "Probing surface and interface morphology with Grazing Incidence Small Angle X-Ray Scattering". In: *Surface Science Reports* 64.8 (2009), pp. 255–380. DOI: 10.1016/j.surfrep.2009.07.002.
- [10] Rémi Lazzari. "IsGISAXS: a program for grazing-incidence small-angle X-ray scattering analysis of supported islands". In: *Journal of Applied Crystallography* 35.4 (Aug. 2002), pp. 406–421. DOI: 10.1107/S0021889802006088.
- [11] Thomas Dobbelaere. "Plasma-enhanced atomic layer depositon of transition metal phosphates". 2017.
- [12] Reimer Ludwig. *Scanning Electron Microscopy: Physics of Image Formation and Microanalysis*. 2nd ed. Springer Series in Optical Sciences. Springer-Verlag Berlin Heidelberg, 1998. ISBN: 978-3-642-08372-3.
- [13] Bo Berglund, Jan Lindgren, and Jörgen Tegenfeldt. "O-H and O-D stretching vibrations in isotopically dilute HDO molecules in some solid hydrates". In: *Journal of Molecular Structure* 43.2 (1978), pp. 169–177. DOI: 10.1016/0022-2860(78)80004-0.
- [14] Mitsuo Tasumi, Akira Sakamoto, and Shukichi Ochiai. *Introduction to experimental infrared spectroscopy: fundamentals and practical methods*. Somerset: Wiley, 2014.
- [15] Derek A. Long. *A Unified Treatment of the Theory of Raman Scattering by Molecules*. 1st ed. John Wiley & Sons, Ltd, 2002. ISBN: 9780471490289.
- [16] Eric Le Ru and Pablo Etchegoin. *Principles of Surface-Enhanced Raman Spectroscopy and Related Plasmonic Effects*. 1st ed. Elsevier Science, 2008. ISBN: 9780444527790.
- [17] In: *Quadrupole Mass Spectrometry and its Applications*. Ed. by Peter H. Dawson. Elsevier, 1976, pp. 345–349. ISBN: 978-0-444-41345-1.
- [18] Bert Voigtländer. *Scanning Probe Microscopy: Atomic Force Microscopy and Scanning Tunneling Microscopy*. 1st ed. NanoScience and Technology. Springer, 2015. ISBN: 1434-4904.

- [19] Wikipedia. *Atomic force microscope block diagram*. URL: commons.wikimedia.org/wiki/File:Atomic_force_microscope_block_diagram.svg. (accessed: 12/03/2020).

Part II



Platino : little silver

"Poco a poco se va lejos"

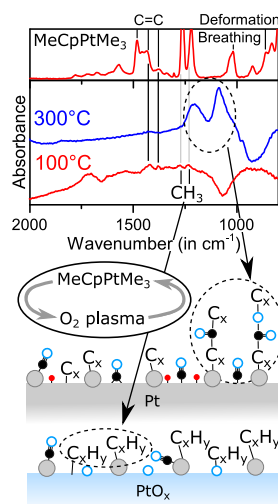
"Little by little one goes a long way"

- Spanish saying,

SOMETIMES WRONGFULLY ATTRIBUTED TO J.R.R. Tolkien

PAPER I: SURFACE SPECIES DURING THERMAL AND PE-ALD OF PLATINUM

Due to the electrical, electrochemical and catalytic properties of platinum, there is a lot of interest to use it as an electrode material for fuel cells, electrolyzers, and as a catalyst in chemical production.^[1-9] However, Pt is an expensive noble metal and therefore synthesis methods are required that allow optimization of the performance and reduce the Pt content. In this context, atomic layer deposition (ALD) of Pt nanoparticles and ultrathin layers is attractive because this technique offers submonolayer control over the metal loading and layer thickness and enables conformal deposition on complex 3D substrates.^[10] The most adopted ALD process for Pt, introduced by Aaltonen et al., is the thermal process at 300 °C using MeCpPtMe₃ as the precursor and O₂ gas as the reactant.^[11] While a significant amount of research has been performed to unravel the reaction mechanism, only a limited number of surface studies have been performed to directly identify the surface species during Pt ALD. In this chapter, thermal ALD and plasma-enhanced ALD (PE-ALD) of Pt, using MeCpPtMe₃ as precursor and O₂ gas or O₂ plasma as reactant, are studied with in situ reflection Fourier Transform Infrared spectroscopy (FTIR) at different substrate temperatures. This is done to identify the functional groups present during Pt ALD and investigate the origin of the temperature dependent growth rate of the thermal process. An in depth description of the existing literature concerning the growth



This chapter was published as a research article in the journal: Physical Chemistry Chemical Physics, titled "Surface species during ALD of platinum observed with in situ reflection IR spectroscopy".^[1] The image on this page is a reworked version of the original TOC-graphic, submitted with the published article. Author contributions: M.V.D. designed the experiments, performed the ALD depositions and FTIR measurements, analyzed and interpreted the results; J.D. and C.D. assisted in designing the experiments and interpreting the results; M.V.D. prepared the manuscript; J.D. and C.D. contributed to revising the manuscript.

mechanism of Pt ALD is given in the introduction chapter of this thesis, see section 1.2.2.1.

3.1 EXPERIMENTAL

3.1.1 *Experimental setup*

All ALD experiments are carried out in a home-built pump type ALD reactor, with a base pressure of 2×10^{-6} mbar.^[12] A Vertex 70v from Bruker is attached to this reactor with a medium band mercury cadmium telluride (MCT) detector cooled with liquid nitrogen. A schematic representation of this reactor is shown in Figure 3.1. The FTIR setup can be used in transmission as well as reflection geometry. In transmission mode the infrared (IR) beam passes through the substrate, while in reflection mode, the IR beam impinges on the substrate under a low angle ($\sim 6^\circ$) and is reflected from the substrate. The system has two optic compartments that contain a set of mirrors to direct the incident beam through the chamber in the desired geometry and to refocus the transmitted or reflected beam on the MCT detector. These compartments are separated from the ALD chamber by KBr windows and protecting gate valves that can be closed during the exposure of the ALD precursors to avoid coating of the windows. In this work, a reference spectrum of the MeCpPtMe₃ precursor is acquired in transmission mode, while the reflection geometry is employed for monitoring the surface chemistry of Pt ALD in the steady growth regime.

The MeCpPtMe₃ (99% Strem Chemicals) precursor is kept in a glass container and argon is used as a carrier gas during the exposures. The argon flow is adjusted by means of a needle valve so that the pressure in the chamber during a precursor pulse reaches 6×10^{-3} mbar. The container is heated to 40 °C and the temperature of the delivery line is set to 45 °C. Oxygen (99,9999%), introduced at a chamber pressure of 6×10^{-3} mbar, is used as reactant for both the thermal and the plasma-enhanced ALD processes. The plasma is generated in a remotely placed RF inductively coupled plasma source powered by a CESAR 136 RF power generator operating at 13.56 MHz. For all PE-ALD experiments a plasma power of 200 W is used. A 10 s exposure time is used for both the precursor and the reactant and each of these exposures is followed by a 30 s pumping step. FTIR measurements are carried out following each ALD half-cycle, after completion of the pumping step. The spectra are acquired with a resolution of 4 cm⁻¹ and are generated by averaging over 200 scans, which corresponds to an acquisition time of ~ 80 s. This implies that in an ALD process where FTIR is performed the effective evacuation time is 110 s.

This prolonged evacuation was verified to have no impact on the growth rate of the Pt ALD process.

3.1.2 Substrates

The depositions are performed on platinum seed layers grown by sputter deposition on Si substrates to eliminate nucleation problems during the ALD processes. A seed layer thickness of 80 nm was selected to prevent interaction between the IR beam and the Pt/Si interface. Prior to the in situ FTIR monitoring, the substrates are pretreated in order to ensure the same starting surface for all experiments. The substrates are first heated to 300 °C, after which they are exposed to O₂ gas during three pulses of 10 s, followed by 20 cycles of the thermal Pt ALD process. Next, when characterizing the Pt ALD processes below 300 °C, the sample is brought to the desired temperature without breaking the vacuum, this means that long cooling times are required (> 30 minutes). Surface oxygen on a platinum substrate is unstable when long pumping times are used, as is the case for this cooling procedure.^[13,14] Therefore, after stabilization of the sample at the required temperature, an additional 10 s O₂ pulse is included in the pretreatment procedure, leaving the platinum surface terminated with oxygen atoms.^[15] After this pretreatment, the experiment is immediately started.

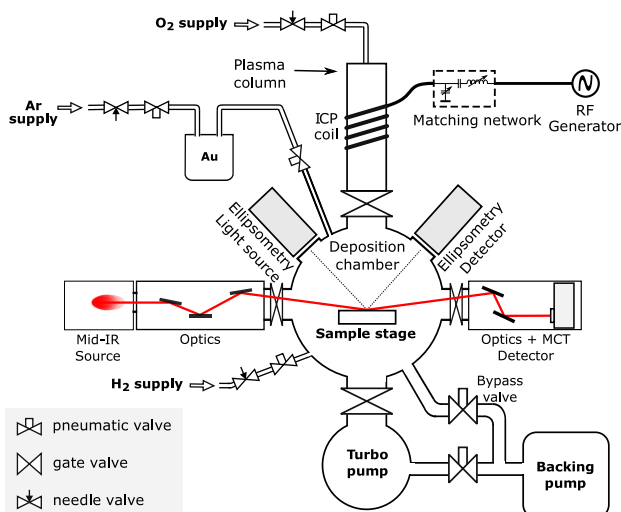


Figure 3.1: Schematic representation of the ALD chamber with FTIR system, showing the IR source and MCT detector.

3.1.3 *In situ FTIR characterization*

Following the pretreatment, ten cycles of the studied process (thermal or plasma-enhanced ALD) are performed without FTIR measurements to ensure that a steady growth regime is reached. During the following ten ALD cycles, FTIR measurements are performed after each precursor and reactant exposure. The spectra recorded after sequential exposures are subtracted from each other resulting in a difference spectrum for each exposure. Finally, the difference spectra obtained for the ten subsequent ALD half-cycles are averaged to improve the signal-to-noise ratio without resorting to very long measurement times and as a result long pump times. This can be done because the IR spectra are measured under steady growth conditions and as a result the obtained difference spectra vary little between ALD cycles. As such each experiment results in two difference spectra, one for the precursor pulse and one for the reactant pulse.

In addition, a reference spectrum of the MeCpPtMe_3 is measured with FTIR in transmission mode. To this end, the chamber is sealed off by closing the gate valve to the turbo pump, after which the precursor is pulsed into the chamber until a pressure of ~ 1 mbar is reached. The temperature of the chamber is set to 50°C to minimize reactions between the chamber walls and the precursor when it is inserted into the chamber.^[16] The reference spectrum is acquired by averaging over 200 scans, equivalent to a measurement time of ~ 80 s.

The same procedure is used for a series of FTIR measurements of the MeCpPtMe_3 molecule in reflection mode. This is performed on a substrate with an 80 nm thick Pt seed layer. The series of measurements are done at different substrate temperatures of 50, 100, 200, and 300°C , while the chamber walls are kept at 50°C .

3.2 RESULTS

3.2.1 *Temperature dependence of the growth per cycle*

First, the temperature dependence of the growth rate of the $\text{MeCpPtMe}_3 / \text{O}_2$ gas and $\text{MeCpPtMe}_3 / \text{O}_2$ plasma processes is evaluated in the ALD setup with *in situ* FTIR capability. To this end, 100 cycle depositions are performed on thin platinum seed layers. The growth per cycle (GPC) is then calculated from thickness measurements performed by X-ray reflectivity (XRR) before and after the deposition. At 300°C , a similar GPC of $0.50 \pm 0.05 \text{ \AA/cycle}$ is obtained for both the thermal and plasma-enhanced ALD process (Figure 3.2), which is close to the value of 0.45 \AA/cycle typi-

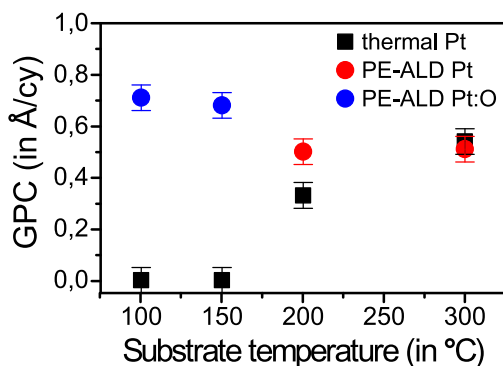


Figure 3.2: The growth per cycle as a function of the substrate temperature for the MeCpPtMe₃/O₂ gas process (thermal ALD) and the MeCpPtMe₃/O₂ plasma process (PE-ALD). At 100 °C and 150 °C, no growth is observed for the thermal process, while the PE-ALD process yields a Pt film with an oxide component (Pt:O). At 200 °C and 300 °C, both the thermal and PE-ALD process result in the deposition of pure Pt.

cally reported for these processes.^[11,17] For the thermal process, the GPC significantly decreases at 200 °C and no growth is found for temperatures below 150 °C, in agreement with earlier reports.^[16,17] For the plasma-enhanced ALD process, the growth rate at 200 °C remains at 0.50 ± 0.05 Å/cycle. At 100 °C and 150 °C, a layer with a PtO component is deposited instead of a pure Pt film, as revealed by density fitting results from the XRR analysis as well as compositional analysis via X-ray photoelectron spectroscopy (XPS, see Supporting Information). Considering the applied plasma conditions, the formation of a Pt film with an oxide component (Pt:O) at these temperatures is in line with earlier work by Erkens et al.^[18] A GPC of 0.72 ± 0.05 Å/cycle is obtained for the Pt:O depositions, which is slightly higher than the reported value of ca. 0.60 Å/cycle at 100 °C.^[17] Overall, the earlier reported trends concerning the temperature dependence of the GPC and the formation of Pt:O vs. Pt are successfully reproduced, allowing us to continue with a systematic study of the surface chemistry of these processes by means of in situ FTIR.

3.2.2 Reference spectrum of the MeCpPtMe₃ precursor

A reference infrared (IR) spectrum of the gas phase MeCpPtMe₃ molecule is shown in Figure 3.3. This spectrum is obtained in transmission mode, using a static precursor pulse at 1 mbar pressure. The IR spectrum of the

Observed wavenumber	Vibration mode
790 cm ⁻¹	CH deformation ^[19]
832 cm ⁻¹	CH bending ^[19,20]
859 cm ⁻¹	Ring distortion ^[19,20]
925 cm ⁻¹	CH bending ^[19,20]
1020 cm ⁻¹	Ring breathing ^[19]
1020 cm ⁻¹	CH bending ^[20]
1040 cm ⁻¹	CH ₃ wagging ^[19,20]
1222 cm ⁻¹	C-CH ₃ stretch ^[19,20]
1262 cm ⁻¹	CH ₃ deformation ^[21]
1375 cm ⁻¹	C=C stretch ^[19,20]
1375 cm ⁻¹	HCH deformation ^[19]
1435 cm ⁻¹	C=C stretch ^[19]
1459 cm ⁻¹	HCH bend ^[19,20]
1483 cm ⁻¹	HCH deformation ^[19]
1483 cm ⁻¹	C=C stretch ^[20]
1570 cm ⁻¹	C=C stretch ^[19]
1612 cm ⁻¹	C=C stretch ^[19]

Table 3.1: Peak assignment of the MeCpPtMe₃ absorption peaks, based on reported vibrations for dimethylferrocene^[19], tricarbonyl-methyl- π -cyclopentadienyl manganese^[20]

precursor molecule shows a clear signal of CH stretching modes, marked by the grey region on the left. These originate from the methyl groups attached to the Pt atom and to the aromatic ring. Furthermore, the CH groups present in the aromatic ring contribute to adsorption in this region. The grey region on the right contains vibrations from the Cp ring and from the methyl groups in the molecule. The C=C stretching vibrations and the ring distortion and breathing modes are indicated in Figure 3.3 and are assigned based on reported spectra of dimethylferrocene^[19] and tricarbonyl-methyl- π -cyclopentadienyl manganese^[20] (Table 3.1). The two strong peaks around 1250 cm⁻¹ can be attributed to the methyl-ring stretching vibration (the right peak at 1222 cm⁻¹)^[19,20] and to methyl deformations of the methyl groups attached to the platinum atom (the left peak at 1262 cm⁻¹).^[21]

In addition to measuring the transmission precursor spectrum another set of measurements was performed using the reflection geometry. For this a pulse of MeCpPtMe₃ gas, with the valve to the turbo pump closed, was used (1 mbar pressure) and a Pt seed layer served as the substrate.

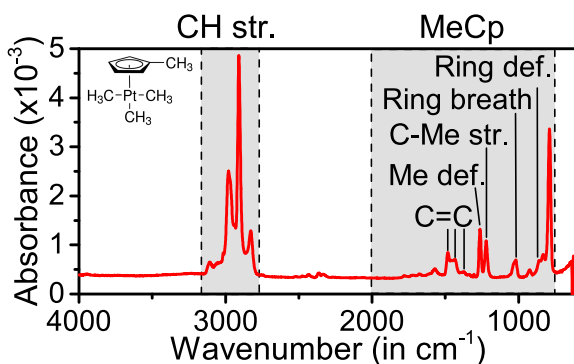


Figure 3.3: Transmission FTIR spectrum of the MeCpPtMe₃ molecule. The regions for the CH stretching modes and vibrations from the aromatic MeCp ring are marked by the left and right grey regions, respectively. The total pathlength of the IR beam through the ALD chamber is 45 cm.

The platinum seed layer was exposed to O₂ gas before exposing to the MeCpPtMe₃ precursor. Exposure at four different substrate temperatures was performed (50, 100, 200, and 300 °C). The obtained spectra can be seen in Figure 3.4. At 50 °C the spectrum in reflection resembles the spectrum in transmission, while at higher temperatures the spectrum changes. The clearest difference is in the CH-stretch region, marked by the grey region on the left side. The absorption in this region decreases with increasing substrate temperature. An explanation for this change is that the MeCpPtMe₃ molecules are able to collide and interact with the substrate and the substrate holder during the long measurement time. For a higher substrate temperature it is more likely that enough energy is transferred to the molecules to cause restructuring over time. The two spectra measured with a substrate temperature of 200 and 300 °C show a dip in their background between 1050 and 800 cm⁻¹, marked by the grey region on the right. This dip could be due to a change in the background and not a feature caused by the removal of functional groups on the surface.

3.2.3 *In situ* FTIR characterization

The thermal MeCpPtMe₃ / O₂ process and PE-ALD process using O₂ plasma are studied with *in situ* FTIR measurements in reflection geometry. The used substrates and pretreatments to achieve a well-defined starting surface for each experiment are described in the substrates section of the experimental section. This is done for substrate temperatures of 100,

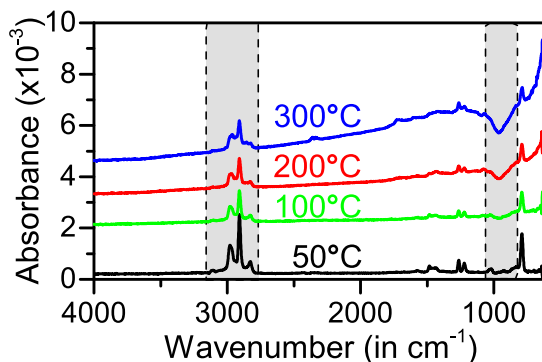


Figure 3.4: FTIR spectra taken in reflection geometry during a static precursor pulse (at 1 mbar pressure) for substrate temperatures of 50, 100, 200, and 300 °C on a Pt seed layer, pre-exposed to O₂ gas. A reference spectrum was taken before each introduction of the precursor into the chamber. The grey region on the left indicates the CH stretch region and the grey box on the right indicates a 'dip' in the spectrum at higher substrate temperatures. The spectra were given an offset for clarity.

200, and 300 °C to gain insight in the temperature dependence of the surface reaction chemistry. As explained in the experimental section, for each process, two difference spectra are acquired, one for the precursor exposure (or the first half-cycle) and one for the reactant exposure (or the second half-cycle). Negative features in these difference spectra are related to species that have been removed during the studied exposure, while positive features are related to species that have been added. As such, insights can be obtained in the functional groups that are being formed and removed during the precursor and reactant steps of the investigated ALD processes.

3.2.4 Thermal MeCpPtMe₃/O₂ process

The difference spectra for the thermal ALD process at 100, 200, and 300 °C are displayed in Figure 3.5a. From the temperature dependence of the growth rate (Figure 3.2) it is expected that no growth is possible for the thermal process below 150 °C. The difference spectra obtained for 100 °C are indeed flat, featureless lines, indicating that no reactions are taking place during either of the half-cycles. It needs to be noted that the displayed spectra are taken under the steady growth regime and due to this the initial adsorption of the MeCpPtMe₃ molecule cannot be seen in these

Observed wavenumber	Functional group	Temperature (in °C)
3740 cm ⁻¹	OH stretching ^[23]	300, 200
2333 cm ⁻¹	antisymmetric CO ₂ ^[24]	300, 200
2050 cm ⁻¹	Pt-CO (linear) ^[25]	300, 200
1850 cm ⁻¹	Pt-CO (bridged) ^[25]	300, 200
1430 cm ⁻¹	C=C ^[19]	300, 200
1430 cm ⁻¹	CH ₃ deformation ^[26]	300, 200

Table 3.2: List of the most important vibration modes that are observed in the difference spectra of the thermal processes at 200 and 300 °C

spectra. At 200 and 300 °C, the most pronounced spectral features are bands due to the Pt-OH stretching vibration, CO that is either linearly or bridge bonded to the Pt surface, and adsorbed CO₂ (see Table 3.2). One expects a bending mode for OH to be present near 1020 cm⁻¹,^[22] but this vibration is difficult to discern in the spectra.

At a substrate temperature of 200 and 300 °C the OH stretching band, which is not hydrogen bonded, is negative after the precursor pulse and positive after the reactant pulse, indicating that OH groups are removed during the precursor exposure and added during the reactant pulse. In contrast, linearly and bridge bonded CO is added during the precursor pulse and is removed upon exposure to the reactant. At 200 °C, an extra peak can be observed at a wavenumber that is lower than the singleton wavenumber of linearly bonded CO. Primet et al. and Barshad et al. have shown that electron donating species on the surface can lower the wavenumber of the CO absorption below the singleton value.^[27,28] The extra peak below the singleton wavenumber is an indication that electron donating species are present.

Figure 3.5b shows a zoom of the CH stretching region. No CH stretches are observed in the difference spectra during the thermal processes. This suggests that the detectable CH groups from the precursor molecule are not present on the surface after the precursor exposure or that the number of them remains below the detection limit.

Figure 3.5c displays a zoom of the lower wavenumber half of the spectrum where vibrations from the Cp-ring are expected. At 200 and 300 °C there is a band visible at 1430 cm⁻¹ which is positive after the precursor exposure and negative after the reactant exposure. This band can originate from two sources, either from C=C vibrations as assigned in Table 3.1 for the MeCpPtMe₃ precursor in gas phase or it can be due to a CH₃ deformation mode. The latter comes from surface science literature,

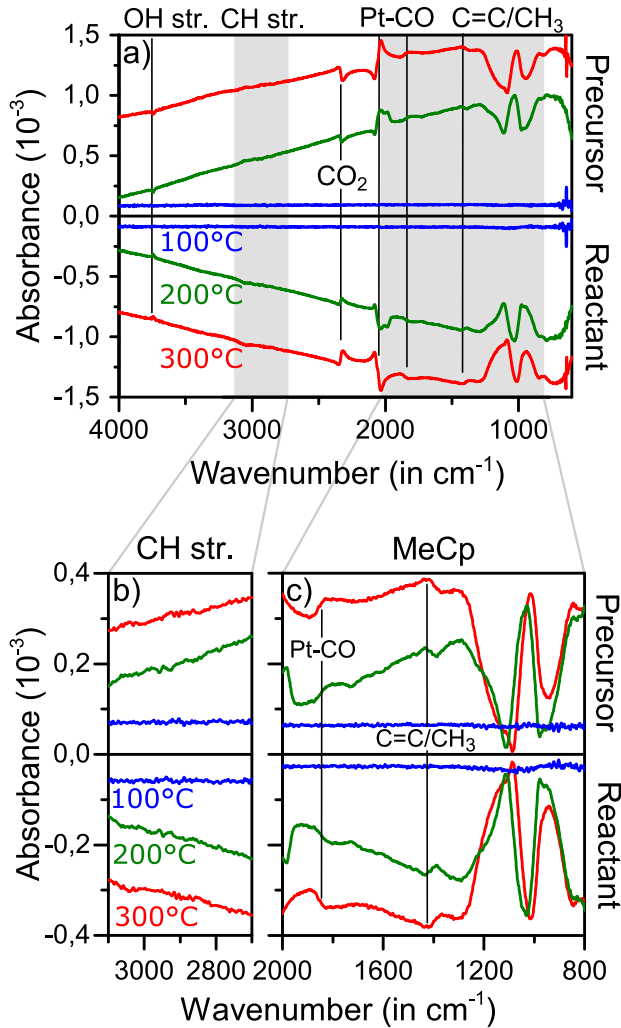


Figure 3.5: The FTIR difference spectra of the thermal process on a Pt seed layer, pre-exposed to O₂ gas followed by 10 ALD cycles to ensure steady growth conditions, deposited at 300 °C, 200 °C, and 100 °C. The displayed spectra are an average of 10 measurements and are given an offset for clarity. a) The full spectrum, b) zoom of the CH stretching region, c) zoom of the region where vibrations from the MeCp ligand are located.

in which they study the adsorption of ethylene on a Pt surface and its transformation to ethylidyne.^[26] As previously noted, there is no clear presence of CH stretching modes, which would be expected when CH₃ species are adsorbed on the surface. However, these modes probably fall in the noise level as they are expected to be about five times less intense than the CH₃ deformation mode, which is already quite small. Both peak assignments, either C=C vibrations or CH₃ deformation modes, are in agreement with recent findings by Vandalon et al. who detected both C=C and adsorbed species over a broad temperature range during the thermal ALD process by means of broadband sum-frequency generation studies.^[29] None of the other CH related features that are present in the MeCpPtMe₃ gas phase spectrum are present in the thermal ALD spectra. The lack of these features in combination with the lack of any clear CH stretching modes indicates that at least part of the hydrogen atoms are removed from the precursor ligands, resulting in unsaturated carbon fragments on the surface. The pronounced negative (positive) feature between 1050 and 800 cm⁻¹ in the precursor (reactant) difference spectrum may be attributed to a temperature induced dip (peak) in the spectral baseline, as mentioned before. The origin of the second broad pronounced feature between 1300 and 1050 cm⁻¹ remains unclear.

The background of the difference spectra has a(n) downward (upward) slope for the reactant (precursor) exposure when going to lower wavenumbers. This is due to changes in the free carrier absorption of the platinum layer.^[30,31] The O₂ gas exposure creates an oxidised platinum layer on the top which means that less free carriers are available resulting in the downward slope, while the opposite is the case for the MeCpPtMe₃ precursor exposure.

3.2.5 Plasma-enhanced MeCpPtMe₃/O₂ plasma process

Figure 3.6 shows the difference spectra obtained for the PE-ALD process at 100, 200, and 300 °C. At 300 °C, the spectra show similar features as observed earlier for the thermal process at 300 °C, originating from isolated OH groups, linearly and bridge bonded CO groups, and adsorbed CO₂ (see Table 3.3). There is an additional OH stretching band present between 3600 and 3400 cm⁻¹ for the process carried out at 200 °C. The additional band at lower wavelengths originates from OH groups that are hydrogen bonded,^[23,32] while the band at 3740 cm⁻¹ is due to stretching vibrations of non-hydrogen bonded OH groups.^[23] When the substrate temperature is further decreased to 100 °C, the isolated OH feature (at 3740 cm⁻¹) is no longer present and the vibrations due to hydrogen bonded OH groups

Observed Wavenumber	Functional group	Temperature (in °C)
3740 cm ⁻¹	OH stretch. ^[23]	300, 200
3600-3400 cm ⁻¹	OH (H bonded). ^[23,32]	200, 100
3100-2700 cm ⁻¹	CH stretches ^[33]	100
2333 cm ⁻¹	antisymmetric CO ₂ ^[24]	300, 200
2050 cm ⁻¹	Pt-CO _{Linear} ^[25]	300, 200, 100
1850 cm ⁻¹	Pt-CO _{Bridged} ^[25]	300, 200
1430 cm ⁻¹	C=C ^[19]	300, 200, 100
1430 cm ⁻¹	CH ₃ deformation ^[26]	300, 200, 100
1375 cm ⁻¹	C=C ^[19,20]	100
1375 cm ⁻¹	CH deform. ^[19]	100
1270 cm ⁻¹	CH ₃ deform. ^[21]	100
1230 cm ⁻¹	C-Me stretch ^[19]	100
1060 cm ⁻¹	Pt-OH bend. ^[22]	100

Table 3.3: List of the most important vibration modes that are observed for the PE-ALD process at 100, 200, and 300 °C. The vibration modes that are also present for the thermal process are indicated in grey.

become more pronounced. In addition an OH bending mode can be observed at $\sim 1060\text{ cm}^{-1}$.^[22] The OH features are positive after the reactant pulse and negative after the precursor pulse for all temperatures, as for the thermal process at 200 and 300 °C.

Bands due to vibrations of linearly and bridge bonded CO are present in the difference spectra measured at 200 and 300 °C. These features are more intense for a substrate temperature of 200 °C. At 100 °C, only the vibration associated with linearly bonded CO is present at 2080 cm^{-1} .^[25] It seems that the CO groups are attached to non-oxidised Pt atoms and are grouped in islands, because the peak position of CO attached to oxidised Pt is expected at 2120 cm^{-1} ,^[27] and CO groups that interact with each other cause a peak shift to higher wavenumbers away from the value for the isolated or singleton value of linearly bonded CO ($\sim 2060\text{ cm}^{-1}$).^[34] The CO groups are added during the precursor pulse and removed during the reactant pulse. This happens at all studied temperatures for the PE-ALD process. At 2333 cm^{-1} a vibration due to adsorbed CO₂ can be seen in the difference spectra obtained for a substrate temperature of 200 and 300 °C.^[24]

There are two pronounced bands present at lower wavenumbers in the difference spectra obtained for the process at 300 °C, which are very broad. One at 1210 cm^{-1} and the other at 1087 cm^{-1} , which appear as peaks af-

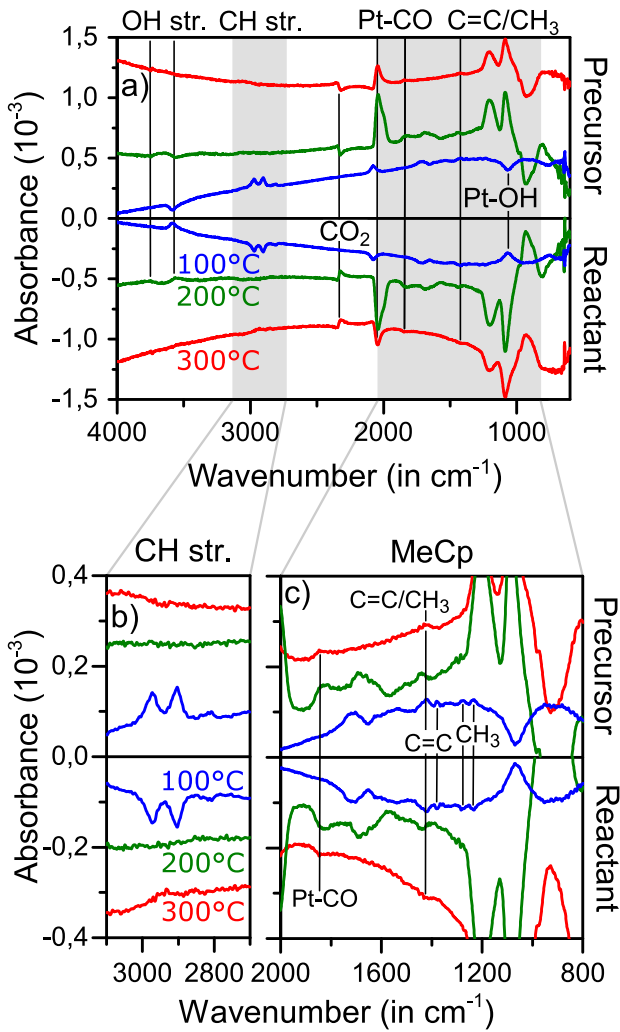


Figure 3.6: In situ FTIR difference spectra for the PE-ALD Pt process on a Pt seed layer, pre-exposed to O₂ gas followed by 10 ALD cycles, deposited at 300°C, 200°C, and 100°C. The displayed spectra are an average of ten measurements and are given an offset for clarity. a) The full spectrum, b) zoom of the CH stretching region, c) zoom of the region where vibrations from the MeCp ligand are located.

Wavenumber (in cm^{-1})	Vibration	Molecule type
1270-1230	C-O-C asymm.	aryl ethers
1310-1210	C-O-C asymm.	aryl alkyl ethers
1120-1020	C-O-C symm.	
1150-1060	C-O-C asymm.	saturated ethers
1225-1200	C-O-C asymm.	vinyl ethers

Table 3.4: Expected C-O vibration modes for several ether types^[21]

ter the precursor exposure and as valleys after the reactant exposure. At 200 °C, these two IR bands are shifted to 1220 and 1075 cm^{-1} , respectively. These two bands can be assigned to C-O vibrations, likely from ether type groups. In Table 3.4 the expected regions for the C-O vibration of several ether types are given. A first possible candidate is an aryl alkyl ether, as this would have two vibration modes close to the observed peaks at 300 °C and 200 °C. This would imply that a decent amount of Cp rings are still intact on the surface. However, there are no breathing or deformation modes present which would prove that there are Cp rings on the surface. Lacking clear evidence for their presence, it is less likely that the C-O-C vibrations are caused by ethers containing a Cp ring. Another possibility is that of vinyl ethers. These have a C=C bond present close to the C-O bond. The expected vibration, for a symmetric molecule, is between 1225-1200 cm^{-1} which can explain one peak that is observed. If the ether-type molecules do not have a C=C bond then the vibration would fall between 1150-1060 cm^{-1} ; depending on the interaction with the surface the peak position might shift close to the observed value of 1080 cm^{-1} . It is also possible that the carbon atoms linked to the O atom are bonded differently to other carbon atoms, this would result in two C-O vibrations and might also explain the presence of these two peaks.

Figure 3.6b shows a zoom of the CH stretching region. Clear stretching modes can only be observed in the difference spectra obtained at 100 °C. At this temperature CH groups are clearly present on the surface after the precursor exposure and are removed by the O₂ plasma. As for the thermal processes at 200 and 300 °C there are no CH stretching vibrations visible for the PE-ALD processes at these temperatures.

The zoom of the MeCp region in Figure 3.6c reveals that the C=C/CH₃ feature at 1430 cm^{-1} is present for all deposition temperatures and is positive after the precursor exposure and negative after the reactant pulse.^[19,26] This is the only IR band that can be assigned to the precursor ligands at 200 °C and 300 °C, while at 100 °C several additional vibrations are visible. These can be linked to the reference spectrum of the MeCpPtMe₃

precursor, as will be discussed in the next section. At 200 °C there is a new broad feature present at 1687 cm⁻¹ and at 100 °C this feature is shifted to 1715 cm⁻¹. This band falls in the region for the carbonyl group (C=O).^[21] Depending on its chemical surrounding and interaction with the surface, the C=O vibration can experience such a shift. From the work of Lavoie et al. it is known that when acetone gets adsorbed on a platinum surface the C=O vibration is observed at 1642 cm⁻¹.^[35] This C=O vibration is blueshifted to 1720 cm⁻¹ when acetone is co-adsorbed with benzene. As will be explained in the next section, our IR data at 100 °C indicates that the MeCp ligands are more intact, compared to higher temperatures. At 200 °C our data suggests that the MeCp ligand is more fragmented, which could be the reason for the smaller shift of the C=O peak. It is possible that unsaturated linear fragments also have an effect on the exact position of the C=O peak and that ring structures are not necessary. Note that our IR data does not contain a clear proof of the presence of Cp rings on the surface.

As noted before, the feature present between 1050 and 800 cm⁻¹ in the difference spectra obtained at 200 and 300 °C may be a temperature induced artefact of the spectrum's baseline. The slope of the background has the same origin as for the thermal process.

3.2.6 Comparison of the thermal and plasma-enhanced processes

In Figure 3.7 the lower wavenumber half of the precursor difference spectra is given for both the thermal and the PE-ALD process at 100 (c), 200 (b), and 300 °C (a). The reference spectrum of the MeCpPtMe₃ is reproduced in the top panel of the figure to serve as a comparison.

The difference spectra of both processes at 300 °C (Figure 3.7a) show only one peak that matches the reference spectrum, which is the peak at 1430 cm⁻¹. This peak corresponds to C=C stretching of the ligands or to a CH₃ deformation.^[19,26] No other peaks from the precursor can be assigned in these two spectra. The same conclusion can be made for the spectra of both processes obtained at 200 °C. In the difference spectrum for the PE-ALD process at 100 °C an extra C=C peak is present at 1375 cm⁻¹,^[19,20] as well as two peaks at 1230 and 1270 cm⁻¹, that are caused by C-CH₃ stretching^[19] and CH₃ deformations^[21] respectively. These extra peaks give an indication that the original MeCp ligands are more intact at lower temperatures. However, none of the spectra show deformation or breathing modes from the Cp-ring.

A large difference between the thermal and PE-ALD process is the presence of C-O-C (300 °C and 200 °C) and C=O vibrations (200 °C and 100 °C)

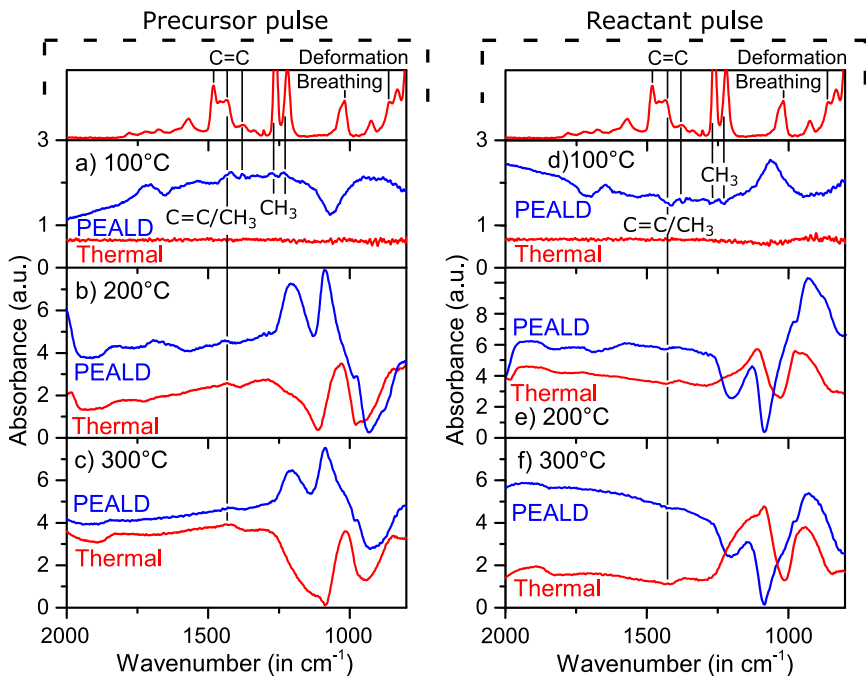


Figure 3.7: Zoom of the ‘aromatic’ and fingerprint region of the difference spectra after the precursor pulse obtained for the thermal and PE-ALD processes at 300 °C a), 200 °C b), and 100 °C c). The same zoom both for the difference spectra after the reactant pulse for the thermal and PE-ALD processes at 300 °C d), 200 °C e), and 100 °C f). The top panel shows the corresponding region of the precursor reference spectrum.

for the PE-ALD process. As discussed in the previous section, these possibly originate from a combination of vinyl ethers, having C=C bonds, and saturated ethers, without C=C bonds. It is remarkable that these are so prominent in the PE-ALD spectra but are totally lacking for the thermal process. A possible reason why there is such a big difference is that more oxygen is expected to be present on the surface when using an O₂ plasma as the reactant compared to O₂ gas. The coverage difference of surface oxygen can vary between 0.25 monolayers (ML) for O₂ gas and 2.9 ML when using atomic oxygen.^[36] Due to this it is possible that more combustion reactions occur in the PE-ALD process and lead to different combustion products that are left on the surface.

In the difference spectra of the thermal ALD process at 200 and 300 °C, there is a broad valley present in the region where the corresponding PE-

ALD process show C-O-C related IR bands, i.e. between 1250 and 800 cm^{-1} . The exact origin of this valley is not clear. When comparing the left slope of the valleys obtained for the thermal processes at 200 and $300\text{ }^{\circ}\text{C}$, a hidden positive feature at around 1200 cm^{-1} may be discerned in the spectrum at $200\text{ }^{\circ}\text{C}$. It is possible that this feature originates from C-O-C groups on the surface, though it goes without saying that this could as well be an over interpretation of the data.

3.2.7 *First exposures during thermal ALD at $100\text{ }^{\circ}\text{C}$*

In the previous sections all data represents the steady growth regime. In this regime no growth occurs for the thermal process at $100\text{ }^{\circ}\text{C}$, while in all other presented cases full growth inhibition does not occur, as shown in Figure 3.2. The surface reactions for the thermal process at $100\text{ }^{\circ}\text{C}$ are therefore limited to the first few cycles. In Figure 3.8, the infrared difference spectra are given for some of the first five ALD cycles during the thermal process at $100\text{ }^{\circ}\text{C}$. The first precursor exposure leads to vibration modes that can be linked to the MeCpPtMe_3 gas phase reference spectrum (Figure 3.3) and are assigned using Table 3.1. The added ligands during the precursor exposure are not removed by the following O_2 gas exposure, as evidenced by the lack of negative features in the difference spectrum. However, some Pt-CO groups are formed during the O_2 gas exposure. The only feature that changes after completion of the first ALD cycle is the Pt-CO peak: with each O_2 gas exposure a small, diminishing portion of CO species are added. After five cycles the addition of CO species stops and the difference spectra of the following exposures are flat lines, as shown in Figure 3.5 by the difference spectra for the steady growth conditions of the thermal process at $100\text{ }^{\circ}\text{C}$.

The poisoning ligands clearly do not undergo a lot of dehydrogenation reactions. This can be seen by the CH stretching modes that are present and that of CH and CH_3 deformation/bending modes. Several C=C groups are also present and a peak that can be assigned to C=O is also visible, as is the case for the PE-ALD process at $100\text{ }^{\circ}\text{C}$. The presence of a possible Cp ring breathing mode (1020 cm^{-1}) in combination with the high wavenumber position of the C=O peak (1720 cm^{-1}) indicates that intact Cp rings may be present on the surface at low temperatures. Though, care needs to be taken to readily assign the peak at 1020 cm^{-1} to a ring vibration mode as it overlaps with a CH bending mode and the expected ring deformation mode is not present. Nevertheless, this peak is not present for the steady PE-ALD growth at $100\text{ }^{\circ}\text{C}$, pointing to a clear difference between the initial precursor adsorption during thermal ALD

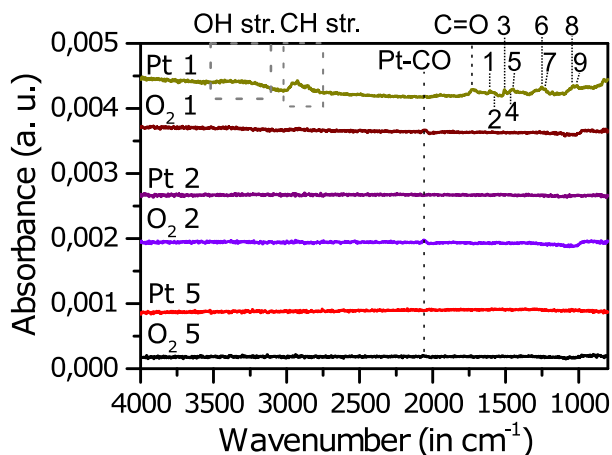


Figure 3.8: The first, second, and fifth ALD cycle of the thermal Pt process at 100 °C, deposited on a sputtered platinum seed layer pre-exposed to O₂ gas. During the first MeCpPtMe₃ precursor exposure several ligands are adsorbed on the surface. These ligands can be related to the MeCpPtMe₃ precursor gas phase reference spectrum and are assigned using Table 3.1. The following vibrations are observed: C=C stretch (1, 2, 3, 5); HCH deformation (3); HCH bending (4); CH₃ deformation (6); C-CH₃ stretch (7); CH₃ wagging (8); Ring breathing or CH bending (9). Other features that are visible are a broad OH stretching band, CH stretches from the ligands and combustion products in the form of C=O species around 1720 cm⁻¹. The first O₂ gas exposure results in the formation of some Pt-CO and does not remove any of the features added during the first precursor exposure. Following exposures lead to no significant changes on the surface.

and the steady precursor adsorption during PE-ALD. If the substrate temperature would be the only factor that plays a role this mode should also be present for the PE-ALD case. The most likely explanation is that by using an O₂ plasma a higher concentration of oxygen surface species is present, inducing more ring opening reactions.

3.3 DISCUSSION

The current understanding of the reaction mechanism of the Pt ALD process based on the MeCpPtMe₃ precursor and O₂ gas or plasma as reactant comprises two competing reactions during the precursor half-cycle. Firstly, the available surface oxygen is used to combust precursor ligands on the

surface and generate CO_2 ($\sim 3\%$ of carbon emission products during a full thermal Pt ALD cycle at 300°C) and H_2O .^[16,37] Secondly, dehydrogenation and hydrogenation reactions play an important role. The hydrocarbon ligands can donate hydrogen atoms to the surface. The released hydrogen atoms can subsequently hydrogenate CH_3 groups to form volatile CH_4 ($\sim 18\%$) reaction products.^[16,37-40] Saturation of the first half-cycle is then determined by the formation of a carbonaceous layer which prevents further ligand decomposition and precursor adsorption, because a single monolayer of carbon suffices to deactivate the decomposition of hydrocarbons on noble metals.^[41] Our experiments give insights in the type of carbonaceous species that are present at the end of the precursor reaction at various substrate temperatures. In line with the aforementioned mechanism, the presented IR data provide evidence for dehydrogenation reactions and reveal the presence of combustion reaction products remaining on the surface.

Table 3.5 lists the groups that are present on the surface after the precursor exposure during Pt ALD, as revealed by our in situ FTIR experiments. We distinguish ligand fragments and combustion reaction products. In addition, we define a low temperature region for temperatures below 150°C and a high temperature region above 150°C . The dividing line is put at 150°C because above this value both thermal and PE-ALD result in metallic Pt and the observed species are similar (apart from the carbonyl and C-O-C groups), while below 150°C , growth with the thermal ALD process is completely inhibited and PE-ALD results in the deposition of a Pt layer with an oxide component. These results enable us to refine the understanding of the reaction mechanism for Pt ALD. Above 150°C , the precursor exposure results in a surface covered with linearly and bridge bonded CO, CH_3 species for both processes and possibly atomic hydrogen from dehydrogenation reactions. Other C_xH_y groups than CH_3 might also be present but are below the FTIR detection limit. For the PE-ALD process ethers and carbonyl groups are also formed. During the reactant step, irrespective of the use of O_2 gas or plasma, the carbon groups are fully combusted and removed from the surface. The Pt surface is oxidised and hydroxyl groups are formed on the surface. Our results thus confirm that OH-groups, which are free and/or hydrogen bonded depending on the substrate temperature, can contribute to the formation of CH_4 as a gas phase reaction product during the precursor exposure, as was suggested before in literature.^[33,38]

In the low temperature region, dehydrogenation and fragmentation reactions are less efficient and a considerable amount of C_xH_y groups and CH_3 species remain on the surface after the precursor exposure. For the

PE-ALD process a higher concentration of surface oxygen species is expected to result in more reactions with the MeCp ligands and eventually ring-opening, while for the thermal process the relatively low concentration of surface oxygen is expected to induce less ring-opening reactions. From surface science literature it is clear that pre-adsorption of benzene on a Pt surface inhibits oxidation reactions from O₂ gas at a substrate temperature of 100 °C.^[42] This suggests that a covering layer of hydrocarbon groups prevents the adsorption of molecular O₂ on the Pt surface and its catalytic dissociation into atomic oxygen. Because molecular O₂ is not able to combust the poisoning hydrocarbons, the growth is prevented due to the presence of these poisoning ligand fragments. Growth is possible when using O₂ plasma or O₃, because reactive oxygen radicals are present which can directly participate in the combustion reactions without the need for dissociation on the surface. This leaves an oxidised platinum surface and hydrogen bonded hydroxyl groups on the surface, allowing the reaction to continue.

Precursor ligand dehydrogenation. As briefly mentioned before, the hydrogenation of methyl surface groups is possible through two reaction pathways. The first was proposed by Elliot, involving the formation of transient hydroxyl groups on the Pt surface by combustion reactions.^[38] Each combustion reaction of a hydrocarbon can yield one surface hydroxyl group and these hydroxyl groups can recombine with other hydroxyl groups to form water or hydrogenate a methyl ligand to form methane. The formed water during both the O₂ gas exposure and the MeCpPtMe₃ precursor exposure can readsorb and dissociate on the Pt surface. This results in extra hydroxyl groups that can hydrogenate methyl groups to methane. Mackus et al. proposed the second reaction pathway. This reaction requires surface hydrogen to hydrogenate methyl groups to form methane.^[39] This idea was based on surface science literature in which the Pt surface exposed to various hydrocarbons and oxidising conditions has been extensively studied. For example the Cp ligands are expected to be stable on a Pt surface up to 207 °C, above this temperature they start to dehydrogenate.^[43] As the thermal Pt ALD process is usually carried out between 250 and 300 °C, this indeed suggests the occurrence of dehydrogenation reactions and the presence of surface hydrogen during the MeCpPtMe₃ exposure.

The precursor IR spectrum has several characteristic absorption peaks due to CH stretching vibrations originating from the CH₃ groups in the ligands and the CH groups in the aromatic ring (Figure 3.3). However, the precursor difference spectra acquired during Pt ALD only show CH stretching modes for the PE-ALD process at 100 °C. For the thermal and

	Thermal	Plasma-enhanced
Low temperature region ($T < 150\text{ }^\circ\text{C}$)	Ligand fragments	C=C bonds C_xH_y possibly in the form of Cp CH_3 species
	Combustion reaction products	C=O species CO linearly bonded to Pt
	Ligand fragments	C=C bonds C_xH_y below detection limit CH_3 species Possibly atomic H
High temperature region ($T > 150\text{ }^\circ\text{C}$)	Combustion reaction products	CO linearly and bridge bonded to Pt Vinyli/saturated ethers C=O (for $200\text{ }^\circ\text{C}$)

Table 3.5: Surface groups present after the precursor exposure during ALD of Pt, these are removed after the reactant exposure. The groups that are observed for the thermal process in the low temperature region are only observed after the first precursor exposure. This does not reflect the steady growth conditions and are not removed or added under these growth conditions.

plasma-enhanced ALD processes at 200 and 300 °C there are no CH stretching vibrations present in the difference spectra. There is a small peak present that could be related to CH₃ deformation modes at all temperatures, which indicates that some CH₃ species possibly remain on the surface. Based on QMS studies it is known that 79% of the carbon from the precursor ligands remains on the surface after the precursor pulse at 300 °C (3% combusted to CO₂, 18% removed as CH₄).^[16,37] The absence of CH stretching or deformation modes, while a considerable amount of carbon is expected to be present on the surface, indicates that a decent amount of the hydrogen atoms are removed from the precursor Cp ligands when depositing at 200 °C and higher temperatures. This is consistent with dehydrogenation of hydrocarbon species on a Pt surface at elevated temperatures.^[40,43-45] The hydrogen atoms can hydrogenate available CH₃ groups, releasing CH₄, or can recombine on the surface and form H₂.^[46] It could be possible for atomic hydrogen to remain on the surface for a significant time period. The Pt-H stretching vibration is expected around 2090 cm⁻¹, but this vibration is not detected in any of the FTIR spectra during ALD.^[47] However, the presence of OH stretches on the Pt surface after the oxygen reactant pulse indicates that there is a source of hydrogen. To exclude that residual H₂O vapour in the ALD reactor contributes to the formation of these OH groups on the Pt surface, an extra experiment was conducted on an O₂ plasma treated platinum substrate. This surface was intentionally exposed to H₂O vapour at 6 × 10⁻³ mbar. The added isolated OH peak near 3740 cm⁻¹ after this exposure was negligible when compared to the peak formed during an ALD process. Therefore, it is concluded that the most likely sources of hydrogen are the remaining CH₃ species on the surface and atomic hydrogen present on the surface after precursor exposure. Finally, the presence of the CH stretching vibrations and additional two methyl related peaks in the precursor difference spectrum of the PE-ALD process at 100 °C shows that precursor ligand dehydrogenation reactions are less efficient at lower temperatures. This is also confirmed in the spectrum for the first precursor exposure in the thermal process at 100 °C.

Precursor ligand combustion. Combustion reactions of precursor ligands occur during the precursor exposure as long as there is available surface oxygen. Our data show that not all combustion products leave the surface as CO₂ and H₂O, but that part of the combustion products remain on the surface. A clear linearly bonded Pt-CO stretching mode is visible for all experiments, except at 100 °C for the thermal process. At 200 and 300 °C, a small broad peak related to bridged CO is present for both the thermal and plasma-enhanced ALD process. The highest surface density of

CO groups is found at 200 °C, as concluded from the high peak intensity for the PE-ALD case. In addition to CO species, the precursor difference spectra recorded for PE-ALD at 200 and 300 °C show strong peaks that are likely due to carbonyl groups and ethers. This is a clear indication that reaction products of the combustion reactions remain on the surface. As mentioned before, it is expected that the oxygen coverage after reactant exposure is a lot higher during the plasma enhanced process than for the thermal process. This can explain why carbonyl and ether like groups are present on the surface after precursor exposure during the plasma enhanced process, while this is not the case for the thermal process. Finally, the CO₂ feature which is present in all difference spectra recorded at 200 and 300 °C also marks the presence of CO₂ on the surface after the precursor exposure.

Cp ring reconstruction. Depending on the sample temperature the Cp ring of the precursor might undergo structural changes due to the catalytic nature of the Pt surface. The surface science study conducted by Avery shows that the Cp ring is stable up to 207 °C and above this temperature it can undergo fragmentation into CH and C₂H₂ species on the surface.^[43] Between 277-477 °C these species can undergo extra dehydrogenation steps, until full dehydrogenation occurs above 477 °C. From this it is expected that the remaining species on the surface after the precursor half-cycle range from a carbon ring to a carbon chain of varying length. The presented IR data provide proof that C=C species are present on the surface, at all temperatures, after exposure to the precursor. In case of intact Cp rings present on the surface, ring deformation and ring breathing vibrations are expected in the difference spectra. The only suggestion that a ring breathing mode is present is after the first precursor exposure for the thermal process at 100 °C, in none of the other spectra is there any presence of this peak. This could mean that the ring is not intact and that these absorption modes are not active. Another possibility is that these absorption peaks are very weak and therefore masked by other features in the spectra (the peaks related to ethers, the Pt-OH bending mode, and the spectral baseline artefact all fall in the same wavelength range as these ring absorption peaks). Only one C=C stretching mode is present in the difference spectra recorded at 200 and 300 °C. However, for the PE-ALD spectrum at 100 °C there is an extra C=C stretching mode that matches the precursor reference spectrum and after the first precursor exposure during the thermal process four of the five C=C stretching modes are present. This shows that the Cp ring is less fragmented at 100 °C than at higher temperatures. While the Cp ring is expected to be stable on a platinum surface at this temperature there is no confirmation that it is

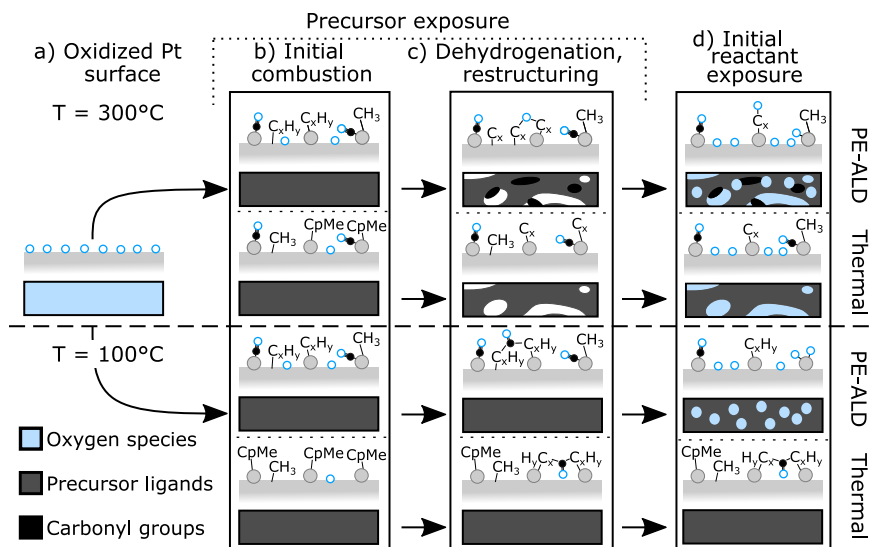


Figure 3.9: Schematic representation of a Pt ALD cycle using MeCpPtMe₃ as precursor and O₂ gas or O₂ plasma as reactant at 300 and 100 °C. a) The surface after exposure to the reactant, b) the surface upon initial adsorption of the precursor molecules, c) the surface after dehydrogenation and restructuring reactions, and d) exposure to the reactant. For each case, a cross-section view is given with representative surface groups, together with a top view that is colored according to the expected presence of oxygen species (blue), precursor ligands (gray) and carbonyl groups (black).

completely intact because the observed breathing mode can be assigned to a CH bending mode and no ring deformation mode is present. Nonetheless, the presence of the additional peaks for the first precursor exposure for the thermal process indicate that the Pt surface does not induce large structural changes to the precursor ligands at 100 °C and for a low surface oxygen concentration. These more intact ligands will block the surface more efficiently for the dissociative adsorption of oxygen on the Pt surface. And this causes the inhibited growth for the thermal ALD process at 100 °C.

Surface poisoning. From QMS data it is clear that a lot of carbon is present on the surface after the precursor exposure.^[16,37,48] These carbon groups form a carbonaceous layer causing deactivation of the surface and saturation of the MeCpPtMe₃ adsorption. The reason is that a single monolayer of carbon suffices to deactivate the decomposition of hydrocarbons

on noble metals.^[41] Surface science studies furthermore showed that pre-adsorbed benzene on a Pt surface inhibits oxidation reactions during exposure to O₂ gas at 100 °C.^[39,42] Only for temperatures above 180 °C it is possible to fully combust the surface carbon. Therefore, surface poisoning by a carbonaceous layer during the precursor step, causing inhibition of combustion reactions during the reactant step, was postulated to be responsible for the significant decrease in growth rate of the MeCpPtMe₃/O₂ gas process at temperatures below 200 °C.

In Figure 3.9 a representation of the Pt surface during an ALD cycle is shown for the thermal and PE-ALD process at a high and a low substrate temperature.

Figure 3.9a If the starting surface is a clean Pt surface exposed to O₂ gas or O₂ plasma it will be oxidised. The density of surface oxygen is expected to be higher when the surface is exposed to the more aggressive O₂ plasma, compared to O₂ gas.^[36,49]

Figure 3.9b The following step in the process is to expose the oxidized Pt surface to the MeCpPtMe₃ precursor. There will be an initial combustion reaction that chemically binds the MeCpPtMe₃ molecules to the surface upon adsorption. Surface oxygen and hydroxyl groups will be consumed during the initial combustion reactions to form CO₂ and H₂O, leaving a surface covered with partially combusted precursor ligands that play a role in the next step. The result of these initial reactions is a poisoning 'ligand layer' that consists of hydrocarbons for both the thermal and the PE-ALD process. This initial stage is expected to look different depending on the process, due to the difference in the concentration of surface oxygen species between both processes. For a high concentration of surface oxygen a lot of combustion reactions are able to occur and open the Cp rings that adsorb on the surface, while for a low concentration less of these reactions occur and the adsorbed Cp rings are expected to remain more intact.

Figure 3.9c After the initial combustion, all reaction sites are taken up by precursor ligands and temperature dependent dehydrogenation and restructuring reactions of the ligands are occurring for both processes. For low substrate temperatures these reactions are less likely to occur and therefore the ligands are expected to retain their original form. When the substrate temperature is high enough, the dehydrogenation reactions result in the conversion of the hydrocarbon ligands to a partially dehydrogenated carbonaceous layer (full dehydrogenation >477 °C), producing CH₄.^[16] A decent fraction of CH₃ groups will still be present and broken up Cp fragments are likely to be transformed into ethylidyne or methylidyne.^[43] The effect of this is that a significant amount of the lig-

and layer gets removed (18% of the carbon atoms). If before the ligand layer can be thought of as completely covering the surface, it is likely that it now has become thinner and exposes parts of the underlying Pt surface. Regions that are large enough for a MeCpPtMe₃ molecule to adsorb onto will probably get filled by fresh precursor molecules, increasing the amount of Pt atoms that can be deposited per ALD cycle. It can be expected that the area that can be exposed to new precursor molecules is proportional to the amount of CH₄ formed. The FTIR data suggests that the composition of the remaining ligand layer differs for both processes. The ligand layer of the thermal process now consists of partially dehydrogenated carbon groups and CH₃ groups, while the ligand layer of the PE-ALD process also has carbonyl/ether groups. The origin of these extra groups in the PE-ALD process likely originate from reactions with remaining surface oxygen that do not result in the formation of CO₂.

Figure 3.9d The final step to complete the ALD cycle is to expose the surface to the reactant, O₂ gas or O₂ plasma. O₂ gas needs a site on the Pt surface where it can adsorb and dissociate into molecular oxygen and then combust the ligand layer, as is the case for high substrate temperatures. For low substrate temperatures the ligand layer fully covers the surface and these sites are not available, poisoning the surface. The O₂ plasma has no need of these adsorption sites because the oxygen species created by the plasma are reactive enough. Hydroxyl groups are formed during this step when the O₂ can combust the ligand layer.

3.4 CONCLUSION

Using in situ reflection FTIR measurements, this work aimed at revealing the surface species during thermal and PE-ALD of Pt at different substrate temperatures. Our data provide experimental evidence for the occurrence of temperature dependent dehydrogenation reactions during the precursor exposure step. Detailed comparison of the MeCpPtMe₃ precursor FTIR spectra with difference spectra acquired for the first half-cycle during thermal and PE-ALD revealed that the precursor ligands undergo less restructuring and dehydrogenation for temperatures below 150 °C than above this temperature. The presence/absence of intact Cp rings in the low temperature region could, however, not be conclusively confirmed from the FTIR difference spectra. Ring breathing and deformation modes from the Cp ring were not detected at high temperatures, but the expected peaks may also be masked by other features. Overall, it can be concluded that in the high temperature region ($T > 150$ °C) the ligands undergo dehydrogenation during the precursor half-cycle and a carbonaceous layer remains

on the surface, while for the low temperature region ($T < 150\text{ }^{\circ}\text{C}$) the ligands are not dehydrogenated and a hydrocarbon layer remains. For the thermal process this hydrocarbon layer prevents the absorption and dissociation of molecular oxygen, meaning that the combustion reaction cannot occur during the O_2 gas exposure. However, the radicals in the O_2 plasma during PE-ALD can directly combust the hydrocarbon layer on the surface. Therefore, this work provides evidence that poisoning of the Pt surface by a hydrocarbon layer is the cause for growth inhibition during thermal ALD below $150\text{ }^{\circ}\text{C}$.

In addition, our in situ data revealed that products from combustion reactions remain on the surface following the precursor exposure. CO groups are detected for both thermal and PE-ALD, which are removed during the reactant exposure. The spectra for the PEALD process show additional carbonyl groups at $100\text{ }^{\circ}\text{C}$ and $200\text{ }^{\circ}\text{C}$ and an indication that ethers are present for temperatures above $150\text{ }^{\circ}\text{C}$. These groups are not present for the thermal ALD case, possibly related to a lower density of oxygen atoms left on the surface following the reactant step.

Finally, the in situ FTIR spectra reveal the formation of hydroxyl groups on the surface during the reactant exposure and consumption of these groups during the precursor exposure at all deposition temperatures. This confirms that OH-groups can be involved in the hydrogenation of CH_3 groups present in the precursor ligands yielding CH_4 as a gas phase reaction product. As such, our in situ FTIR study suggests that both proposed reaction pathways for the formation of CH_4 during the precursor step, i.e. via OH-groups and via atomic hydrogen released through dehydrogenation of the ligands, are occurring during Pt ALD.

3.5 SUPPORTING INFORMATION

XRR MEASUREMENTS of films grown by a Pt PE-ALD process, using MeCpPtMe_3 as precursor and O_2 plasma as the reactant, for a substrate temperature of 100 and 200 °C are shown in Fig.3.10. To obtain these samples a Pt seed layer of 6.9 nm was sputtered on a silicon substrate. The substrate was pretreated inside the ALD chamber before deposition using an O_2 plasma to remove contaminants from the surface. An ALD process of 50 Pt PE-ALD cycles was performed on a plasma pretreated sample for a substrate temperature of 100 °C or 200 °C.

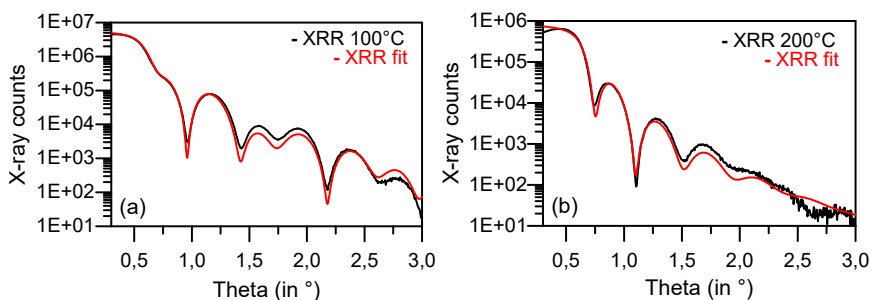


Figure 3.10: XRR measurements of the Pt layers after 50 cycles of the Pt PE-ALD process for a substrate temperature of 100 and 200 °C. The thickness of the Pt seed layer before deposition was 6.9 nm for both samples. (a) Data and fit for a substrate temperature of 100 °C, from the fit after deposition a Pt thickness of 6.3 nm and a Pt:O thickness of 4.2 nm is obtained. (b) Data and fit for a substrate temperature of 200 °C, the fit after deposition gives a platinum thickness of 9.4 nm.

The XRR fit for the deposition performed at 200 °C gives a Pt thickness of 9.4 nm after deposition (Fig. 3.10b), resulting in a growth of 0.05 nm per cycle. For a substrate temperature of 100 °C, the fit for the XRR data gives a platinum thickness of 6.3 nm and an extra Pt:O layer of 4.2 nm (Fig. 3.10a). This extra Pt:O layer is necessary to get a decent fit of the data. The decrease in thickness of the seed layer, by 0.6 nm, might be due to oxidation of the platinum top layer by the plasma pretreatment. This yields a Pt:O growth of 0.72 nm/cycle for a substrate temperature of 100 °C, when correcting for the oxidation of 0.6 nm.

XPS MEASUREMENTS: At low substrate temperatures (< 150 °C) the use of O_2 plasma as the reactant in the Pt PE-ALD process results in the growth of Pt:O instead of pure Pt. To confirm this, an XPS depth profile was taken

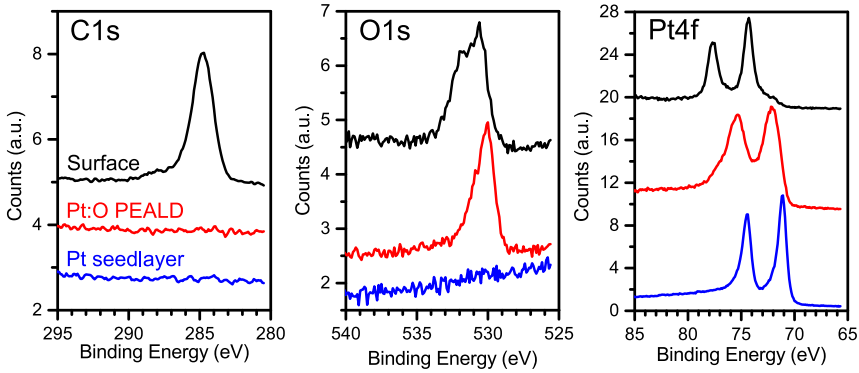


Figure 3.11: C1s, O1s, and Pt4f regions for a PE-ALD grown Pt film at 100 °C on a Pt seed layer.

	C (at. %)	O (at. %)	Pt (at. %)
Surface	15.76	20.15	64.09
Bulk	0	10.4	89.6
Seed	0	0	100

Table 3.6: Atomic percentage of C, O and Pt in PE-ALD grown Pt films at 100 °C. Oxygen is present in the bulk of the grown film and not only on the surface.

of a Pt PE-ALD film grown at 100 °C on a Pt seed layer to determine if oxygen was present in the deposited film. A ThermoScientific XPS was used equipped with a thetaprobe and an aluminium anode. The XPS measurements were performed with a pass energy of 20 eV, the achieved FWHM of the instrument is 0.63 eV. In Figure 3.11 the XPS regions for the C1s, O1s, and Pt4f peaks are shown for three levels of the depth profile of the sample: the surface, the Pt:O layer, and the Pt seed layer. Carbon is only present on the surface and can be sputtered away. Oxygen is present on the surface and throughout the deposited film, the sputtered Pt seed layer has no oxygen and the binding energy of the Pt 4f peaks match to metallic Pt. The surface of the Pt film is in an oxidised state. The deposited film itself has an oxidised component and a metallic component for the Pt 4f peaks. The atomic concentrations can be found in Table 3.6.

REFERENCES

- [1] Yu-Hung Lin, Yang-Chih Hsueh, Po-Sheng Lee, Chih-Chieh Wang, Jyh Ming Wu, Tsong-Pyng Perng, and Han C. Shih. "Fabrication of tin dioxide nanowires with ultrahigh gas sensitivity by atomic layer deposition of platinum". en. In: *Journal of Materials Chemistry* 21.28 (2011), p. 10552. DOI: 10.1039/c1jm10785b.
- [2] A. J. M. Mackus, J. J. L. Mulders, M. C. M. van de Sanden, and W. M. M. Kessels. "Local deposition of high-purity Pt nanostructures by combining electron beam induced deposition and atomic layer deposition". en. In: *Journal of Applied Physics* 107.11 (June 2010), p. 116102. DOI: 10.1063/1.3431351.
- [3] James A. Enterkin, Worajit Setthapun, Jeffrey W. Elam, Steven T. Christensen, Federico A. Rabuffetti, Laurence D. Marks, Peter C. Stair, Kenneth R. Poeppelmeier, and Christopher L. Marshall. "Propane Oxidation over Pt/SrTiO₃ Nanocuboids". en. In: *ACS Catalysis* 1.6 (June 2011), pp. 629–635. DOI: 10.1021/cs200092c.
- [4] Chueh Liu, Chih-Chieh Wang, Chi-Chung Kei, Yang-Chih Hsueh, and Tsong-Pyng Perng. "Atomic Layer Deposition of Platinum Nanoparticles on Carbon Nanotubes for Application in Proton-Exchange Membrane Fuel Cells". In: *Small* 5.13 (2009), pp. 1535–1538. DOI: 10.1002/sml.200900278.
- [5] Steven Novak, Bongmook Lee, Xiangyu Yang, and Veena Misra. "Platinum Nanoparticles Grown by Atomic Layer Deposition for Charge Storage Memory Applications". en. In: *Journal of The Electrochemical Society* 157.6 (2010), H589. DOI: 10.1149/1.3365031.
- [6] Anca Faur Ghenciu. "Review of fuel processing catalysts for hydrogen production in PEM fuel cell systems". In: *Current Opinion in Solid State and Materials Science* 6.5 (2002), pp. 389–399. DOI: 10.1016/S1359-0286(02)00108-0.
- [7] Hans-Ulrich Blaser, Hans-Peter Jalett, Manfred Müller, and Martin Studer. "Enantioselective hydrogenation of α -ketoesters using cinchona modified platinum catalysts and related systems: A review". In: *Catalysis Today* 37.4 (1997). Heterogenous Catalysis in Organic Reactions, pp. 441–463. DOI: 10.1016/S0920-5861(97)00026-6.
- [8] R. Burch, J.P. Breen, and F.C. Meunier. "A review of the selective reduction of NOx with hydrocarbons under lean-burn conditions with non-zeolitic oxide and platinum group metal catalysts". In: *Applied Catalysis B: Environmental* 39.4 (2002), pp. 283–303. DOI: 10.1016/S0926-3373(02)00118-2.
- [9] Shengsheng Zhang, Xiao-Zi Yuan, Jason Ng Cheng Hin, Haijiang Wang, K. Andreas Friedrich, and Mathias Schulze. "A review of platinum-based catalyst layer degradation in proton exchange membrane fuel cells". In: *Journal of Power Sources* 194.2 (2009), pp. 588–600. DOI: 10.1016/j.jpowsour.2009.06.073.
- [10] Jolien Dendooven et al. "Independent tuning of size and coverage of supported Pt nanoparticles using atomic layer deposition". In: *Nature Communications* 8.1 (2017), p. 1074. DOI: 10.1038/s41467-017-01140-z.
- [11] Titta Aaltonen, Mikko Ritala, Timo Sajavaara, Juhani Keinonen, and Markku Leskelä. "Atomic Layer Deposition of Platinum Thin Films". en. In: *Chemistry of Materials* 15.9 (May 2003), pp. 1924–1928. DOI: 10.1021/cm021333t.
- [12] E. Levrau, K. Van de Kerckhove, K. Devloo-Casier, S. P. Sree, J. A. Martens, C. Detavernier, and J. Dendooven. "In Situ IR Spectroscopic Investigation of Alumina ALD on Porous Silica Films: Thermal versus Plasma-Enhanced ALD". en. In: *The Journal of Physical Chemistry C* 118.51 (Dec. 2014), pp. 29854–29859. DOI: 10.1021/jp5088288.

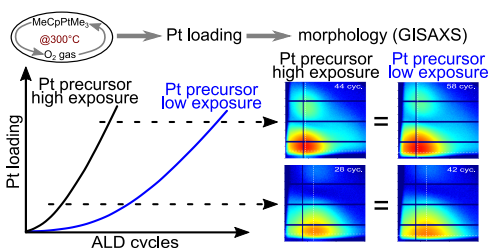
- [13] Jolien Dendooven, Ranjith K. Ramachandran, Kilian Devloo-Casier, Geert Rampelberg, Matthias Filez, Hilde Poelman, Guy B. Marin, Emiliano Fonda, and Christophe Detavernier. "Low-Temperature Atomic Layer Deposition of Platinum Using (Methylcyclopentadienyl)trimethylplatinum and Ozone". In: *The Journal of Physical Chemistry C* 117.40 (2013), pp. 20557–20561. DOI: 10.1021/jp403455a.
- [14] Matthias Filez, Hilde Poelman, Ranjith K. Ramachandran, Jolien Dendooven, Kilian Devloo-Casier, Emiliano Fonda, Christophe Detavernier, and Guy B. Marin. "In situ XAS and XRF study of nanoparticle nucleation during O₃-based Pt deposition". en. In: *Catalysis Today* 229 (June 2014), pp. 2–13. DOI: 10.1016/j.cattod.2014.01.011.
- [15] C.T. Campbell, G. Ertl, H. Kuipers, and J. Segner. "A molecular beam study of the adsorption and desorption of oxygen from a Pt(111) surface". In: *Surface Science* 107.1 (1981), pp. 220–236. DOI: 10.1016/0039-6028(81)90622-1.
- [16] I. J. M. Erkens, A. J. M. Mackus, H. C. M. Knoops, P. Smits, T. H. M. van de Ven, F. Roozeboom, and W. M. M. Kessels. "Mass Spectrometry Study of the Temperature Dependence of Pt Film Growth by Atomic Layer Deposition". en. In: *ECS Journal of Solid State Science and Technology* 1.6 (Sept. 2012), P255–P262. DOI: 10.1149/2.006206jss.
- [17] H. C. M. Knoops, A. J. M. Mackus, M. E. Donders, M. C. M. van de Sanden, P. H. L. Notten, and W. M. M. Kessels. "Remote Plasma ALD of Platinum and Platinum Oxide Films". In: *Electrochemical and Solid-State Letters* 12.7 (2009), G34. DOI: 10.1149/1.3125876.
- [18] Ivo J. M. Erkens, Marcel A. Verheijen, Harm C. M. Knoops, Tatiana F. Landaluce, Fred Roozeboom, and Wilhelmus M. M. Kessels. "Plasma-Assisted Atomic Layer Deposition of PtOx from (MeCp)PtMe₃ and O₂ Plasma". en. In: *Chem. Vap. Deposition* 20.7-8-9 (Sept. 2014), pp. 258–268. DOI: 10.1002/cvde.201407109.
- [19] Raymond T. Bailey and Ellis R. Lippincott. "The vibrational spectrum of dimethylferrocene". In: *Spectrochimica Acta* 21.3 (1965), pp. 389–398. DOI: 10.1016/0371-1951(65)80130-8.
- [20] David J. Parker. "Vibrational spectra of tricarbonyl-methyl- π -cyclopentadienyl manganese and bis (tricarbonyl-methyl- π -cyclopentadienyl) dimolybdenum". In: *Spectrochimica Acta Part A: Molecular Spectroscopy* 31.12 (1975), pp. 1789–1798. DOI: 10.1016/0584-8539(75)80234-0.
- [21] G. Socrates. *Infrared and Raman characteristic group frequencies: tables and charts*. 3rd ed. Chichester ; New York: Wiley, 2001. ISBN: 978-0-471-85298-8.
- [22] G. Gilarowski, W. Erley, and H. Ibach. "Photochemical reactions of water adsorbed on Pt(111)". In: *Surface Science* 351.1 (1996), pp. 156–164. DOI: 10.1016/0039-6028(95)01360-1.
- [23] F.T. Wagner and T.E. Moylan. "A comparison between water adsorbed on Rh(111) and Pt(111), with and without predosed oxygen". In: *Surface Science* 191.1 (1987), pp. 121–146. DOI: 10.1016/S0039-6028(87)81052-X.
- [24] R. C. Hanson and L. H. Jones. "Infrared and Raman studies of pressure effects on the vibrational modes of solid CO₂". In: *The Journal of Chemical Physics* 75.3 (1981), pp. 1102–1112. DOI: 10.1063/1.442183.
- [25] D. W. Daniel. "Infrared studies of carbon monoxide and carbon dioxide adsorption on platinum/ceria: the characterization of active sites". In: *The Journal of Physical Chemistry* 92.13 (1988), pp. 3891–3899. DOI: 10.1021/j100324a042.

- [26] H. Hoffmann, P.R. Griffiths, and F. Zaera. "A RAIRS study on the surface chemistry of ethyl iodide on Pt(111)". In: *Surface Science* 262.1-2 (1992), pp. 141–150. DOI: 10.1016/0039-6028(92)90466-J.
- [27] M. Primet, J.M. Basset, M.V. Mathieu, and M. Prettre. "Infrared study of CO adsorbed on PtAl₂O₃. A method for determining metal-adsorbate interactions". In: *Journal of Catalysis* 29.2 (1973), pp. 213–223. DOI: 10.1016/0021-9517(73)90225-X.
- [28] Yoav Barshad, Xiaochuan Zhou, and Erdogan Gulari. "Carbon monoxide oxidation under transient conditions: A fourier-transform infrared transmission spectroscopy study". In: *Journal of Catalysis* 94.1 (1985), pp. 128–141. DOI: 10.1016/0021-9517(85)90088-0.
- [29] Vincent Vandalon, Adrie Mackus, and W. M.M Kessels. In: *Presented at the AVS Topical Conference on ALD* (Denver, United States of America, July 16-18, 2017), Surface Chemistry during Atomic Layer Deposition of Pt Studied with Vibrational Sum-frequency Generation.
- [30] J. H. Weaver. "Optical properties of Rh, Pd, Ir, and Pt". In: *Phys. Rev. B* 11 (4 Feb. 1975), pp. 1416–1425. DOI: 10.1103/PhysRevB.11.1416.
- [31] W. S. Choi, S. S. A. Seo, K. W. Kim, T. W. Noh, M. Y. Kim, and S. Shin. "Dielectric constants of Ir, Ru, Pt, and IrO₂: Contributions from bound charges". In: *Phys. Rev. B* 74 (20 Nov. 2006), p. 205117. DOI: 10.1103/PhysRevB.74.205117.
- [32] Galen B. Fisher and Brett A. Sexton. "Identification of an Adsorbed Hydroxyl Species on the Pt(111) Surface". In: *Phys. Rev. Lett.* 44 (10 Mar. 1980), pp. 683–686. DOI: 10.1103/PhysRevLett.44.683.
- [33] W. M. M. Kessels, H. C. M. Knoop, S. A. F. Dielissen, A. J. M. Mackus, and M. C. M. van de Sanden. "Surface reactions during atomic layer deposition of Pt derived from gas phase infrared spectroscopy". en. In: *Applied Physics Letters* 95.1 (July 2009), p. 013114. DOI: 10.1063/1.3176946.
- [34] Alison Crossley and David A. King. "Adsorbate island dimensions and interaction energies from vibrational spectra: Co on Pt 001 and Pt 111". In: *Surface Science* 95.1 (1980), pp. 131–155. DOI: 10.1016/0039-6028(80)90132-6.
- [35] Stéphane Lavoie and Peter H. McBreen. "Evidence for C–H···OC Bonding in Coadsorbed Aromatic–Carbonyl Systems on Pt(111)". In: *The Journal of Physical Chemistry B* 109.24 (2005), pp. 11986–11990. DOI: 10.1021/jp051216w.
- [36] G.N. Derry and P.N. Ross. "High coverage states of oxygen adsorbed on Pt(100) and Pt(111) surfaces". In: *Surface Science* 140.1 (1984), pp. 165–180. DOI: 10.1016/0039-6028(84)90389-3.
- [37] Steven T. Christensen and Jeffrey W. Elam. "Atomic Layer Deposition of Ir–Pt Alloy Films". In: *Chemistry of Materials* 22.8 (2010), pp. 2517–2525. DOI: 10.1021/cm9031978.
- [38] Simon D. Elliott. "Mechanism, Products, and Growth Rate of Atomic Layer Deposition of Noble Metals". en. In: *Langmuir* 26.12 (June 2010), pp. 9179–9182. DOI: 10.1021/la101207y.
- [39] Adriaan J. M. Mackus, Noémi Leick, Layton Baker, and Wilhelmus M. M. Kessels. "Catalytic Combustion and Dehydrogenation Reactions during Atomic Layer Deposition of Platinum". en. In: *Chemistry of Materials* 24.10 (May 2012), pp. 1752–1761. DOI: 10.1021/cm203812v.
- [40] Francisco Zaera. "Study of the surface chemistry of methyl iodide coadsorbed with hydrogen on Pt(111)". In: *Surface Science* 262.3 (1992), pp. 335–350. DOI: 10.1016/0039-6028(92)90130-X.

- [41] E Loginova, N C Bartelt, P J Feibelman, and K F McCarty. "Factors influencing graphene growth on metal surfaces". In: *New Journal of Physics* 11.6 (June 2009), p. 063046. DOI: 10.1088/1367-2630/11/6/063046.
- [42] Anderson L. Marsh, Daniel J. Burnett, Daniel A. Fischer, and John L. Gland. "Benzene Intermediates and Mechanisms during Catalytic Oxidation on the Pt(111) Surface Using In-Situ Soft X-ray Methods". In: *The Journal of Physical Chemistry B* 107.45 (2003), pp. 12472–12479. DOI: 10.1021/jp0344038.
- [43] Neu R. Avery. "Bonding and reactivity of cyclopentene on Pt(111)". In: *Surface Science* 146.2 (1984), pp. 363–381. DOI: 10.1016/0039-6028(84)90437-0.
- [44] J.R. Creighton and J.M. White. "A SIMS study of the dehydrogenation of ethylene on Pt(111)". In: *Surface Science* 129.2 (1983), pp. 327–335. DOI: 10.1016/0039-6028(83)90183-8.
- [45] Paul S. Cremer, Xingcai Su, Y. Ron Shen, and Gabor A. Somorjai. "Hydrogenation and Dehydrogenation of Propylene on Pt(111) Studied by Sum Frequency Generation from UHV to Atmospheric Pressure". In: *The Journal of Physical Chemistry* 100.40 (1996), pp. 16302–16309. DOI: 10.1021/jp9613394.
- [46] J.T. Miller, B.L. Meyers, F.S. Modica, G.S. Lane, M. Vaarkamp, and D.C. Koningsberger. "Hydrogen Temperature-Programmed Desorption (H₂ TPD) of Supported Platinum Catalysts". In: *Journal of Catalysis* 143.2 (1993), pp. 395–408. DOI: 10.1006/jcat.1993.1285.
- [47] David Paleček, Gökçen Tek, Jिंगgang Lan, Marcella Iannuzzi, and Peter Hamm. "Characterization of the Platinum–Hydrogen Bond by Surface-Sensitive Time-Resolved Infrared Spectroscopy". In: *The Journal of Physical Chemistry Letters* 9.6 (2018), pp. 1254–1259. DOI: 10.1021/acs.jpcl.8b00310.
- [48] Titta Aaltonen, Antti Rahtu, Mikko Ritala, and Markku Leskelä. "Reaction Mechanism Studies on Atomic Layer Deposition of Ruthenium and Platinum". In: *Electrochemical and Solid-State Letters* 6.9 (2003), p. C130. DOI: 10.1149/1.1595312.
- [49] Jason F. Weaver, Jau-Jiun Chen, and Alex L. Gerrard. "Oxidation of Pt(111) by gas-phase oxygen atoms". In: *Surface Science* 592.1 (2005), pp. 83–103. DOI: 10.1016/j.susc.2005.07.010.

PAPER II: MONITORING OF NUCLEATION AND ISLAND GROWTH MODE DURING ALD OF PLATINUM

Although ALD is traditionally perceived as a layer-by-layer technique, ALD processes for noble metals are often characterized by a nucleation controlled growth on oxide surfaces. Despite numerous reports on noble metal nanoparticle deposition by ALD and tuning of the particle size by the number of ALD cycles,^[1-6] the mechanisms that govern the very initial stages of growth are still not fully understood. Surface processes such as diffusion of deposited atoms,^[1,6-11] adsorption of precursor ligands on the substrate,^[1,11-15] thermal decomposition of the metal precursor,^[11,16,17] and reactions catalyzed by the deposited nanoparticles^[1,11] are suggested to play a role. The kinetics of these processes are expected to vary with the noble metal loading and morphology and will therefore likely evolve during the ALD process.^[1] Moreover, the nucleation and island growth mechanisms and kinetics are influenced by the choice of ALD process conditions, e.g. precursor/reactant type, exposure and deposition temperature, resulting in different incubation times and nanoparticles morphologies.



Most experimental studies concerning the nucleation of noble metal ALD are limited by the fact that they rely on the *ex situ* study of static morphologies alone, without providing detailed insights into how the structure evolves during the ALD process. The effect of a certain deposition parameter is, for example, typically studied by transmission electron mi-

This chapter is submitted as a research article to the journal: Physical Chemistry Chemical Physics, titled "Surface mobility and impact of precursor dosing during atomic layer deposition of platinum: *in situ* monitoring of nucleation and island growth". The image on this page is the original TOC-graphic, submitted with the article. Author contributions: J.D. designed the experiments, performed SEM, XRF and GISAXS measurements and analyzed the results; E.S., A.R., R.K.R., M.M.M, A.V., G.P. and C.D. assisted in performing XRF and GISAXS measurements; M.V.D. and E.S. assisted in analyzing and interpreting the results; C.D. assisted in designing the experiments and interpreting the results; M.V.D. prepared the manuscript; All the authors contributed to revising the manuscript.

croscopy (TEM) and a comparison of the nanoparticle size (distribution) is made for a specific number of ALD cycles. However, dynamic knowledge about how the nucleation and particle growth evolve during ALD for different process conditions is crucial to deepen our understanding of the underlying mechanisms, and this can only be achieved by applying *in situ* probing techniques. In this chapter, we present findings from the combined use of GISAXS and XRF to monitor *in situ* Pt ALD growth. Results are shown for the Pt ALD process using MeCpPtMe₃ and O₂ gas at 300 °C, which is considered a model system for the O₂-based noble metal ALD processes.^[18] An analysis strategy is introduced to correlate the amount of deposited material with the evolution of structural parameters such as Pt cluster shape, average size, and areal density. As a proof of concept the influence of the MeCpPtMe₃ precursor pressure on the morphology of the deposited Pt particles is investigated. A broader description of the known nucleation behaviour of Pt ALD processes is given in the introduction chapter, see section 1.2.2.2.

4.1 EXPERIMENTAL SECTION

4.1.1 *Transportable setup for in situ investigation of ALD with synchrotron radiation*

A drawing and picture of the custom-built synchrotron-compatible ALD setup, used in this work, are shown in Figure 4.1.^[19] The setup consists of a stainless steel chamber equipped with a turbo pump and rotary vane backing pump, enabling a base pressure of 10⁻⁶ mbar. The main ALD components include a flange with heated sample stage, computer-controlled gas inlet valves and a remote RF plasma source. The setup can be transported and installed at synchrotron beamlines, in particular on the MED diffractometer with hexapod of the SixS beamline at the SOLEIL synchrotron facility and on the Huber goniometer of the DUBBLE BM26B beamline at the ESRF synchrotron facility. The chamber is equipped with three Be windows, allowing exposure of the sample to an intense monochromatic X-ray beam and detection of the scattered and fluorescent radiation from the sample. For *in situ* GISAXS studies, the setup is expanded with motorized anti-scattering slits that can be positioned close to the path of the X-ray beam to eliminate unwanted scattered X-rays. This is obtained by placing tungsten slits and a knife edge inside the vacuum, right after the entrance Be window. Right before the exit Be window a tungsten rod-like beamstop is placed in-vacuum to largely block the intense direct and specular reflected X-ray beams, thus suppressing background scattering from

the exit window. Precise alignment and rotation of the sample relative to the incoming X-ray beam is enabled by the aforementioned positioning devices that are available at the SixS (SOLEIL) and DUBBLE BM26B (ESRF) beamlines.

4.1.2 Substrate preparation and ALD of Pt

Si wafers with native SiO₂ are used as substrates. Prior to ALD growth, the substrate and support are heated to 300 °C and exposed to a remote O₂ plasma (10 s, 1.2×10^{-3} mbar, at 200 W) to clean the sample surface and improve reproducibility between the different experiments. ALD of Pt is conducted at 300 °C using MeCpPtMe₃ (Strem Chemicals, 99%) and O₂ gas. The Pt precursor is kept in a stainless steel container heated to 30 °C and Ar is used as a carrier gas. Unless stated otherwise, a static exposure mode is applied, meaning that the valves to the pumping system are closed during exposure of the sample to the Pt precursor or to O₂ gas. The other precursor exposure mode that is used is a pump exposure mode, during which the valves to the pumping system are kept open during the exposure. For both static and pump exposure modes the precursor exposure time is 15 s, the precursor pumping time is 30 s, the O₂ exposure time is 10 s, and the O₂ pumping time is 15 s. The pressure in the chamber during the static precursor exposure reaches ~ 1 mbar, during the pump precursor exposure it is $\sim 6 \times 10^{-3}$ mbar, and ~ 1 mbar during the O₂ exposure.

4.1.3 GISAXS geometry

A schematic representation of the GISAXS experiment is shown in Figure 4.2. The X-ray beam hits the sample under a grazing angle (α_i) and is scattered by the ensemble of Pt nanoparticles on the surface. The scattered intensity as a function of the exit angles α_f and $2\theta_f$ is recorded by a 2D area detector. The angular coordinates of the detector are related to the wavevector transfer ($\mathbf{q} = \mathbf{k}_f - \mathbf{k}_i$) and the detector plane is converted to reciprocal q-space coordinates using the equations: $q_y = (2\pi/\lambda)\sin(2\theta_f)\cos(\alpha_f)$ and $q_z = (2\pi/\lambda)(\sin(\alpha_i) + \sin(\alpha_f))$ with q_y and q_z the scattering vector components parallel and perpendicular to the sample surface, respectively. The $q_x = (2\pi/\lambda)(\cos(2\theta_f)\cos(\alpha_f) - \cos(\alpha_i))$ scattering vector component has a very low value due to the low incident and exit angles that are used in GISAXS and can be neglected. The scattered intensity $I(\mathbf{q})$ is modulated by the form factor $F(\mathbf{q})$ and the structure factor $S(\mathbf{q})$, describing the scattering contribution from the particle shape

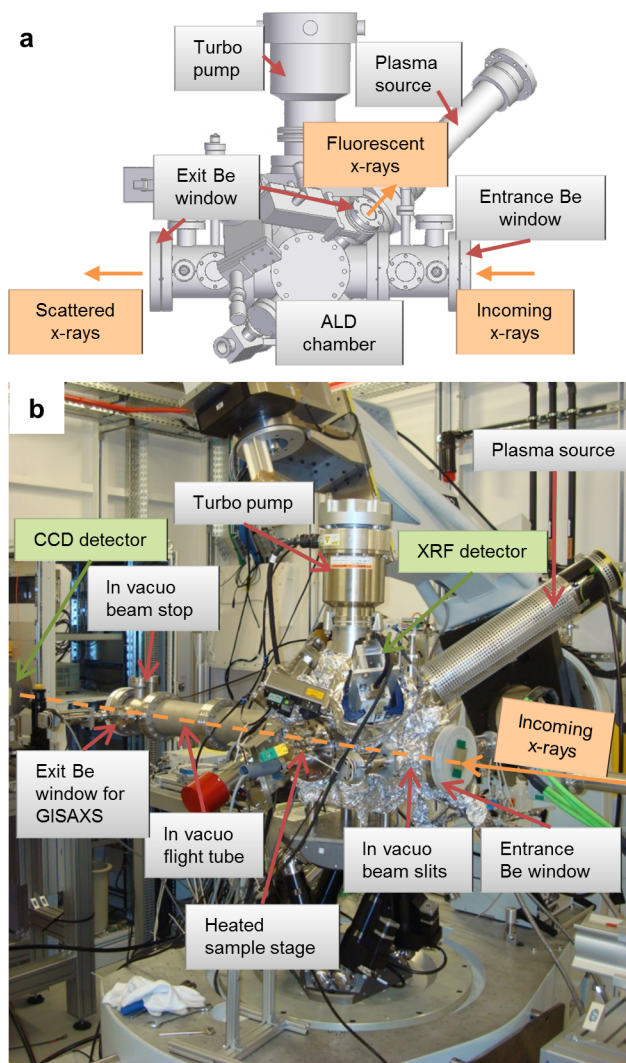


Figure 4.1: (a) Drawing of the transportable synchrotron-compatible high-vacuum ALD setup, dedicated for *in situ* XRF and GISAXS measurements during ALD. (b) Picture of the setup, installed at the SixS beamline of the SOLEIL synchrotron facility.

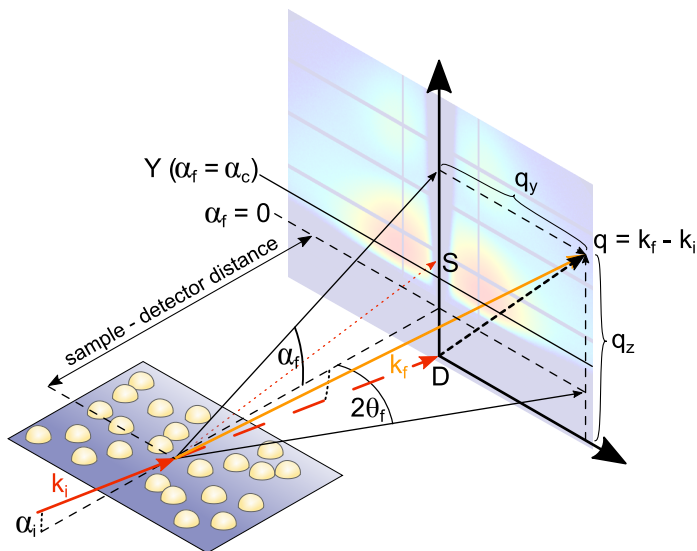


Figure 4.2: Schematic representation of the GISAXS geometry. A monochromatic X-ray beam hits the sample at an incidence angle α_i . The exit angles of the scattered beam are denoted by α_f and $2\theta_f$. The position of the direct beam D (at $\alpha_f = -\alpha_i$) marks the origin for the q_y and q_z components of the scattering vector. The specular reflected beam S (at $\alpha_f = \alpha_i$) is masked by a rod-shaped beamstop, placed in vacuum between the sample and exit Be window. The Yoneda peak (Y) is observed at the critical angle of the sample ($\alpha_f = \alpha_c$).

and organization of the nanoparticles, respectively. The key features that are observed in the scattering pattern are directly linked to the real-space morphology of the nanoparticles ensemble. Intensity modulations along the q_z direction contain information about dimensions perpendicular to the sample surface, such as the particle height. Modulations along the q_y direction contain information about average lateral dimensions, such as the particle width and center-to-center distance between neighbouring nanoparticles. Another scattering feature is the Yoneda (or Vineyard) peak, i.e. an enhancement of the scattered intensity for the exit angle α_f that is equal to the critical angle of the sample α_c . Therefore, the dependence of the Yoneda peak on the optical surface properties provides information about the surface composition.

4.1.4 *In situ* XRF and GISAXS measurements

In situ XRF and GISAXS measurements during ALD were performed at the SixS (SOLEIL) and DUBBLE BM26B (ESRF) beamlines. To avoid decomposition of the Pt precursor by the X-rays, the sample is only illuminated after the reactor is pumped to base pressure. Samples were exposed to the X-rays after every second ALD cycle and a fluorescence spectrum and scattering pattern are recorded. To enable excitation of the Pt $L\alpha$ emission lines for XRF, the X-ray energy is set to 12 keV, which is slightly above the L_3 absorption edge of Pt at 11.56 keV. An incidence angle of 1.2° was used for XRF measurements, each spectrum was acquired in 30 s with an energy-dispersive silicon drift detector (Röntek and Vortex at SixS (SOLEIL) and DUBBLE BM26B (ESRF), respectively). GISAXS patterns were recorded at an incidence angle of 0.5° , which is well above the critical angle of Pt ($\alpha_c = 0.38^\circ$, at 12 keV). Firstly, this ensures full penetration of the Pt layer and, secondly, clear separation of the Pt Yoneda peak and the specular peak in the scattering pattern. The sample-detector distance was calibrated with a silver behenate sample.

At the SixS (SOLEIL) beamline, the X-ray beam at the sample position was $0.3 \text{ mm} \times 0.4 \text{ mm}$ (horizontal and vertical, respectively) and the 2D GISAXS patterns were acquired with a MarCCD detector (2048×2048 pixels, each pixel has a size of $80 \times 80 \mu\text{m}^2$) using a counting time of 20 s during the pumping step. The detector was positioned roughly 1.7 m from the sample. The in-vacuum flight tube was used to reduce background scattering and absorption from air. In addition to the in-vacuum beamstop, a lead strip was placed after the window to completely shield the detector from the intense direct beam and the scattered radiation from the exit Be window.

At the DUBBLE (ESRF) beamline, the X-ray beam was focused at the detector position, which results in a beam size of $1.0 \text{ mm} \times 0.4 \text{ mm}$ (horizontal and vertical, respectively) at the sample position. The GISAXS patterns were acquired with a Dectris Pilatus 1M detector (981×1043 pixels $H \times V$, each pixel having a size of $172 \times 172 \mu\text{m}^2$) using a counting time of 30 s during the pumping step and a sample-detector distance of 4.4 m was used. The pathway between the exit Be window of the ALD chamber and the detector was mostly evacuated by using a pumped flight tube with entrance and exit Kapton windows. A second beamstop was installed in front of the detector at the position of the direct and specular beam to prevent detector saturation and damage.

4.1.5 GISAXS data analysis

In this work, we introduce an analysis approach, based on a geometrical model, to extract average real space parameters such as the Pt nanoparticle shape, size, and areal density from the q-space scattering data. To validate the proposed strategy, the measured GISAXS data were compared to simulated 2D GISAXS patterns that were calculated with the IsGISAXS software,^[20] using the extracted morphological parameters as input for the simulation. The best agreement between simulation and data was obtained when two particle shapes in a 1:1 ratio were taken into account, being full spheroids and hemispheroids. Both particle geometries were described by the same particle height and radius. A lognormal distribution function was selected for the particle radius, and the distribution width was described by the geometric standard deviation σ . A joint distribution for the particle height was implemented in IsGISAXS assuming a Gaussian distribution for the particle aspect ratio height/radius, the distribution width being described by 0.05 times the central particle aspect ratio value. The distorted-wave Born approximation (DWBA) was used to calculate the form factor, the model of the graded interface was used to describe the perturbations caused by densely packed particles on a surface.^[21] The calculations furthermore use the local monodisperse approximation (LMA) formalism, which is commonly used for polydispersed systems. A 1D paracrystal model was used to calculate the structure factor, which is a regular 1D lattice with loss of long-range order. A Gaussian function with disorder parameter ω , calculated as $\omega = 0.4 \times D$ described the distribution of the center-to-center distance D . Supplementary Figure 1 shows the most relevant parameters in the input file for the IsGISAXS software.

4.1.6 Complementary SEM and XRR measurements

The GISAXS data analysis approach is corroborated by *ex situ* X-ray reflectivity (XRR) and scanning electron microscopy (SEM) measurements. XRR is performed in a Bruker D8 system, equipped with a Cu $K\alpha$ source and a point detector. SEM is performed in a FEI Quanta 200F instrument.

4.2 RESULTS

4.2.1 *In situ* XRF: growth curve

XRF and GISAXS data was acquired after every two ALD cycles during Pt deposition. The integrated Pt L_{α} emission line was calibrated using Rutherford backscattering spectrometry (RBS).^[6] This allows the determination of the Pt surface density as a function of the intensity of the Pt L_{α} signal, depicted as a function of the number of ALD cycles in Figure 4.3a. During the first ALD cycles (0 to 12) a slow growth regime was observed and a theoretical monolayer (TML) of Pt was obtained after 10 ALD cycles, indicating that the XRF setup is sensitive enough to detect a sub-monolayer surface coverage of Pt atoms. After the first slow growth a constant growth regime is quickly obtained (~ 26 ALD cycles) and after roughly 80 cycles the growth per cycle decreases to a lower value. The growth curve has an elongated S-shape, indicative of Pt nucleation followed by particle growth and coalescence.^[22,23]

Additional samples with selected Pt surface densities (marked points 1-4) were prepared and measured by *ex situ* SEM. The obtained SEM micrographs (Figure 4.3b) provide snapshots of the particle morphology and distribution at different Pt surface densities (i.e. different ALD cycles). The SEM micrograph of the low Pt surface density (~ 160 atoms/nm², Figure 4.3b(1)) indicates that the Pt nucleates, and forms particles, on the SiO₂ surface. The other SEM micrographs indicate that after the particles are formed they increase in size and start to coalesce (2), forming larger and more irregular particle shapes. They continue growing and merging, resulting into even larger worm-like structures (3) and finally start to form a percolating Pt layer across the substrate when the Pt loading is high enough (4). For even higher Pt surface densities the slope of the growth curve decreases, indicating that the available surface area for precursor absorption starts to decrease after percolation.

4.2.2 *In situ* GISAXS: particle nucleation

The Pt nucleation stage on native SiO₂ was investigated using *in situ* 2D GISAXS measurements. The GISAXS scattering patterns that were recorded during the first 12 ALD cycles are displayed in Figure 4.4a. After the first ALD cycles there is an increase of the background scattering intensity in the pattern ($q_y \neq 0$ nm⁻¹). Additional ALD cycles cause the scattering intensity to increase further and make it clear that a single scattering peak is present in the pattern. This indicates that there are corre-

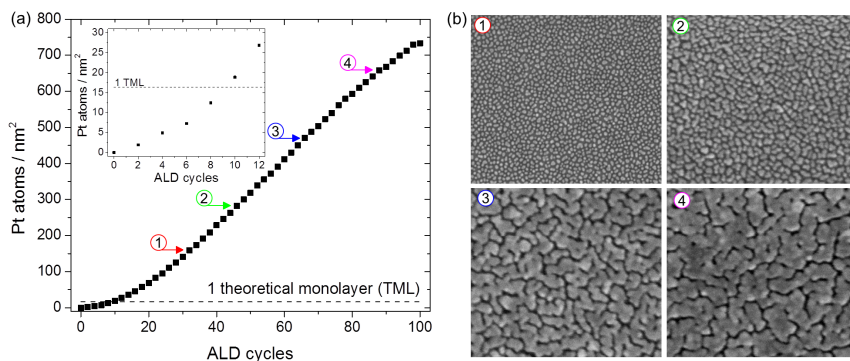


Figure 4.3: (a) RBS-calibrated *in situ* XRF data: surface density of Pt atoms as a function of the number of ALD cycles. The inset shows a detail of the nucleation stage during the first 12 ALD cycles. (b) SEM images for selected Pt loadings: (1) ~ 160 , (2) ~ 280 , (3) ~ 470 , (4) ~ 660 Pt atoms per nm^2 . Each SEM image is 500 nm in width and height.

lated Pt clusters distributed on the surface during the nucleation stage. To study the evolution of the scattering peak along the q_y direction, horizontal cuts were taken at the q_z position of maximum intensity (Yoneda peak) and are depicted in Figure 4.4b. Fits with Lorentzian functions were performed for all but the first cut (0 ALD cycles) and are displayed as the black lines, overlapping the data. From these cuts it is clear that an off-specular scattering signal is already present after 2 ALD cycles, with the maximum scattering intensity observed at $q_y = 0.59 \text{ nm}^{-1}$, indicating that Pt clusters were already present on the surface. Additional ALD cycles result in an increase in intensity and shifts in the q_y position of maximum intensity of the scattering peak.

The q_y maximum of the scattering peak ($q_{y,\text{max}}$) can be approximated to the mean center-to-center distance (D) between scattering centra by using: $D = 2\pi/q_{y,\text{max}}$.^[24] Therefore, lower $q_{y,\text{max}}$ values are related to larger mean center-to-center distances and *vice versa*. The $q_{y,\text{max}}$ value for each horizontal cut is obtained from a fit through the data and these are plotted (with a 95 % confidence interval) as a function of the number of ALD cycles and Pt surface density in Figure 4.4c. The inset shows the $q_{y,\text{max}}$ values converted from q -space to real space values (D). The $q_{y,\text{max}}$ position shows a considerable shift towards higher values during the first 6 ALD cycles, which indicates a decrease for the mean particle distance and a rise in the number of deposited nuclei on the surface. New nuclei are deposited between the existing clusters until a critical or saturated coverage is reached, giving an estimated saturated particle density of $N \sim 1.8 \times 10^{12} \text{ nuclei/cm}^2$ ($N \sim D^{-2}$)

after 6 ALD cycles. This value for the particle density corresponds with particle densities that can be expected for metal particles on an oxide surface (10^{12} - 10^{13} nuclei/cm²) in literature.^[1,25] Additional ALD cycles result in a gradual shift of the $q_{y,max}$ position towards lower q_y values, showing an increase in the particle center-to-center distance and indicates a reduction in the number of scattering nuclei due to coalescence. Surface diffusion will rather result in the growth of existing islands instead of the formation of a new stable nucleus.

4.2.3 *In situ* GISAXS: particle growth and coalescence

After the nucleation stage the Pt ALD process exhibits enhanced growth behaviour until layer closure starts to occur, see the *in situ* XRF curve (Figure 4.3a). This intermediate stage was also investigated during the ALD

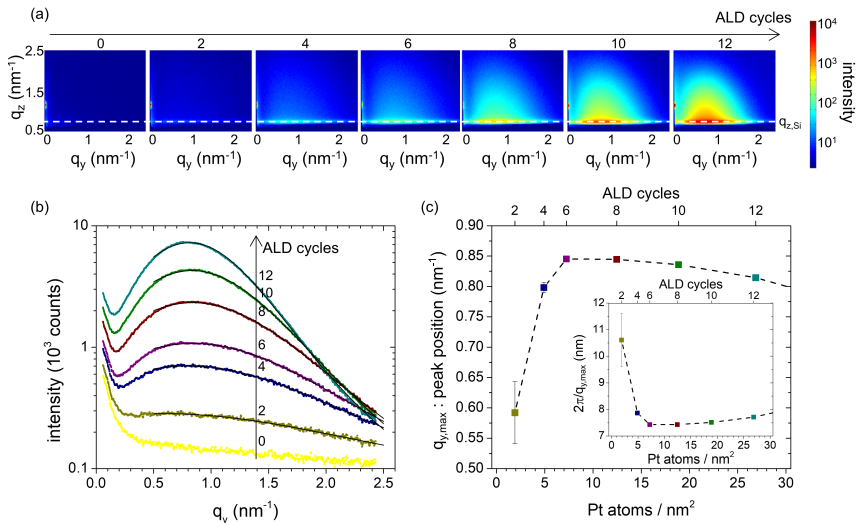


Figure 4.4: (a) *In situ* GISAXS patterns measured during the nucleation stage. The dashed white line marks the position of the Si Yoneda. (b) Horizontal line profiles are taken at the q_z position of maximum intensity, which correspond to the Si Yoneda position. The black lines are fits to the data points. (c) The peak position, $q_{y,max}$ of the horizontal cuts as a function of the number of ALD cycles (top x-axis) and the surface density of Pt atoms (bottom x-axis). The peak positions were obtained from the fits shown in (b). The inset shows the values which correspond to: $2\pi/q_{y,max}$. The error bars represent the 95 % confidence intervals for the fitted $q_{y,max}$ values

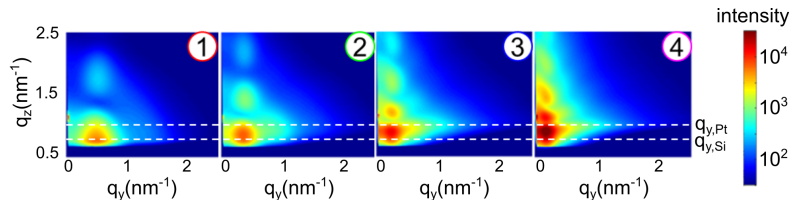


Figure 4.5: *In situ* GISAXS patterns measured during the growth and coalescence stage of the Pt ALD process. The selected patterns correspond to (1) 32, (2) 46, (3) 66, (4) 88 ALD cycles and a Pt surface density of (1) 160, (2) 280, (3) 470, (4) 660 atoms per nm². The Si and Pt Yoneda positions are indicated by the dashed white lines.

process. Figure 4.5 displays selected *in situ* 2D GISAXS patterns with Pt surface densities (Pt loading) that correspond to the marked points on the *in situ* XRF curve and the *ex situ* SEM micrographs, shown in Figure 4.3. The GISAXS patterns show that the main scattering peak increases in intensity as a function of the Pt loading and that the position of the maximum shifts to lower q_y values and higher q_z values. The shift in q_y to lower values indicates an increase in the mean center-to-center particle distance with higher Pt loadings due to nanoparticle coalescence. The q_z position of maximum scattering intensity (Yoneda peak) depends on the critical angle of the scattering surface and is therefore dependent on the material density of the scattering volume. The dashed white lines in Figure 4.5 mark the expected Yoneda positions for a Si and Pt surface. It is clear that the Yoneda peak in the pattern starts at the position for a Si surface, as expected by the low Pt loading on the surface. Increasing the Pt loading results in a shift of the Yoneda peak position towards the expected value of Pt, due to the fact that the average density of the scattering volume increases with Pt loading. Both shifts in the position of the main scattering peak are consistent with the growth and coalescence behaviour of the Pt particles, as seen in the *ex situ* SEM micrographs (Figure 4.3b). In addition to the shift of the main scattering peak, secondary scattering maxima and minima appear above the main peak with increasing Pt loading and shift towards lower q_z values. This indicates that the mean particle height increases as a function of the Pt loading. Finally, the arc-like features that can be observed in the out-of-plane scattering recorded at ALD cycles 32 and 46 (respectively, patterns 1 and 2 in Figure 4.5) can be associated with a spheroidal particle shape.^[6,26]

Figure 4.5 shows the 2D scattering patterns for selected Pt loadings, which allows for a quick qualitative assessment of the surface morphology. However, further analysis is required to obtain quantitative informa-

tion about the evolution of the scattering features as a function of the Pt surface density. As a first step towards quantitative analysis, horizontal and vertical cuts were taken and plotted in a 2D colour map as a function of the Pt surface density.

The horizontal cuts were taken at the q_z position of maximum intensity of the main scattering peak and are shown in Figure 4.6a. The solid black line indicates the evolution of the first maximum and its data points are displayed in Figure 4.6b. As detailed in Figure 4.4c, the $q_{y,max}$ position starts around 0.6 nm^{-1} , increases during the first 6 ALD cycles to 0.85 nm^{-1} , and then smoothly shifts to lower values. The $q_{y,max}$ position is related to the mean center-to-center distance between the Pt particles and the corresponding real space value is shown in the insert of Figure 4.6b. This again shows that after an initial decrease of the inter-particle distance it gradually increases, indicating that after nucleation and reaching the saturated particle coverage the scattering centra are spaced further apart with every consecutive ALD cycle, due to coalescence of the Pt particles.

A second scattering feature appears after roughly 22 cycles ($\sim 80 \text{ Pt atoms/nm}^2$) and upon its appearance gradually shifts to lower q_y values. This behaviour is also present for the minimum position between both maxima, as can be seen in Figure 4.6c and by the dashed line in Figure 4.6a. This minimum is a feature of the form factor of the particles. As the horizontal scattering features give information about the in-plane dimensions, the change in the position of this minimum is related to the size of the particles and can be used to deduce an approximate value for the mean particle radius. Simulations of the form factor of full spheroids and hemi-spheroids with a range of relevant particle widths and heights were performed to obtain a relation between the $q_{y,min}$ value and the particle radius, which gave the following relation: $\text{radius} = 4.4/q_{y,min}$ (see Supporting Information). The estimated values for the particle radius are displayed in the insert of Figure 4.6c. This shows that the mean radius of the particles keeps increasing as a function of the Pt loading, which is to be expected from the *ex situ* SEM images. The coloured numbers and arrows correspond to Pt loadings that are marked on the XRF curve and the SEM micrographs in Figure 4.3.

The vertical cuts were taken at the q_y position of maximum intensity for the main scattering peak and are shown in Figure 4.7a; the Si and Pt Yoneda positions are marked. The evolution in q_z position of the main scattering peak is displayed in Figure 4.7b. It is clear that the maximum intensity in q_z starts at the position for the Si Yoneda and by increasing the Pt loading it shifts towards the position that is expected for a bulk Pt surface, showing an abrupt transition around a surface density of 250

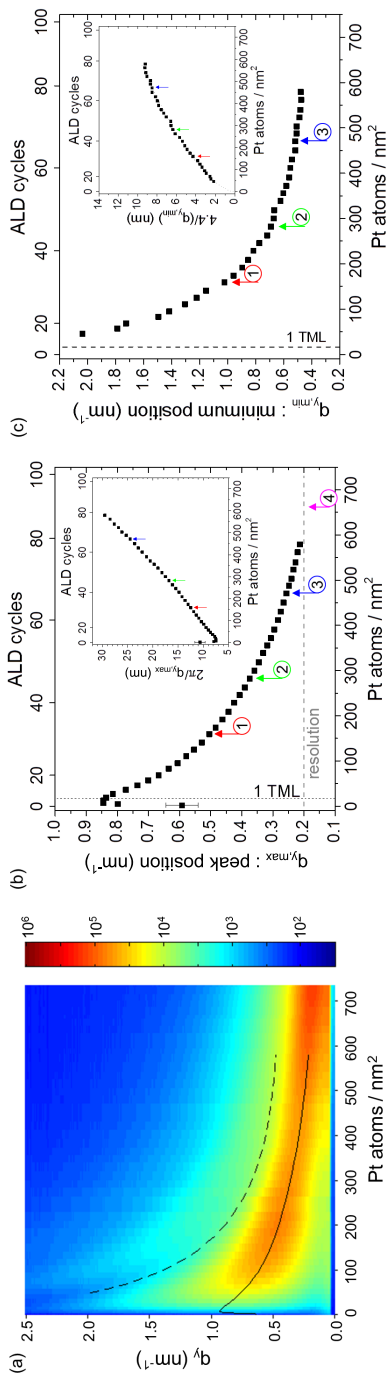


Figure 4-6: (a) Intensity evolution of the horizontal line profiles as a function of Pt surface density. The horizontal cuts were taken at the q_z position of maximum intensity of the main scattering peak. The q_y positions of the first maximum and minimum are indicated by the solid and dashed black lines, respectively. (b) $q_{y,max}$ position of the first maximum versus ALD cycles (top x-axis) and Pt surface density (bottom x-axis). The corresponding $2\pi/q_{y,max}$ values are shown in the insert. (c) $q_{y,min}$ position of the first minimum versus ALD cycles and Pt surface density. The corresponding estimated mean particle radius values ($4.4/q_{y,min}$) are shown in the insert. The coloured numbers and arrows correspond to the marked points in Figure 4-3.

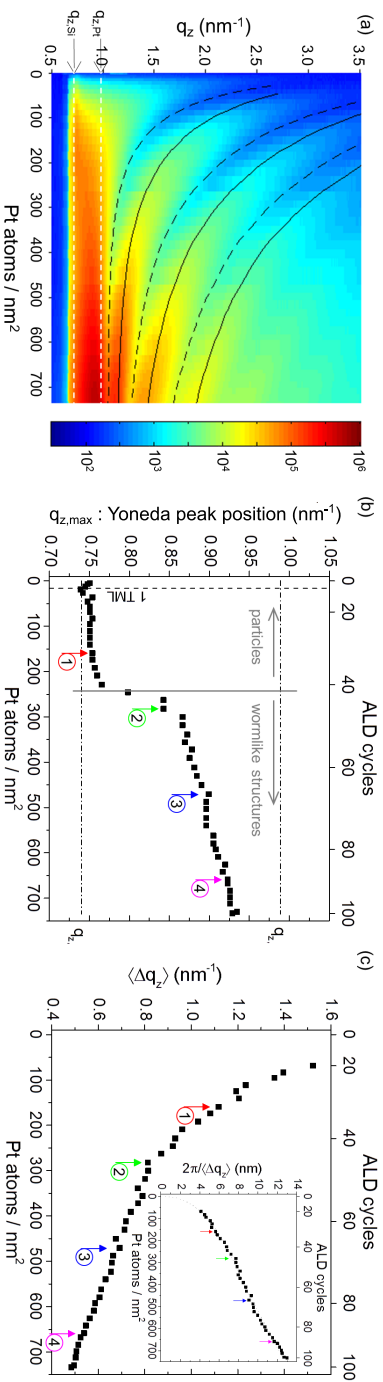


Figure 4.7: (a) 2D colour map showing vertical line profiles of the main scattering peak as a function of Pt surface density. Each vertical line profile is taken at the q_y position of maximum intensity of the main scattering peak. The dashed white lines mark the Si and Pt Yoneda positions. The solid and dashed black lines indicate the evolution of the higher order maxima and minima, respectively. (b) Position of the q_z maximum of the main scattering peak as a function of ALD cycles and Pt surface density. (c) Average distance between two adjacent maxima and/or minima, $\langle q_z \rangle$, versus ALD cycles and Pt surface density. The inset shows the corresponding values for $2\pi / \langle \Delta q_z \rangle$. The coloured numbers and arrows (1-4) refer to the data/SEM micrographs in Figure 4.3.

Pt atoms per nm^2 . Comparing the *ex situ* SEM micrographs (Figure 4.3b) before (1) and after (2) this transition show a large difference in morphology for the Pt particles. Before the transition (Figure 4.3b-1) the particles can still be considered isolated and isotropic in shape. After the transition (Figure 4.3b-2) the particles are merging and form elongated, worm-like structures. The abrupt shift in the $q_{z,\text{max}}$ position seems to coincide with a change in the morphology of the Pt particles. For high Pt loadings, the SEM micrographs reveal a morphology that can be considered as a Pt thin film with gap-like voids.

After a few ALD cycles secondary vertical scattering maxima appear, marked in Figure 4.7a by the solid black lines. The minima between two adjacent maxima are marked by the dashed black lines. These maxima gradually shift towards lower q_z positions with increasing Pt surface density, indicating that the deposited Pt particles are increasing in height. The average distance between two adjacent maxima or minima is taken and plotted in Figure 4.7c. By using the approximation $H = 2\pi / \langle \Delta q_z \rangle$ it is possible to estimate the mean height (H) of the deposited film, the corresponding values are shown in the inset of Figure 4.7c. Based on these results the obtained final thickness of the Pt layer was ~ 13 nm.

After 100 ALD cycles the deposition was stopped and the sample was characterized using X-ray reflectivity (XRR) and SEM, see Figure 4.8. The SEM image shows the worm-like structure of the deposited Pt layer. A thickness of 12.1 nm and roughness of 1.2 nm was obtained from the XRR fit, matching closely with the calculated final thickness from the GISAXS measurements (Figure 4.7c).

4.2.4 Strategy for analysing the GISAXS patterns

4.2.4.1 Geometrical model for "fast analysis" of GISAXS patterns

As outlined in the previous section, estimations for the mean particle height and width, and mean inter-particle distance can be deduced by evaluating the minima and maxima in the horizontal and vertical line profiles taken at the maximum intensity of the 2D GISAXS patterns. This approach is considered a "rapid" or "fast" data analysis.^[24] Inspired by the work of Schwartzkopf et al.^[26], we use this "fast" analysis as a basis for a simplified geometrical model that captures the essential parameters of the particle morphology on the sample, such as the average particle height, radius, and center-to-center distance, and is accurate enough to quickly determine changes in the morphology of the Pt particles during the initial stages of the ALD process, i.e. before agglomeration leads to wormlike features. In this model, the particles are modelled as full spheroids, without

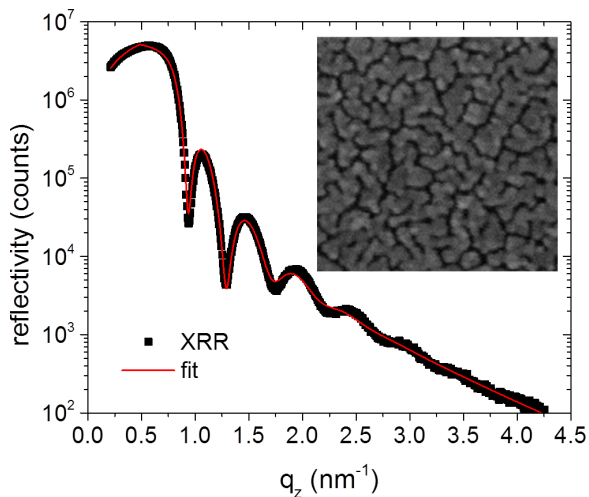


Figure 4.8: *Ex situ* characterization after 100 cycles of Pt ALD. X-ray reflectivity pattern with fit to the data, the fitted thickness is equal to 12.1 nm. The SEM image has a width of 500 nm.

size distribution, on a regular 2D lattice. The average particle dimensions are derived from the above mentioned “fast” data analysis, i.e. the average particle height ($H = 2\pi/\Delta q_z$) and radius ($R = 4.4/q_{y,\min}$), but takes into account a deviation for the inter-particle spacing based on the *in situ* recorded XRF data. Indeed, while a common approach to estimate the center-to-center distance D is to use the approximation $D = 2\pi/q_{y,\max}$, often large discrepancies are observed with values obtained from real space TEM imaging, because the GISAXS intensity is governed by the interplay between the interference function and the form factor. Due to the latter, the observed $q_{y,\max}$ peak position does not exactly correspond to the maximum of the interference function. The limitations of the approximation $D = 2\pi/q_{y,\max}$ in our data become clear in Figure 4.9b, where the Pt surface density is calculated based on the estimated values for the average particle height, radius, and center-to-center distance. The mismatch between the measured Pt surface density by XRF (black squares) and the calculated Pt surface density with the geometrical model (open circles) can be attributed to a deviation in the estimated value of the center-to-center distance from its real value. Therefore, an alternative approach was developed, for which the XRF Pt surface density is used as the input for calculating the value of the center-to-center distance. In this approach the H , and R values (Figure 4.9c, black triangles) are determined from the GISAXS pattern using

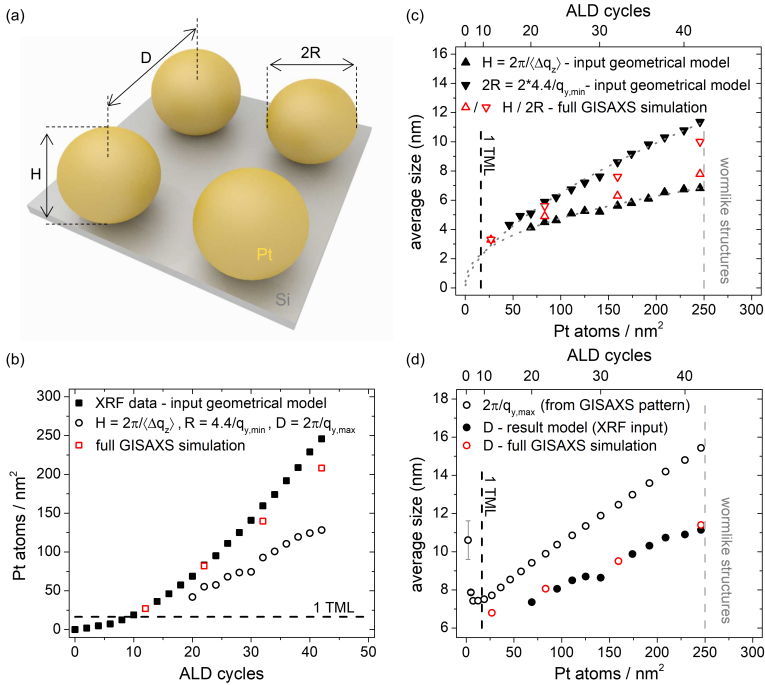


Figure 4.9: (a) Schematic representation of the particle geometry and distribution, as assumed in the geometrical model for "fast analysis". (b) Pt surface density versus ALD cycles, measured by XRF (black squares), calculated from extracted H , R , and D values from "fast" GISAXS line profile analysis (circles), and extracted from "full" GISAXS simulations (open red squares). (c) Average particle height H (upward triangles) and width $2R$ (downward triangles) as a function of ALD cycles (top x-axis) and Pt surface density (bottom x-axis). The full black symbols are extracted from the line profile analysis and the open red symbols originate from simulations. (d) Average particle center-to-center distance D as a function of ALD cycles and Pt surface density, calculated from the proposed geometrical model (black circles) and extracted from GISAXS simulations (open red circles). The $2\pi/q_{y,\text{max}}$ values extracted from GISAXS line profiles are plotted as open black circles. The input and output values for the GISAXS simulations are displayed in Table 4.1.

the “fast” data analysis and the following relation is used to determine the center-to-center distance D:

$$D = \sqrt{\frac{2}{3}\pi R^2 H \frac{66.24 \text{ atoms / nm}^3}{S_{Pt}}} \quad (4.1)$$

with S_{Pt} the Pt surface density and 66.24 being the number of Pt atoms that are present in a cubic nm of bulk Pt. As will be discussed in the next section, simulation results (open red symbols in Figure 4.9) confirm that this approach is more reliable than the common approach of using the approximation $D = 2\pi/q_{y,\max}$ to estimate the center-to-center distance. Note that Figure 4.9c suggests that the initial nuclei have an aspect ratio close to 1:1, marked by a similar mean particle width and height. With increasing Pt loading, the mean particle width increases faster than the mean particle height, pointing towards lateral growth of the nanoparticles, giving rise to laterally elongated particles.

4.2.4.2 Simulation of GISAXS patterns

The purpose of the simple geometrical model is to quickly extract parameters for the average particle height, radius, and inter-particle distance from the quasi real time feedback of the particle morphology during the experiments. However, validation of this model is required by simulating full 2D GISAXS patterns and demonstrating that good agreement is achieved with the experimental patterns. In the next paragraphs we describe a step-by-step approach that we applied to model the nanoparticle shape, dimensions, and spacing and obtain reasonable agreement between data and simulation (see Supporting Information for a schematic representation of the analysis approach). The parameters extracted from the simplified geometrical model (full black symbols in Figure 4.9b-d, with values for D determined by Eq. 4.1) served as initial input parameters for the simulations, which required only slight optimization during the simulation procedure, yielding the data depicted by the open red symbols in Figure 4.9b-d as the simulation output. The optimized H and R values only differ slightly from the initial input parameters, and the optimized average center-to-center distance D does not differ much from its initial input value. This provides a good indication that the proposed geometrical model is a physically relevant model that yields valuable information on the evolution of the average particle height, radius and center-to-center distance during the ALD process, without the complexity of a full 2D GISAXS simulation.

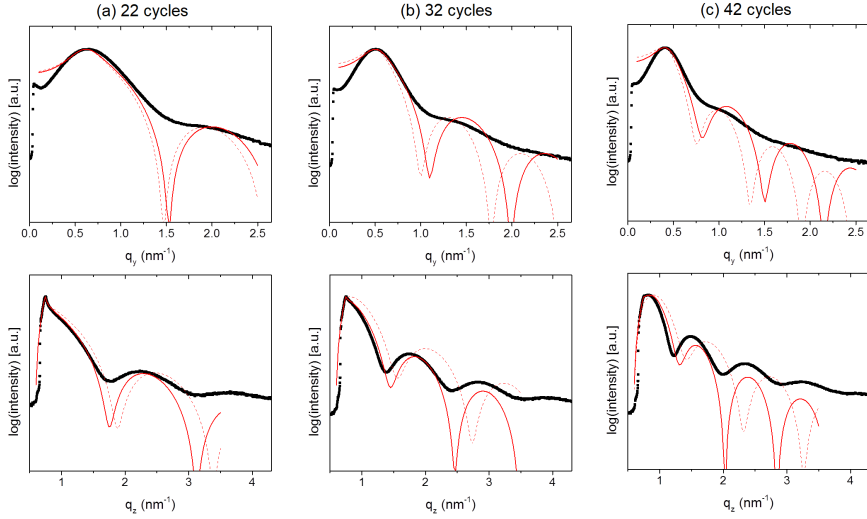


Figure 4.10: Experimental (black data points) and calculated (red curves) horizontal (top) and vertical (bottom) line profiles of the GISAXS patterns obtained after 22 (a), 32 (b), and 42 (c) ALD cycles. The dashed red curves used the H , R , and D values extracted from the geometrical model as input for the calculations. The full red curves used optimized values for H , R , and D . The line profiles for 12 ALD cycles are displayed in the Supporting Information. All input parameters for the simulations are listed in Table 4.1.

ALD cycle	XRF at./nm ²	Geometrical model			ω_i	Optimized values (simulations)				
		H_i	$2R_i$	D_i		H_o	$2R_o$	D_o	ω_o	at./nm ²
22	83.14	4.50	5.89	8.06	3.22	4.9	5.6	8.06	3.22	82.04
32	159.42	5.62	8.60	9.51	3.80	6.3	7.6	9.51	3.80	139.55
42	245.86	6.82	11.36	11.15	4.46	7.8	10	11.4	4.56	208.16

Table 4.1: Morphological parameters used for the line profile simulations in Figure 4.10. H_i , $2R_i$ and D_i (in nm) were extracted from the geometrical model. The simulations used a model consisting of spheroid particles without size distribution on a regular 1D lattice with loss of long-range order described by the disorder parameter $\omega = 0.4D$. H_o , $2R_o$ and D_o are the optimized parameters.

The optimization of the initial input values is illustrated in Figure 4.10. It shows the experimental (black data points) and simulated (red curves) line profiles of the GISAXS patterns recorded at 22, 32, and 42 ALD cycles. The line profiles for 12 ALD cycles can be found in the Supporting Information. The form factor was calculated for full spheroids without size distributions. The interference function was described by the mean correlation length D and a Gaussian distribution function with disorder parameter ω . The shape of the main scattering peak in the horizontal line profiles was found to be well reproduced for an ω value equal to $0.4D$. Simulations with the initial average H , R and D values extracted from the geometrical model yielded the dashed red curves as output. The obtained curves are able to decently reproduce the maxima and minima of the horizontal line profiles (top panels), although their q_y positions are slightly underestimated. For the vertical line profiles (bottom panels), it is only possible to reproduce the first profile (a), for the other profiles the number of minima and maxima is reproduced but their position is shifted to higher q_z values, indicating that the input underestimates the height of the particles. Better agreement can be obtained after optimizing the initial H , R , and D values (solid red curves). It is clear that the used input parameters already yield a decent simulation of the line profiles and that optimizing the input values does not lead to significant changes in the relevant parameters H , R and D (Table 4.1).

After optimizing the main parameters (H , R , D , ω) based on 1D line profiles, the next step concerns the simulation of the entire 2D GISAXS images. During this task, it became clear that the inclusion of two particle shapes in the average form factor is needed to obtain a good reproduction of the intensity distribution of the scattering features in the 2D GISAXS patterns. For illustration, Figure 4.11 shows the experimental GISAXS image of ALD cycle 32 (a) together with three simulated patterns, assuming different particle shapes (b-d). The experimental pattern shows a main scattering maximum with several secondary scattering features along the q_z and q_y directions. In addition, there is an incomplete semi-circle present that is connecting the first secondary maxima and a diffuse background for higher q_y and q_z values. Full spheroids and half spheroids were mainly considered as possible particle shapes to describe the Pt particles, cylindrical shapes and rectangular cuboids were excluded based on the overall shape of the measured GISAXS patterns (see Supporting information). The first semi-circular shape is reproduced when full spheroids are used (Figure 4.11b). However, the dip in scattering intensity around $q_y = 1.0 \text{ nm}^{-1}$, $q_z = 1.5 \text{ nm}^{-1}$ is not simulated and the higher order semi-circle is too distinctly present in the simulated pattern. While the dip in

scattering intensity is reproduced when half spheroids are used as the particle shape (Figure 4.11d), it does not reproduce the diffuse arc-like background scattering. The best correspondence to the particular scattering features is obtained when combining both particle shapes in a 1 to 1 ratio, see Figure 4.11c. Both particle types are assumed to have the same average particle height and width. Therefore, both particle shapes yield the same volume per particle and this means that the previous manner to calculate D (Eq. 4.1) can be used to ensure that the simulated surface has the same amount of Pt as is experimentally determined from XRF.

While the main features of the GISAXS pattern are now reproduced and the introduction of two particle shapes already smooths out the line profiles, the intensity of the minima in the simulated line profiles does

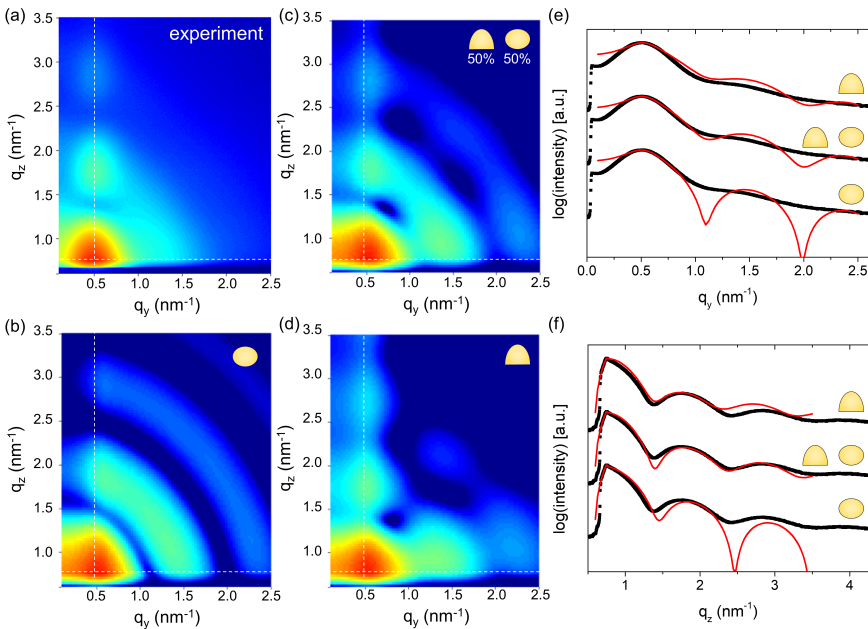


Figure 4.11: Experimental (a) and simulated (b-d) 2D GISAXS patterns, obtained at 32 ALD cycles. The assumed particle shapes for the calculations are schematically represented in the top right corner of the images. Horizontal (e) and vertical (f) line profiles of the experimental (black data points) and calculated (red curves) GISAXS patterns. The profiles were given an offset for clarity. The morphological parameters used for the simulations were extracted from the optimized line profile simulations in Figure 4.10: $H_0 = 6.30$ nm, $2R_0 = 7.60$ nm, $D_0 = 9.51$ nm, $\omega_0 = 3.80$. No size distributions are taken into account.

not fully coincide with the experimental data points, see Figure 4.11e-f, due to the fact that no size distribution was assumed for the Pt particles. Therefore, the complexity of the particle model is further increased by imposing size distributions on the particles to improve agreement between simulation and experiment. Good agreement is obtained by assuming a Gaussian distribution with relative width 0.05 for the particle aspect ratio H/R and a lognormal distribution for the particle radius R . The same size distributions are used for both particle shapes in the model (full spheroids and half spheroids). Simulations with variation in the radius distribution width, parameterized by the geometric standard deviation σ , are displayed in Figure 4.12 for the GISAXS pattern obtained after 32 ALD cycles. Figure 4.12a shows the experimental GISAXS pattern while

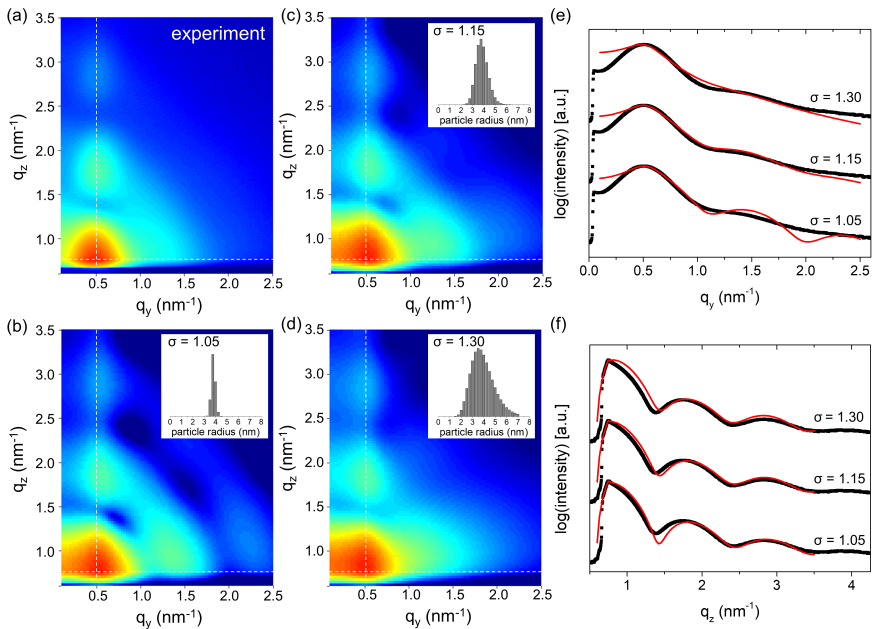


Figure 4.12: Experimental (a) and calculated (b-d) 2D GISAXS patterns, obtained at 32 ALD cycles. The particle radius distributions are varied for the simulated patterns and are represented in the top right corner of the images. Horizontal (e) and vertical (f) line profiles of the experimental (black data points) and calculated (red curves) GISAXS patterns. The profiles were given an offset for clarity. The morphological parameters used for the simulations were extracted from the optimized line profile simulations in Figure 4.10: $H_0 = 6.30$ nm, $2R_0 = 7.60$ nm, $D_0 = 9.51$ nm, $\omega_0 = 3.80$.

(b-d) represent the simulated patterns with different radius distributions, which are depicted in the inserts. Figure 4.12e-f show the simulated horizontal and vertical line profiles (red curves) compared to the experimental line profiles (black data points). It is clear that using a size distribution results in further smoothing of the 1D line profiles. Based on the simulated line profiles (Figure 4.12e-f) the radius distribution with $\sigma = 1.05$ yields the worst fit to the experimental data and $\sigma = 1.15$ the best fit to the experimental line profiles. It is instructive to compare these particle radius distributions with the one extracted from the SEM image (Figure 4.3a), see Supporting Information. This comparison supports the mean R value that is obtained from the GISAXS analysis, but indicates that the distribution with a σ value of 1.30 (Figure 4.12d) corresponds best to the real size distribution, while its simulated line profiles do not fit as well as the simulation result using $\sigma = 1.15$ (Figure 4.12c). The reason for this mismatch is that there are some limitations when simulating GISAXS patterns, such as the assumption of the particle shapes and ratios between the particle shapes. In this case a one to one ratio of full and half spheroids is assumed while the real sample may have a different ratio. Nonetheless, good agreement between experiment and simulation can be achieved, without requiring large changes to the initial input parameters. This indicates that the proposed geometrical model can be used for a quantitative assessment of the 2D GISAXS images that are obtained during the Pt ALD process.

4.2.5 Effect of precursor dose on the Pt nucleation

The previous sections provided insights into how *in situ* recorded XRF signals and scattering patterns, in particular the q positions of the minima and maxima in the patterns and line profiles, can provide information on the morphological parameters during the ALD process. In this part of the chapter, the *in situ* XRF and GISAXS methodology is used to study the influence of the precursor dosing on the Pt nucleation and island growth mode. Generally, in the steady growth regime of ALD processes the surface reactions are in saturation, provided that a sufficiently large precursor dose is applied, which is determined from saturation experiments. Using a precursor exposure that is larger than the saturation exposure has no effect on the growth, instead it results in waste of the excess precursor. However, surface reactions of a different nature are taking place during the nucleation and island growth regime, and the precursor dose obtained from typical steady growth saturation experiments may not lead to saturation of these initial surface reactions. As a result, increasing the precursor exposure beyond the point of saturation for steady growth can have an in-

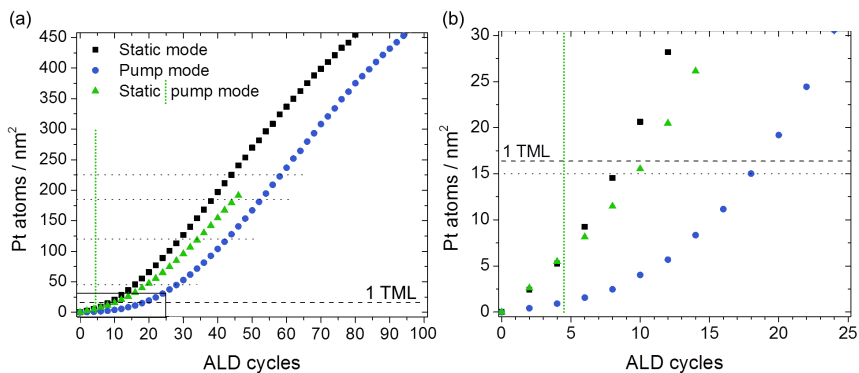


Figure 4.13: (a) Pt surface density as a function of ALD cycles for three experiments using different Pt precursor dose modes. RBS was used to calibrate the *in situ* XRF data. (b) Detail of the nucleation stage. The dotted horizontal lines correspond to the Pt loadings for which the *in situ* GISAXS patterns are shown in Figure 4.14

fluence on the growth and deposition rate (number of Pt atoms deposited per cycle),^[1] motivating the study presented below.

Two experiments were performed, using either a pump mode or static mode precursor exposure. During pump mode the ALD chamber is actively pumped during the precursor exposure and the pressure (precursor and argon) in the chamber reaches 6×10^{-3} mbar. To perform an exposure in static mode, the valve between the ALD chamber and turbomolecular pump needs to be closed. This is followed by precursor injection, until the pressure (precursor and argon) in the chamber reaches 1 mbar. It should be noted that both these precursor doses yield saturated growth in the steady regime, as verified by saturation experiments on sputtered Pt thin films.^[27,28] The Pt surface density as a function of the number of ALD cycles for these experiments is displayed in Figure 4.13a. As seen in the zoom of the first 25 ALD cycles (Figure 4.13b) the static mode results in a higher deposition rate (number of Pt atoms per cycle) during the nucleation regime than the use of pump mode exposures. For larger Pt loadings, the XRF curves follow the same trend, so the deposition rate becomes similar. To investigate whether the precursor dosing mode only has an effect on the amount of Pt that is deposited per cycle during the formation of the initial nuclei or also during the coalescence and growth stage, a mixed experiment (green triangles) was performed during which the first 4 ALD cycles used static mode precursor exposures and the following cycles used pump mode precursor exposures. In this combination experiment the nu-

creation occurs faster due to the first 4 ALD cycles that use static exposures modes. However, after these initial cycles the amount of Pt atoms that is deposited per cycle is lower than for the purely static mode experiment. Thus the effect of the used precursor exposure on the Pt deposition per cycle extends further than these first 4 ALD cycles.

The difference in nucleation behaviour between static and pump mode might also induce a difference in morphology of the Pt particles on the surface. As the GISAXS patterns reflect the specific morphology on the surface, comparing them for the different exposure experiments will highlight the differences in morphology of the Pt particles. Comparing the dif-

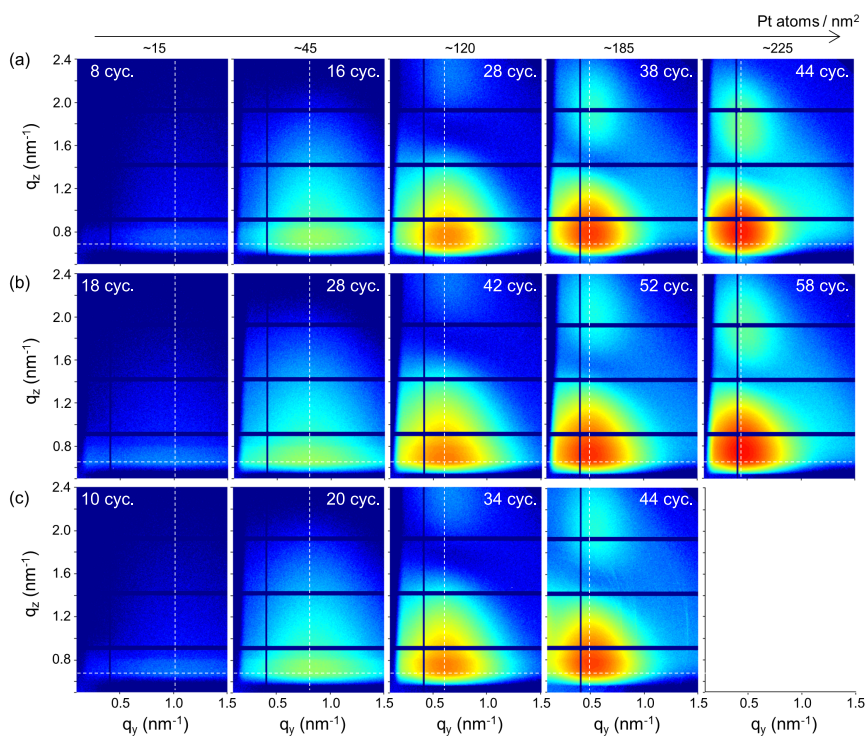


Figure 4.14: *In situ* measured 2D GISAXS patterns for Pt surface densities of ~ 15 , ~ 45 , ~ 120 , ~ 185 , ~ 225 Pt atoms per nm^2 during three experiments, using different Pt precursor dose modes: (a) static mode, (b) pump mode, and (c) static mode during the first 4 ALD cycles, followed by pump mode. The number of performed ALD cycles to obtain the GISAXS pattern is labelled in every pattern. Horizontal and vertical cuts of these patterns are compared in the Supporting Information.

ferent experiments as a function of ALD cycles leads to different GISAXS patterns for all experiments (see Supporting Information), which is to be expected since the same number of ALD cycles will not lead to similar Pt loadings for the different experiments. Therefore, it is more relevant to compare the GISAXS patterns of the three experiments for similar Pt surface densities, see Figure 4.14. Each row represents a different experiment and the columns show patterns that represent similar Pt surface densities on the surface for the three experiments. The vertical and horizontal line profiles of these GISAXS patterns can be found in the Supporting Information. From these GISAXS patterns and line profiles it is clear that a similar Pt loading leads to a similar scattering pattern, regardless of the used exposure mode. This is a clear indication that the surface morphology is not significantly influenced by the deposition rate and the exposure mode that is used during the process. This observation can be linked to the effect of surface mobility that plays an important role on the morphology of the Pt particles that are formed on the surface. As highlighted before, the GISAXS pattern sequence clearly shows a continuous shift of the main scattering peak towards lower q_y values during the Pt depositions. This shift can only be explained by a continuous diffusion-driven coalescence.^[26,29] Remarkably, it seems that during the deposition at a substrate temperature of 300 °C and for an O₂-based reactant the particle morphology is dominated by surface diffusion and completely determined by the loading. Further tuning of the morphology is possible by post-deposition annealing,^[30] which causes sintering of the particles, or using another co-reactant during the deposition.^[6]

4.3 DISCUSSION

4.3.1 Particle nucleation

Information about the behaviour of the Pt particles during the nucleation stage can be obtained by analysing the evolution of the main scattering peak during the initial ALD cycles. A theoretical monolayer of Pt is only obtained after 10 ALD cycles. During these initial ALD cycles the resulting GISAXS pattern does not exhibit secondary maxima and minima for the observable reciprocal q -space, which makes it very difficult to accurately obtain a value for the average particle height and radius. While the center-to-center distance estimated from the relation $D = 2\pi/q_{y,\max}$ overestimates the distance, though only slightly for low Pt loadings (see simulation for 12 ALD cycles in Figure 4.9), the evolution of the main scattering lobe can still provide information about the particles that are deposited. After the

main scattering peak appears it shifts to higher q_y values during the first 6 ALD cycles, indicating a decrease of the mean particle distance and an increase in the number of deposited nuclei on the surface. This is followed by a shift to lower q_y values after the 6th ALD cycle, indicating that there is a critical or saturated particle coverage that cannot be exceeded. The data gives an estimated saturated particle density of $N \sim 1.8 \times 10^{12}$ nuclei/cm² after 6 ALD cycles, which is followed by an increase in the center-to-center distance indicating a reduction in the number of scattering nuclei due to coalescence. After the saturated coverage is achieved small clusters will rather fuse with existing islands instead of forming new stable nuclei. At the end of the nucleation stage, at ca. 12 ALD cycles, the analysis yields Pt clusters of a size of ca. 3 nm with an aspect ratio of 1:1 and a center-to-center spacing of ca. 7 nm.

4.3.2 Particle growth and coalescence

After reaching the saturated particle coverage the main scattering peak keeps shifting towards lower q_y and higher q_z values with every GISAXS measurement and secondary maxima and minima start to appear, which can be used to estimate the particle radius and particle height. The appearance of secondary maxima and minima on the main scattering peak and their shift to lower q_z values correlates to an increase of the particle height with every ALD cycle. The shift in q_y of the main lobe indicates that the center-to-center distance increases with every ALD cycle, which is also obtained from the geometrical model (Figure 4.9d). The evolution of the horizontal secondary maxima and minima indicates that the radius of the particles increases with every ALD cycle and it seems that the particle width increases faster than the particle height. All this is consistent with the growth and coalescence of the Pt nanoparticles. Generally, one can distinguish two main coalescence mechanisms, a static and a dynamic coalescence mechanism.^[24,31–33] A static coalescence mechanism means that the formed nuclei grow until neighbouring islands start to touch, which leads to merging of the islands into a larger particle geometry. On the other hand, dynamic coalescence involves the diffusion and adsorption of adatom clusters or small particles, and can result in a laterally elongated particle geometry when the supply of material from the gas phase is smaller than the supply via migrating surface species and clusters.^[26] The *in situ* GISAXS data indicate that the Pt ALD process using O₂ as a co-reactant is governed by a dynamic growth and coalescence mechanism. The end of the nucleation stage – where the model yields ca. 3 nm wide Pt islands at a center-to-center spacing of ca. 7 nm, leaving a gap

of ca. 4 nm between neighboring particles – is immediately followed by a continuous increase in center-to-center distance and hence a decrease in particle areal density. This can only be explained by diffusion-driven particle coalescence. Hence, our *in situ* GISAXS and XRF method provides a powerful way to probe surface mobility during the nucleation and island growth stages of ALD processes and distinguish between static and dynamic particle growth and coalescence. Finally, as more Pt is added to the surface the q_z position of maximum scattering intensity shifts to larger values, towards the expected value of a Pt surface, due to the increase of the average density of the scattering volume. This shift in q_z exhibits a rapid increase around a surface density of 250 Pt atoms per nm^2 and based on the *ex situ* SEM micrographs (Figure 4.3b) it coincides with a change in the morphology of the Pt particles, transitioning from spherical shapes to more worm-like particle shapes. Once these worm-like features appear the Pt particles can no longer be approximated by spherical shapes and the geometrical model is no longer used as more complex particle shapes need to be assumed.

4.3.3 Influence of precursor dose

The standard precursor exposure mode in this work made use of a high-exposure static pulse, which reached a pressure of 1 mbar during the exposure. The influence of a low exposure mode, in pump mode with a pressure of 6×10^{-3} mbar, was also investigated to study its influence on the nucleation and island growth behaviour of the ALD process. The higher exposure leads to faster nucleation of the Pt nanoparticles, which is seen by the need of 20 ALD cycles to reach a theoretical monolayer of Pt with the low exposure mode compared to 10 ALD cycles for the high exposure mode. However, once the nucleation stage has ended both high and low exposure modes lead to a similar growth curve, indicating that the difference for both exposure modes is mainly related to the nucleation process. The combined exposure mode experiment shows that this nucleation stage extends beyond the first 4 ALD cycles, because the growth curve after the initial 4 cycles in this experiment starts to deviate from the purely high exposure mode experiment. Next to its effect on the nucleation speed, the use of different exposure modes might also influence the final morphology of the deposited Pt particles. However, matching the GISAXS patterns with similar Pt loadings from the different experiments shows that a similar Pt loading results in a similar scattering pattern and therefore a similar particle morphology on the surface. The surface mobility of the Pt atoms seems to drive the particles to a certain morphology, which depends on

the Pt surface density. Therefore, at a substrate temperature of 300 °C and using oxygen as the co-reactant an important parameter to tune the morphology of the Pt particles is the loading.

4.4 CONCLUSION

We investigated the nucleation and growth behaviour of Pt ALD on planar SiO₂ substrates by combining *in situ* XRF and GISAXS measurements. A simple geometrical model and fast analysis approach of the 2D GISAXS patterns was used and its validity was verified by simulating the model with the IsGISAXS software and comparing the results to the experimentally obtained scattering patterns. This showed that the geometrical model and initial input parameters obtained from the fast analysis provide a good description of the Pt nanoparticles during the ALD process, before they start coalescing in irregular shapes.

Analysis of the 2D GISAXS patterns during the nucleation stage indicates that in the initial stage new nuclei are formed until a critical coverage is reached after 6 ALD cycles, estimated to be $N \sim 1.8 \times 10^{12}$ nuclei/cm² which is in agreement with expected values from literature. Additional ALD cycles lead to an increase in the center-to-center distance of the particles, indicating a reduction in the number of scattering nuclei due to diffusion-driven coalescence. After this point the center-to-center distance keeps increasing, as does the particle radius and height. For a coverage above 250 Pt atoms per nm² the *ex situ* SEM micrographs reveal that the Pt particles coalesce into irregular shapes, which coincides with an abrupt increase of the q_z position of the scattering maximum in the 2D GISAXS pattern towards the expected q_z position of a pure Pt surface.

Finally, the effect of a lower precursor exposure during the ALD process is investigated. Using a lower precursor exposure results in a remarkably slower nucleation process. However, once the nucleation process is finished both precursor exposures lead to similar slopes in the growth curves. It was found that while using a larger precursor exposure leads to remarkably faster nucleation it does not influence the particle morphology, instead the morphology is determined by the Pt surface density that is reached when oxygen is used as the co-reactant. These results prove that combining *in situ* GISAXS and XRF measurements provides an excellent experimental strategy to obtain new fundamental insights into the role of deposition parameters on the morphology of Pt ALD depositions.

4.5 SUPPORTING INFORMATION

```

#####
GISAXS SIMULATIONS : INPUT PARAMETERS
#####

##### Framework and beam parameters #####
# Framework Diffuse, Multilayer, Number of index slices
  DWBA LMA 1 25
# Beam Wavelength : Lambda (nm), W1_distribution
  0.0972 none
# Beam Alpha_i : Alpha_i (deg), Ai_distribution
  0.516 none
# Beam 2Theta_i : 2Theta_i (deg), Ti_distribution
  0. none
# Substrate : n-delta_S, n-beta_S
  3.e-6 2.8e-8
# Particle : n-delta_I, n-beta_I
  2.e-5 2.5e-6

##### Grid parameters #####
# Ewald mode
  F
# Output q(nm-1) : Qx min-max, Qy min-max, Qz min-max, n(1), n(2), n(3)
  -2 0 0.1 2.5 0.6 3.5 1 80 100

##### Particle parameters #####
# Number of different particle types
  2
# Particle type, Probability
  spheroid 0.5
  spheroid 0.5
# Geometrical parameters : Flattening
  0.83
  1.66
# H_uncoupled
  T
  T
# Size of particle : Radius (nm), R_distribution, SigmaR/R, Rmin (nm), Rmax(nm), nR, xR
  3.8 3.8 log_normal 1.15 1 7 25 -2
  3.8 log_normal 1.15 1 7 25 -2
# Height aspect ratio : Height/R, H_distribution, SigmaH/H, Hmin/R, Hmax/R, nH, xH, rho_H
  1.66 1.66 gaussian 0.05 0.83 1.66 25 -2 0
  1.66 gaussian 0.05 0.83 1.66 25 -2 0

##### Lattice parameters #####
# Particle distribution : type
  1DDL
# Interference function : Peak position D (nm), w (nm), Statistics, Cut-off
  9.51 3.804 gau 100000

```

Figure 4.15: Input parameters used for the Isgisaxs simulations.

4.5.1 Geometrical model for fast analysis

In order to quickly analyse the 2D GISAXS patterns, a simplified geometrical model was developed to determine changes in the morphology of the Pt particles that are deposited during the ALD process. The model assumes that the Pt particles consist of full spheroids without a size distribution and are placed on a regular 2D lattice. The average particle height and radius are obtained from a fast analysis of line profiles taken from the *in situ* 2D GISAXS patterns, respectively, using the relations $H = 2\pi / \langle \Delta q_z \rangle$ and $R = 4.4/q_{y,\min}$. The most common approach to estimate the center-to-center distance is by using the approximation D

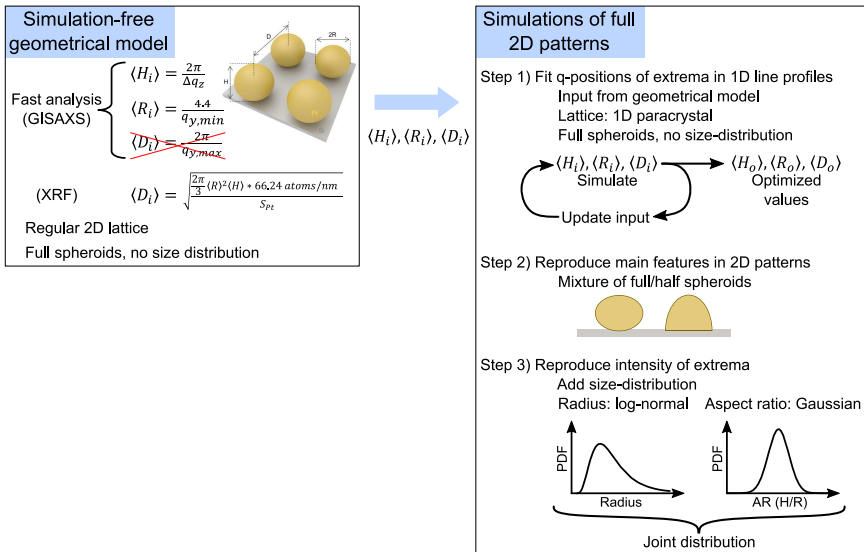


Figure 4.16: The three steps involved in the GISAXS analysis approach to obtain a full simulation of the measured GISAXS patterns, starting from a simplified geometrical model.

$= 2\pi/q_{y,max}$.^[29] However, using this approach leads to a significant underestimation of the Pt loading on the surface, as measured by *in situ* XRF. The reason is that the GISAXS intensity is governed by the interplay between the interference function and form factor of the particles that are present on the sample. While the center-to-center distance can be obtained from the interference function, in a GISAXS pattern the peak position originating from the interference function is shifted from its actual value by the influence of the particle form factor and as a result estimating the distance from the peak position of the first scattering lobe can lead to significant deviations from the actual center-to-center distance.^[29] Therefore, we propose another approach, in which the GISAXS measurements are combined with *in situ* XRF measurements to estimate the center-to-center distance by using Equation 4.1. The Pt loading, obtained from the additional XRF data, can be used as an input value for the model to obtain a value for the center-to-center distance. The validity of this approach is verified by using the input values to perform full-scale, detailed, simulations of selected patterns using the IsGISAXS software. A first optimization of the H, R, and D values does not cause significant change to the initial input values, illustrating that the fast analysis method combined with the XRF data can be used to obtain reliable values for the average particle

properties. Further optimization by including other particle shapes, and particle size distributions leads to an even better fit to the experimentally obtained 2D GISAXS patterns. However, typically fully simulating such patterns requires some computational time and it is generally not feasible to perform such calculations fast enough to provide accurate feedback during the ALD process. The important aspect is that the simulation-free geometrical model combined with the fast analysis approach provides sufficiently accurate information about the properties of the particles without resorting to time consuming full-scale 2D simulations of the experimentally obtained GISAXS patterns.

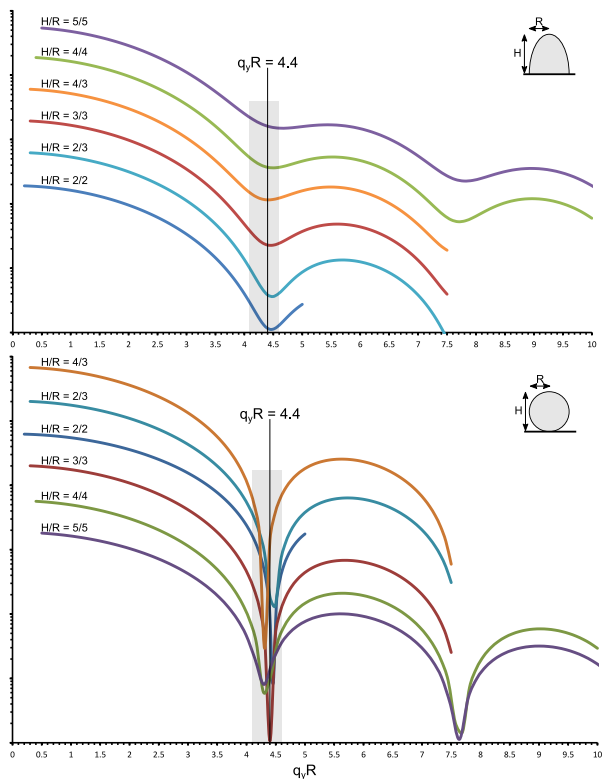


Figure 4.17: Form factor contribution for hemi-ellipsoids and full ellipsoids with H and R values between 2-5 nm. The scattering contribution is expressed as a function of $q_y R$. The position of the first minimum lies close to the $q_y R$ value of 4.4 for every line profile, which means that the particle radius can be estimated by determining the q_y position of the first minimum along the q_y direction in the GISAXS pattern and applying the formula: $R = 4.4/q_y$.

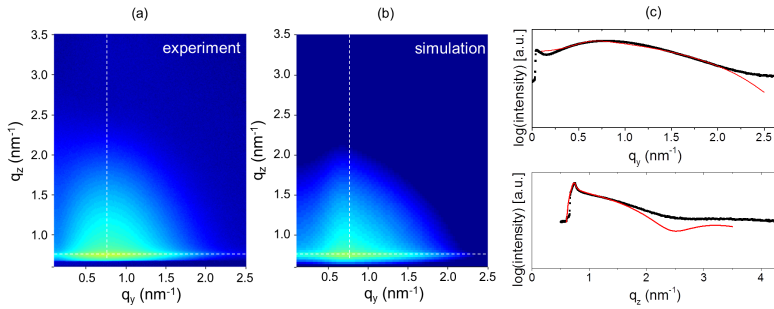


Figure 4.18: Experimental (a) and calculated (b) 2D GISAXS pattern obtained at 12 ALD cycles. (c) Experimental (black data points) and calculated (red curves) horizontal (top) and vertical (bottom) line profiles of the GISAXS patterns obtained at 12 ALD cycles.

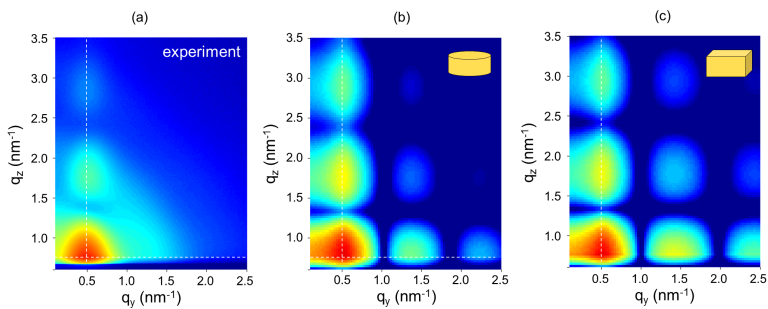


Figure 4.19: Experimental (a) and calculated (b,c) 2D GISAXS patterns obtained at 32 ALD cycles. The particle shapes assumed for the calculations are schematically represented in the top right corner of the images.

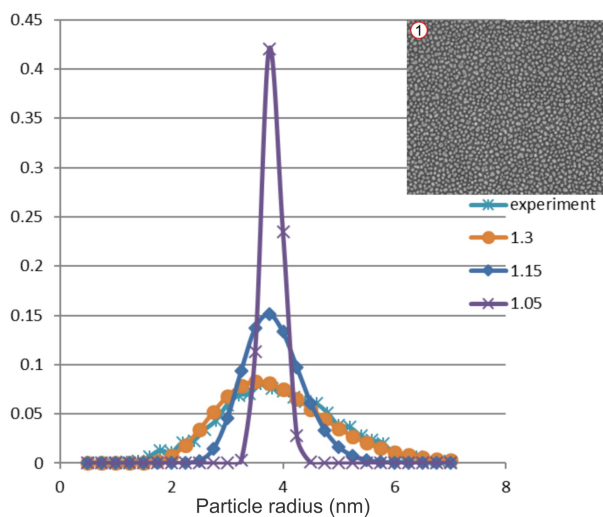


Figure 4.20: Particle size distributions, for the particle radius, obtained from the sample of a sample with 32 Pt ALD cycles and simulated particle size distribution with varying widths ($\sigma = 1.05/1.15/1.30$) of the log-normal size distribution. The best match between the size distribution from SEM and simulation is obtained for $\sigma = 1.30$.

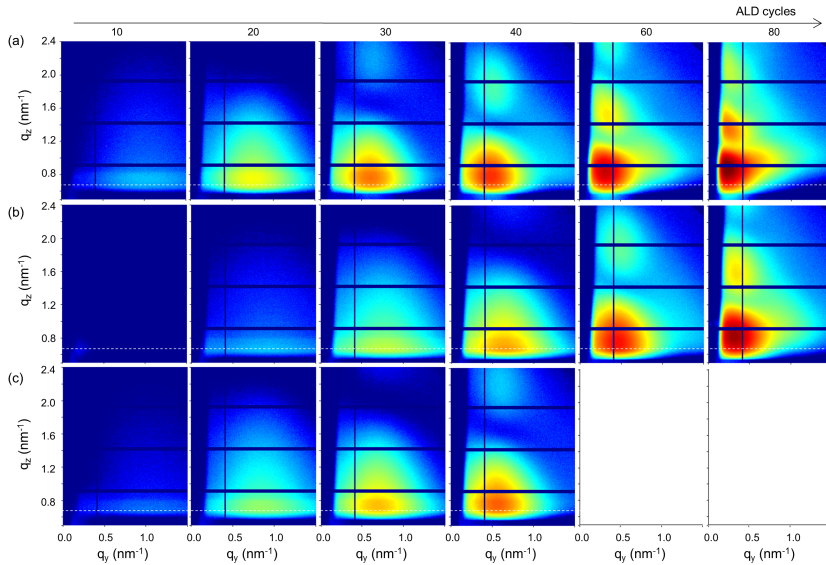


Figure 4.21: Experimental 2D GISAXS patterns obtained at 10, 20, 30, 40, 60 and 80 ALD cycles as measured in situ during three experiments using different Pt precursor dose modes: (a) static mode, (b) pump mode, and (c) static mode during 4 ALD cycles followed by pump mode.

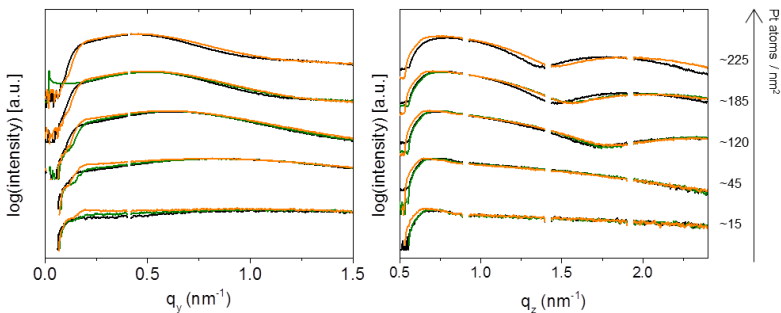


Figure 4.22: Experimental horizontal (left) and vertical (right) line profiles of the GISAXS patterns in Figure 14 obtained at surface densities of ~ 15 , ~ 45 , ~ 120 , ~ 185 and ~ 225 Pt atoms per nm^2 as measured in situ during three experiments using different Pt precursor dose modes: static mode (black curves), pump mode (green curves), and static mode during 4 ALD cycles followed by pump mode (orange).

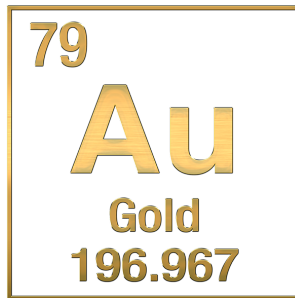
REFERENCES

- [1] Adriaan J M Mackus, Matthieu J Weber, Nick F W Thissen, Diana Garcia-Alonso, René H J Vervuurt, Simone Assali, Ageeth A Bol, Marcel A Verheijen, and Wilhelmus M M Kessels. "Atomic layer deposition of Pd and Pt nanoparticles for catalysis: on the mechanisms of nanoparticle formation". In: *Nanotechnology* 27:3 (Dec. 2015), p. 034001. DOI: 10.1088/0957-4484/27/3/034001.
- [2] Han-Bo-Ram Lee, Marja N. Mullings, Xirong Jiang, Bruce M. Clemens, and Stacey F. Bent. "Nucleation-Controlled Growth of Nanoparticles by Atomic Layer Deposition". In: *Chemistry of Materials* 24:21 (2012), pp. 4051–4059. DOI: 10.1021/cm3014978.
- [3] Junling Lu, Jeffrey W. Elam, and Peter C. Stair. "Synthesis and Stabilization of Supported Metal Catalysts by Atomic Layer Deposition". In: *Accounts of Chemical Research* 46:8 (2013), pp. 1806–1815. DOI: 10.1021/ar300229c.
- [4] Yu Lei et al. "Synthesis of Porous Carbon Supported Palladium Nanoparticle Catalysts by Atomic Layer Deposition: Application for Rechargeable Lithium–O₂ Battery". In: *Nano Letters* 13:9 (2013), pp. 4182–4189. DOI: 10.1021/nl401833p.
- [5] Matthias Filez, Hilde Poelman, Ranjith K. Ramachandran, Jolien Dendooven, Kilian Devloo-Casier, Emiliano Fonda, Christophe Detavernier, and Guy B. Marin. "In situ XAS and XRF study of nanoparticle nucleation during O₃-based Pt deposition". In: *Catalysis Today* 229 (June 2014), pp. 2–13. DOI: 10.1016/j.cattod.2014.01.011.
- [6] Jolien Dendooven et al. "Independent tuning of size and coverage of supported Pt nanoparticles using atomic layer deposition". In: *Nature Communications* 8:1 (2017), p. 1074. DOI: 10.1038/s41467-017-01140-z.
- [7] Steven T. Christensen, Jeffrey W. Elam, Byeongdu Lee, Zhenxing Feng, Michael J. Bedzyk, and Mark C. Hersam. "Nanoscale Structure and Morphology of Atomic Layer Deposition Platinum on SrTiO₃ (001)". In: *Chemistry of Materials* 21:3 (2009), pp. 516–521. DOI: 10.1021/cm8026863.
- [8] Adriaan J. M. Mackus, Marcel A. Verheijen, Noémi Leick, Ageeth A. Bol, and Wilhelmus M. M. Kessels. "Influence of Oxygen Exposure on the Nucleation of Platinum Atomic Layer Deposition: Consequences for Film Growth, Nanopatterning, and Nanoparticle Synthesis". In: *Chemistry of Materials* 25:9 (2013), pp. 1905–1911. DOI: 10.1021/cm400562u.
- [9] Fabio Grillo, Hao Van Bui, Jacob A. Moulijn, Michiel T. Kreutzer, and J. Ruud van Ommen. "Understanding and Controlling the Aggregative Growth of Platinum Nano particles in Atomic Layer Deposition: An Avenue to Size Selection". In: *The Journal of Physical Chemistry Letters* 8:5 (2017), pp. 975–983. DOI: 10.1021/acs.jpcllett.6b02978.
- [10] Fabio Grillo, Jacob A. Moulijn, Michiel T. Kreutzer, and J. Ruud van Ommen. "Nano particle sintering in atomic layer deposition of supported catalysts: Kinetic modeling of the size distribution". In: *Catalysis Today* 316 (2018), pp. 51–61. DOI: 10.1016/j.cattod.2018.02.020.
- [11] Nathaniel E. Richey, Camila de Paula, and Stacey F. Bent. "Understanding chemical and physical mechanisms in atomic layer deposition". In: *The Journal of Chemical Physics* 152:4 (2020), p. 040902. DOI: 10.1063/1.5133390.
- [12] D. N. Goldstein and S. M. George. "Enhancing the nucleation of palladium atomic layer deposition on Al₂O₃ using trimethylaluminum to prevent surface poisoning by reaction products". In: *Applied Physics Letters* 95:14 (2009), p. 143106. DOI: 10.1063/1.3238558.

- [13] D.N. Goldstein and S.M. George. "Surface poisoning in the nucleation and growth of palladium atomic layer deposition with Pd(hfac)₂ and formalin". In: *Thin Solid Films* 519.16 (2011), pp. 5339–5347. DOI: 10.1016/j.tsf.2011.02.037.
- [14] Adriaan J. M. Mackus, Noémi Leick, Layton Baker, and Wilhelmus M. M. Kessels. "Catalytic Combustion and Dehydrogenation Reactions during Atomic Layer Deposition of Platinum". en. In: *Chemistry of Materials* 24.10 (May 2012), pp. 1752–1761. DOI: 10.1021/cm203812v.
- [15] Camila de Paula, Nathaniel E. Richey, Li Zeng, and Stacey F. Bent. "Mechanistic Study of Nucleation Enhancement in Atomic Layer Deposition by Pretreatment with Small Organometallic Molecules". In: *Chemistry of Materials* 32.1 (2020), pp. 315–325. DOI: 10.1021/acs.chemmater.9b03826.
- [16] Worajit Setthapun et al. "Genesis and Evolution of Surface Species during Pt Atomic Layer Deposition on Oxide Supports Characterized by in Situ XAFS Analysis and Water-Gas Shift Reaction". In: *The Journal of Physical Chemistry C* 114.21 (2010), 9758–9771. DOI: 10.1021/jp911178m.
- [17] Xinhua Liang, Yun Zhou, Jianhua Li, and Alan W. Weimer. "Reaction mechanism studies for platinum nanoparticle growth by atomic layer deposition". In: *Journal of Nanoparticle Research* 13 (2011), pp. 3781–3788. DOI: 10.1007/s11051-011-0299-x.
- [18] Titta Aaltonen, Mikko Ritala, Timo Sajavaara, Juhani Keinonen, and Markku Leskelä. "Atomic Layer Deposition of Platinum Thin Films". en. In: *Chemistry of Materials* 15.9 (May 2003), pp. 1924–1928. DOI: 10.1021/cm021333t.
- [19] Jolien Dendooven, Eduardo Solano, Matthias M. Minjauw, Kevin Van de Kerckhove, Alessandro Coati, Emiliano Fonda, Giuseppe Portale, Yves Garreau, and Christophe Detavernier. "Mobile setup for synchrotron based in situ characterization during thermal and plasma-enhanced atomic layer deposition". In: *Review of Scientific Instruments* 87.11 (2016), p. 113905. DOI: 10.1063/1.4967711.
- [20] Rémi Lazzari. "IsGISAXS: a program for grazing-incidence small-angle X-ray scattering analysis of supported islands". In: *Journal of Applied Crystallography* 35.4 (Aug. 2002), pp. 406–421. DOI: 10.1107/S0021889802006088.
- [21] Rémi Lazzari, Frédéric Leroy, and Gilles Renaud. "Grazing-incidence small-angle x-ray scattering from dense packing of islands on surfaces: Development of distorted wave Born approximation and correlation between particle sizes and spacing". In: *Phys. Rev. B* 76 (12 Sept. 2007), p. 125411. DOI: 10.1103/PhysRevB.76.125411.
- [22] Riikka L. Puurunen and Wilfried Vandervorst. "Island growth as a growth mode in atomic layer deposition: A phenomenological model". In: *Journal of Applied Physics* 96.12 (2004), pp. 7686–7695. DOI: 10.1063/1.1810193.
- [23] R.L. Puurunen. "Random Deposition as a Growth Mode in Atomic Layer Deposition". In: *Chemical Vapor Deposition* 10.3 (2004), pp. 159–170. DOI: 10.1002/cvde.200306283.
- [24] G. Renaud, R. Lazzari, and F. Leroy. "Probing surface and interface morphology with Grazing Incidence Small Angle X-Ray Scattering". In: *Surface Science Reports* 64.8 (2009), pp. 255–380. DOI: 10.1016/j.surfrep.2009.07.002.
- [25] Charles T. Campbell. "Ultrathin metal films and particles on oxide surfaces: structural, electronic and chemisorptive properties". In: *Surface Science Reports* 27.1 (1997), pp. 1–111. DOI: 10.1016/S0167-5729(96)00011-8.
- [26] Matthias Schwartzkopf et al. "From Atoms to Layers: in situ Gold Cluster Growth Kinetics during Sputter Deposition". In: *Nanoscale* 5 (11 2013), pp. 5053–5062. DOI: 10.1039/C3NR34216F.

- [27] D. Longrie, K. Devloo-Casier, D. Deduytsche, S. Van den Berghe, K. Driesen, and C. Detavernier. "Plasma-Enhanced ALD of Platinum with O₂, N₂ and NH₃ Plasmas". In: *ECS Journal of Solid State Science and Technology* 1.6 (2012), Q123–Q129. DOI: 10.1149/1.009206jss.
- [28] Jolien Dendooven, Ranjith K. Ramachandran, Kilian Devloo-Casier, Geert Rampelberg, Matthias Filez, Hilde Poelman, Guy B. Marin, Emiliano Fonda, and Christophe Detavernier. "Low-Temperature Atomic Layer Deposition of Platinum Using (Methylcyclopentadienyl)trimethylplatinum and Ozone". In: *The Journal of Physical Chemistry C* 117.40 (2013), pp. 20557–20561. DOI: 10.1021/jp403455a.
- [29] Gilles Renaud et al. "Real-Time Monitoring of Growing Nanoparticles". In: *Science* 300.5624 (2003), pp. 1416–1419. DOI: 10.1126/science.1082146.
- [30] Eduardo Solano, Jolien Dendooven, Ranjith K. Ramachandran, Kevin Van de Kerckhove, Thomas Dobbelaere, Daniel Hermida-Merino, and Christophe Detavernier. "Key role of surface oxidation and reduction processes in the coarsening of Pt nanoparticles". In: *Nanoscale* 9 (35 2017), pp. 13159–13170. DOI: 10.1039/C7NR04278G.
- [31] Martin Zinke-Allmang, Leonard C. Feldman, and Marcia H. Grabow. "Clustering on surfaces". In: *Surface Science Reports* 16.8 (1992), pp. 377–463. DOI: 10.1016/0167-5729(92)90006-W.
- [32] Pierre Deltour, Jean-Louis Barrat, and Pablo Jensen. "Fast Diffusion of a Lennard-Jones Cluster on a Crystalline Surface". In: *Phys. Rev. Lett.* 78 (24 June 1997), pp. 4597–4600. DOI: 10.1103/PhysRevLett.78.4597.
- [33] M. Zinke-Allmang. "Phase separation on solid surfaces: nucleation, coarsening and coalescence kinetics". In: *Thin Solid Films* 346.1 (1999), pp. 1–68. DOI: 10.1016/S0040-6090(98)01479-5.

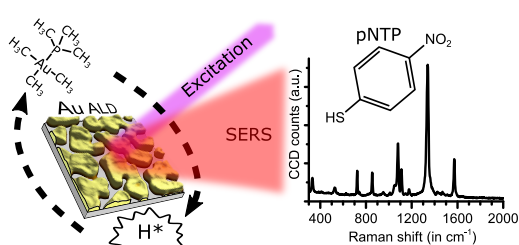
Part III



Aurum : shining dawn

"Yet dawn is ever the hope of men."
- J.R.R. Tolkien, *The Two Towers*

Gold as a bulk material has found a widespread use in jewellery, coinage, and decorative pieces due to its unreactive nature. However, nanoparticulate gold has very interesting and useful catalytic and optical properties. Certain applications will require the deposition of gold layers on complex 3D substrates, making atomic layer deposition (ALD) an extremely useful method to deposit gold layers on such demanding substrates. Therefore, over the past decades, there has been a large drive to develop ALD processes to deposit metallic gold layers. However, metallic gold is extremely challenging to deposit by ALD: only three gold ALD processes have been reported to this date,^[1-3] although many chemical vapour deposition (CVD) precursors exist to deposit gold.^[4-8] This chapter will cover the third reported Au ALD process. It is a plasma-enhanced atomic layer deposition (PE-ALD) process using $\text{Me}_3\text{Au}(\text{PMe}_3)$ in combination with H_2 plasma. Gold films deposited with this process have a high purity, low resistivity, a nanoparticulate morphology, and are polycrystalline in nature. The process enables deposition of ALD gold at a low temperature of 50°C , making it interesting for applications on temperature sensitive substrates, such as flexible electronics.^[9-11] The deposited films have an intrinsic nanoparticle structure, interesting for heterogeneous catalysis^[12-14] and plasmonic^[15,16] applications.



This chapter was published as a research article in the journal: ACS Applied Materials and Interfaces, titled "Plasma-enhanced atomic layer deposition of nanostructured gold near room temperature".^[2] The image on this page is the original TOC-graphic, submitted with the published article. Author contributions: M.V.D. designed the experiments, performed the ALD depositions and thin film characterizations, analyzed and interpreted the results; M.B.E.G. produced the precursors; A.R. performed free space Raman measurements and assisted in analyzing the data; M.M.M. performed XPS measurements and assisted in analyzing the data; E.S., J.F., R.K.R. and J.D. assisted in performing GISAXS measurements and J.D. assisted in analyzing the data; S.C. and R.B. assisted in interpreting the Raman results; S.T.B., C.D. and J.D. assisted in designing the experiments and interpreting the results; M.V.D. prepared the manuscript; All the authors contributed to revising the manuscript.

5.1 EXPERIMENTAL SECTION

All atomic layer depositions were carried out in a home-built pump type ALD reactor with a base pressure of 2×10^{-6} mbar.^[17] Computer-controlled pneumatic valves and manually adjustable needle valves were used to control the dose of precursor vapour and reactant gas. The $\text{Me}_3\text{Au}(\text{PMe}_3)$ precursor ($\geq 95\%$ purity) was synthesised using the method described in the Supporting Information of the paper by Griffiths, Pallister, Mandia, and Barry.^[1] The precursor was kept in a glass container which was heated to 50°C during deposition processes, and the delivery line was heated to 55°C . Argon was used as the carrier gas during all deposition processes. The flow of the carrier gas was adjusted to reach 6×10^{-3} mbar in the chamber when pulsing. The precursor exposure during the ALD processes were carried out by injecting the $\text{Me}_3\text{Au}(\text{PMe}_3)$ vapour after closing the gate valve between the turbomolecular pump and the reactor chamber. By varying the injection time, the pressure during the pulse varied between 6×10^{-3} mbar and 5 mbar. After injection the precursor vapour was kept in the ALD chamber for an additional 5 seconds before evacuating the chamber. H_2 plasma (20% H_2 in argon) was used as the reactant for all depositions. Previously, some of the authors reported that using H_2 gas or H_2 plasma as the reactant in combination with the $\text{Me}_3\text{Au}(\text{PMe}_3)$ precursor does not lead to gold deposition. However, they used a low concentration of H_2 gas in comparison to the 20% that was used in this work, possibly explaining this different result. The H_2 gas was introduced through the plasma column mounted on top of the chamber and the flow of H_2 gas was limited by a needle valve to obtain a chamber pressure of 6×10^{-3} mbar during all depositions. A 13.56 MHz RF generator (Advanced Energy, Model CESAR 136) and a matching network were used to generate an inductively coupled plasma in the plasma column. For all experiments a plasma power of 200 W was used and the impedance matching parameters were adjusted to minimise the reflected power. A H_2 plasma exposure of 10 seconds was used before each deposition. The used substrates were pieces of p-type silicon (100) with native or thermal silicon oxide, or 10 nm sputtered gold films on p-type silicon (100). The samples were mounted directly on a heated copper block. The temperature of the copper block was adjusted with a PID controller. The chamber walls were heated to 100°C for all experiments, except for the experiments to determine the temperature window, for those experiments the chamber walls were heated to 50°C . This was necessary to allow the copper block to be heated at temperatures below 80°C since it was not possible to use active cooling of the copper block.

Several *ex situ* measurement techniques were used to determine the physical properties of the deposited Au films. X-ray diffraction (XRD) patterns were acquired to determine the crystallinity of the deposited films. XRD measurements were done on a diffractometer (Bruker D8) equipped with a linear detector (Vantec) and a copper X-ray source (Cu K α radiation). Thickness determination *via* X-ray reflectivity (XRR) measurements was done on a diffractometer (Bruker D8) equipped with a copper X-ray source (Cu K α radiation) and a scintillator point detector. However, because the gold ALD films were generally too rough for accurate thickness determination with XRR, X-ray fluorescence (XRF) measurements were used to determine an equivalent film thickness based on a calibration line of sputtered gold films. The obtained standard deviation of the data points from the obtained calibration line was multiplied by three and used as an estimated error for each XRF measurement. The XRF measurements were performed using a Mo X-ray source and an XFlash 5010 silicon drift detector, respectively, placed at an angle of 45° and 52° with the sample surface. An integration time of 200 s was used to acquire the fluorescence spectra. X-ray photoelectron spectroscopy (XPS) was used to determine the chemical composition and binding energy of the deposited films. The XPS measurements were carried out on a Thermo Scientific Theta Probe XPS instrument. The X-rays were generated using a monochromatic Al source (Al K α). To etch the surface of the deposited films an Ar⁺ ion gun was used at an acceleration voltage of 3 keV and a current of 2 μ A. An FEI Quanta 200F instrument was used to perform scanning electron microscopy (SEM) using secondary electrons and energy-dispersive X-ray spectroscopy (EDX) on the deposited films. Four point probe measurements were performed to determine the resistivity of the deposited gold films. Atomic force microscopy (AFM) measurements were performed on a Bruker Dimension Edge system to determine the surface roughness of the films. The AFM was operated in tapping mode in air.

To study the morphology of the gold nanostructures, *ex situ* Grazing-Incidence Small-Angle X-ray Scattering (GISAXS) measurements were performed at the DUBBLE BM26B beamline of the European Synchrotron Radiation Facility.^[18,19] The used energy for the X-ray beam was 12 keV, with an incidence angle of 0.5°. The GISAXS patterns were recorded with a Dectris Pilatus3S 1M detector, which consisted of a pixel array of 1043 \times 981 (V \times H) with a pixel size of 0,172 \times 0,172 μ m² and a sample-detector distance of 4.4 m was used. The samples were measured in a vacuum chamber, that had primary slits and a beamstop inside the chamber to reduce scattering. For each GISAXS scattering pattern an acquisition time of 60 s was used. Standard corrections for primary beam intensity fluctuations,

solid angle, polarization, and detector efficiency were applied to the collected images. The IsGISAXS software was used to perform the data analysis of the GISAXS scattering patterns, a distorted-wave Born approximation was used and graded interfaces were assumed for the perturbed state caused by the gold particles. A spheroid particle shape was assumed with a Gaussian distribution for the particle size. The particle arrangement on the surface was modelled using a 1D paracrystal model, *i.e.* a 1D regular lattice with loss of long-range order. Initial input parameters for the simulation were obtained from the 2D scattering data, by taking horizontal (q_y) and vertical (q_z) line profiles at the position of the main scattering peak. The maximum in the horizontal line profile gave information about the mean center-to-center particle distance, while information about the particle height was obtained from the minima and maxima observed in the vertical line profile. The input parameters for the simulation were refined until a decent agreement between experiment and simulation was obtained.

In order to determine the surface enhancement of the deposited gold films free space surface enhanced Raman spectroscopy (SERS) was performed on several samples. A monolayer of 4-nitrothiophenol (pNTP, obtained from Sigma-Aldrich) was used as an analyte that selectively binds to the gold surface using a Au-thiol bond. The SERS samples were thoroughly rinsed with acetone, isopropanol, and deionised water and dried using a N_2 gun. This was followed by a short O_2 plasma exposure, using a PVA-TEPLA GIGAbatch, to remove remaining contaminants and enhance the binding. The SERS samples were then immersed in a 1 mM pNTP solution for three hours. Finally the samples were extensively rinsed using ethanol and water to remove unbound pNTP molecules. The number of adsorbed pNTP molecules on the different samples was estimated based on Au surface area calculations and the reported pNTP density value on Au (see Supplementary Information). A commercial confocal Raman microscope (WITEC Alpha300R+) was used to perform the Raman measurements. A 785 nm excitation diode laser (Toptica XTRA II) was used as the free space pump source. The laser was operated at a low pump power of 0.2 mW to avoid burning or photo-reduction of the pNTP molecules. High NA objectives (100x/0.9 EC Epiplan NEOFLUAR; $\infty/0$) were used to excite the sample and collect the Raman signal. A 100 μm multimode fiber was used as a pinhole connected to a spectrometer equipped with a 600-lpm grating and a CCD camera cooled to -70°C (ANDOR iDus 401 BR-DD). All Raman spectra were acquired after optimising the 1339 cm^{-1} peak using a 1 second integration time.

5.2 RESULTS AND DISCUSSION

5.2.1 ALD properties

The reaction of the $\text{Me}_3\text{Au}(\text{PMe}_3)$ precursor with H_2 plasma was previously reported to not occur.^[1] By using a higher vacuum and higher H_2 concentration, this surface reaction was found to proceed in a self-limiting manner. One of the properties of an ALD process is that both reactions show self-limiting behaviour. The saturation behaviour of $\text{Me}_3\text{Au}(\text{PMe}_3)$ and H_2 plasma exposures was investigated by determining the equivalent growth per cycle ($^{\text{eq}}\text{GPC}$, obtained by dividing the equivalent thickness by the number of ALD cycles) on gold seed layers as a function of the respective exposure time (Figure 5.1). The injection time for the precursor was varied between 1 and 20 seconds, while the reactant exposure was kept fixed at 20 seconds. Likewise, the exposure time of the reactant was varied between 1 and 20 seconds, while the precursor injection time was kept fixed at 20 seconds. The depositions were performed at a substrate temperature of $100\text{ }^\circ\text{C}$ on silicon substrates coated with a thin sputtered

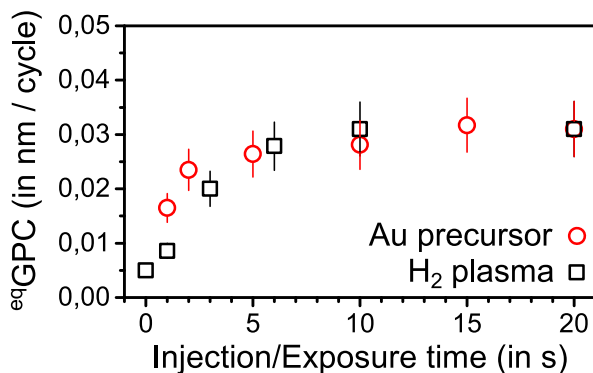


Figure 5.1: Equivalent growth per cycle as a function of the injection time and exposure time for the $\text{Me}_3\text{Au}(\text{PMe}_3)$ precursor (\circ) and H_2 plasma (\square), respectively, in the steady growth regime. Depositions were performed on a gold seed layer at a substrate temperature of $100\text{ }^\circ\text{C}$. 100 ALD cycles were performed during each deposition to determine the $^{\text{eq}}\text{GPC}$ value. The exposure time of the reactant was kept at 20 seconds during the saturation experiments of the precursor. The injection time of the precursor was 20 seconds during the saturation experiments of the reactant. The precursor exposure consisted of an injection time, that was varied, followed by a fixed dwell time of 5 seconds.

gold seed layer (10 nm). The gate valve between the reaction chamber and the turbomolecular pump was closed during the precursor exposures. As mentioned in the experimental section, the exposure time consisted of a variable injection time, followed by a fixed dwell time of 5 seconds. As a result of the varying injection time, the pressure during the precursor exposure varied between 6×10^{-3} mbar and 5 mbar. As can be seen in Figure 5.1, saturation was achieved for $\text{Me}_3\text{Au}(\text{PMe}_3)$ after an injection time of 10 s and after an exposure time of 10 s for the H_2 plasma, yielding an $^{\text{eq}}\text{GPC}$ of 0.030 ± 0.002 nm per cycle in the steady growth regime.

Pulsing the precursor on a gold substrate without any co-reactant resulted in an $^{\text{eq}}\text{GPC}$ of 0.005 nm per cycle, implying a minor CVD component for this ALD process. The monolayer of adsorbed precursor was most likely not perfectly stable and underwent a very slow decomposition to $\text{Au}(0)$, forming additional adsorption sites for new precursor molecules. Importantly, there was no deposition when exposing a silicon substrate to only the precursor.

Test depositions under thermal conditions were performed using high pressure H_2 gas (20% H_2 in argon at 25 mbar) instead of H_2 plasma as the

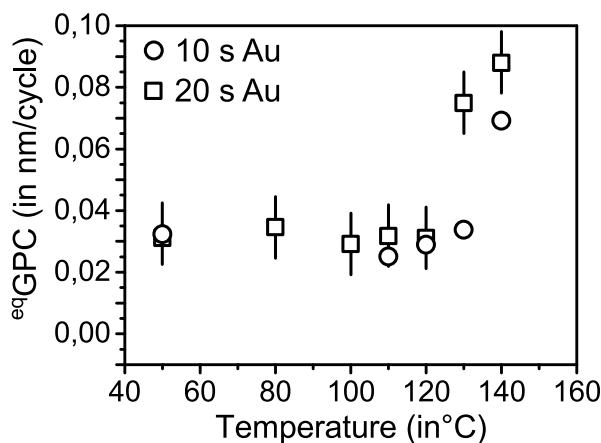


Figure 5.2: The equivalent GPC as a function of the substrate temperature for two $\text{Me}_3\text{Au}(\text{PMe}_3)$ precursor injection times, 10 seconds and 20 seconds with a dwell time of 5 seconds for both. An exposure time of 15 s was used for the H_2 plasma. Depositions were performed on a gold seed layer. 100 ALD cycles were performed during each deposition to determine the $^{\text{eq}}\text{GPC}$ value. The error bars for the 10 s Au injection times were omitted for clarity. Decomposition of the precursor occurs above 120 °C.

reactant. An injection time of 15 seconds and a dwell time of 5 seconds were used for the $\text{Me}_3\text{Au}(\text{PMe}_3)$ exposure (*i.e.* saturating conditions for the PE-ALD process). On silicon substrates, these thermal test depositions did not yield gold deposition in our ALD reactor. However, on gold seed layers some deposition was achieved with an $^{\text{eq}}\text{GPC}$ equal to 0.005 nm per cycle, likely originating from the above-mentioned CVD component rather than a chemical reaction with the H_2 gas.

The temperature dependence of the $^{\text{eq}}\text{GPC}$ for the PE-ALD process with H_2 plasma is shown in Figure 5.2. The $^{\text{eq}}\text{GPC}$ was determined for two precursor injection times, 10 seconds and 20 seconds, combined with a 15 s H_2 plasma exposure. Decomposition of the precursor occurred for substrate temperatures above 120 °C, as can be concluded from the increase in $^{\text{eq}}\text{GPC}$ at 130 °C and 140 °C. While the decomposition remained limited for the lower injection time of 10 seconds, especially at 130 °C, it was severely increased for the 20 s injection time. On the other side of the temperature curve, the growth rate remained constant when lowering the substrate temperature. Moreover, over the whole 50 °C to 120 °C temperature range, the $^{\text{eq}}\text{GPC}$ achieved with a 10 s precursor injection time was equal to the $^{\text{eq}}\text{GPC}$ achieved for the 20 s precursor injection time. This confirms saturation behaviour in this temperature range, implying that there is an ALD temperature window from 50 °C to 120 °C. The lower temperature limit of 50 °C is equal to the temperature of the precursor bottle. Lowering

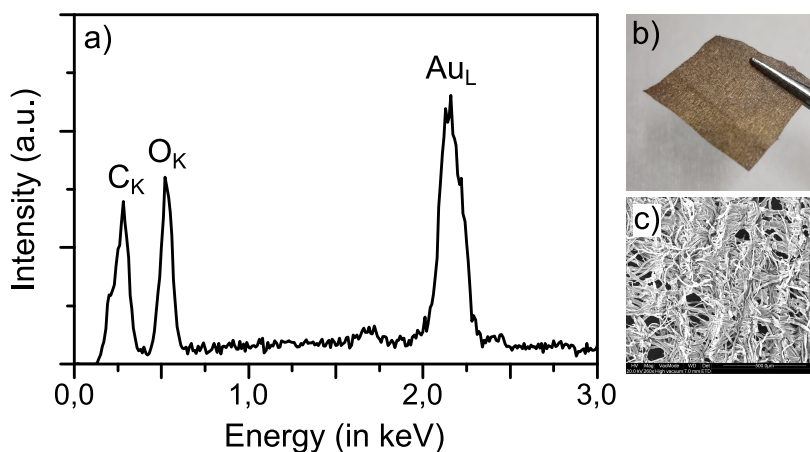


Figure 5.3: a) EDX spectrum taken of a gold coated piece of tissue paper. The deposition was performed at a substrate temperature of 50 °C. b) A picture of the measured piece of paper, and c) a SEM image of the sample (the image has a width and height of 1.1 μm).

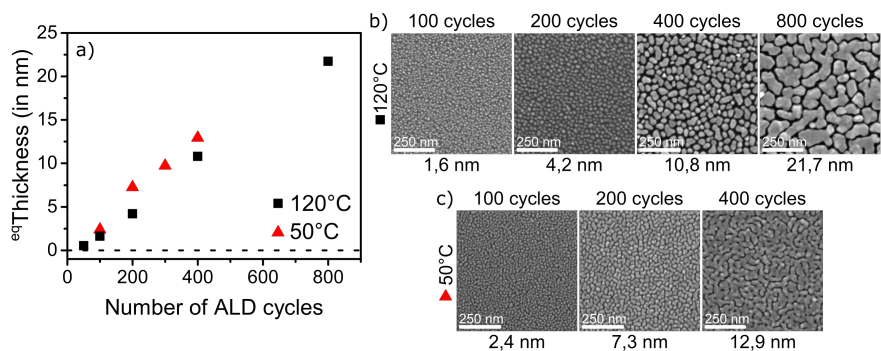


Figure 5.4: a) Equivalent thickness of gold as a function of the number of ALD cycles performed on a silicon substrate (native oxide) for a substrate temperature of 50 °C and 120 °C. Saturating conditions were used for all depositions (*i.e.* a 15 s exposure time for both $\text{Me}_3\text{Au}(\text{PMe}_3)$ and H_2 plasma). b) Top SEM micrographs for PE-ALD films deposited at 120 °C. c) Top SEM micrographs for PE-ALD films deposited at 50 °C.

the substrate temperature below the precursor bottle temperature may induce condensation, leading to uncontrolled deposition conditions. On the other hand, decreasing the precursor bottle temperature below 50 °C gave unreliable results in our setup, likely related to limited volatility of the precursor at those temperatures. The 50 °C lower limit of the temperature window makes it possible to deposit gold on temperature sensitive materials, such as textiles and paper; significantly extending the potential of Au ALD compared to the previously reported processes.^[1,2] This was verified by depositing a PE-ALD gold film on a piece of tissue paper, at a substrate temperature of 50 °C. EDX measurements were performed on the substrate and showed the presence of gold, as can be seen in Figure 5.3. This shows that the reported process can be used to deposit gold films on temperature sensitive substrates, which have potential applications for flexible and wearable electronic devices.^[9,10]

The growth of the process on silicon substrates, with native oxide and thermal oxide, was investigated up to an equivalent thickness of 65.6 nm. The PE-ALD depositions were carried out at a substrate temperature of 120 °C, using saturating exposure times. The thickness of the depositions as a function of the number of ALD cycles and the ^{eq}GPC as a function of the number of ALD cycles are shown in the Supporting Information (respectively, Figure 5.11a and Figure 5.11b). This latter plot reveals a constant ^{eq}GPC when 400 cycles or more are applied. A similar value of 0.029 ± 0.003 nm per cycle was obtained on both the native and the ther-

mal SiO₂ surface, which is in agreement with the ^{eq}GPC on gold seed layers. The deviation of the ^{eq}GPC below 400 cycles is indicative of a nucleation controlled growth mechanism on a silicon oxide surface. This is not that surprising since metal ALD processes are often characterized by the deposition of particles on oxide surfaces.^[1,19,20] These particles coalesce and ultimately form a closed layer when the amount of deposited metal is sufficient. The equivalent thickness as a function of the number of ALD cycles is displayed up to 800 cycles in Figure 5.4a for depositions carried out at 120 °C and 50 °C. *Ex situ* SEM images of Au films deposited at 120 °C confirmed that this H₂ plasma process is governed by an island growth mode (Figure 5.4b). The *ex situ* SEM images of films deposited at 50 °C also revealed that island growth occurs at this temperature. At both substrate temperatures the mean particle size clearly increased with the equivalent Au thickness and the general shape of the particles changed as well. Initially, the particle shapes were mainly circular but with increasing film thickness the particle shape became more irregular, attributed to the coalescence of particles with progressing deposition. When the thickness of the film was further increased worm-like structures were observed for both cases which finally resulted in percolating films when sufficient material was deposited. Here the threshold to form a percolating path on the surface and obtain measurable in-plane electronic conductivity was found to be different for both deposition temperatures. At 50 °C percolating films were obtained at a thickness of 12.9 nm (a resistivity value of 16.5±0.8 μΩ cm could be measured), while at 120 °C even at a thickness of 21.7 nm a percolating path was not yet obtained. As will be detailed in the following section, even thicker layers were necessary to form a percolating path on the surface. This shows that the temperature can have an impact on the surface mechanisms dictating the nucleation behaviour for this process.

A final characteristic that was evaluated for the developed Au ALD process was the conformality of deposition on arrays of silicon micropillars. The silicon micropillars had a length of 50 μm, a width of 2 μm, and a center-to-center spacing of 4 μm, yielding an equivalent aspect ratio (EAR) of 10. The EAR is derived from Monte Carlo simulations and is defined as the aspect ratio of a hypothetical cylindrical hole that would require the same reactant exposure to achieve a conformal coating.^[21] A 15 second exposure time was used for Me₃Au(PMe₃) and 10 seconds for the H₂ plasma exposures during the depositions, performed at a substrate temperature of 120 °C. Using SEM and EDX measurements, the surface morphology and Au loading were investigated along the length of the pillars (Figure 5.5). The SEM images (Figure 5.5a) clearly show that Au was deposited on the

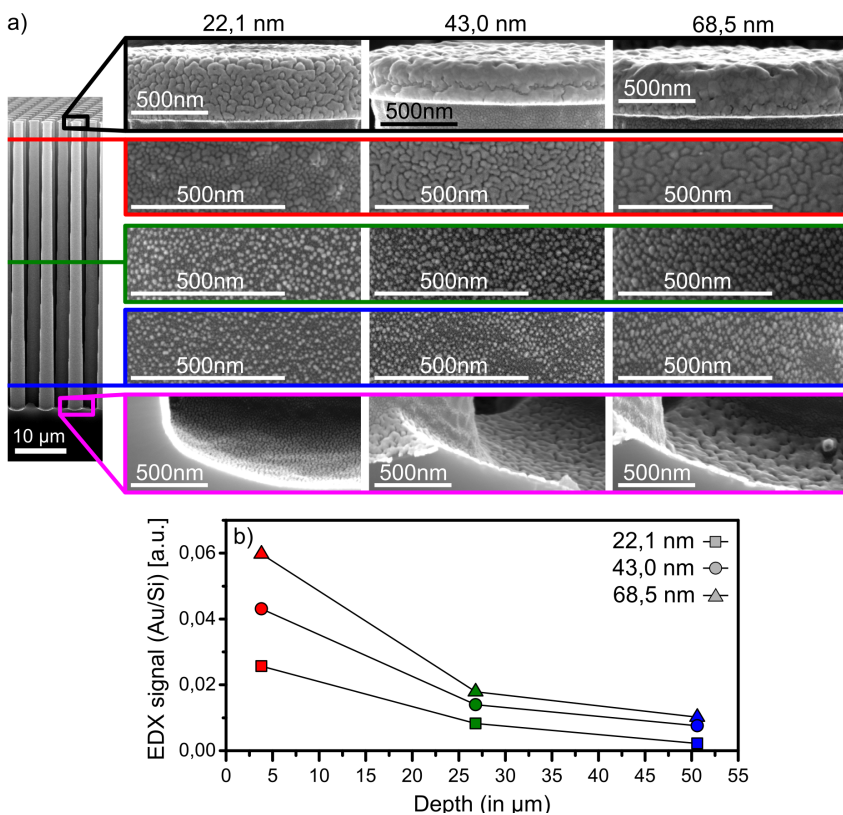


Figure 5.5: SEM images and EDX signal of gold films, deposited on silicon pillar structures (EAR = 10) at a substrate temperature of 120 °C. a) SEM images for three film thicknesses (as measured on a planar silicon surface): 22.1 nm (800 cycles), 43.0 nm (1600 cycles), 68.5 nm (2400 cycles). b) EDX signal ratio of the Au peak to the Si peak as a function of distance from the top of the pillar structure.

entire substrate, also between the pillars on the bottom surface of the structure. Increasing the thickness of the deposited film resulted in larger particles and more irregular shapes, as expected from the SEM images on planar substrates in Figure 5.4b-c. The morphology of the gold layer changed from being worm-like at the top of the pillar to smaller rounded particles near the bottom, suggesting that the amount of deposited gold on the side walls decreased when going from the top of the pillar to the bottom. To evaluate the Au loading, EDX line scans were taken at the height at which the SEM images were taken and the ratio of the Au signal to the Si signal is displayed in Figure 5.5b as a function of depth in the structure. The data confirms that less gold was present on the side walls deeper in the structure, in agreement with the SEM images. The most likely reason for the non-ideal conformality is a too low H_2 plasma exposure. Plasma radicals are known to recombine due to surface collisions, thus limiting the conformality,^[22,23] in particular during metal ALD due to the larger recombination rates on metallic surfaces.^[24] Note that the SEM images visualising the bottom of the structure, between the pillars, revealed worm-like features. This points to a higher Au loading on the area between the pillars than on the bottom region of the pillars' side walls. This can be explained by the fact that the bottom of the structure was in direct line-of-sight to the plasma, meaning that those surfaces received a larger direct flux of H radicals than the adjacent walls. Though this 'bottom effect' is often predicted by simulation models,^[21] the results presented here provide one of the few experimental examples. Overall, these initial depositions show that it is possible to deposit gold films on 3D structures.

5.2.2 *Physical properties and film composition*

XRD measurements were performed on the deposited Au films to confirm their metallic nature. The obtained XRD patterns for films deposited at 120 °C and 50 °C are respectively displayed in Figure 5.6a and Figure 5.6b. The patterns showed that the films were polycrystalline, due to the presence of diffraction peaks from the Au(111) and Au(200) planes of the cubic gold crystals. These diffraction patterns hint that the as-deposited Au films are polycrystalline for all deposited thicknesses and for the full range of the ALD temperature window.

The composition of the deposited gold films was investigated using XPS measurements. Figure 5.7 shows the Au 4f, C 1s, O 1s, and P 2p spectra. The sample was a silicon substrate on which 800 ALD cycles were performed at 120 °C, yielding an equivalent gold thickness of 21.7 nm. This deposition temperature, at the higher limit of the temperature window,

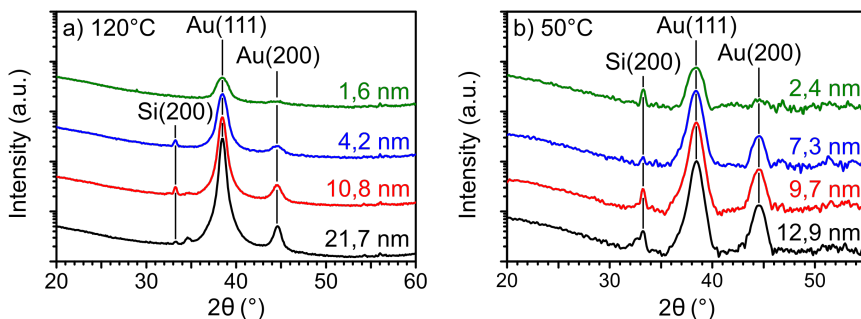


Figure 5.6: XRD patterns for deposited gold films with an equivalent thickness between 1.6 and 21.7 nm. For all thicknesses the Au(111) and Au(200) peaks are visible at 38.5° and 44.6° , respectively. The patterns were given an offset for clarity. a) Films deposited at 120°C , b) films deposited at 50°C .

was purposefully selected for comparison with the previously reported gold ALD processes.^[1,2] XPS spectra were measured on the as-deposited film (contaminated by air exposure) and after removing the contaminating top layer by Ar sputtering in the XPS chamber. The surface composition for both cases is given in Table 5.1. This shows that the grown films are pure gold films with <1 atomic % carbon and oxygen impurities and no phosphorous (below the detection limit, <0.1 atomic %) present in the film, values that are clearly lower than obtained with the previous processes (Griffiths, Pallister, Mandia, and Barry reported 6.7 atomic % carbon and 1.8 atomic % oxygen impurities in their films deposited at 120°C and Mäkelä, Hatanpää, Mizohata, Räisänen, Ritala, and Leskelä reported 2.9 atomic % oxygen, 0.9 atomic % hydrogen, 0.2 atomic % carbon, and 0.2 atomic % nitrogen impurities in their films deposited at 180°C).^[1,2] The lack of phosphorous is a good indication that the $\text{P}(\text{CH}_3)_3$ ligands are effectively removed during the ALD surface reactions. After removal of the top layer of the film by argon sputtering an O1s peak remained with a binding energy of 832.8 eV, which corresponded to SiO_2 . Therefore, the likely origin of the O1s signal was the SiO_2 layer of the substrate. Alternatively, it is possible that minor oxygen contamination in the gold film originated from the glass tube of the plasma column, which may have been slightly etched during the H_2 plasma.^[25] The SEM image of the 21.7 nm thick gold film (Figure 5.4b) indicates that the film is not a closed layer and therefore a silicon peak (99.4 eV) was expected, but a clear silicon 2p peak is missing. Because the information depth of XPS is limited to 5-10 nm, the gold film was most likely blocking the silicon substrate from

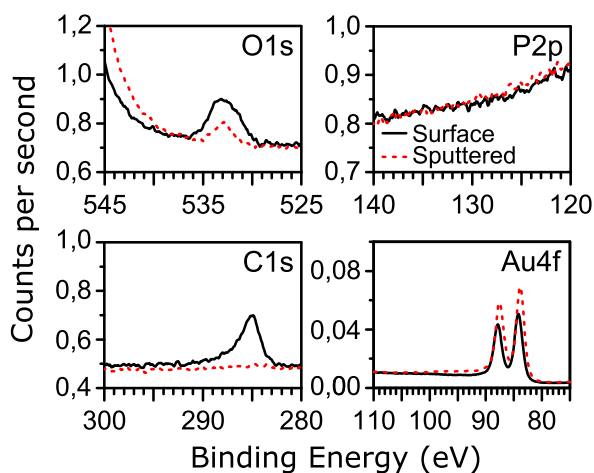


Figure 5.7: XPS spectra for a PE-ALD grown Au film deposited at 120 °C with an equivalent thickness of 21.7 nm. The signals are given for the as-deposited film and after removing surface contamination by Ar sputtering. The Si 2p peak (99.4 eV) is not visible.

the detector's line of sight. The Au 4f_{7/2} peak is located at 84.1 eV, close to the expected value of 84.0 eV indicating gold in the metallic state. Furthermore, the Au 4f region had spin-orbit peaks that were separated in energy by the expected value of 3.7 eV.

While the deposited films had very few impurities and were crystalline, films grown at 120 °C are not fully closed films at a thickness of 21.7 nm, as indicated by the SEM image in Figure 5.4b. The series of SEM images reveals the evolution from isolated circular Au nanoparticles to larger coalesced worm-like structures. However, the latter do not form a conductive path on the surface. In order to measure the resistivity of the deposited gold films, a thicker film with an equivalent thickness of 65.6 nm was deposited at 120 °C on a silicon substrate and four point probe resistance measurements were performed. For this film, a resistivity value of $5.9 \pm 0.3 \mu\Omega \text{ cm}$ was obtained. This value is a factor of 2.4 larger than the bulk value of gold ($2.44 \mu\Omega \text{ cm}$) and comparable to the resistivity value recently obtained for gold films grown by ALD using the $\text{Me}_2\text{Au}(\text{S}_2\text{CNEt}_2)$ precursor ($4.6\text{--}16 \mu\Omega \text{ cm}$).^[2] From the top SEM image of the gold film (Figure 5.8a) it is clear that a percolating film was grown but there seem to be voids present in the film. Figure 5.8b shows a cross section SEM image on a cleaved edge of the Si substrate, allowing for a visual estimation of the film thickness. The physical thickness varied between 62.0 nm and

	Au 4f (atomic %)	C 1s (atomic %)	O 1s (atomic %)	P 2p (atomic %)
Surface	95.5	3.4	1.1	<0.1
Sputtered	99.4	0.3	0.3	<0.1

Table 5.1: XPS concentrations of Au, C, O, and P of a PE-ALD grown Au film deposited at 120 °C with an equivalent thickness of 21.7 nm. The atomic concentration is given for the surface of the (air-exposed) as-deposited film on the first row. On the second row the atomic concentration is given after removing surface contamination from the sample by Ar sputtering in the XPS chamber.

78.1 nm, which is in reasonable agreement with the equivalent thickness of 65.6 nm (obtained from XRF). Both images show that the deposited films were very rough, with an RMS roughness value of 6.5 nm obtained from AFM measurements (see Figure 5.12 in the Supporting Information section). The reason for the higher resistivity, compared to the bulk value of gold, is probably the very rough surface morphology and the presence of holes in the film, lengthening the electrical path.

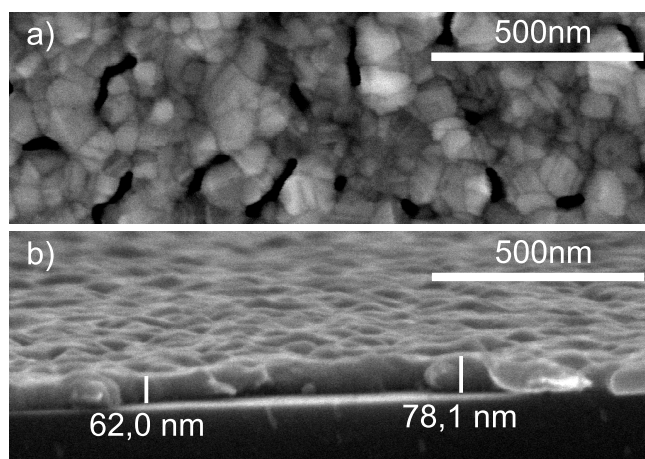


Figure 5.8: SEM images of a gold film (2400 cycles) deposited at 120 °C on a Si substrate with native oxide. The measured equivalent thickness *via* XRF is 65.6 nm. a) A top SEM image showing a percolating film with the presence of voids, b) Cross-section SEM image on a cleaved edge of the Si substrate.

5.2.3 Surface morphology and Raman

Due to the rough, void-filled nature of the gold films, we speculated that these would be effective SERS substrates. Localized surface plasmon resonances (LSPR) are needed for a substrate to exhibit SERS properties, and creating very narrow (nanometer sized) gaps between regular nanostructures made out of Au or Ag is a common approach to create LSPR hotspots on a substrate. The enhancement factor (EF) of the SERS signal scales with the inverse of the squared gap-size (d_g): $EF \sim 1/d_g^2$.^[26] The gaps between the PE-ALD deposited gold nanoparticles are of nanometer size, indicating that these can act as LSPR hotspots. To verify this, free space Raman spectroscopy measurements were performed on a series of four PE-ALD samples deposited at 120 °C, with different gold loadings (Figure 5.4b). The obtained Raman spectra and the calculated pump to Stokes conversion efficiencies (P_s/P_p) are shown in Figure 5.9. The pump to Stokes conversion efficiencies were based on the 1339 cm^{-1} Raman mode, using the method described by Peyskens, Wuytens, Raza, Van Dorpe, and Baets.^[27] The thinnest sample (1.6 nm) did not show a decent Raman spectrum of the pNTP molecule, while the other samples clearly did.^[28] A stronger Raman signal was observed with increasing equivalent thickness of the PE-ALD gold film. This can also be seen by the trend for the P_s/P_p conversion efficiencies, with the largest increase (x56) between the two thinnest samples (1.6 nm and 4.2 nm).

To understand why a stronger Raman signal is measured for the higher gold loadings it is necessary to determine the surface morphology of the measured samples. Top view SEM images can provide information about the mean particle diameter, gap-size, and coverage. SEM images were acquired after the Raman measurement for each sample (Figure 5.10I) and compared to the SEM images of the as-deposited samples (Figure 5.4b and inserts in Figure 5.10I). This was done to see if the deposited gold nanoparticles remained stable under the processing steps that were needed to bind the pNTP molecules to the surface as well as the actual Raman measurements. It is easy to see that the two thinnest samples (a and b) did not retain their morphology. Instead, the gold nanoparticles agglomerated into irregular clusters, leaving large gaps between the formed clusters. The other two samples seemed to be stable, since no agglomerates of particles appeared. The final SEM images were used to determine the mean particle diameter and gap-size. This was done by manually analysing a small section of the SEM images (300 x 300 nm). The obtained values are tabulated with their standard deviation in Table 5.2. These values indicate that

the mean particle diameter increased with increasing gold loading and a moderate increase was seen for the gap-size.

The SEM images give a top down view of the surface and do not contain information about the height of the particles. *Ex situ* GISAXS measurements were performed on the samples to determine the mean particle height. The obtained 2D scattering patterns can be seen in the Supporting Information (Figure 5.13). Modulations on the main scattering peak, along the q_z direction, contain information about the mean particle height. A line profile through the maximum of the scattering peak and along the q_z direction was extracted from each 2D pattern. The resulting profiles, together with their corresponding simulated line profiles, are displayed in Figure 5.10 II. The expected q_z position of the scattering maximum (Yoneda peak) depends on the composition of the measured surface and is marked on the line profiles for a silicon and a gold surface.^[29–31] The observed Yoneda peak started close to the expected value for a silicon surface with low gold loading (on sample a) and progressed with increasing gold loading towards the expected value for a pure gold surface. The particle height can be estimated using the relation $H_p = 2\pi\Delta q_z^{-1}$ where Δq_z is the distance between adjacent maxima or minima on the

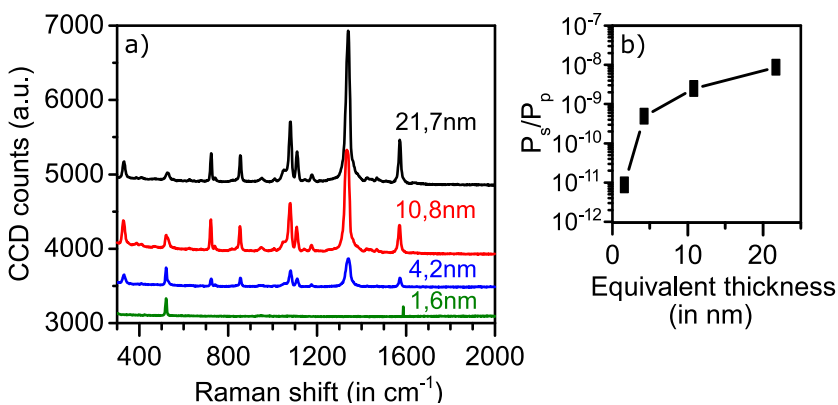


Figure 5.9: a) Free space Raman spectroscopy measurements on gold films for different equivalent thicknesses, deposited at 120 °C. The observed SERS spectra originate from pNTP molecules bound to the surface. The spectra were given an offset for clarity. b) The calculated pump to Stokes conversion efficiency (P_s/P_p), based on the 1339 cm^{-1} Raman mode of pNTP, as a function of the equivalent thickness of the gold film. Note that the data points were not corrected for the number of adsorbed pNTP molecules because the estimated amount was found to be similar for all samples (see Supporting Information).

Sample (t_{eq})	d_g (in nm)	d_p (in nm)	H_p (in nm)	P_s/P_p
a) 1.6 nm	9.6 ± 4.6	13.2 ± 2.9	11.02	9×10^{-12}
b) 4.2 nm	9.2 ± 4.1	19.9 ± 4.2	17.51	5×10^{-10}
c) 10.8 nm	10.4 ± 4.1	36.8 ± 9.2	23.49	2.5×10^{-9}
d) 21.7 nm	12.7 ± 4.5	54.4 ± 17	(26.22)	8.7×10^{-9}

Table 5.2: The equivalent thickness (t_{eq}), mean particle diameter (d_p), gap-size (d_g), particle height (H_p), and pump to Stokes conversion efficiency (P_s/P_p) for each sample. The standard deviation for the mean particle diameter and gap-size are reported next to the tabulated values.

line profile. The distance between the maxima/minima of the line profile decreased with increasing gold loading, which indicates an increase in particle height for the samples with a higher gold loading. The line profile of sample d) shows that the deposited gold layer was very rough, since only one maximum can be clearly distinguished in the line profile. For samples a), b), and c) the particle height was determined from the final input parameters used for the simulation (Table 5.2). The shape of the gold nanoparticles can be expected to resemble oblate spheroids, since the height of the particles is smaller than the particle diameter. The GISAXS pattern of sample d) was not simulated, due to the worm-like shapes of the gold nanoparticles. An estimation for the particle height for sample d) was obtained, by analysing the difference in the maxima's position for the line profiles of sample c) and d).

Figure 5.10III depicts the mean gap between particles (and particle ensembles) for each sample. The particle gaps on sample a) exhibited two length scales, the distance between particle clusters and the distance between individual particles in those clusters. While the individual particles had very small gaps between them it does not seem to benefit the Raman signal. The gaps are either too small or the particles are merged at their boundaries and do not contribute to the Raman signal. This leaves interactions between the clusters which is clearly not sufficient to obtain a decent enhancement. For sample b) the mean gap-size decreases slightly. However, this cannot explain the large increase (x56) for the Raman signal, compared to sample a). The average particle is larger, which can be one factor that plays a role for the larger efficiency, as a size dependent effect of the gold nanoparticles cannot be excluded.^[32] This could mean that the gold nanoparticles on sample a) are too small to exhibit a decent SERS signal. However, the different morphologies of both samples most likely play a larger role. For sample a) the particles have agglomerated and most likely the particles in the clusters are merged, losing the very small particle

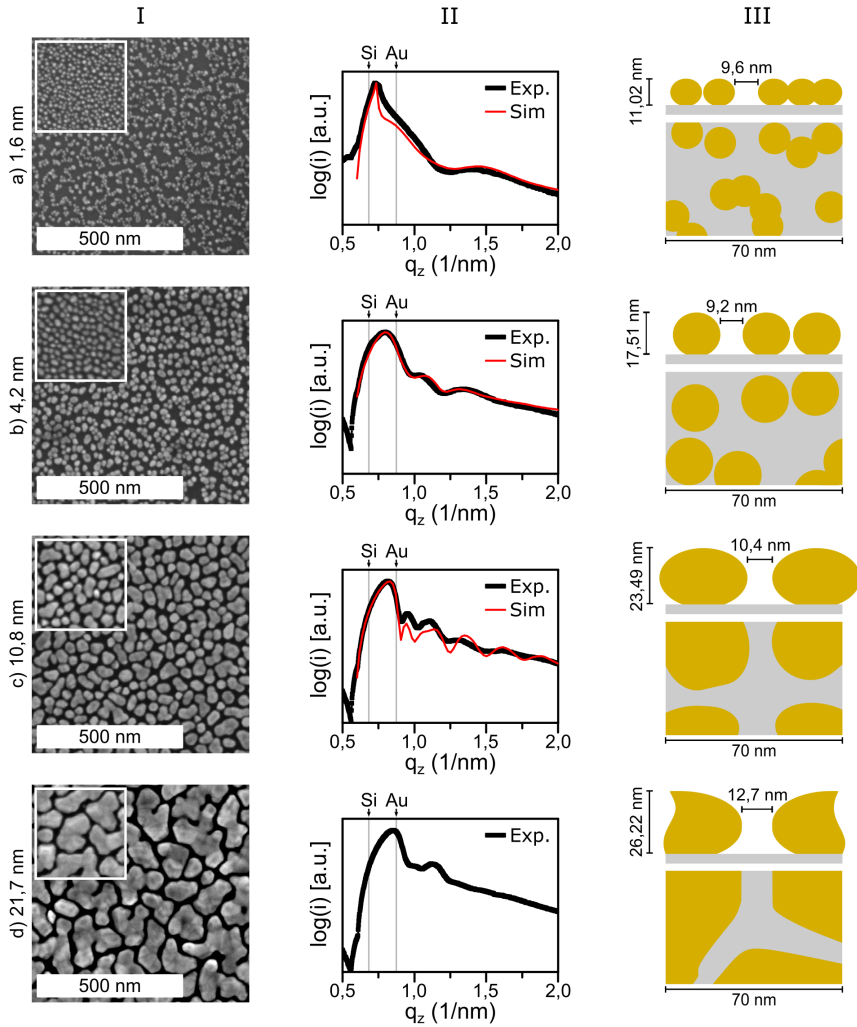


Figure 5.10: (I) SEM images of the samples after the Raman measurements, the inserts represent the sample before binding pNTP to the Au surface. (II) Vertical cut taken through the scattering maximum of the 2D GISAXS pattern and the simulation result of the cut. (III) Schematic depiction of the side view and top view of the mean particle gap on each sample.

gap. The nanoparticles on sample b) have also agglomerated. However, in this case the boundaries between particles are better defined. This means that on this sample the small gaps between the particles are accessible for the pNTP molecules and thus can contribute to the SERS signal.

Another possible cause for the difference in the obtained SERS signal could be a difference in the number of adsorbed, and thus measured, pNTP molecules on each sample. To investigate this we estimated the number of measured pNTP molecules on each sample based on an estimate of the accessible gold surface area and the reported adsorption density for pNTP on gold (see Supporting Information).^[33] We found no significant difference in the estimated number of adsorbed pNTP molecules when comparing the 4 ALD samples. This suggests that a difference in the number of measured pNTP molecules cannot solely explain the observed differences in the SERS signal intensity.

For the two samples with the highest gold loadings, the mean gap-size increased but the conversion efficiency also increased, while the increase in gap-size is expected to decrease the SERS signal. However, for these samples the coalescence of particles during the PE-ALD process starts to have a visible effect on the shape of the gold nanoparticles. The particle shape starts to change from spheroids to more irregular shapes (*e.g.* triangular, elongated spheroids, rods). On sample c), this results in the formation of particles that have straight edges on them. The gaps between particles start to have a structure that resembles a channel. Due to this, the LSPR hotspots do not originate from the interaction of neighbouring rounded particles but between the straight edges of the formed channels. The straight edges of the channel will cause a more stable gap-size, along the length of the formed channel, compared to the gap between round particles. This increases the interaction volume where the LSPR hotspots occur, which counteracts the increase in the gap-size. The largest gold loading is present on sample d) and for this sample the gold nanoparticles have coalesced even more than on sample c). The resulting nanoparticles form very irregular, worm-like shapes. As a result, it is possible for a channel to surround large portions of a particle. This starts to resemble the formation of 'racetracks' on the surface, which can exhibit strong SERS enhancements due to their particular morphology. Such types of nanostructures fall in the class of 'spoof plasmonics' in which the presence of gaps in a metal can cause LSPR hotspots.^[34] Prokes, Glembocki, Cleveland, Caldwell, Foos, Niinistö, and Ritala demonstrated that this phenomenon can occur in PE-ALD deposited silver thin films, due to the formation of 'racetrack' structures in the silver thin film.^[35] Here, this par-

ticular morphology seems to cause a further increase in the Raman signal, despite the increase of the mean gap-size compared to sample c).

While the optimal point of the PE-ALD deposited gold films for SERS enhancement has not been determined, we believe this point must lie somewhere between the surface of sample d) and a fully closed gold layer. Based on a reported study for sputtered silver films, the best Raman signal is expected at the percolation threshold of the film.^[36] This could also be the case for the PE-ALD deposited gold films.

To conclude, the strongest Raman signal is obtained for the sample with an equivalent thickness of 21.7 nm (sample d). Previously, a Stokes to pump conversion efficiency of 6×10^{-8} was reported for state of the art gold nanodome substrates.^[37] Correcting for a roughly 3 times higher accessible gold surface area for the ALD samples (meaning a 3 times higher pNTP concentration), we can conclude that our best sample has a slightly more than one order of magnitude weaker conversion efficiency (factor 21). This is promising given that there is still room for optimization of the Au ALD films. While ALD layers have already been used to form protective coatings on SERS substrates, and to design the gap of the slot on SiN waveguides for on-chip SERS applications,^[38,39] this work shows that it is possible to create an effective SERS substrate using the reported PE-ALD process, without the need for lithography or a sequence of processing steps.

5.3 CONCLUSION

Growth of pure, metallic gold films at the lowest reported temperature to date has been demonstrated with a plasma-enhanced ALD process, using $\text{Me}_3\text{Au}(\text{PMe}_3)$ and H_2 plasma as the precursor and reactant, respectively. The process exhibits saturation of the precursor and reactant halfcycles on gold seed layers with a steady growth rate of 0.030 ± 0.002 nm per cycle. A similar steady growth rate is obtained on bare SiO_2 surfaces, after a sufficient number of cycles. Initially, the growth rate is lower due to nucleation, leading to island-like growth and high film roughness, but percolating films are obtained when the films are sufficiently thick. A resistivity value of $5.9 \pm 0.3 \mu\Omega \text{ cm}$ is obtained for the thickest films, close to the bulk resistivity value of gold ($2.44 \mu\Omega \text{ cm}$). The deposited films are pure gold with <1 atomic % carbon and oxygen impurities in the film. The particular nanostructure of as-deposited films offers stable free-space Raman enhancement, slightly more than one order of magnitude lower than state-of-the-art solid-state substrates, but with room for further optimization. The SERS-active Au ALD substrates can be fabricated with relative

ease without the need for complex processing or lithography steps. Beyond SERS, nanoparticulate gold has very interesting and useful catalytic properties,^[12-14] making the reported gold nanoparticle ALD process also highly relevant towards heterogeneous catalysis applications.

5.4 SUPPORTING INFORMATION

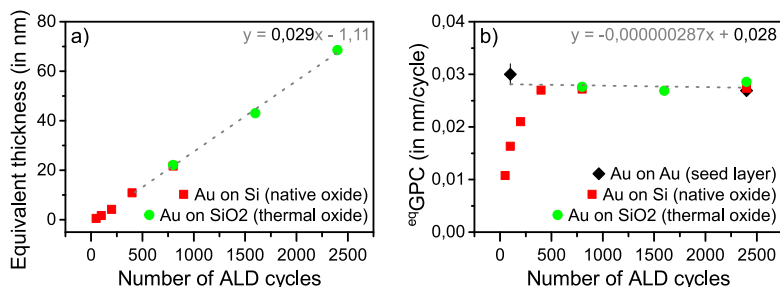


Figure 5.11: Equivalent thickness and GPC for PE-ALD deposited gold layers as a function of the number of used ALD cycles, deposited on three different types of substrates: on a sputtered Au seed layer (black diamonds), on silicon (100) with native silicon oxide (red squares), on silicon with a thick thermally grown silicon oxide layer (green circles). a) Equivalent thickness as a function of number of ALD cycles, the plotted line is the best fit through the data points obtained for 400 ALD cycles and more, to exclude the initial nucleation behaviour. The fit gives a slope of 0.029 ± 0.003 nm per cycle and an intercept of -1.11 nm. b) ^{eq}GPC as a function of the number of ALD cycles. The plotted line is the best fit through the data points, excluding the deviating ^{eq}GPC points of the Au depositions on silicon (native oxide), as these are located in the nucleation regime of the growth on silicon. The fit gives a slope of 2.87×10^{-7} and an intercept of 0.028 ± 0.003 nm per cycle.

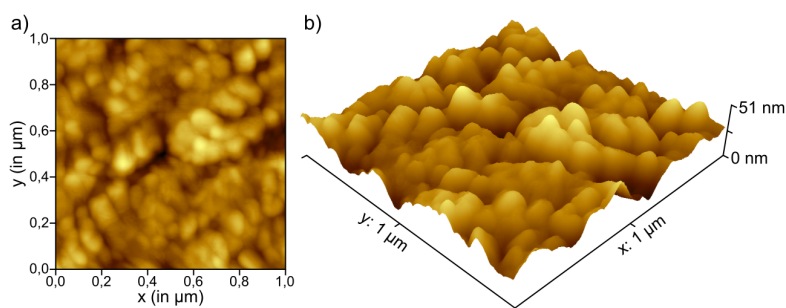


Figure 5.12: AFM image of a 65.6 nm thick gold film on top of a silicon substrate. a) 2D image of the sample, b) 3D image of the sample.

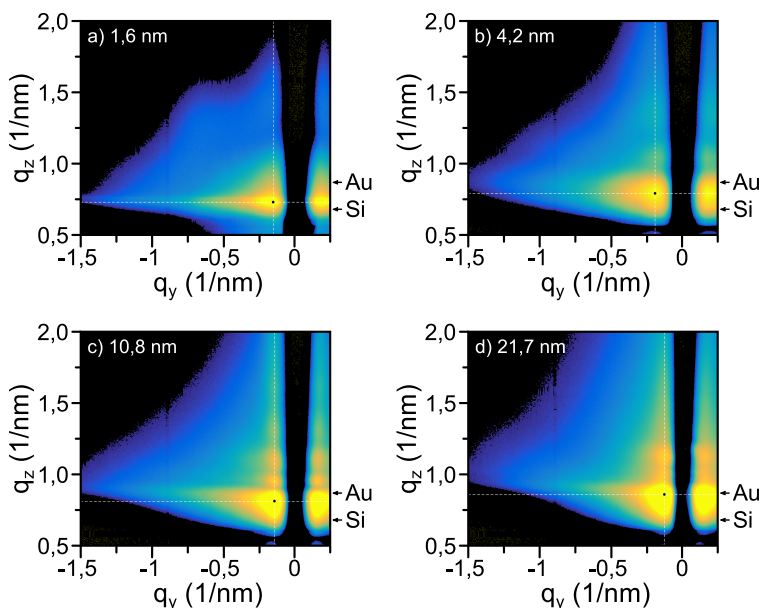


Figure 5.13: (a-d) Ex situ 2D GISAXS scattering patterns of the samples that were measured with Raman spectroscopy (Figure 5.9). The dotted lines indicate the horizontal and vertical q -position at the maximum of the main scattering peak.

MEASURED AMOUNT OF PNTP MOLECULES: To compare Raman measurements it is necessary to determine how many pNTP molecules are measured on each sample. To do this the total Au surface area needs to be estimated on each sample. This total Au surface area is obtained by analysing the SEM images of the samples and combining this information with the mean particle height of the gold particles, obtained from *ex situ* GISAXS measurements.

The particles are treated as extruded polygons for all samples. To start a top-down SEM image is taken (Figure 5.14a) and a mask is put over the visible particles (Figure 5.14b). The area of each mask is determined and is taken as the area of the top-surface for each particle. The length of the boundary line for each particle is multiplied by the mean particle height to obtain the area of each particle's side wall (Figure 5.14c). Both areas are added to obtain the surface area for a single particle. By doing this for every particle in the SEM image the total Au surface area of the sample is obtained. This value is then multiplied by the expected surface density

for pNTP to get a final estimate for how many molecules were measured on each sample.^[33]

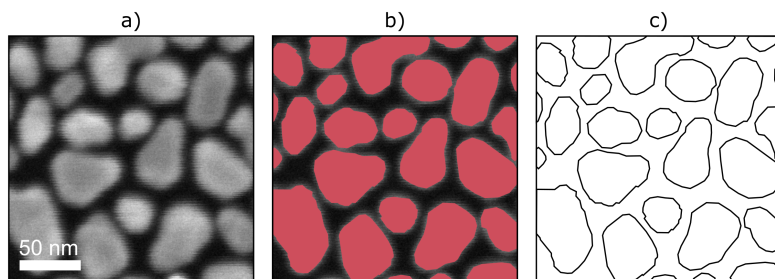


Figure 5.14: a) cropped SEM image of an ALD Au sample. b) Masks placed over the individual gold particles. c) The border of the individual masks, the length of each border is used to calculate the surface area of the side wall of each particle.

This analysis was performed on all samples that were measured with the Raman microscope. The estimated number of pNTP molecules that were measured during the Raman measurements on each sample can be seen in Table S1. These values indicate that the amount of pNTP molecules that contribute to the measured Raman signal are comparable for the measured samples.

Sample	Au surface area (in μm^2)	Amount of pNTP molecules
a)	3.2	1.4×10^7
b)	4.2	1.9×10^7
c)	3.7	1.6×10^7
d)	3.4	1.5×10^7

Table 5.3: Estimated Au surface area and number of adsorbed pNTP molecules on the samples that were measured using Raman microscopy.

REFERENCES

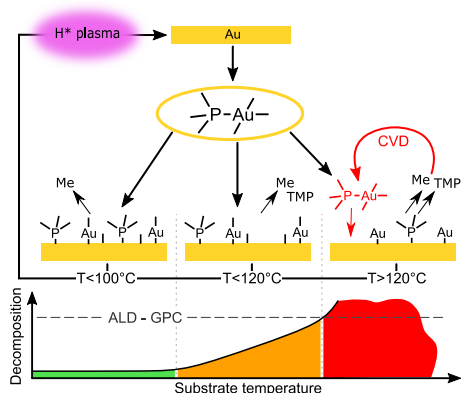
- [1] Matthew B. E. Griffiths, Peter J. Pallister, David J. Mandia, and Seán T. Barry. "Atomic Layer Deposition of Gold Metal". In: *Chemistry of Materials* 28.1 (2016), pp. 44–46. DOI: 10.1021/acs.chemmater.5b04562.
- [2] Maarit Mäkelä, Timo Hatanpää, Kenichiro Mizohata, Jyrki Räisänen, Mikko Ritala, and Markku Leskelä. "Thermal Atomic Layer Deposition of Continuous and Highly Conducting Gold Thin Films". In: *Chemistry of Materials* 29.14 (2017), pp. 6130–6136. DOI: 10.1021/acs.chemmater.7b02167.
- [3] Michiel Van Daele et al. "Plasma-Enhanced Atomic Layer Deposition of Nanostructured Gold Near Room Temperature". In: *ACS Applied Materials & Interfaces* 11.40 (2019), pp. 37229–37238. DOI: 10.1021/acsmi.9b10848.
- [4] Mark J. Hampden-Smith and Toivo T. Kodas. "Chemical Vapor Deposition of Metals: Part 1. An Overview of CVD Processes". In: *Chemical Vapor Deposition* 1.1 (1995), pp. 8–23. DOI: 10.1002/cvde.19950010103.
- [5] A.A. Bessonov, N.B. Morozova, N.V. Gelfond, P.P. Semyannikov, S.V. Trubin, Yu.V. Shevtsov, Yu.V. Shubin, and I.K. Igumenov. "Dimethylgold(III) carboxylates as new precursors for gold CVD". In: *Surface and Coatings Technology* 201.22 (2007), pp. 9099–9103. DOI: 10.1016/j.surfcoat.2007.04.030.
- [6] J. Messelhäuser, E. B. Flint, and H. Suhr. "Direct Writing of Gold Lines by Laser-Induced Chemical Vapor Deposition". In: *Applied Physics A* 55.2 (Aug. 1992), pp. 196–202. DOI: 10.1007/BF00334223.
- [7] Thomas H. Baum and Carol R. Jones. "Laser Chemical Vapor Deposition of Gold". In: *Applied Physics Letters* 47.5 (1985), pp. 538–540. DOI: 10.1063/1.96119.
- [8] Mark M. Banaszak Holl, Paul F. Seidler, Steven P. Kowalczyk, and F. Read McFeely. "Surface reactivity of alkylgold(I) complexes: substrate-selective chemical vapor deposition of gold from $\text{RAuP}(\text{CH}_3)_3$ ($\text{R} = \text{CH}_2\text{CH}_3, \text{CH}_3$) at remarkably low temperatures". In: *Inorganic Chemistry* 33.3 (1994), pp. 510–517. DOI: 10.1021/ic00081a019.
- [9] Shu Gong, Willem Schwalb, Yongwei Wang, Yi Chen, Yue Tang, Jye Si, Bijan Shirinzadeh, and Wenlong Cheng. "A Wearable and Highly Sensitive Pressure Sensor with Ultrathin Gold Nanowires". en. In: *Nature Communications* 5.1 (May 2014). DOI: 10.1038/ncomms4132.
- [10] Sara Fateixa, Paula C. Pinheiro, Helena I.S. Nogueira, and Tito Trindade. "Gold Loaded Textile Fibres as Substrates for SERS Detection". In: *Journal of Molecular Structure* 1185 (2019), pp. 333–340. DOI: 10.1016/j.molstruc.2019.03.001.
- [11] J. H. Kim, K. M. Twaddle, J. Hu, and H. Byun. "Sunlight-Induced Synthesis of Various Gold Nanoparticles and Their Heterogeneous Catalytic Properties on a Paper-Based Substrate". In: *ACS Applied Materials & Interfaces* 6.14 (2014), pp. 11514–11522. DOI: 10.1021/am503745w.
- [12] M.C. Daniel and D. Astruc. "Gold Nanoparticles: Assembly, Supramolecular Chemistry, Quantum-Size-Related Properties, and Applications toward Biology, Catalysis, and Nanotechnology". In: *Chemical Reviews* 104.1 (2004), pp. 293–346. DOI: 10.1021/cr030698+.
- [13] A. Stephen K. Hashmi and Graham J. Hutchings. "Gold Catalysis". In: *Angewandte Chemie International Edition* 45.47 (2006), pp. 7896–7936. DOI: 10.1002/anie.200602454.
- [14] Yan Zhang, Xinjiang Cui, Feng Shi, and Youquan Deng. "Nano-Gold Catalysis in Fine Chemical Synthesis". In: *Chemical Reviews* 112.4 (2012), pp. 2467–2505. DOI: 10.1021/cr200260m.

- [15] Yan Yu, Pan Zeng, Cheng Yang, Junyi Gong, Rongqing Liang, Qiongrong Ou, and Shuyu Zhang. "Gold-Nanorod-Coated Capillaries for the SERS-Based Detection of Thiram". In: *ACS Applied Nano Materials* 2.1 (2019), pp. 598–606. DOI: 10.1021/acsnanm.8b02075.
- [16] Hyeong-Min Kim, Minhee Uh, Dae Hong Jeong, Ho-Young Lee, Jae-Hyoung Park, and Seung-Ki Lee. "Localized Surface Plasmon Resonance Biosensor using Nanopatterned Gold Particles on the Surface of an Optical Fiber". In: *Sensors and Actuators B: Chemical* 280 (2019), pp. 183–191. DOI: 10.1016/j.snb.2018.10.059.
- [17] E. Levrau, K. Van de Kerckhove, K. Devloo-Casier, S. P. Sree, J. A. Martens, C. Detavernier, and J. Dendooven. "In Situ IR Spectroscopic Investigation of Alumina ALD on Porous Silica Films: Thermal versus Plasma-Enhanced ALD". en. In: *The Journal of Physical Chemistry C* 118.51 (Dec. 2014), pp. 29854–29859. DOI: 10.1021/jp5088288.
- [18] G. Portale, D. Cavallo, Giovanni Carlo A., D. Hermida-Merino, M. van Drongelen, L. Balzano, G.W.M. Peters, J.G.P. Goossens, and W. Bras. "Polymer Crystallization Studies under Processing-Relevant Conditions at the SAXS/WAXS DUBBLE Beamline at the ESRF". English. In: *Journal of applied crystallography* 46.6 (2013), pp. 1681–1689. DOI: 10.1107/S0021889813027076.
- [19] Jolien Dendooven et al. "Independent tuning of size and coverage of supported Pt nanoparticles using atomic layer deposition". In: *Nature Communications* 8.1 (2017), p. 1074. DOI: 10.1038/s41467-017-01140-z.
- [20] Matthias M. Minjauw et al. "Plasma-Enhanced Atomic Layer Deposition of Silver Using Ag(fod)(PEt₃) and NH₃-Plasma". In: *Chemistry of Materials* 29.17 (2017), pp. 7114–7121. DOI: 10.1021/acs.chemmater.7b00690.
- [21] Véronique Cremers, Riikka L. Puurunen, and Jolien Dendooven. "Conformality in Atomic Layer Deposition: Current Status Overview of Analysis and Modelling". In: *Applied Physics Reviews* 6.2 (2019), p. 021302. DOI: 10.1063/1.5060967.
- [22] J. Dendooven, D. Deduytsche, J. Musschoot, R. L. Vanmeirhaeghe, and C. Detavernier. "Conformality of Al₂O₃ and AlN Deposited by Plasma-Enhanced Atomic Layer Deposition". In: *Journal of The Electrochemical Society* 157.4 (2010), G111–G116. DOI: 10.1149/1.3301664.
- [23] H. C. M. Knoop, E. Langereis, M. C. M. van de Sanden, and W. M. M. Kessels. "Conformality of Plasma-Assisted ALD: Physical Processes and Modeling". In: *Journal of The Electrochemical Society* 157.12 (2010), G241–G249. DOI: 10.1149/1.3491381.
- [24] I. J. M. Erkens, M. A. Verheijen, H. C. M. Knoop, W. Keuning, F. Roozeboom, and W. M. M. Kessels. "Plasma-Assisted Atomic Layer Deposition of Conformal Pt Films in High Aspect Ratio Trenches". In: *The Journal of Chemical Physics* 146.5 (2017), p. 052818. DOI: 10.1063/1.4972120.
- [25] R. P. H. Chang, C. C. Chang, and S. Darack. "Hydrogen Plasma Etching of Semiconductors and their Oxides". In: *Journal of Vacuum Science and Technology* 20.1 (1982), pp. 45–50. DOI: 10.1116/1.571307.
- [26] Jeffrey M. McMahon, Shuzhou Li, Logan K. Ausman, and George C. Schatz. "Modeling the Effect of Small Gaps in Surface-Enhanced Raman Spectroscopy". In: *The Journal of Physical Chemistry C* 116.2 (2012), pp. 1627–1637. DOI: 10.1021/jp207661y.
- [27] Frédéric Peyskens, Pieter Wuytens, Ali Raza, Pol Van Dorpe, and Roel Baets. "Waveguide Excitation and Collection of Surface-Enhanced Raman Scattering from a Single Plasmonic Antenna". eng. In: *Nanophotonics* 7.7 (2018), pp. 1299–1306. DOI: 10.1515/nanoph-2018-0003.

- [28] Gregory Q. Wallace, Mohammadali Tabatabaei, and François Lagugné-Labarthet. "Towards Attomolar Detection using a Surface-Enhanced Raman Spectroscopy Platform Fabricated by Nanosphere Lithography". In: *Canadian Journal of Chemistry* 92 (Jan. 2014). DOI: 10.1139/cjc-2013-0340.
- [29] Y. Yoneda. "Anomalous Surface Reflection of X Rays". In: *Phys. Rev.* 131 (5 Sept. 1963), pp. 2010–2013. DOI: 10.1103/PhysRev.131.2010.
- [30] V. Holý and T. Baumbach. "Nonspecular X-ray Reflection from Rough Multilayers". In: *Phys. Rev. B* 49 (15 Apr. 1994), pp. 10668–10676. DOI: 10.1103/PhysRevB.49.10668.
- [31] Matthias Schwartzkopf et al. "From Atoms to Layers: in situ Gold Cluster Growth Kinetics during Sputter Deposition". In: *Nanoscale* 5 (11 2013), pp. 5053–5062. DOI: 10.1039/C3NR34216F.
- [32] Steven E. J. Bell and Maighread R. McCourt. "SERS Enhancement by Aggregated Au Colloids: Effect of Particle Size". In: *Phys. Chem. Chem. Phys.* 11 (34 2009), pp. 7455–7462. DOI: 10.1039/B906049A.
- [33] P. C. Wuytens, A. G. Skirtach, and R. Baets. "On-Chip Surface-Enhanced Raman Spectroscopy using Nanosphere-Lithography Patterned Antennas on Silicon Nitride Waveguides". In: *Opt. Express* 25.11 (May 2017), pp. 12926–12934. DOI: 10.1364/OE.25.012926.
- [34] J. B. Pendry, L. Martín-Moreno, and F. J. Garcia-Vidal. "Mimicking Surface Plasmons with Structured Surfaces". In: *Science* 305.5685 (2004), pp. 847–848. DOI: 10.1126/science.1098999.
- [35] S. M. Prokes, O. J. Glembocki, E. Cleveland, J. D. Caldwell, E. Foos, J. Niinistö, and M. Ritala. "Spoo-like Plasmonic Behavior of Plasma Enhanced Atomic Layer Deposition Grown Ag Thin Films". In: *Applied Physics Letters* 100.5 (2012), p. 053106. DOI: 10.1063/1.3679106.
- [36] G. Santoro, S. Yu, M. Schwartzkopf, P. Zhang, Sarathlal Koyiloth Vayalil, J. F. H. Risch, M. A. Rübhausen, M. Hernández, C. Domingo, and S. V. Roth. "Silver Substrates for Surface Enhanced Raman Scattering: Correlation between Nanostructure and Raman Scattering Enhancement". In: *Applied Physics Letters* 104.24 (2014), p. 243107. DOI: 10.1063/1.4884423.
- [37] P. C. Wuytens, A. Z. Subramanian, W. H. De Vos, A. G. Skirtach, and R. Baets. "Gold Nanodome-Patterned Microchips for Intracellular Surface-Enhanced Raman Spectroscopy". In: *Analyst* 140 (24 2015), pp. 8080–8087. DOI: 10.1039/C5AN01782C.
- [38] Eric V. Formo, Shannon M. Mahurin, and Sheng Dai. "Robust SERS Substrates Generated by Coupling a Bottom-Up Approach and Atomic Layer Deposition". In: *ACS Appl. Mater. Interfaces* 2.7 (July 2010), pp. 1987–1991. DOI: 10.1021/am100272h.
- [39] Ali Raza, Stéphane Clemmen, Pieter Wuytens, Muhammad Muneeb, Michiel Van Daele, Jolien Dendooven, Christophe Detavernier, Andre Skirtach, and Roel Baets. "ALD Assisted Nanoplasmonic Slot Waveguide for On-Chip Enhanced Raman Spectroscopy". In: *APL Photonics* 3.11 (2018), p. 116105. DOI: 10.1063/1.5048266.

The $\text{Me}_3\text{Au}(\text{PMe}_3)/\text{H}_2$ plasma gold ALD process has several potential applications. However, the reaction mechanism for $\text{Me}_3\text{Au}(\text{PMe}_3)$ based gold ALD processes and how this precursor and its ligands behave during an ALD process is poorly understood.

The existing CVD and surface science literature provide a good starting point to unravel the reaction mechanism of the $\text{Me}_3\text{Au}(\text{PMe}_3)/\text{H}_2$ plasma ALD process. Understanding possible decomposition pathways of the used precursor can provide valuable information about how the chemical reactions can occur on a substrate. The existing decomposition investigations of Au(I) and Au(III) compounds, similar to the $\text{Me}_3\text{Au}(\text{PMe}_3)$ molecule, are limited to the study of the liquid phase, which nonetheless provide important insights in the chemistry of these gold compounds. Gold compounds of the form RAuPR'_3 and $\text{R}_3\text{AuPR}'_3$ (with R = methyl, ethyl; R' = methyl, ethyl, phenyl) generally decompose into coupled R-R species, elemental gold, and the phosphine ligand.^[1-4] The decomposition pathway usually starts with the elimination of two neighbouring alkyl groups, resulting in the formation of R-R and RAuPR'_3 species. It was found that adding the phosphine ligand to the liquid results in retardation of the decomposition, indicating that for liquids the rate-limiting step in the decomposition of RAuPR'_3 molecules is the loss of the phosphine ligand. David-



This chapter was published as a research article in the journal: Physical Chemistry Chemical Physics, titled "Reaction mechanism of the $\text{Me}_3\text{Au}(\text{PMe}_3)$ - H_2 plasma-enhanced ALD process".^[3] The image on this page is the original TOC-graphic, submitted with the published article. Author contributions: M.V.D. designed the experiments, performed the ALD depositions and FTIR, XPS and QMS measurements, analyzed and interpreted the results; M.B.E.G. produced the precursors and measured their NRM spectra; M.M.M. performed XPS measurements and assisted in analyzing the data; M.B.E.G., S.T.B., C.D. and J.D. assisted in designing the experiments and interpreting the results; M.V.D. prepared the manuscript; All the authors contributed to revising the manuscript.

son et al. reported laser induced CVD of gold tracks using MeAuPMe_3 , MeAuPEt_3 , and EtAuPEt_3 using an argon ion laser at 257 nm.^[5] The elemental composition and inclusion of precursor ligands on the surface was studied using laser ionization microprobe analysis. They observed the presence of chemisorbed PMe_3 species on the gold surface, which remained present on the surface for prolonged periods under high vacuum conditions. They inferred that the Au-Me surface species were less stable compared to the Au- PMe_3 surface species. In addition, they found indications for the non-dissociative adsorption of MeAuPMe_3 on the gold surface. These observations are interesting for elucidating the reaction mechanism of $\text{Me}_3\text{Au}(\text{PMe}_3)$ and MeAuPMe_3 based processes on gold surfaces during gold deposition.

This chapter will cover several topics regarding the gold ALD processes that use the $\text{Me}_3\text{Au}(\text{PMe}_3)$ molecules as the precursor. These include the reaction mechanism of the $\text{Me}_3\text{Au}(\text{PMe}_3)$ - H_2 plasma gold ALD process, the temperature dependent decomposition behaviour of the molecule, the use of different co-reactants, and reactive sites used by the precursor molecule for chemisorption on SiO_2 .

6.1 EXPERIMENTAL SECTION

A home-built pump type ALD reactor, able to reach a base pressure of 2×10^{-6} mbar, is used to carry out all atomic layer depositions, unless stated otherwise.^[6] The $\text{Me}_3\text{Au}(\text{PMe}_3)$ precursor ($\geq 95\%$ purity) is synthesised *via* the method used by Griffiths *et al.*^[7] The $(\text{CD}_3)_3\text{Au}(\text{PMe}_3)$ precursor ($\geq 95\%$ purity, and $>99\%$ deuteration) is synthesised as described in the paper of Shaw and Tobias.^[8] The purity of the precursor liquids is verified by NMR measurements (see Supporting Information). The precursor liquids are kept in glass containers, heated to 50°C and the delivery lines are heated to 55°C . Argon is used as a carrier gas for the precursors during all depositions. The flow of the carrier gas is adjusted to reach a pressure of 6×10^{-3} mbar, when pulsing the precursor in the chamber. The precursor exposures during the atomic layer depositions are carried out by injecting the $\text{Me}_3\text{Au}(\text{PMe}_3)$ vapour after closing the gate valve between the turbomolecular pump and the reactor chamber. By varying the injection time, the pressure during the pulse varied between 6×10^{-3} mbar and 5 mbar. H_2 plasma (20% H_2 in argon) is used as the reactant for all depositions. The H_2 gas is introduced through the plasma column mounted on top of the chamber and the flow of H_2 gas is limited by a needle valve to obtain a chamber pressure of 6×10^{-3} mbar for all depositions. A 13.56 MHz RF generator (Advanced Energy, Model CESAR 136) and a

matching network are used to generate an inductively coupled plasma in the plasma column. For all experiments a plasma power of 200 W is used and the impedance matching parameters are adjusted to minimise the reflected power. The substrates used are pieces of p-type silicon (100) with native silicon oxide or 10 nm sputtered Au films on p-type silicon (100). The samples are mounted directly on a heated copper block. The temperature of the copper block is adjusted with a PID controller. The chamber walls are heated to 90 °C for all experiments unless stated otherwise.

In this work films deposited using a home-built pump type reactor are compared to films deposited using a commercial flow-type reactor. The major differences between both reactor-types are the used operating pressures and how the purge step between precursor and co-reactant exposures is implemented. Typical operation pressures of a flow-type reactor are of the order of 1 mbar. While a pump-type reactor can reach these pressures during an exposure it usually needs to have a base pressure on the order of 10^{-6} mbar to avoid CVD side reactions. In pump-type reactors the purge step is achieved by lowering the pressure in the chamber to the base pressure which removes the gas-phase molecules in the reactor chamber, while a flow-type reactor uses an inert gas to flush/purge the gas-phase molecules from the reactor chamber.

To study the ALD reaction mechanism, *in situ* infrared spectroscopy, *in-vacuo* X-ray photoelectron spectroscopy (XPS), mass spectrometry. The infrared measurements are carried out with a Vertex 70V from Bruker and a medium band mercury cadmium telluride (MCT) detector cooled with liquid nitrogen. The infrared measurements can be performed in two different geometries, either in reflection or in transmission. For the Reflection Absorption Infra-Red Spectroscopy mode (RAIRS), a thick gold seed layer of 60 nm is used to avoid nucleation effects and to ensure proper reflection of the IR beam.^[9] *In-vacuo* XPS measurements were performed with a Thermo Scientific Theta Probe XPS instrument on an ALD-XPS cluster.^[10] Using this cluster it is possible to perform through-vacuum transfer of samples from the ALD chamber (10^{-7} mbar) to the XPS analysis chamber (10^{-10} mbar) in less than 60 seconds. *In situ* mass spectrometry experiments are carried out using a Hiden HPR-30 mass spectrometer, 70 eV electron impact ionisation and a quadrupole mass filter combined with a Faraday detector. The reactor is loaded with ~ 2 grams of alumina powder with a diameter of $1\mu\text{m}$, providing an estimated surface area of 3m^2 . The tube between the ALD chamber has a length of 1 m and a width of 4 cm and is heated to 90 °C to avoid cold spots. The connection between the ALD chamber and fine valve has a diameter of 10 cm (the fine valve is located between the chamber and the turbomolecular pump). The pressure in the

QMS chamber during the experiments was $\sim 10^{-7}$ mbar. The reactor and powder are pretreated with 100 Au ALD cycles before performing the QMS measurements.

Several *ex situ* measurement techniques are used to determine the physical properties of the deposited Au films. Thickness determination *via* X-ray reflectivity (XRR) measurements is done on a diffractometer (Bruker D8) equipped with a copper source (Cu $K\alpha$ radiation) and a scintillator point detector. However, because the Au ALD films are generally too rough for accurate thickness determination with XRR, X-ray fluorescence (XRF) measurements are used to determine an equivalent film thickness based on a calibration curve of sputtered gold films. XRF measurements are performed using a Mo X-ray source and an XFlash 5010 silicon drift detector, respectively placed at an angle of 45° and 52° with the sample surface. An integration time of 200 s is used to acquire the fluorescence spectra. *Ex situ* XPS is used to determine the chemical composition and binding energy of the deposited films. The XPS measurements are carried out in the same tool that is used for *in-vacuo* XPS. The X-rays are generated using a monochromatic Al source (Al $K\alpha$). To etch the surface of the deposited films an Ar^+ ion gun is used at an acceleration voltage of 3 keV and a current of 2 μA .

6.2 RESULTS AND DISCUSSION

6.2.1 Precursor saturation and decomposition

The saturation behaviour of the $\text{Me}_3\text{Au}(\text{PMe}_3) - \text{H}_2$ plasma ALD process was demonstrated in the previous work.^[6] It is important to consider the precursor supply during the saturation experiments as the precursor dose in the chamber will be dependent on the vapour content in the precursor container, which is carried to the ALD reactor in a flow of Argon. The amount of vapour in the container and thus the partial pressure of the precursor during the exposure depends on the container temperature, the exact pulse and purge sequence and the amount of liquid precursor in the container. As long as the precursor dose is sufficient to achieve saturation in the ALD process, these variations will not have impact on the ALD growth per cycle. On the other hand, a too limited buildup of vapour in the container may also invoke an apparent saturated growth behaviour. To rule out the latter, additional ALD saturation experiments were performed at different substrate temperatures for which two precursor containers were used simultaneously during the precursor exposures. The obtained GPC's of these experiments (red diamonds) and the previ-

ously reported GPC of the ALD process (black squares) are shown in Figure 6.1 as a function of substrate temperature. At 50 °C and 90 °C the GPC showed no increase with respect to the expected GPC of the ALD process, verifying the previously reported saturating behaviour of the ALD process. However, at 120 °C the GPC was doubled when two precursor containers were used, indicating that at this substrate temperature the ALD process is dominated by decomposition and that its growth is governed by the precursor supply.

The observed saturating behaviour of the ALD process requires that the surface will get covered by the precursor ligands during the $\text{Me}_3\text{Au}(\text{PMe}_3)$ exposure, preventing further precursor adsorption. However, as we reported previously, this process exhibits a minor decomposition component on gold substrates, which we attributed to slow decomposition of the surface ligands.^[6] The double precursor container experiments indicate that between a substrate temperature of 90 °C and 120 °C this minor decomposition component increases in magnitude and heavily influences the growth behaviour at 120 °C. Additional experiments were performed to investigate the onset temperature and evolution of this precursor behaviour. This was done by exposing gold seed layers to the $\text{Me}_3\text{Au}(\text{PMe}_3)$ vapour only (without co-reactant) at temperatures spanning the entire ALD temperature window (50 °C-120 °C). While these experiments are not

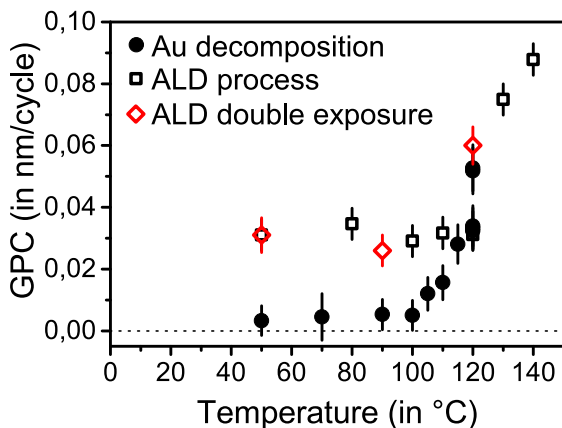


Figure 6.1: Decomposition of the $\text{Me}_3\text{Au}(\text{PMe}_3)$ molecule (black dots) as a function of substrate temperature and the reported GPC for the gold PEALD process using 1 precursor container (black squares) and 2 precursor containers simultaneously (red diamonds). The decomposition experiments were performed on gold seed layers, using 20 second precursor exposures.

real ALD processes, the observed increase in gold thickness was divided by the number of used precursor exposures and expressed as GPC as a function of substrate temperature in Figure 6.1 (black dots). The decomposition curve shows that there are two regions with a threshold substrate temperature at 100 °C. Below the threshold the decomposition is limited to the previously reported value of 0.005 nm per cycle and above a substrate temperature of 100 °C the decomposition component increases with the substrate temperature. At 120 °C the decomposition component becomes larger than the expected GPC of the ALD process with a large spread on the obtained GPC, most likely due to differences in precursor supply. The observed Au decomposition curve indicates that the previously reported upper limit of the ALD temperature window needs to be lowered from 120 °C to 100 °C.

No precursor decomposition is observed on SiO₂ substrates for temperatures below 120 °C. This suggests that the observed decomposition on a gold substrate is not due to thermal decomposition of the precursor itself, but depends on how the precursor and its ligands interact with the gold surface. Therefore, the surface species need to be identified and their stability on the surface investigated.

6.2.2 *Surface species*

Using *in situ* Reflection Absorption Infrared Spectroscopy (RAIRS) it is possible to determine which surface groups are present after each precursor or reactant exposure. To this end, we employed *in situ* RAIRS measurements on a sputtered gold seed layer (60 nm), at a substrate temperature of 90 °C. In addition to the use of the regular precursor molecule (Me₃Au(PMe₃)) we also performed experiments using a partially deuterated molecule in which the methyl groups attached to the gold atom were replaced by deuterated methyl groups ((CD₃)₃Au(PMe₃)), where the PMe₃ ligand remained unaltered. The spectra measured after each exposure in the ALD cycle were subtracted from each other to obtain differences in absorption that are related to the addition/removal of surface species after each exposure and the average of 10 spectra was taken to improve the signal to noise ratio. The obtained difference spectra for both precursor variants are displayed in Figure 6.2. After the precursor exposure, peaks appear for the vibration modes of methyl and trimethylphosphine (TMP, PMe₃) surface groups, originating from the precursor ligands. Zooms of the CH-stretching, CD-stretching, and fingerprint regions after a precursor exposure are displayed in Figure 6.2 a-c, assignment of the peaks can be found in Table 6.1. The C-H stretching region (Figure 6.2a) has the

same four peaks (1-4) for both gold precursor variants. For the deuterated precursor ($(\text{CD}_3)_3\text{Au}(\text{PMe}_3)$) it is expected that these peaks originate exclusively from the TMP ligand, while for the regular precursor ($\text{Me}_3\text{Au}(\text{PMe}_3)$) contributions from both the TMP and methyl ligands are expected. The similarity between both spectra indicates that these peaks mainly originate from the TMP ligand. It is hence difficult to uniquely distinguish between the C-H stretching modes of the TMP ligand and the methyl groups, in turn motivating the use of the partially deuterated molecule. The C-D stretching region (Figure 6.2b) shows a clear contribution from C-D species (5 and 6) for the deuterated precursor, indicating that Au- CD_3 species are present on the gold surface after the precursor exposure. The zoom of the fingerprint region is shown in Figure 6.2c. The methyl deformation and rocking modes (7, 8, 10) originate from the TMP ligand and in combination with the PC_3 stretching mode (11) give a good indication that the TMP ligands remain intact. Remarkable is the lack of vibration modes between 1250 cm^{-1} and 1150 cm^{-1} where methyl deformation modes of Au- $(\text{CH}_3)_3$ species are expected. On the other hand, there is a feature present in the spectrum of the regular precursor at 1100 cm^{-1} (9), which might originate from single methyl species bound to a gold atom.^[11] This feature disappears for the deuterated precursor and a new feature appears at a lower position (9') most likely from deuterated methyl species bound to the gold surface.

The symmetrical difference spectra for the precursor and reactant exposure indicate that the H_2 plasma exposure is able to remove all of the surface groups that are added during the precursor exposures. It is possible that Au-H surface species are formed during the H_2 plasma exposure, for which vibration modes are expected around $2230\text{-}2170\text{ cm}^{-1}$ and 1642 cm^{-1} .^[13] However, no absorption is visible in those regions after a H_2 plasma exposure, indicating that any formed Au-H species remain below the detection limit of our setup. Furthermore, it is unlikely that a significant amount of Au-H species would be stable for prolonged periods of time on a large gold surface and at temperatures above $-148\text{ }^\circ\text{C}$.^[14,15]

To verify that the H_2 plasma is able to remove the CH_3 and PMe_3 groups from the surface an *in-vacuo* XPS experiment was performed on a gold seed layer. The used sample was a silicon oxide substrate, on which a thick gold layer was sputtered. Before performing the *in-vacuo* experiment the sample was coated with 300 gold ALD cycles at a substrate temperature of $90\text{ }^\circ\text{C}$. This was done to eliminate the measurement of an XPS signal from the underlying sputtered gold layer. After the ALD deposition was finished, ending with a H_2 plasma, the sample was transferred within 1 minute from the ALD chamber to the XPS analysis chamber with-

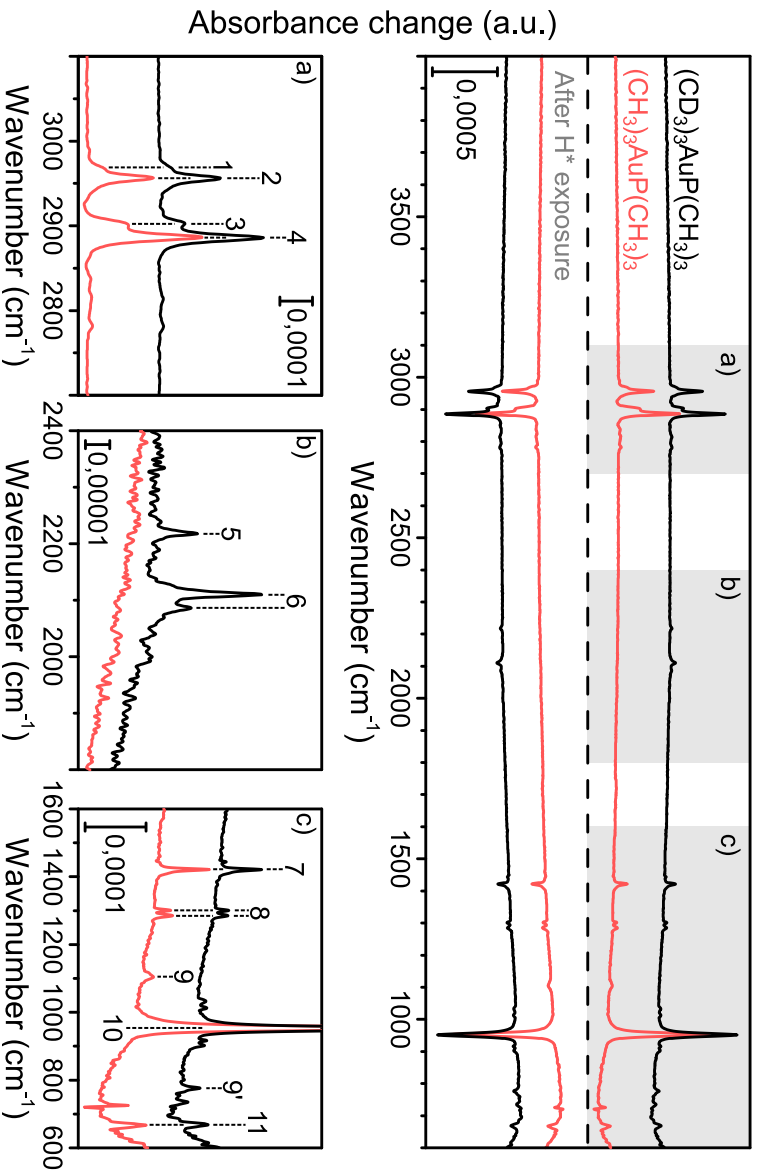


Figure 6.2: Difference spectra for the $\text{Me}_3\text{Au}(\text{PMe}_3)\text{-H}_2$ plasma and $(\text{CD}_3)_3\text{Au}(\text{PMe}_3)\text{-H}_2$ plasma ALD processes. Thick sputtered gold layers (60 nm) were used as substrates and depositions were performed at a substrate temperature of 90°C . The regions marked by a), b), and c) are zooms of the CH -stretching, CD -stretching, and fingerprint regions, respectively, after a precursor exposure. Assignments for the marked peaks can be found in Table 6.1.

Peak	Position (in cm^{-1})	Vibration mode
1	2968	$\nu_{as}(\text{CH}_3)\text{-[P]}$
2	2958	$\nu_{as}(\text{CH}_3)\text{-[P/Au]}$
3	2901	$\nu_s(\text{CH}_3)\text{-[P/Au]}$
4	2887	$\nu_s(\text{CH}_3)\text{-[P/Au]}$
5	2218	$\nu_{as}(\text{CD}_3)\text{-Au}$
6	2110 and 2086	$\nu_s(\text{CD}_3)\text{-Au}$
7	1422	$\delta_{as}(\text{CH}_3)\text{-[P]}$
8	1285 and 1301	$\delta_s(\text{CH}_3)\text{-[P]}$
9	1100	$\delta_{as}(\text{CH}_3)\text{-[Au]}$
9'	778	$\delta_{as}(\text{CD}_3)\text{-[Au]}$
10	954	$\rho(\text{PCH}_3)$
11	667	$\nu_s(\text{PC}_3)$

Table 6.1: Position and assigned vibration modes of the observed features in the FTIR difference spectra displayed in Figure 6.2. The assignment of these peaks is based on a reference IR spectrum for the $\text{Me}_3\text{Au}(\text{PMe}_3)$ molecule and for the PMe_3 ligand.^[8,11,12] (ν stretching, δ deformation, ρ rocking, as = asymmetric, s = symmetric)

out breaking vacuum. The measured P2p, C1s, and Au4f peaks are shown in Figure 6.3. The Au4f peaks show that the gold is present in one oxidation state. The Au4f 5/2 peak was set to 84.0 eV and used to calibrate the spectra. It is clear that no P2p or C1s signals were detected on the sam-

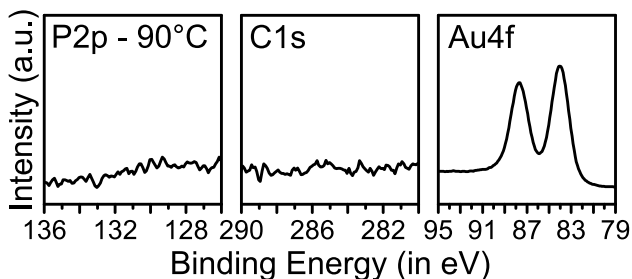


Figure 6.3: P2p, C1s, Au4f peaks measured by XPS on a gold seed layer after performing a gold ALD process ending with a H_2 plasma exposure. The deposition was performed at a substrate temperature of 90°C . After ending the ALD process the sample was transferred within 1 minute from the ALD chamber to the XPS analysis chamber without breaking vacuum.

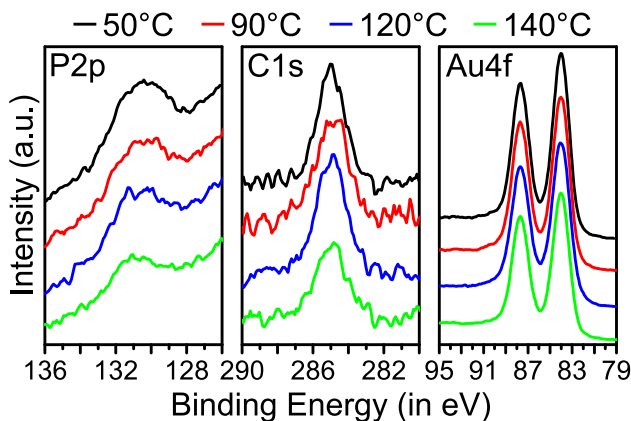


Figure 6.4: P2p, C1s, Au4f peaks measured by XPS on a gold seed layer after performing a gold ALD process ending with a precursor exposure. Depositions were performed at a substrate temperature of 50 °C, 90 °C, 120 °C, and 140 °C. After ending the ALD process the samples were transferred as quickly as possible from the ALD chamber to the XPS analysis chamber without breaking vacuum.

ple after the H₂ plasma pulse, indicating that the CH₃ and PMe₃ groups are removed from the surface by the H₂ plasma, corroborating the RAIRS measurements.

In-vacuo XPS measurements were also performed after the precursor exposure and this was done at four substrate temperatures: 50 °C, 90 °C, 120 °C, and 140 °C. The obtained Au4f, P2p, and C1s peaks of these experiments are displayed in Figure 6.4. It is clear that in all cases the Au surface remains in a metallic state and that there is carbon and phosphorous present from the CH₃ and TMP precursor ligands. The atomic concentrations and C/P ratios of these samples and of samples that were transferred after an 18 hour waiting period are displayed in Table 6.2a and Table 6.2b, respectively. The latter samples remained on the heated copper block for the entire waiting period. The C/P ratio yields information about the ratio of CH₃ to TMP species that are present on the surface. For the samples that were transferred immediately there is an increase in the atomic concentration of the Au4f peak with increasing temperature, which indicates that the amount of C and P on the surface is lower at higher temperatures. A C/P ratio of 6 would indicate that all of the precursor ligands remain on the surface, while lower values indicate the partial removal of the [Au]-CH₃ species from the surface with a value of 3 indicating that only the TMP ligand remains on the surface. The C/P ratios fluctuate between 2.5

	Substrate Temp.	Au4f (atom %)	C1s (atom %)	P2p (atom %)	C/P
a)	50 °C	86 ± 1	10 ± 1	4 ± 1	2.5
	90 °C	88 ± 1	9 ± 1	3 ± 1	3
	120 °C	87 ± 1	10 ± 1	3 ± 1	3.3
	120 °C	89 ± 1	8 ± 1	3 ± 1	2.7
	140 °C	91 ± 1	7 ± 1	2 ± 1	3.5
b)	50 °C	84 ± 1	12 ± 1	4 ± 1	3
	90 °C	83 ± 1	14 ± 1	3 ± 1	4.7
	120 °C	85 ± 1	12 ± 1	3 ± 1	4.3
	140 °C	84 ± 1	13 ± 1	3 ± 1	4.3

Table 6.2: XPS determined atomic concentrations of Au, C, P, and the C/P ratio of $\text{Me}_3\text{Au}(\text{PMe}_3)$ exposures on a gold seed layer at different temperatures. The samples were transferred from the ALD chamber to the XPS analysis chamber without breaking vacuum. a) Samples transferred immediately after the final precursor exposure. b) Samples transferred 18 hours after the final precursor exposure.

and 3.5 which is in agreement with the presence of TMP groups on the surface and only a minority component of CH_3 species, which are contributed by the gold centre. The amount of phosphorous present on the surface is the largest at 50 °C and at the other temperatures there is roughly a quarter to a half less phosphorous present. The amount of phosphorous is directly linked to the amount of TMP on the surface and this result suggests that TMP is less stable on the gold surface with increasing substrate temperature, which is supported by surface science literature, based on temperature programmed desorption (TPD) experiments of dimethylphenylphosphine from $\text{Au}(111)$ surfaces.^[16] The TPD experiments indicated the onset of desorption of chemisorbed dimethylphenylphosphine at a substrate temperature of 60 °C with the peak of desorption above a substrate temperature of 170 °C. For the samples that were transferred after an 18 hour waiting period (Table 6.2b), no significant change in the P2p atomic concentration is observed, but an increase in the carbon signal is present for all of them. The phosphorous signal indicates that at least a fraction of the TMP ligands remains on the surface. Adventitious carbon contaminating the surface can explain the increase in the carbon signal.

6.2.2.1 Stability of surface species

Reports in literature indicate that phosphorous based molecules can form strong bonds with a gold surface,^[16–21] in line with the *in situ* RAIRS

and *in-vacuo* XPS measurements, confirming the presence of TMP groups on the gold surface after the precursor exposure. The *in situ* RAIRS data also revealed the presence of CH₃ groups on the gold surface. However, the C/P ratios determined from the *in-vacuo* XPS measurements indicate that the CH₃ species are removed from the surface and over time mainly the TMP ligands remain. It needs to be noted that the measurement time of both methods differs significantly. Each IR measurement is completed within 2 minutes after the precursor exposure, while each *in-vacuo* XPS experiment lasted for several hours. To bridge this gap, we performed several RAIRS measurements over the course of an hour after a precursor exposure. This was done at a substrate temperature of 90 °C and 120 °C. The obtained results can be seen in Figure 6.5. The normalized intensity of the main TMP rocking mode (954 cm⁻¹) is plotted as a function of time after precursor exposure in Figure 6.5a. The intensity decays over time for both temperatures and this decay occurs faster at 120 °C than at 90 °C, suggesting that these groups are less stable at higher substrate temperatures. Figure 6.5b shows the 1250-900 cm⁻¹ region of the first two spectra that were obtained during these experiments at 90 °C and 120 °C. A first thing to note is that the initial spectrum obtained at 90 °C shows the [Au]-Me mode at 1100 cm⁻¹, while the spectrum obtained at 120 °C does not, indicating that the [Au]-Me groups are less stable at higher substrate tem-

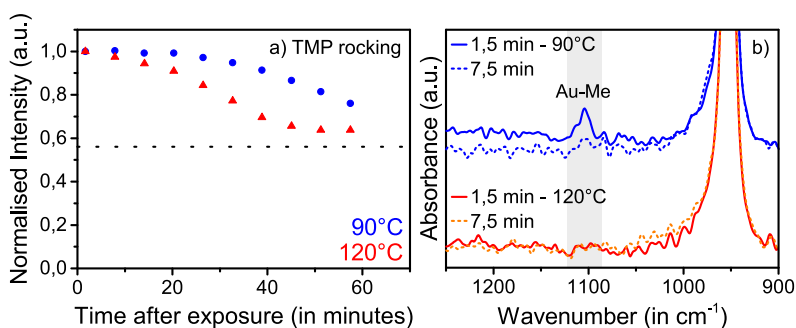


Figure 6.5: RAIRS data for a precursor exposure on a thick sputtered gold layer at a substrate temperature of 90 °C and 120 °C. a) Normalized intensity of the main TMP rocking mode at 954 cm⁻¹ as a function of the elapsed time after a precursor exposure. The dotted line represents the normalized intensity at 120 °C after 2 hours and 30 minutes. b) finger-print region, covering the $\delta_{as}(\text{CH}_3)$ -[Au] deformation mode (grey box, 1100 cm⁻¹) and the main TMP rocking mode. The shown spectra are recorded 30 seconds after the precursor exposure and 6 minutes and 30 seconds after the precursor exposure.

peratures. The second spectrum obtained at 90 °C shows that the [Au]-Me vibration mode has decreased to the noise level, indicating that the CH₃ groups quickly desorb from the surface, which is in agreement with the observed *in-vacuo* XPS results.

6.2.3 Reaction by-products

While the *in situ* RAIRS and *in-vacuo* XPS data yield information about the surface groups that are present after each exposure, they do not provide information about the reaction by-products that are being formed during the process. In order to study the formed by-products we used *in situ* quadrupole mass-spectrometry (QMS) during the ALD process. Mass-to-charge ratios for methyl, methane, ethane, PH_x, PMe_x, and H_yPMe_x (x, y = 1-3) were followed. This was done during five ALD cycles, each exposure lasted for 15 seconds with a 15 seconds pump steps between exposures. Three precursor exposures were given before performing the ALD cycles to saturate the surface and after the ALD cycles three H₂ plasma exposures were given. The obtained data for mass to charge ratios 15 (CH₃) and 16 (CH₄) as a function of time is displayed in Figure 6.6. The signal for the other mass to charge ratios did not exceed the noise level.

The signal for mass 15 is part of the cracking pattern for a pure methane gas. In this case the signals of masses 15 and 16 coincide with the expected ratio for a methane cracking pattern. This indicates that CH₄ groups are formed during the H₂ plasma exposures. While this accounts for the removal of the methyl groups from the surface, it does not reveal how the phosphorous of the PMe₃ ligands is removed from the surface as the signals for the phosphine and (tri,di)methylphosphine related masses did not exceed the noise level during the exposure. It is possible that they reacted with the side walls of the flexible tube that connects the chamber to the QMS detector and did not reach the QMS detector.

The QMS data also reveal that a minor fraction of CH₄ is formed during the precursor exposure and the ratio of the signals for masses 15 and 16 coincides with the expected ratio for a pure CH₄ gas. This indicates that the observed signal originates from CH₄ groups instead of CH₃ radicals. Otherwise, the signal for mass 15 can be expected to be much larger than the signal for mass 16. There are a few possible explanations for the formation of CH₄: CH₃ ligands on the surface are able to react with hydrogen, either present on the surface or impinging on the surface from residual molecular hydrogen in the chamber. Another possibility is that CH₃ radicals desorb from the surface and pick up a hydrogen atom when colliding with the walls/inlet of the chamber/QMS inlet or residual hydrogen in

the chamber. The latter case is less likely as it can be expected that this would lead to a larger signal for CH_3 species, compared to that of CH_4 . A final possibility is that CH_3 ligands abstract a hydrogen atom from neighbouring CH_3 ligands, as is the case in the thermal $\text{MeCpPtMe}_3 - \text{O}_2$ ALD process.^[22] It has been observed that Au^+ and Au_2^+ cations are able to dehydrogenate methane to CH_2 and for the Au_2^+ cations the adsorption of multiple methane molecules leads to the formation of ethylene.^[23-27] However, larger gold particles are not able to cleave more than one C-H bond of methane and for particles that contain more than 15 Au atoms even the adsorption of methane is not observed.^[28]

Interestingly, there is no ethane detected during the precursor exposure, while its formation is to be expected from the decomposition literature of similar liquid gold compounds. The first step in the reduction of Au(III) compounds to Au(o) occurs by alkyl-coupling, causing the removal of two

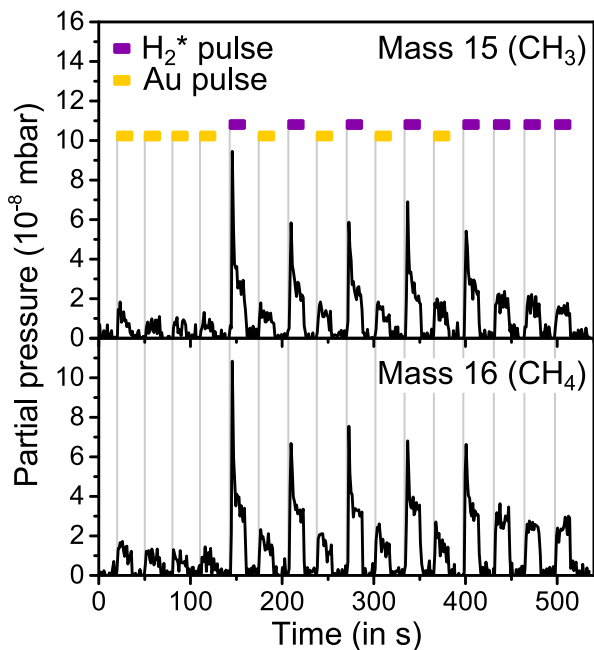


Figure 6.6: Mass spectrometry measurements for mass to charge ratios 15 (CH_3) and 16 (CH_4) during a $\text{Me}_3\text{Au}(\text{PMe}_3) - \text{H}_2$ plasma process. The data shows 3 precursor pulses, followed by 5 ALD cycles and ending with an additional 3 H_2 plasma pulses. The deposition was carried out using a substrate temperature of 90°C .

of the CH_3 groups, forming ethane, and reducing the gold atom from a +3 to a +1 oxidation state.^[2-4] This is also seen when adsorbing alkyl-halide molecules on gold surfaces with the onset of ethane desorption at -33°C from Au(111) planes and at 27°C from Au(100) planes.^[29,30] However, when co-adsorbing $\text{CH}_3\text{-I}$ with trimethylphosphine on a Au(100) surface the formation of ethane does not occur and instead the CH_3 species desorb as CH_3 -radicals above a substrate temperature of 100°C .^[30] The removal of CH_3 groups from Au(111) planes can thus occur below 0°C ,^[29,30] which in our case would mean that the CH_3 groups that are adsorbed during the precursor exposure will quickly be removed from the gold surface. And, as no ethane is detected in the QMS, it is likely that the co-adsorption of trimethylphosphine on Au(111) planes has a similar effect as the co-adsorption on Au(100) planes, preventing the coupling of the alkyl groups on the surface.

6.2.4 Reaction scheme

Based on the *in situ* RAIRS, *in-vacuo* XPS, and *in situ* QMS data it is possible to propose a reaction mechanism for the $\text{Me}_3\text{Au}(\text{PMe}_3) - \text{H}_2$ plasma ALD process under steady growth conditions. This reaction scheme is depicted in Figure 6.7 for three different temperature regimes: $T < 100^\circ\text{C}$, $100^\circ\text{C} < T < 120^\circ\text{C}$, and $T > 120^\circ\text{C}$ with the main reaction scheme given by the first temperature regime, the other temperature regimes extend on it to include additional effects that cause the precursor decomposition on a gold surface (see Figure 6.1).

The first step in the ALD process will be to expose this surface to the $\text{Me}_3\text{Au}(\text{PMe}_3)$ molecules, which will physisorb on the surface (step a). After physisorption, the precursor molecules can undergo reactions with the surface and chemisorb. Based on how similar gold molecules behave in a liquid the most likely pathway for chemisorption on the gold surface is by breaking the Au-P bond (step b).^[3,4] The *in situ* RAIRS measurements (Figure 6.2) show that both CH_3 and PMe_3 ligands remain on the gold surface after chemisorption. The surface coverage with CH_3 and PMe_3 ligands will prevent further adsorption of $\text{Me}_3\text{Au}(\text{PMe}_3)$ molecules and cause self-limiting behaviour during the $\text{Me}_3\text{Au}(\text{PMe}_3)$ exposure. During the chemisorption step the CH_3 species start to desorb from the surface, most likely in the form of CH_4 , as evidenced by the QMS data (step c). Most likely the CH_3 ligands react with residual hydrogen in the chamber or atomic hydrogen that is present on the surface to form CH_4 . It is also possible that the CH_3 groups abstract a hydrogen atom from a neighbouring CH_3 group to form CH_4 and leave a CH_2 group on the surface.

However, it is expected that this effect only occurs for very small gold particles (less than 15 Au atoms).^[28]

The C/P ratio obtained from the *in-vacuo* XPS data shows that this desorption of CH₃ groups occurs at all substrate temperatures. Based on the results from Paul and Bent this is expected for Au(111) planes at the used substrate temperatures, while on Au(100) planes this should only occur above a substrate temperature of 100 °C.^[30] The *in situ* RAIRS experiments (Figure 6.5b) indicate that at 90 °C there are still CH₃ groups present after several minutes, while they are undetectable at 120 °C, showing that the removal of CH₃ species occurs faster at higher temperatures.

The RAIRS and XPS data show that the TMP ligand is rather stable on the gold surface. There are reports of the behaviour of the TMP ligand on a gold surface in literature. Jewell et al. reported that annealing one monolayer of adsorbed TMP on a Au(111) surface to 77 °C results in a coverage of 88 % of a monolayer.^[20] Temperature programmed desorption experiments of dimethylphenylphosphine on Au(111) indicate an onset of desorption around 77 °C, although the maximum of the desorption peak is located above 177 °C.^[16] In addition, it is expected that in the class of alkylphosphine molecules swapping the phenyl groups with a CH₃ group results in a stronger Au-P bond,^[19] which would indicate a higher desorption temperature for TMP compared to dimethylphenylphosphine, meaning that the TMP groups remain stable for a longer period of time at substrate temperatures below 100 °C. This is also corroborated by the *in situ* RAIRS experiments (Figure 6.5a), showing that while at 90 °C the TMP groups are being removed from the surface they remain stable for a rather long time period.

As mentioned in step b of the ALD cycle, it is likely that the chemisorption step involves breaking the Au-P bond, leaving TMP and CH₃ groups on the surface. The stability of these groups has an influence on the observed precursor decomposition behaviour (see Figure 6.1). If these surface species are unstable on the gold surface they will desorb over time and in doing so create additional physisorption sites for the precursor molecules, leading to precursor decomposition. Based on the decomposition curve of Figure 6.1 there are three regions that can be distinguished: T = 50 - 100 °C, T = 100 - 120 °C, and T > 120 °C, the stability of the surface species for each temperature region is depicted in step c.

Below 100 °C only a minor decomposition component is observed and based on the discussion of the RAIRS and XPS data it seems likely that the main desorption component originates from the CH₃ ligands (most likely in the form of CH₄), or at least on the timescale of a single ALD cycle. In addition the coverage of TMP on a gold surface can be expected to be not

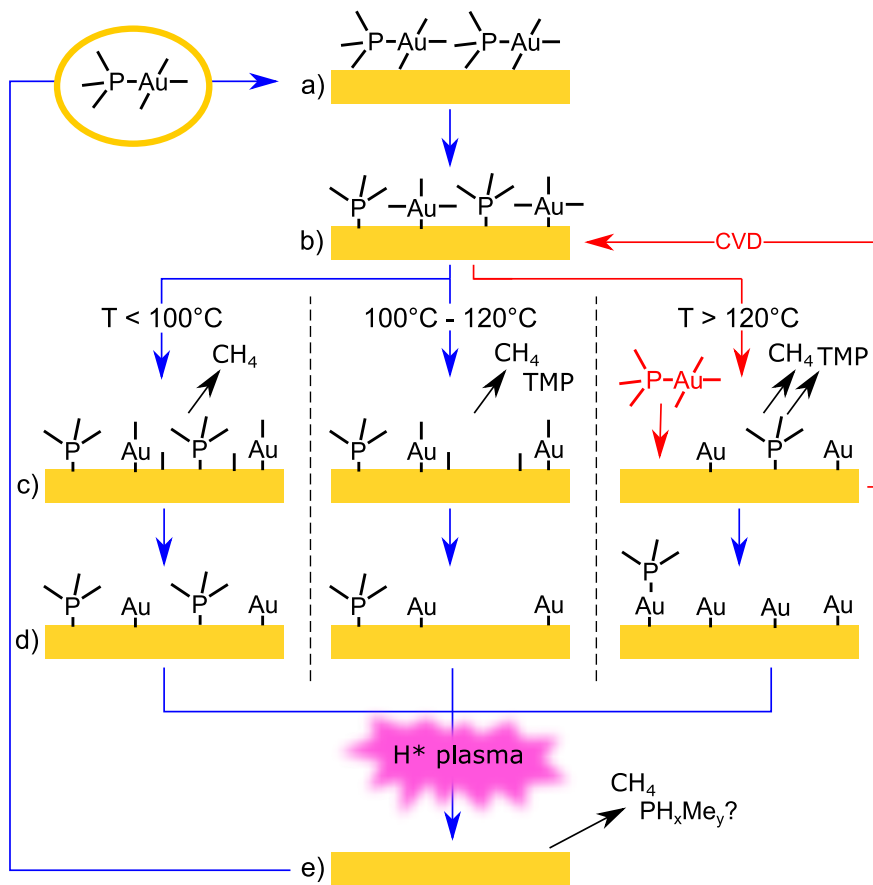


Figure 6.7: Schematic drawing of the $\text{Me}_3\text{Au(PMe}_3\text{)}$ - H_2 plasma ALD process for different substrate temperatures. (TMP = PMe_3 , each dangling bar (-) represents a CH_3 group) a) Physisorption of the precursor on a clean gold surface. b) Initial chemisorption on the surface. c) Desorption of CH_4 and TMP species. d) Final surface state after pumping. e) Removal of remaining surface groups by H_2 plasma.

more than 88% of a monolayer, which can already account for the most part of the observed decomposition component at this temperature.

For substrate temperatures between 100 °C and 120 °C the decomposition increases with temperature, surpassing the expected GPC of the ALD process at 120 °C. Based on the above discussion, this increase in decomposition as a function of substrate temperature indicates that both CH₃ and TMP are able to desorb in reasonable amounts from the surface within the timescale used for ALD, providing additional adsorption sites for the precursor during the next exposure.

The large and uncontrolled decomposition at substrates temperature above 120 °C indicates that the desorption of CH₃ and TMP is able to occur fast enough during the precursor exposure in such a way that during ALD the GPC exceeds the value of 0.03 nm per cycle, which is obtained for saturated reactions below 100 °C. The result is that during exposure additional adsorption sites are created for the precursor, which leads to additional deposition of gold on the surface and uncontrolled growth rates at high temperatures. In addition, above 120 °C thermal decomposition is expected to occur.^[7]

Based on the C/P ratio of 3 determined from the XPS experiments all CH₃ groups will be removed from the surface after the precursor exposure when sufficient time is given and the surface will be covered by a varying amount of TMP molecules, dependent on the substrate temperature (step d). This coverage will determine the amount of adsorption sites for precursor molecules when the surface is again exposed to the precursor, which can explain the observed precursor decomposition curve.

After the precursor exposure the surface is exposed to a H₂ plasma (step e). The plasma removes the contaminating PMe₃ and remaining CH₃ groups from the surface, evidenced by the RAIRS and XPS measurements. Insufficiently long plasma exposures result in the incomplete removal of the precursor ligands, indicated by *ex situ* XPS measurements on gold films deposited with short plasma exposures, see Supporting Information. This means that after a too short plasma exposure a part of the precursor adsorption sites are blocked by remaining precursor ligands, which results in a lower GPC for the ALD process. Based on the QMS data the CH₃ species are liberated and converted to CH₄. It is unclear in exactly what form the phosphorous is removed from the surface, as no phosphorous containing species were detected in the QMS measurements. However, it is likely that it is removed as methylphosphine or phosphine species (PH_xMe_y, x,y=0-3). The end result is expected to be a clean gold surface, because there was no direct evidence of atomic hydrogen on the gold surface. Although it cannot be excluded that a small concentration of atomic

hydrogen remains on the surface, aiding with the removal of the CH_3 species as CH_4 in step c of the reaction. After the plasma exposure the ALD cycle can start over on this clean gold surface.

6.2.5 Nucleation on SiO_2

Precursor decomposition happens on a gold surface; however, it does not on a silicon oxide surface. Using a co-reactant it is possible to deposit gold on an oxide surface, indicating that the precursor is present on the surface after an exposure. This raises the question whether the precursor is physisorbed or chemisorbed on the surface and what are the possible nucleation sites on the surface. The adsorption of $\text{Me}_3\text{Au}(\text{PMe}_3)$ on high surface area silica at 100°C was studied previously by Pallister and Barry using solid-state NMR spectroscopy measurements.^[31] They found that after the $\text{Me}_3\text{Au}(\text{PMe}_3)$ exposure several surface species were present, including AuPMe_3 , reduced gold phosphine, methylated phosphoxides, and graphitic carbon. The precursor preferentially reacts with lone silanol groups and an overall precursor coverage of 10% of the surface is observed. Here, we will discuss *in situ* transmission FTIR experiments to provide additional data of the nucleation sites of the $\text{Me}_3\text{Au}(\text{PMe}_3)$ precursor on a silicon oxide surface.

To study the nucleation stage of the $\text{Me}_3\text{Au}(\text{PMe}_3)$ - H_2 plasma ALD process, we performed *in situ* transmission absorption infrared measurements on double polished silicon substrates, with native oxide. IR measurements were performed during the first 40 ALD cycles of the process. An oxygen plasma pre-treatment was used to remove carbon contamination from the substrate and a substrate temperature of 90°C was used during the deposition.

When the sample was mounted with the surface normal parallel to the incident IR beam there was no visible difference in absorption that can be attributed to the ALD process, see Supporting Information. However, mounting the sample with the surface normal at an angle of 75° with respect to the incident IR beam resulted in noticeable absorption modes from the precursor ligands. This angle lies close to the Brewster angle for silicon in the wavelength region of $2.5\ \mu\text{m}$ to $25\ \mu\text{m}$, i.e. 73.8° assuming a refractive index of 3.44. The transmitted IR beam will therefore be partially P-polarized, indicating that the vibration modes of the precursor ligands are preferentially oriented out of plane. The difference spectra for the first four ALD cycles are displayed in Figure 6.8.

After the first precursor exposure, there is absorption at $960\ \text{cm}^{-1}$, originating from the PMe_3 ligand of the precursor. This indicates that chemisorp-

tion of the precursor occurs during the first exposure. In addition, isolated Si-OH groups (at 3745 cm^{-1}) are consumed during the precursor exposure of the first three ALD cycles.^[32]

After the first H_2 plasma there is a shift in absorption from 3745 cm^{-1} to 3680 cm^{-1} . The vibration mode at 3680 cm^{-1} can be linked to hydrogen bonded Si-OH groups.^[32] In addition, two broad absorption features appear in the region of 2400 cm^{-1} to 1950 cm^{-1} . Absorption due to the stretching mode of metal-hydrogen bonds is expected to occur in this region. These two features most likely originate from Si-H species that are formed during the H_2 plasma exposure.^[33] This suggests that the first H_2 exposure is able to break some of the surface Si-O-Si bonds and forms Si-OH and Si-H species.^[34] The following gold exposures also consume a fraction of the Si-OH groups that are present, but this effect stops after the fourth

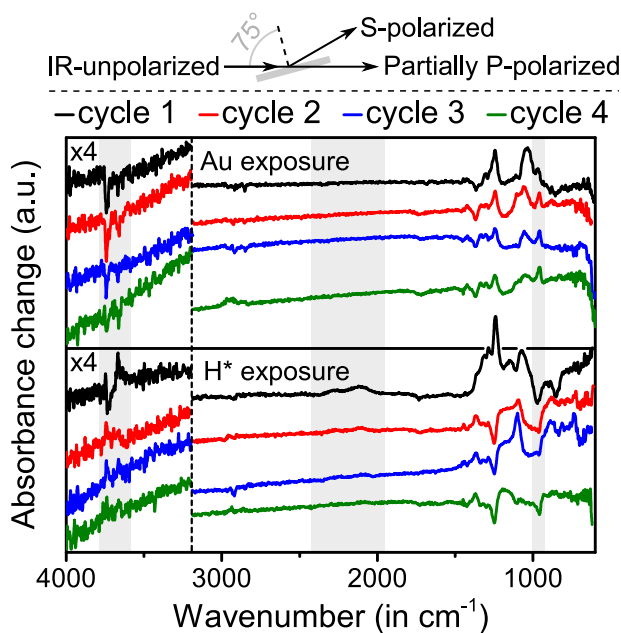


Figure 6.8: Transmission difference spectra of the ALD process on a silicon (native oxide) substrate. The substrate temperature was $90\text{ }^\circ\text{C}$ during this experiment. The angle between the surface normal of the substrate and the incident beam was 75° . A schematic representation of the geometry is drawn above the image. The grey box on the left marks the OH stretching region, which is multiplied by a factor of 4. The middle box marks the Si-H stretching region and the box on the right marks the main PMe_3 deformation mode (at 960 cm^{-1}).

ALD cycle. This indicates that these groups are mainly consumed during the initial nucleation stage. After several cycles the obtained difference spectra start to resemble the steady growth spectra that were recorded in RAIRS mode on a gold seed layer (Figure 6.2 and see Supporting Information). These results are in agreement with the results obtained by Pallister and Barry, as they also observed that the $\text{Me}_3\text{Au}(\text{PMe}_3)$ has a preference for lone silanol groups as reactive sites on the surface.^[31]

6.2.6 Comparison of $\text{Me}_3\text{Au}(\text{PMe}_3)$ -based PE-ALD processes with different co-reactants

Two $\text{Me}_3\text{Au}(\text{PMe}_3)$ -based gold ALD processes have been reported.^[6,7] Up till now we have only presented results for the H_2 plasma process, neglecting the existing $\text{Me}_3\text{Au}(\text{PMe}_3) - \text{O}_2$ plasma - H_2O ALD process reported by Griffiths et al.^[7] However, it is noteworthy that applying the 3-step process with O_2 plasma and H_2O in our pump-type reactor did not result in the reproducible formation of metallic gold, but rather in the growth of an amorphous gold containing film.

By swapping the H_2O exposure in the three-step process by a H_2 plasma ($\text{Me}_3\text{Au}(\text{PMe}_3) - \text{O}_2^* - \text{H}_2^*$) it was possible to deposit metallic gold films. XRD patterns for the above mentioned deposition processes (H_2^* , $\text{O}_2^* - \text{H}_2\text{O}$, $\text{O}_2^* - \text{H}_2^*$ in pump-type) are shown in Figure 6.9, together with a reference of a sample grown by the $\text{O}_2^* - \text{H}_2\text{O}$ process in a flow-type reactor. The patterns indicate that the only process that does not yield crystalline gold films is the $\text{Me}_3\text{Au}(\text{PMe}_3) - \text{O}_2$ plasma - H_2O process performed in a pump-type reactor, in contrast to the same process applied in a flow-type reactor. The other films show diffraction peaks for $\text{Au}(111)$ and $\text{Au}(200)$ planes, proving their crystalline nature.

XPS measurements were also performed on these samples, the measured $\text{O}1s$, $\text{C}1s$, $\text{P}2p$, and $\text{Au}4f$ peaks on the air-exposed surface and after 100 seconds of argon sputtering are displayed in Figure 6.10. For all samples there is adventitious carbon present on the surface, but no carbon is present in the film itself. The $\text{Au}4f$ peaks are not in a pure metallic state for the $\text{Me}_3\text{Au}(\text{PMe}_3) - \text{O}_2$ plasma - H_2O process in a pump-type reactor showing gold in a $\text{Au}(0)$ and $\text{Au}(+1)$ oxidation state. After sputtering the $\text{Au}4f$ peaks are of a metallic nature, however it is most likely that the $\text{Au}(+1)$ species are reduced to $\text{Au}(0)$ as a consequence of the sputtering process and as such this cannot be taken as an indication that the underlying gold is in a metallic state, which would otherwise conflict with the observed XRD pattern of this film (Figure 6.9). The gold in the other three samples is in a metallic state, as deposited and after sputtering, which is

in agreement with the measured XRD patterns (Figure 6.9). On all samples there is a O1s peak visible, which for the $\text{Me}_3\text{Au}(\text{PMe}_3)$ - O_2 plasma - H_2O flow-type process and for the $\text{Me}_3\text{Au}(\text{PMe}_3)$ - H_2 plasma process has a binding energy around 532.9 eV and most likely originates from the silicon oxide of the substrate. For these two samples, there is also no phosphorous present on the surface or after sputtering, showing that these films consist of pure gold. For the other two samples, there is a clear presence of phosphorous, both on the surface and after sputtering. The P2p peaks have a binding energy between 133.5 eV and 134.6 eV, which is consistent with P-O and P=O bonds, originating from phosphate groups.^[35,36] These results show that pure gold films can be deposited in a flow-type reactor using O_2 plasma and H_2O as co-reactants and in a pump-type reactor when using H_2 plasma. In a pump-type reactor, the use of an O_2 plasma results in the formation of a gold containing phosphate layer, and reducing the deposited layer to metallic gold is not possible using H_2O but can be achieved when using H_2 plasma as the second co-reactant. How-

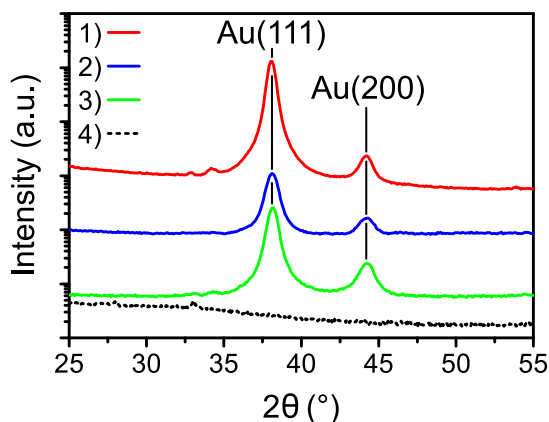


Figure 6.9: XRD patterns of four ALD deposited gold films on silicon (native oxide), all depositions were performed at a substrate temperature of 120 °C. The Au(111) and Au(200) peaks are respectively marked at 38.3° and 44.5°. 1) $\text{Me}_3\text{Au}(\text{PMe}_3)$ - H_2 plasma process, performed in a pump-type reactor (equivalent to 21 nm of sputtered gold). 2) $\text{Me}_3\text{Au}(\text{PMe}_3)$ - O_2 plasma - H_2 plasma process, performed in a pump-type reactor (equivalent to 6 nm of sputtered gold). 3) a $\text{Me}_3\text{Au}(\text{PMe}_3)$ - O_2 plasma - H_2O process, performed in a flow-type reactor (equivalent to 9 nm of sputtered gold). 4) a $\text{Me}_3\text{Au}(\text{PMe}_3)$ - O_2 plasma - H_2O process, performed in a pump-type reactor (equivalent to 10 nm of sputtered gold). The displayed patterns were given an offset.

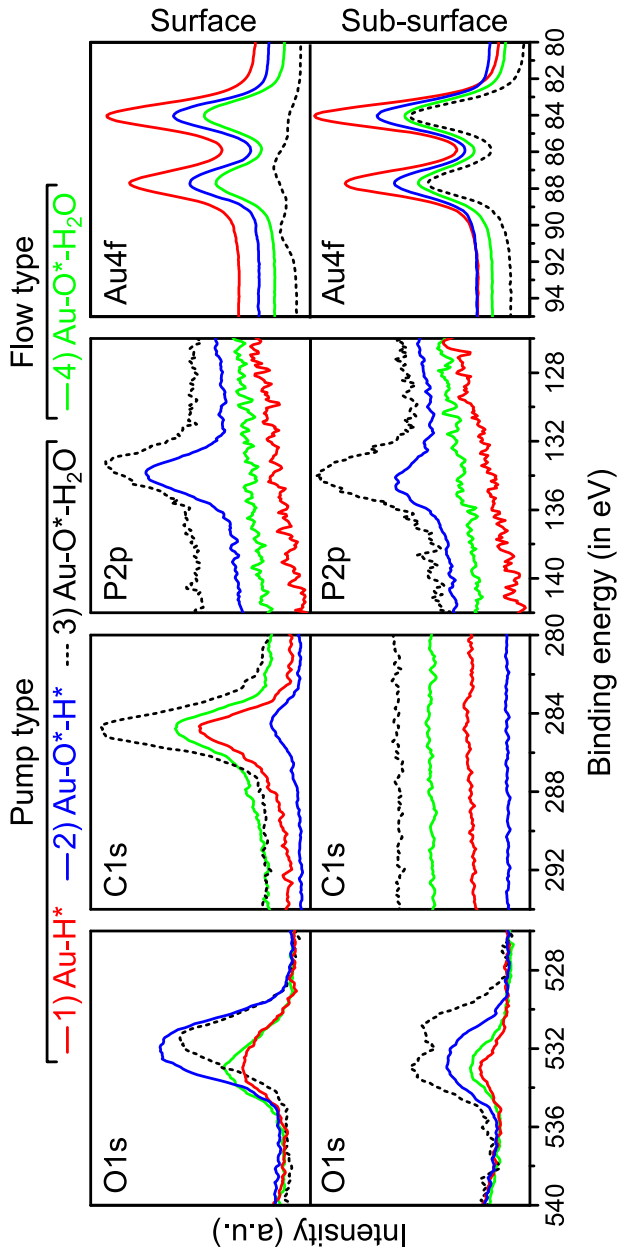


Figure 6.10: XPS spectra of four gold films on silicon (native oxide) substrates for the air-exposed samples (top panels) and after removal of the top surface by argon sputtering (bottom panels). 1) a $\text{Me}_3\text{Au}(\text{PMe}_3)$ - H_2 plasma process, performed in a pump-type reactor (equivalent to 21 nm of sputtered gold). 2) a $\text{Me}_3\text{Au}(\text{PMe}_3)$ - O_2 plasma - H_2 plasma process, performed in a pump-type reactor (equivalent to 6 nm of sputtered gold). 3) a $\text{Me}_3\text{Au}(\text{PMe}_3)$ - O_2 plasma - H_2O process, performed in a flow-type reactor (equivalent to 9 nm of sputtered gold). 4) a $\text{Me}_3\text{Au}(\text{PMe}_3)$ - O_2 plasma - H_2O process, performed in a pump-type reactor (equivalent to 10 nm of sputtered gold). The displayed spectra were given an offset.

ever, even the use of H_2 plasma is not able to easily remove the phosphate layer that is formed during the O_2 plasma exposure. It is possible that a difference in pressure for the used H_2O exposure between both reactor types leads to the incomplete removal of the phosphate layer, with a maximum H_2O partial pressure of 0.17 mbar in the flow-type reactor. For this reason, the used pressure during the H_2O exposure was varied between 6×10^{-3} mbar and 5 mbar; however, there was no difference in the gold-phosphate films that were formed in these experiments. It is possible that hydrogenating the phosphate layer to form phosphoric acid is followed by dehydrogenation in a pump-type reactor, instead of removing it from the surface. Another, more likely, possibility is that differences in the O_2 plasma properties that are used during the process lead to significantly different phosphate layers, making it more difficult to remove from the surface with a water exposure in a pump-type system.

Depositions using the $Me_3Au(PMe_3) - O_2$ plasma - H_2O process in our pump-type reactors always yielded amorphous gold containing phosphate films, which is a clear difference compared to the results obtained for this process in a flow-type reactor.

6.3 CONCLUSION

The reaction mechanism and ligand stability of the $Me_3Au(PMe_3) - H_2$ plasma process in the steady growth regime has been investigated in a pump-type reactor. During the main reaction mechanism, the PMe_3 and CH_3 ligands of the precursor remain on the gold surface after chemisorption of the $Me_3Au(PMe_3)$ molecules, causing self-saturating behaviour during the precursor exposure. The precursor ligands are removed by the H_2 plasma exposure, resulting in the formation of CH_4 and possibly (tri-, di-)methylphosphine / phosphine groups.

A minor fraction of precursor decomposition occurs due to the desorption of the ligands from the surface, as this effect creates additional adsorption sites for the next precursor exposure in a decomposition experiment. For substrate temperatures above $100^\circ C$ the amount of precursor decomposition increases with substrate temperature and at $120^\circ C$ the decomposition becomes larger than the GPC of the ALD process. At this temperature the deposition occurs through CVD as there is no self-limiting behaviour of the surface during the precursor exposure. At all substrate temperatures the CH_3 groups get removed from the surface over time, most likely in the form of CH_4 . This occurs faster at higher substrate temperatures. The desorption of the PMe_3 groups from the surface, which

increases with temperature, seems to be the main factor that determines the precursor decomposition behaviour.

Importantly, precursor decomposition does not occur on a SiO₂ surface, hence another reaction mechanism must be responsible for the nucleation of Au PE-ALD on this surface. Transmission IR measurements on SiO₂ substrates indicate that Si-OH surface groups are consumed during the initial Me₃Au(PMe₃) exposures, which makes them the most likely candidates to act as nucleation sites for the Me₃Au(PMe₃) - H₂ plasma process. This observation is in agreement with the results of Pallister and Barry of the adsorption of Me₃Au(PMe₃) on high surface area silica powder.^[31]

Finally, we used O₂ plasma and H₂O as co-reactants in our pump-type ALD systems and compared the obtained film to a metallic and chemically pure gold film that was deposited in a commercial flow-type reactor, using the Me₃Au(PMe₃) - O₂ plasma - H₂O gold ALD process.^[7] Instead of a metallic gold film we obtained amorphous gold-containing phosphate films, as verified by XPS and XRD measurements. Swapping the H₂O exposure step with a H₂ plasma resulted in the formation of metallic gold films, showing that a stronger reducing co-reactant is required in pump-type systems. However, the use of a H₂ plasma in the process was not sufficient to completely remove the phosphate layer that is formed during the O₂ plasma step. This indicates that, once formed, it is difficult to remove the phosphate layer in a pump-type ALD system, where the Me₃Au(PMe₃) - H₂ plasma two step process is the preferred process for obtaining high quality gold films.

6.4 SUPPORTING INFORMATION

NMR MEASUREMENTS were performed on both types of precursor that were used for the ALD experiments. Results for the $\text{Me}_3\text{Au}(\text{PMe}_3)$ liquid are shown in Figure 6.11a, the spectrum confirms that the $\text{Me}_3\text{Au}(\text{PMe}_3)$ liquid has a purity of 95%, with < 5% of MeAuPMe_3 . The NMR results for the $(\text{CD}_3)_3\text{Au}(\text{PMe}_3)$ liquid (Figure 6.11b) show that the used precursor liquid has a purity of at least 95% and a deuteration of more than 99%.

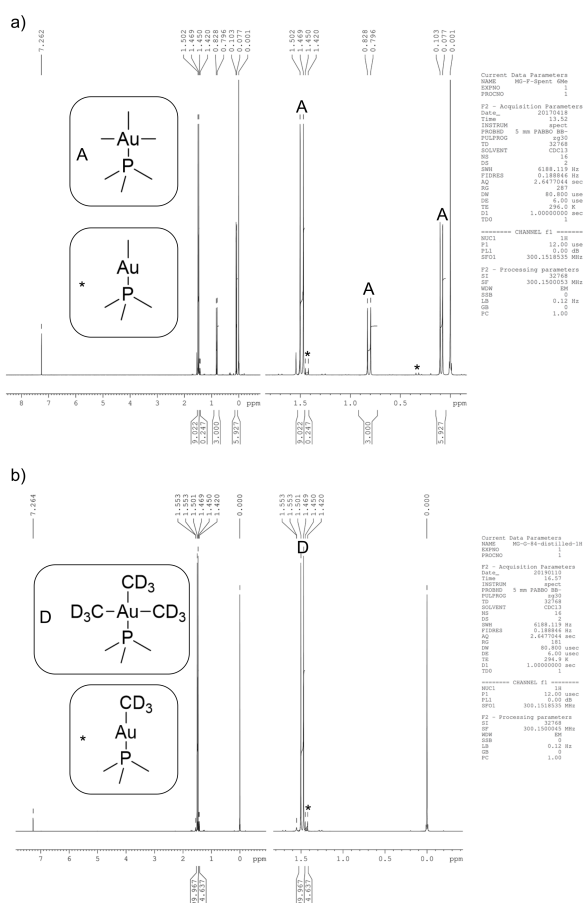


Figure 6.11: NMR spectra of the used precursor liquids. a) spectrum of $\text{Me}_3\text{Au}(\text{PMe}_3)$, indicating that the liquid has only a minor component of MeAuPMe_3 (<5%). b) spectrum showing a pure $(\text{CD}_3)_3\text{Au}(\text{PMe}_3)$ (< 5%, $\text{CD}_3\text{AuPMe}_3$), with at least >99% deuteration.

VARYING THE PLASMA EXPOSURE: *In situ* RAIRS experiments show that the CH_3 groups and PMe_3 groups are removed from the surface by the H_2 plasma exposures. This was verified by *in vacuo* XPS measurements, showing that a H_2 plasma exposure of 10 seconds is sufficient to remove the contaminating surface groups. Beside this, we also performed *ex situ* XPS measurements on three ALD gold samples, deposited using different plasma exposure lengths. These samples were deposited on silicon oxide substrates at a substrate temperature of 90°C , with saturating precursor exposures. The C1s and P2p peaks for these samples are displayed in Figure 6.12. The samples were measured after air-exposure (top panel) and after removing the surface contamination by argon sputtering (bottom panel).

On the air-exposed samples, there is a clear P2p peak present for the sample with a plasma exposure of 2 seconds, while for the longer exposures this peak is not clearly present and remains below the detection

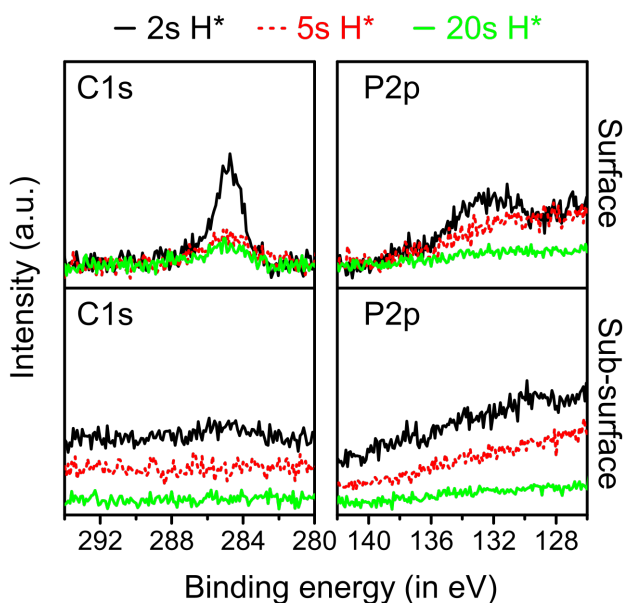


Figure 6.12: *Ex situ* XPS spectra for the C1s and P2p peaks of three ALD deposited gold samples using different plasma exposures. The depositions were carried out on silicon oxide substrates at 90°C , using saturating $\text{Me}_3\text{Au}(\text{PMe}_3)$ exposures. Air-exposed samples are displayed in the top panel, while the bottom panel show the same samples after 100s of argon sputtering.

limit. After removing the top-layer by argon sputtering there is no clear presence of phosphorous for the longer plasma exposures and there is a small remnant visible of the P2p peak, around 130 eV, for the shortest plasma exposure. For the carbon peak (C1s) there is also a clear difference on the air-exposed surface for the shortest plasma exposure and the other two samples. The 5 s and 20 s plasma exposed samples have a comparable C1s peak, which can be attributed to adventitious carbon from exposure to the atmosphere. For the 2 s plasma exposed sample the C1s peak is significantly larger compared to the other samples. While there will be a contribution of adventitious carbon for all three samples, the air-exposure for all three samples was similar. The most likely origin of this additional carbon is from the CH₃ groups of the PMe₃ ligand. A lower GPC is observed for shorter plasma exposures, indicating that something is prohibiting the chemisorption of additional precursor molecules during the precursor exposure, causing the lower GPC. From the *ex situ* XPS measurements it is to be expected that there are still PMe₃ ligands present on the surface for shorter plasma exposures, which occupy possible chemisorption sites, reducing the amount of gold atoms that can be deposited during each Me₃Au(PMe₃) exposure.

NUCLEATION DATA: *In situ* transmission FTIR measurements were used to study the nucleation stage of the Me₃Au(PMe₃) - H₂ plasma ALD process. For this a silicon substrate (with native oxide) was used and was heated to 90 °C during the ALD deposition. The sample could be mounted on the substrate holder with different incidence angles of the IR beam, with respect to the surface normal of the sample. Experiments were performed in which the IR beam had an incidence angle of 0° and 75° with respect to the surface normal. Difference spectra for ALD cycle 1; 20, and 40 of both experiments are displayed in Figure 6.13. At an incidence angle of 0° (Figure 6.13a) it is not possible to identify any of the expected absorption peaks from the precursor, while at an incidence angle of 75° (Figure 6.13b) there are clearly changes in absorption present after the first precursor exposure. And after 20 ALD cycles the difference spectra start to resemble the steady state case of the process. The displayed spectra of Figure 6.13b are scaled down to compensate for the increase in measured surface area due to the larger incidence angle.

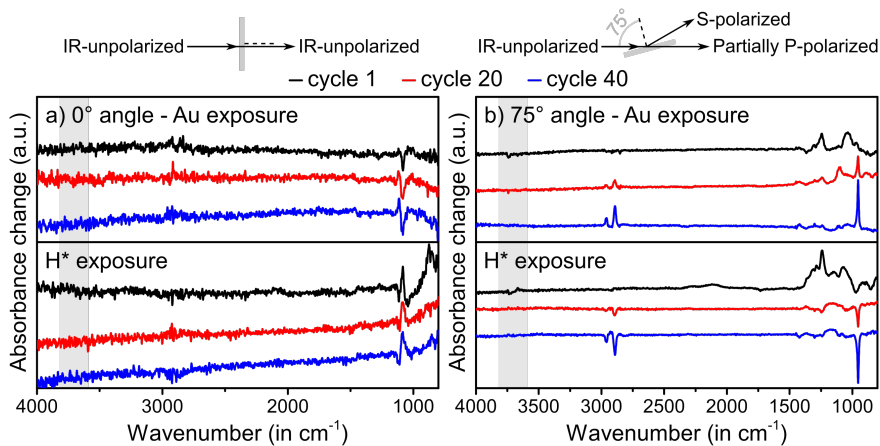


Figure 6.13: Transmission infrared difference spectra for the precursor and co-reactant exposures for ALD cycles 1, 20, and 40. The spectra were measured after each exposure during the gold ALD deposition and was performed at a substrate temperature of 90 °C. The grey box marks the OH stretching region. a) Sample mounted with its surface normal parallel to the incident IR beam. b) Sample mounted with the surface normal angled at 75° with respect to the incident IR beam. The spectra were scaled down by a factor of 3,86 to correct for increase in measured surface area. The geometry of the incident IR beam and the substrate is drawn above the figure for both cases. The dash black line represents the surface normal of the sample.

REFERENCES

- [1] G. E. Coates and C. Parkin. "Tertiary phosphine complexes of trimethylgold: infrared spectra of complexes of gold and some other metals". In: *J. Chem. Soc.* (o 1963), pp. 421–429. DOI: 10.1039/JR9630000421.
- [2] A. Tamaki and J.K. Kochi. "Formation and decomposition of alkyl-gold(I) complexes". In: *Journal of Organometallic Chemistry* 61 (1973), pp. 441–450. DOI: 10.1016/S0022-328X(00)86574-2.
- [3] Sanshiro Komiya, Thomas A. Albright, Roald Hoffmann, and Jay K. Kochi. "Reductive elimination and isomerization of organogold complexes. Theoretical studies of trialkylgold species as reactive intermediates". In: *Journal of the American Chemical Society* 98.23 (1976), pp. 7255–7265. DOI: 10.1021/ja00439a024.
- [4] S. Komiya and J. K. Kochi. "Electrophilic cleavage of organogold complexes with acids. The mechanism of the reductive elimination of dialkyl(aniono)gold(III) species". In: *Journal of the American Chemical Society* 98.24 (1976), pp. 7599–7607. DOI: 10.1021/ja00440a025.
- [5] Jack L. Davidson, Phillip John, Peter G. Roberts, Michael G. Jubber, and John I. B. Wilson. "Laser Photochemical Deposition of Gold from Trialkylphosphine Alkyl-gold(I) Complexes". In: *Chemistry of Materials* 6.10 (1994), pp. 1712–1718. DOI: 10.1021/cm00046a025.
- [6] Michiel Van Daele et al. "Plasma-Enhanced Atomic Layer Deposition of Nanostructured Gold Near Room Temperature". In: *ACS Applied Materials & Interfaces* 11.40 (2019), pp. 37229–37238. DOI: 10.1021/acsami.9b10848.
- [7] Matthew B. E. Griffiths, Peter J. Pallister, David J. Mandia, and Seán T. Barry. "Atomic Layer Deposition of Gold Metal". In: *Chemistry of Materials* 28.1 (2016), pp. 44–46. DOI: 10.1021/acs.chemmater.5b04562.
- [8] C. Frank Shaw and R. Stuart Tobias. "Bonding in methygold(I) and trimethygold(III) compounds. Nuclear magnetic resonance, Raman, and infrared spectra and normal coordinates". In: *Inorganic Chemistry* 12.5 (1973), pp. 965–978. DOI: 10.1021/ic50123a001.
- [9] Michiel Van Daele, Christophe Detavernier, and Jolien Dendooven. "Surface species during ALD of platinum observed with in situ reflection IR spectroscopy". In: *Phys. Chem. Chem. Phys.* 20 (39 2018), pp. 25343–25356. DOI: 10.1039/C8CP03585G.
- [10] Matthias M. Minjauw, Hannes Rijckaert, Isabel Van Driessche, Christophe Detavernier, and Jolien Dendooven. "Nucleation Enhancement and Area-Selective Atomic Layer Deposition of Ruthenium Using RuO₄ and H₂ Gas". In: *Chemistry of Materials* 31.5 (2019), pp. 1491–1499. DOI: 10.1021/acs.chemmater.8b03852.
- [11] Han-Gook Cho and Lester Andrews. "Infrared Spectra of CH₃-MX and CH₂X-MH Prepared in Reactions of Laser-Ablated Gold, Platinum, Palladium, and Nickel Atoms with CH₃Cl and CH₃Br". In: *Organometallics* 32.9 (2013), pp. 2753–2759. DOI: 10.1021/om400192v.
- [12] D. C. McKean, G. P. McQuillan, W. F. Murphy, and F. Zerbetto. "Vibrational spectrum and harmonic force field of trimethylphosphine". In: *The Journal of Physical Chemistry* 94.12 (1990), pp. 4820–4831. DOI: 10.1021/j100375a014.
- [13] Xuefeng Wang and Lester Andrews. "Infrared Spectra and DFT Calculations for the Gold Hydrides AuH, (H₂)AuH, and the AuH₃ Transition State Stabilized in (H₂)AuH₃". In: *The Journal of Physical Chemistry A* 106.15 (2002), pp. 3744–3748. DOI: 10.1021/jp0014105f.

- [14] Masatake Haruta. "Size- and support-dependency in the catalysis of gold". In: *Catalysis Today* 36.1 (1997), pp. 153–166. DOI: 10.1016/S0920-5861(96)00208-8.
- [15] L. Stobiński and R. Duś. "Molecular hydrogen chemisorption on thin unsintered gold films deposited at low temperature". In: *Surface Science* 298.1 (1993), pp. 101–106. DOI: 10.1016/0039-6028(93)90085-X.
- [16] H. Kariis, G. Westermark, I. Persson, and B. Liedberg. "Infrared Spectroscopic and Temperature-Programmed Desorption Studies of Dimethylphenylphosphine Adsorbed on the Coinage Metals". In: *Langmuir* 14.10 (1998), pp. 2736–2743. DOI: 10.1021/la971232n.
- [17] Kajsa Uvdal, Ingmar Persson, and Bo Liedberg. "Tricyclohexylphosphine Adsorbed on Gold". In: *Langmuir* 11.4 (1995), pp. 1252–1256. DOI: 10.1021/la00004a034.
- [18] Ulrich B. Steiner, Peter Neuenschwander, Walter R. Caseri, Ulrich W. Suter, and Fredi Stucki. "Adsorption of triphenylamine, triphenylphosphine, triphenylarsine, triphenylstibine, and triphenylbismuthine on gold and copper". In: *Langmuir* 8.1 (1992), pp. 90–94. DOI: 10.1021/la00037a018.
- [19] Gunnar Westermark, Hans Kariis, Ingmar Persson, and Bo Liedberg. "An infrared study on the chemisorption of tertiary phosphines on coinage and platinum group metal surfaces". In: *Colloids and Surfaces A: Physicochemical and Engineering Aspects* 150.1 (1999), pp. 31–43. DOI: 10.1016/S0927-7757(98)00536-6.
- [20] April D. Jewell, Heather L. Tierney, and E. Charles H. Sykes. "Gently lifting gold's herringbone reconstruction: Trimethylphosphine on Au(111)". In: *Phys. Rev. B* 82 (20 Nov. 2010), p. 205401. DOI: 10.1103/PhysRevB.82.205401.
- [21] Matthew B. E. Griffiths, Sara E. Koponen, David J. Mandia, Jennifer F. McLeod, Jason P. Coyle, Jeffrey J. Sims, Javier B. Giorgi, Eric R. Sirianni, Glenn P. A. Yap, and Seán T. Barry. "Surfactant Directed Growth of Gold Metal Nanoplates by Chemical Vapor Deposition". In: *Chemistry of Materials* 27.17 (2015), pp. 6116–6124. DOI: 10.1021/acs.chemmater.5b02712.
- [22] Adriaan J. M. Mackus, Noémi Leick, Layton Baker, and Wilhelmus M. M. Kessels. "Catalytic Combustion and Dehydrogenation Reactions during Atomic Layer Deposition of Platinum". In: *Chemistry of Materials* 24.10 (May 2012), pp. 1752–1761. DOI: 10.1021/cm203812v.
- [23] Feng-Xia Li and P. B. Armentrout. "Activation of methane by gold cations: Guided ion beam and theoretical studies". In: *The Journal of Chemical Physics* 125.13 (2006), p. 133114. DOI: 10.1063/1.2220038.
- [24] S. M. Lang, T. M. Bernhardt, R. N. Barnett, and U. Landman. "Size-Dependent Binding Energies of Methane to Small Gold Clusters". In: *ChemPhysChem* 11.7 (2010), pp. 1570–1577. DOI: 10.1002/cphc.200900844.
- [25] S. M. Lang, T. M. Bernhardt, R. N. Barnett, and U. Landman. "Temperature-Tunable Selective Methane Catalysis on Au₂⁺: From Cryogenic Partial Oxidation Yielding Formaldehyde to Cold Ethylene Production". In: *The Journal of Physical Chemistry C* 115.14 (2011), pp. 6788–6795. DOI: 10.1021/jp200160r.
- [26] S. M. Lang, T. M. Bernhardt, R. N. Barnett, and U. Landman. "Methane Activation and Catalytic Ethylene Formation on Free Au₂⁺". In: *Angewandte Chemie International Edition* 49.5 (2010), pp. 980–983. DOI: 10.1002/anie.200905643.
- [27] Sandra M. Lang, Thorsten M. Bernhardt, Valeriy Chernyy, Joost M. Bakker, Robert N. Barnett, and Uzi Landman. "Selective C-H Bond Cleavage in Methane by Small Gold Clusters". In: *Angewandte Chemie International Edition* 56.43 (2017), pp. 13406–13410. DOI: 10.1002/anie.201706009.

- [28] D. M. Cox, R. Brickman, K. Creegan, and A. Kaldor. "Gold clusters: reactions and deuterium uptake". In: *Zeitschrift für Physik D Atoms, Molecules and Clusters* 19 (1991), pp. 353–355. DOI: 10.1007/BF01448327. URL: doi.org/10.1007/BF01448327.
- [29] Anumita Paul, Michael X. Yang, and Brian E. Bent. "Disproportionation and coupling reactions of alkyl iodides on a Au(111) surface". In: *Surface Science* 297.3 (1993), pp. 327–344. DOI: 10.1016/0039-6028(93)90221-5.
- [30] A.M. Paul and B.E. Bent. "Alkyl Coupling on Copper, Silver, and Gold: Correlation Between the Coupling Rate and the Metal-Alkyl Bond Strength". In: *Journal of Catalysis* 147.1 (1994), pp. 264–271. DOI: 10.1006/jcat.1994.1137.
- [31] Peter J. Pallister and Seán T. Barry. "Surface chemistry of group 11 atomic layer deposition precursors on silica using solid-state nuclear magnetic resonance spectroscopy". In: *The Journal of Chemical Physics* 146.5 (2017), p. 052812. DOI: 10.1063/1.4968021.
- [32] P Gupta, A.C Dillon, A.S Bracker, and S.M George. "FTIR studies of H₂O and D₂O decomposition on porous silicon surfaces". In: *Surface Science* 245.3 (1991), pp. 360–372. DOI: 10.1016/0039-6028(91)90038-T.
- [33] A. Venkateswara Rao, F. Ozanam, and J. N. Chazalviel. "In Situ Fourier-Transform Electromodulated Infrared Study of Porous Silicon Formation: Evidence for Solvent Effects on the Vibrational Linewidths". In: *Journal of The Electrochemical Society* 138.1 (1991), pp. 153–159. DOI: 10.1149/1.2085526.
- [34] Shu Qin, James D. Bernstein, and Chung Chan. "Hydrogen etching for semiconductor materials in plasma doping experiments". In: *Journal of Electronic Materials* 25 (1996), pp. 507–511. DOI: 10.1007/BF02666628.
- [35] E.C. Onyiriuka. "Zinc phosphate glass surfaces studied by XPS". In: *Journal of Non-Crystalline Solids* 163.3 (1993), pp. 268–273. DOI: 10.1016/0022-3093(93)91304-L.
- [36] M. T. Edmonds, A. Tadich, A. Carvalho, A. Ziletti, K. M. O'Donnell, S. P. Koenig, D. F. Coker, B. Özyilmaz, A. H. Castro Neto, and M. S. Fuhrer. "Creating a Stable Oxide at the Surface of Black Phosphorus". In: *ACS Applied Materials & Interfaces* 7.27 (2015), pp. 14557–14562. DOI: 10.1021/acsami.5b01297.

Part IV

CONCLUSIONS AND OUTLOOK

*"Go back?" he thought. "No good at all! Go sideways?
Impossible! Go forward? Only thing to do! On we go!"*
- J.R.R. Tolkien, *The Hobbit*

SUMMARY AND FUTURE OUTLOOK

In this thesis, the steady growth and nucleation behaviour of the standard thermal platinum atomic layer deposition (ALD) process was investigated and a new gold plasma-enhanced atomic layer deposition (PE-ALD) process was developed and investigated. The main results and insights from this research are summarized below.

REACTION MECHANISM OF PLATINUM ALD Thermal ALD and PE-ALD of platinum, using MeCpPtMe_3 as precursor and O_2 gas or O_2 plasma as reactant, are studied with *in situ* reflection absorbance infrared spectroscopy (RAIRS) at different substrate temperatures. This is done to identify the functional groups that are present during platinum ALD and investigate the origin of the temperature dependent growth rate of the thermal process.

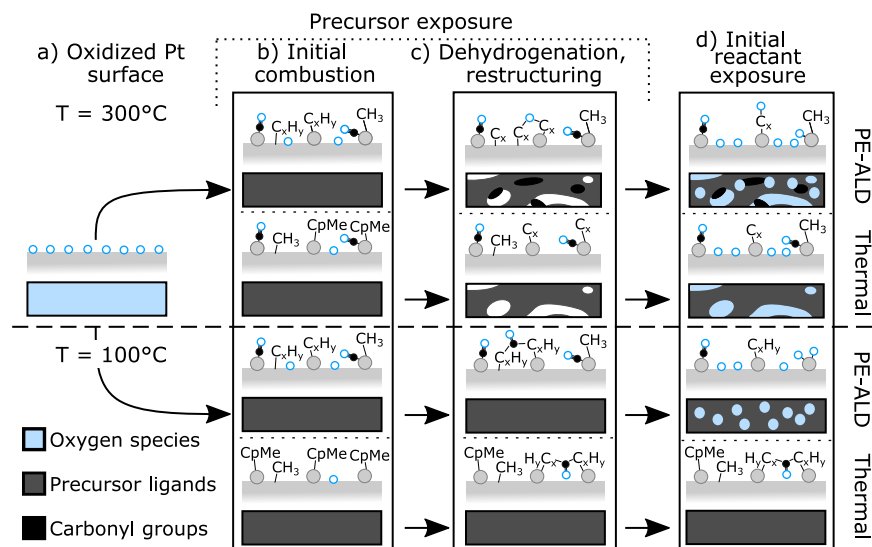


Figure 7.1: Schematic representation of *in situ* RAIRS results of the thermal Pt ALD cycle at 300 °C and 100 °C. Oxygen species (blue), precursor ligands (gray) and carbonyl groups (black).

Evidence is given that CH and C=C containing species are present on the surface after precursor exposure at low substrate temperatures ($<150^{\circ}\text{C}$), poisoning the surface during thermal ALD. Both species are removed by O_2 plasma enabling PE-ALD below 150°C through combustion reactions. Above 150°C , no CH stretching modes were detected and the C=C vibration diminished, indicating dehydrogenation reactions and ligand restructuring. In addition, the PE-ALD Fourier transform infrared spectroscopy (FTIR) spectra revealed the presence of combustion reaction products on the surface after precursor exposure. These were removed during the reactant exposure and during this exposure the formation of surface OH groups was found for both high and low substrate temperatures. We conclude that the decrease in growth rate for the thermal process is caused by the inability of the surface to properly dehydrogenate and restructure the poisoning precursor ligands.

NUCLEATION OF THERMAL PLATINUM ALD Understanding the nucleation behaviour of metal ALD processes is of significant importance for several applications. Therefore, *in situ* investigations of thermal platinum ALD at 300°C on planar SiO_2 substrates by means of X-ray fluorescence (XRF) and grazing-incidence small-angle X-ray scattering (GISAXS) are presented. The evolution in key scattering features provides insights in the growth kinetics of platinum deposits from small nuclei to isolated islands and coalesced worm-like structures. An analysis approach is introduced and validated to extract dynamic information on the average real space parameters, such as Pt cluster shape, size, and spacing. The results indicate a nucleation stage, followed by a diffusion-mediated particle growth regime which is marked by a decreasing average areal density and formation of laterally elongated Pt clusters. Growth of the Pt nanoparticles is thus not only governed by the adsorption of Pt precursor molecules from the gas-phase and subsequent combustion of the ligands, but is largely determined by the dynamic exchange of migrating Pt species on the surface between neighbouring Pt nanoparticles and diffusion-driven particle coalescence.

Moreover, the influence of the Pt precursor dose on the particle nucleation and growth is investigated. It is found that the precursor dose has a large influence on the nucleation speed, while the evolution of particle morphology as a function of Pt loading is in fact not influenced at all by the used precursor dose for oxygen based co-reactants. These results show that combining *in situ* GISAXS and XRF measurements provides an excellent experimental strategy to obtain new fundamental insights into the role of deposition parameters on the morphology of Pt ALD depositions.

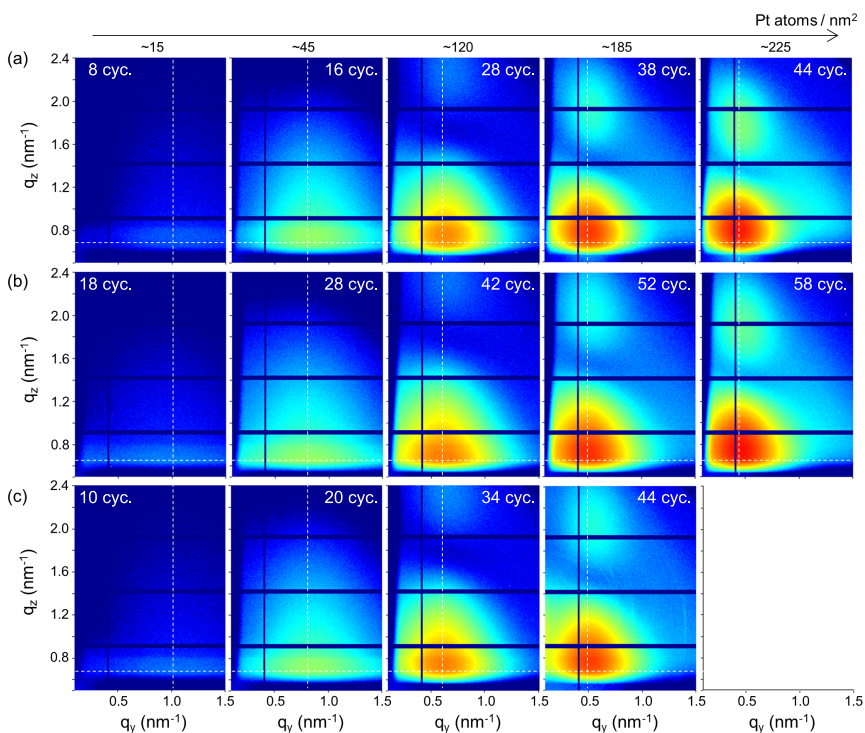


Figure 7.2: *In situ* measured 2D GISAXS patterns, obtained during three experiments, using different Pt precursor dose modes: (a) static mode, (b) pump mode, and (c) static mode during the first 4 ALD cycles, followed by pump mode. Independent of the used precursor mode, samples with the same Pt loading (columns) exhibit the same Pt nanoparticle morphology.

GOLD ALD A new PE-ALD process for gold deposition was developed. The process utilizes $\text{Me}_3\text{Au}(\text{PMe}_3)$ as the precursor and H_2 plasma as the co-reactant. A growth rate of 0.030 ± 0.002 nm per cycle on gold seed layers is achieved and both precursor and co-reactant exposures exhibit saturating behaviour across a broad temperature window: 50°C to 100°C . The deposited gold films are very pure with <1 atomic % carbon and oxygen impurities, and <0.1 atomic % phosphorous, as obtained from X-ray photoelectron spectroscopy (XPS). The gold film is deposited as nanoparticles on oxide surfaces, which coalesce into worm-like nanostructures during deposition. The particular nanostructure of as-deposited films offers stable free-space Raman enhancement, slightly more than

one order of magnitude lower than state-of-the-art solid-state substrates, but with room for further optimization. Beyond surface-enhanced Raman spectroscopy (SERS), nanoparticulate gold has very interesting and useful catalytic properties, making the reported gold nanoparticle ALD process also highly relevant towards heterogeneous catalysis applications.

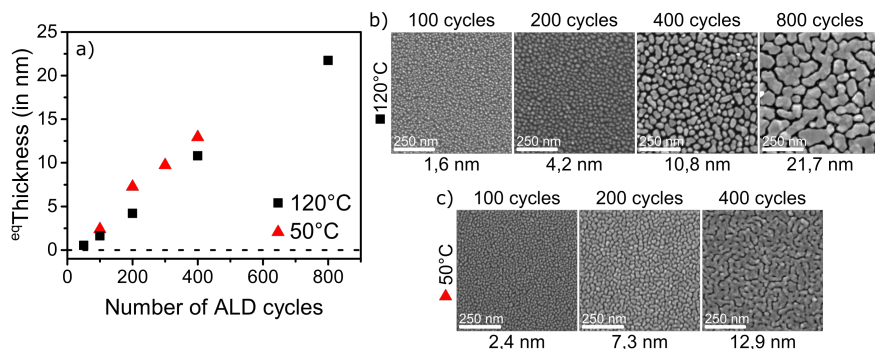


Figure 7.3: a) Equivalent thickness of gold as a function of the number of ALD cycles performed on a silicon substrate (native oxide) for a substrate temperature of 50 °C and 120 °C. b) SEM micrographs of Au films deposited at 120 °C. c) SEM micrographs of Au films deposited at 50 °C.

UNDERSTANDING THE NEW GOLD ALD PROCESS *In situ* RAIRS and *in vacuo* XPS measurements confirm that CH₃ and PMe₃ ligands remain on the gold surface after chemisorption of the precursor, causing self-limiting adsorption. Remaining surface groups are removed by the H₂ plasma in the form of CH₄ and likely as PH_xMe_y groups (x,y: 0-3), allowing chemisorption of new precursor molecules during the next exposure. The decomposition behaviour is investigated and it is found that above 100 °C the amount of precursor decomposition increases with substrate temperature and at 120 °C the decomposition becomes larger than the GPC of the ALD process, leading to chemical vapour deposition (CVD) growth behaviour. This decomposition behaviour is linked to the stability of the precursor ligands that govern the self-limiting growth during ALD. Desorption of the CH₃ ligands occurs at all substrate temperatures during evacuation to high vacuum, occurring faster at higher temperatures. The PMe₃ ligand is found to be less stable on a gold surface at higher substrate temperatures and its desorption is accompanied by an increase in precursor decomposition on a gold surface, indicating that the temperature dependent stability of the precursor ligands is an important factor to ensure self-limiting precursor adsorption during ALD. Remarkably, precursor

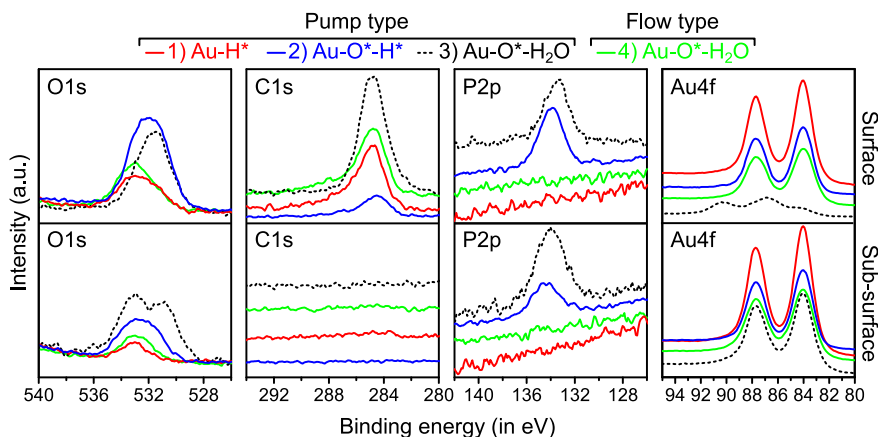


Figure 7.4: XPS spectra of four gold films on silicon (native oxide) substrates for the air-exposed samples (top panels) and after removal of the top surface by argon sputtering (bottom panels). The processes that produce pure gold films are the $\text{Me}_3\text{Au}(\text{PMe}_3) - \text{H}_2$ plasma process and the $\text{Me}_3\text{Au}(\text{PMe}_3) - \text{O}_2$ plasma - H_2O process in a flow type reactor. Using O_2 plasma and H_2O in a pump type system leads to the formation of amorphous gold-containing phosphate films. Swapping the H_2O exposure with H_2 plasma leads to metallic gold films, however, the phosphate impurities are not completely removed.

decomposition does not occur on a SiO_2 surface, *in situ* transmission absorption infrared experiments indicate that nucleation on a SiO_2 surface occurs on Si-OH groups. The use of O_2 plasma and H_2O as co-reactants in a pump-type ALD system is compared to the gold films that are obtained in a flow-type reactor. Instead of a metallic gold film, amorphous gold-containing phosphate films were obtained. Changing the H_2O exposure to H_2 plasma leads to the formation of metallic films, although it is not sufficient to remove the phosphate impurities.

7.1 INVESTIGATE AN ALD PROCESS, START TO FINISH

It is possible to investigate and characterize any ALD process by using the experimental techniques presented in this thesis. This section will present a general strategy to investigate an ALD process from start to finish. In a pump type ALD reactor, every ALD process requires a volatile precursor that can be introduced into the reaction chamber and some co-reactant(s) that can react with the precursor to deposit material on the substrate.

The first thing to verify is whether a decent precursor exposure can be delivered to the surface of a sample. This can be done by monitoring the pressure in the chamber and an increase should be observed when the precursor is introduced in the chamber. However, when a carrier gas is used for the precursor this is not a valid approach, as the pressure in the chamber will reflect the pressure of the carrier gas. Luckily there exist other methods to determine if the precursor can enter the chamber. For example, by using QMS measurements to detect fragmentation products that can be linked to the precursor molecule, by monitoring the mass gain of a sample with quartz crystal microbalance measurements, or by heating the substrate above the decomposition temperature of the precursor to intentionally cause precursor decomposition and deposition on the substrate. These deposits can then be measured *ex situ* with, for example, XRF.

With the precursor reaching the substrate it is possible to determine the ALD characteristics of the process. This entails determination of saturating behaviour for both the precursor and co-reactant, determine the temperature window for which saturating behaviour occurs, and the growth per cycle of the process (which might vary with deposition temperature).

For materials that are not metallic it is possible to use *in situ* spectroscopic ellipsometry (SE) to determine the saturation behaviour of the precursor and co-reactant. Changes in film thickness can be monitored with *in situ* SE during the ALD process. Based on the change in film thickness after a few ALD cycles it is possible to determine the GPC for the used deposition parameters. This makes it possible to investigate a broad range of deposition parameters and determine the influence on the GPC with only a few depositions.

The use of *in situ* SE works great on materials that do not heavily absorb in the used wavelength region used by SE, which is the case for metallic films. As a result it is not possible to use *in situ* SE to characterize an entire set of deposition parameters during a single ALD deposition. Instead, a new experiment needs to be performed to investigate a change to the deposition parameters and the deposited layer needs to be analysed after the experiment. Typically, a few 100 ALD cycles are required to get a sufficiently thick layer that can be analysed with XRR (for smooth layers) or XRF (for rough layers).

When the saturating behaviour of a precursor is determined it is important to verify that the saturation is real and not caused by supply limitations of the precursor. To verify this it is possible to use conditions for which intentional over exposure occurs. This can be done by connecting an additional precursor source in parallel and utilizing both sources simultaneously during the ALD process. Then it is possible to verify that the

process behaves linearly with respect to the number ALD cycles, which is the expected behaviour for ALD processes.

After saturating behaviour is proven and supply limitations are proven to lead to fake saturating behaviour, it is important to investigate if there are any combinations of substrate types and substrate temperatures that can lead to interesting behaviour during the precursor exposure. As seen in Chapter 6 during this thesis for Au ALD, for which the precursor exposure leads to deposition on Au layers without the use of a co-reactant above a substrate temperature of 100 °C. Of course additional experiments are required to determine if such behaviour occurs for certain combinations of substrate type and substrate temperature.

At this stage it is possible to reliably deposit films with the investigated ALD process. However, the composition, crystallinity, morphology of the deposited films are unknown. These properties can be determined with several *ex situ* measurements. The composition and purity of the deposited films can be obtained from XPS measurements, as carbon and oxygen impurities are harder to detect with XRF or EDX measurements. In addition, information about the oxidation state of the material can be obtained from XPS measurements. XRD can be used to determine the presence of crystalline phases in the deposited films. And the morphology of the films can be investigated with SEM/TEM measurements.

With the process characterized and the properties of the deposited films known, all that is left is to determine the reaction mechanism of the process and determine its nucleation behaviour. Both can be very challenging to investigate and require a lot of carefully planned experiments, this is clearly reflected by the amount of publications that are solely dedicated to the reaction mechanism and nucleation behaviour of the 'standard' Pt ALD process.

Investigating the reaction mechanism of the process requires several separate experiments, each uncovering a part of the puzzle. A good way to start is by investigating which by-products are produced during the precursor and co-reactant exposures, these by-products can be identified with *in situ* QMS measurements. Of course, these by-products originate from chemical reactions on the surface of the substrate and therefore it is important to investigate which surface groups are present during the ALD process. One way to investigate the surface species is by using *in situ* FTIR measurements. This method can be used during both the nucleation of the deposited material and during the steady growth regime. If the deposited material is not transparent for IR radiation then it will not be possible to investigate the steady growth regime in transmission mode. Instead it will be necessary to perform FTIR measurements in re-

flection mode. It might be necessary to obtain an absorption spectrum of the precursor in the gas phase, this can act as a reference for the FTIR measurements and in addition help with identifying the chemical groups that might be present on the surface. A downside to using FTIR measurements is that it is difficult to correlate the signal intensity of the surface groups to their actual concentration. It is possible that a small fraction of surface groups lead to a very large absorption signal in the spectrum, this makes it necessary to obtain a library of well calibrated spectra for every type of surface group. An easier method to determine the concentration of surface groups is by using *in-vacuo* XPS measurements. This provides the atomic concentration of the elements that are present on the surface of the sample, which provides complementary information to the FTIR measurements. In addition, the binding energy of the obtained XPS signal contains information about the oxidation state and binding environment of the atoms that are present on the surface. By using both measurement techniques it is possible to determine the surface groups that are present on the surface and their relative concentrations. Of course there might be other measurement techniques required to get a complete picture of the reaction mechanism, but using *in situ* QMS, *in situ* FTIR and *in-vacuo* XPS will reveal a lot of information about the reaction mechanism.

To properly investigate the nucleation behaviour it is necessary to have a good understanding of how the process behaves under certain conditions. The nucleation behaviour can be investigated by performing a lot of depositions, under different deposition conditions and for different numbers of ALD cycles. After every deposition it is possible to measure the ALD films with SEM/TEM measurements, which provide direct information about the properties of the imaged particles. The number of required depositions can be severely reduced and semi real-time information can be obtained when *in situ* GISAXS measurements are used during the ALD process, although it might require the use of a synchrotron X-ray source and evidently a compatible ALD chamber. The advantage of using *in situ* GISAXS is that one experiment provides a lot of information on how the particles evolve during the deposition. In principle it is possible to obtain a scattering pattern after every ALD cycle, which makes it possible to obtain very nice insights into how the morphology of the particles evolves during the deposition process. It should be noted that analysing the physical characteristics of the nanoparticles and their evolution during the ALD process, by SEM/TEM/ GISAXS measurements, does not directly reveal why the morphology changes during the process. To answer this question it will be necessary to link the chemistry of the ALD process to the evolution of the nanoparticles. Therefore, the insights that FTIR, XPS mea-

surements and other investigations provide into the reaction mechanism of the ALD process are crucial to explain why a process nucleates and its morphology changes the way it does.

7.2 SUGGESTIONS FOR FUTURE WORK

PLATINUM The two presented studies about platinum ALD expand on the knowledge of the steady state growth reaction mechanism and the nucleation process for the thermal and plasma-enhanced MeCpPtMe₃ - O₂ ALD processes. The investigation of the surface groups with *in situ* RAIRS measurements can be complemented by the use of *in-vacuo* XPS experiments at several substrate temperatures. In addition, this complementary method of *in situ* RAIRS and *in vacuo* XPS investigations can also be employed to investigate the reaction mechanism when other co-reactants are used, for example ozone, N₂ plasma, and NH₃ plasma. Concerning the nucleation aspect of the thermal platinum ALD process, the effect of other parameters than the precursor exposure can be investigated using the *in situ* XRF/GISAXS combination and the developed analysis method, such as substrate temperature, type of substrate, the influence of co-reactant exposure...

GOLD The existing gold ALD processes use a plasma or ozone as the co-reactant and therefore a true thermal gold ALD process has still not been developed. In that regard, the search for a true thermal process continues and probably requires some very specific chemistries that employ a highly oxidising or reducing chemical that does not decompose when it comes in contact with the substrate material or lead to the incorporation of impurities in the deposited film. There is very little known about the nucleation behaviour of the reported gold ALD processes, apart from the indication that lower substrate temperatures lead to less mobility and therefore a faster layer closure. In that regard, investigating the gold ALD processes with the combination of *in situ* XRF/GISAXS can yield a better understanding of how these processes nucleate. For some applications it can be interesting to deposit closed gold layers as quickly as possible and therefore research into enhancing the nucleation and adhesion to oxide substrates would be interesting. Investigating methods to limit the mobility of the gold atoms on the surface can lead to interesting pathways to obtain fast layer closure. One option would be to enhance the adhesion of the atoms to the surface by using substrates/pretreatments creating functional groups that strongly bind to gold, such as sulphur based groups. Another option can be the exposure of the substrate to other molecules which physically reduce the mobility of the atoms on the surface.

PUBLICATIONS

PUBLICATIONS / SUBMITTED / TO BE SUBMITTED IN INTERNATIONAL JOURNALS

- *In situ Monitoring of Nucleation and Island Growth Mode during Atomic Layer Deposition of Platinum*
J. Dendooven, **M. Van Daele**, E. Solano, A. Resta, R. K. Ramachandran, M. M. Minjauw, A. Vlad, G. Portale, and C. Detavernier
journal title, (2020)
- *Reaction mechanism of the $Me_3Au(PMe_3)-H_2$ plasma-enhanced ALD process*
M. Van Daele, M. B. E. Griffiths, M. M. Minjauw, S. T. Barry, C. Detavernier, and J. Dendooven
Physical Chemistry Chemical Physics, (2020)
- *In situ study on the thermal stability of supported Pt nanoparticles and their stabilization via Atomic Layer Deposition overcoating*
E. Solano, J. Dendooven, J. Feng, P. Brüner, M. M. Minjauw, R. K. Ramachandran, **M. Van Daele**, K. Van de Kerckhove, T. Dobbelaere, A. Coati, D. Hermina Merino, and C. Detavernier
Nanoscale, (2020)
- *Atomic layer deposition of localised boron- and hydrogen-doped aluminium oxide using trimethyl borate as a dopant precursor*
F. Mattelaer, **M. Van Daele**, M. M. Minjauw, M. Nisula, S. D. Elliott, T. Sajavaara, J. Dendooven, and C. Detavernier
Chemistry of Materials, (2020)
- *Study of the surface species during thermal and plasma-enhanced atomic layer deposition of titanium oxide films using in situ IR-spectroscopy and in vacuo X-ray photoelectron spectroscopy*
S. S. T. Vandenbroucke, E. Levrau, M. M. Minjauw, **M. Van Daele**, E. Solano, R. Vos, J. Dendooven, and C. Detavernier
Physical Chemistry Chemical Physics, (2020)
- *The co-reactant role during plasma-enhanced atomic layer deposition of palladium*
J. Feng, M. M. Minjauw, R. K. Ramachandran, **M. Van Daele**, H. Poelman, T. Sajavaara, J. dendooven, and C. Detavernier
Physical Chemistry Chemical Physics, (2020)

- *Plasma-enhanced atomic layer deposition of nanostructured gold near room temperature*
M. Van Daele, M. B. E. Griffiths, A. Raza, M. M. Minjauw, E. Solano, J. Feng, R. K. Ramachandran, S. Clemmen, R. Baets, S. T. Barry, C. Detavernier, and J. Dendooven
 ACS applied materials & interfaces, **11** (2019), 37229
- *Chemical and Structural Configuration of Pt-Doped Metal Oxide Thin Films Prepared by Atomic Layer Deposition*
 R. K. Ramachandran, M. Filez, E. Solano, H. Poelman, M. M. Minjauw, **M. Van Daele**, J. Feng, A. La Porta, T. Altantzis, E. Fonda, A. Coati, Y. Garreau, S. Bals, G. B. Marin, C. Detavernier, J. Dendooven
 Chemistry of Materials, **31** (2019), 9673
- *Comparison of Free-Space and Waveguide-Based SERS Platforms*
 N. Turk, A. Raza, P. Wuytens, H. Demol, **M. Van Daele**, C. Detavernier, A. Skirtach, K. Gevaert, and R. Baets
 Nanomaterials, **9** (2019), 1401
- *Integrated silicon nitride electro-optic modulators with atomic layer deposited overlays*
 A. Hermans, **M. Van Daele**, J. Dendooven, S. Clemmen, C. Detavernier, and R. Baets
 Optics letters, **44** (2019), 1112
- *Surface species during ALD of platinum observed with in situ reflection IR spectroscopy*
M. Van Daele, C. Detavernier, and J. Dendooven
 Physical Chemistry Chemical Physics, **20** (2018), 25343
- *ALD assisted nanoplasmonic slot waveguide for on-chip enhanced Raman spectroscopy*
 A. Raza, S. Clemmen, P. Wuytens, M. Muneeb, **M. Van Daele**, J. Dendooven, C. Detavernier, A. Skirtach, and R. Baets
 APL Photonics, **3** (2018), 116105
- *Plasma-Enhanced Atomic Layer Deposition of Silver Using Ag (Fod)(PET₃) and NH₃-Plasma*
 M. M. Minjauw, E. Solano, S. P. Sree, R. Asapu, **M. Van Daele**, R. K. Ramachandran, G. Heremans, S. W. Verbruggen, S. Lenaerts, J. A. Martens, C. Detavernier, and J. Dendooven
 Chemistry of Materials, **29** (2017), 7114

DANKWOORD

Bij deze eindigt een lange rit van iets meer dan vier jaar, waardoor het nu ook tijd is om een aantal mensen te bedanken voor hun steun tijdens de afgelopen jaren zowel binnen als buiten de context van dit doctoraat. Eerst en vooral wil ik mijn promotoren bedanken, hun bijdrage was van onschatbare waarde. Christophe, bedankt om in je drukke agenda tijd te vinden om een presentatie of manuscript bij te schaven zodat de boodschap beter tot zijn recht kwam. Ik kan wel zeggen dat, mits voldoende opsplitsing, elke taak inderdaad 'maar vijf minuutjes werk was'. Jolien, bedankt om telkens tijd te willen nemen om de laatste resultaten te bespreken. Dit heeft ongelofelijk geholpen om doorheen de experimentele bomen het bos niet uit het oog te verliezen.

Gelukkig ben je in een onderzoeksgroep zoals CoCooN nooit alleen. Dit is uitermate handig in een aantal gevallen, zoals wanneer er eens een klein defectje is in het labo, je gedachten eens op orde moeten gesteld worden doormiddel van een korte koffiepauze of om een levensbedreigende situatie, zoals het gebrek aan koekjes, op te lossen.

En dan zijn er familie en vrienden die zich voornamelijk buiten de universiteitsgebouwen bevinden. In het bijzonder moet ik mijn ouders bedanken. Ze hebben er altijd voor gezorgd dat ik elke kans zonder zorgen kon oarmen, zonder hun steun zou ik niet staan waar ik nu sta. Matthijs, bedankt om de beste broer te zijn die ik mij kan voorstellen.

Als laatste en uiteraard belangrijkste, Ségolène, mijn meest enthousiaste supporter. Je aanhoudende steun en optimisme heeft mij door elk moeilijk moment geholpen, al heeft dat soms frustrerend veel enthousiasme geverg'd van jouw kant. Als je mij de voorbije vier jaar hebt kunnen uitstaan, kunnen we samen alles aan.

Michiel Van Daele
October 2020